Structural Evolution in the Dynamic Plasticity of FCC Metals

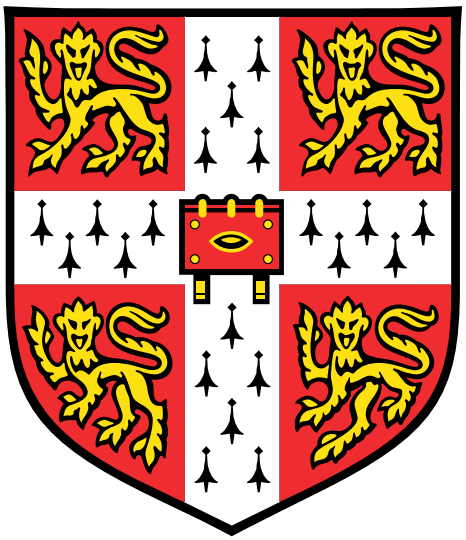

Lewis John Lea

Department of Physics

University of Cambridge

This dissertation is submitted for the degree of

Doctor of Philosophy

Downing College February 2018

For my family.

Declaration

I hereby declare that except where specific reference is made to the work of others, the contents of this thesis are original and have not been submitted in whole or in part for consideration for any other degree or qualification in this, or any other university. This thesis is my own work and contains nothing which is the outcome of work done in collaboration with others, except as specified in the text and Acknowledgements.

Lewis John Lea

February 2018

Abstract

Above true strain rates of 10^4 s^{-1} FCC metals exhibit a rapid increase in strength. Understanding of the physical mechanisms behind this strength transition is hindered by the number and interdependence of candidate mechanisms. Broadly, contributions to strength can be split into 'instantaneous' effects and the more permanent 'structural' ones. In this thesis a series of experiments are presented which are designed to separate the two types of contribution.

Chapter 2 outlines the basics of dislocation plasticity, based on the seminal works of Taylor and Orowan. It then progresses on to discuss recent experimental and theoretical work on the understanding of slip as avalanche behaviour.

Chapter 3 summarises traditional modelling approaches for instantaneous strength contributions which are routinely applied below 10^4 s^{-1}. It then continues on to outline a number of different approaches which have been adopted to attempt to explain and model the strength transition.

Chapter 4 outlines the methods used in the earliest stages of the study: Instron and split Hopkinson pressure bar methods. Both methods are well established, and cover the majority of the range of rates under study. Emphasis is made on minimising experimental sources of error, and subsequently accounting for those which are unavoidable. Finally, the specimen material is introduced and is shown to be fit for purpose.

Chapter 5 presents a set of mechanical tests of specimens at strain rates between $10^4 - 10^5$ s^{-1}. The softening of the specimens with increased temperature is observed to increase with strain rate, both in absolute terms and when normalised to the 300 K measurement for

each strain rate. The observations are most easily explained if the strength transition is due to an increase in early stage work hardening, however, some anomalous behaviours remain.

Chapter 6 introduces a new experimental technique; direct impact Hopkinson pressure bars, required to perform experiments shown to be necessary by the results of Chapter 5. Photon Doppler velocimetry is applied to the projectiles used in experiments, removing one of the most significant flaws of the technique, and creating a more confident basis with which to perform further experimental work.

Chapter 7 presents a series of 'jump tests' at ambient temperatures. Specimens are deformed at strain rates ranging from 10^{-2} to 10^{5} s^{-1} to a fixed strain of 0.1, then reloaded to yield at a strain rate of 10^{-1}. The yield point at reload is shown to have the same rapid upturn as seen when the specimens were deforming at high rates, providing strong evidence that the increase in strength is due to changes in the underlying dislocation structure, rather than a dynamic effect, as it remains even when the high strain rate is removed.

Chapter 8 continues on from the conclusions of Chapter 7. Jump tests are expanded to a variety of temperatures and strains, to provide a more complete characterisation of metal behaviour. No dramatic change in the saturation of work hardening is observed to coincide with the increase in early stage work hardening.

Chapter 9 discusses discrepancies between contemporary high rate models and recent developments in the understanding of plasticity being an avalanche process. Potential consequences of incorporating avalanche plasticity into high rate models are explored. Particular attention is paid to Brown's observation that based on quasi static observations of avalanche behaviour, the formation of dislocation avalanches will begin to fail at strain rates of approximately 10^{4} s^{-1}. Consequences of the progressive breakdown of avalanche behaviour are discussed with respect to the experimental observations presented in earlier chapters.

In Chapter 10, we will discuss the key conclusions of the work. Finally, a number of avenues are proposed for building upon the current work both theoretically and experimentally.

Publications

Invited: 'High Strain Rate Material Response'
Chapter in The Encyclopaedia of continuum mechanics
In preparation for Springer Nature
L. Lea and S. Walley

Enhanced structural evolution in the dynamic plasticity of FCC metals
In preparation for submission to Physical Review Letters.
L. Lea and A. Jardine

Measuring structural evolution in the dynamic plasticity of FCC metals
The proceedings of the 20th Biennial APS Conference
on the Shock Compression of Condensed Matter
L. Lea and A. Jardine

Impact performance of aluminium foams in a direct impact Hopkinson bar
The proceedings of the 20th Biennial APS Conference
on the Shock Compression of Condensed Matter
T. Cowie, C. Gurnham, C. Braithwaite, L. Lea

Characterisation of high rate plasticity in the uniaxial deformation of high purity copper at elevated temperatures
Under review for the International Journal of Plasticity
Provisionally Accepted
L. Lea and A. Jardine

A review on the strain rate dependency of the dynamic viscoplastic response of FCC metals
Progress in Materials Science (**2017**)
DOI: 10.1016/j.pmatsci.2017.04.004
F. Teixeira-Dias, F. Salvado, S. Walley, L. Lea, J. Cardoso

Constitutive analysis of biomedical grade Co-27Cr-5Mo alloy at high strain rates
Material Science and Engineering A (**2017**)
DOI: https://doi.org/10.1016/j.msea.2016.11.071
D. Trimble, H. Shipley, L. Lea, A. Jardine, G. E O'Donnell

Application of photon Doppler velocimetry to direct impact Hopkinson pressure bars
Review of Scientific Instruments (**2016**)
DOI: 10.1063/1.4940935
L. Lea and A. Jardine

Two-wave photon Doppler velocimetry measurements in direct impact Hopkinson pressure bar experiments
The European Physical Journal Conferences (**2015**)
DOI: 10.1051/epjconf/20159401063
L. Lea and A. Jardine

Acknowledgements

The research presented in this thesis was performed in the Surface, Microstructure and Fracture (SMF) group of the Cavendish Laboratory, under the supervision of Dr. Andrew Jardine. I am grateful to Dr. Jardine for the opportunity, as well as his supervision and support throughout.

I would like to thank Dr. David Williamson, who helped me with many of the finer parts of Hopkinson bar experiments. Notably, he introduced me to laser based measurements, which went on to become both a major part of my work, and a small obsession. On behalf of all of SMF, I would also like to thank David for representing the group in some of the more abstract traditions of international conferences.

Dr. Nick Taylor was an invaluable sounding board for virtually all of my research. Nick wrote the exceptionally thorough routine with which my laser based measurements were analysed. He also provided a stable foundation key to building group pub trips.

Dr. Christopher Braithwaite also provided an invaluable daily sanity check, personal or otherwise. I would like to thank him for his support, especially the opportunity to run two master's research projects, expanding the applications of methods developed for this thesis. Of marginally less relevance to my research, he also taught me the ways of the cryptic crossword.

I am thankful to Dr. Stephen Walley, who provided me with a number of publishing opportunities. He also tirelessly worked to provide me with notifications of any publications

related to my work (or, for reasons I am still not sure of, by authors in any field with my surname.)

Dr. Mick Brown was kind enough to give me a lot of his time, discussing the core workings of his avalanche plasticity theories. He also provided extremely important discussion regarding some of the key experimental outcomes of my work.

I would like to thank Sue Gymer for many things, most importantly making me feel welcome from the moment I joined the group.

I would like to thank all of the fellow PhD students that I was lucky enough to share my time at SMF with; Sarah Ward, Arthur Henderson, Ryan Potter, James Edgeley, Sara French, Neil Hamilton, Ben Butler and Dr. Rachael Boddy. In particular, I would like to thank Dr. James Perry: much of the proof of principle for my work was performed using laser equipment he designed and built. During my time in the group, SMF had many administrators, I would like to thank them all for their hard work, in particular Olga Kotlyar and Daniel Sargent.

My PhD was financially supported by the EPSRC, QinetiQ and Downing College. I am exceptionally grateful to Peter Gould and Phillip Church at QinetiQ, both for their personal efforts in creating the studentship and their insight in the formative stages of the study.

Outside of the lab, I would like to thank the Downing College MCR committee for the 2013-2014 term. My time spent working with the committee was some of the most enjoyable of my time as a student.

I would also like to thank those I lived with during my PhD. Firstly, from my time in Oxford Road, Dr. Tom Talbot and the (hopefully) soon to be doctors Jordan Rush, David Roche and James McTavish. There is little I can write about these people that is fit for the current publication. It was fun.

In my final year I lived with Dr. Maite Ortiz-Suarez and Dr. Clare Rumsey. I would like to thank them both for their efforts towards keeping me relatively sane during the final stretch.

Finally, I am grateful to my family for their seemingly limitless patience and encouragement. My mother, Sally, and my father, Graham, have done more to support me than anybody could ever ask for, and I will always be thankful for them. The same is true for my sister, India, and grandmother, Shirley. I am lucky to have them.

Table of contents

Nomenclature

Roman Symbols

A	Area
$\mathbf{a}$	Lattice vector
B	Dislocation drag coefficient
$\mathbf{b}$	Burgers vector
$\mathbf{C}$	Stiffness tensor
C_l	Longitudinal wave speed
c_p	Specific heat capacity
C_s	Shear wave speed
C_Z	Axial wave velocity in a Hopkinson bar
d	Average grain size
E	Energy
$\bar{E}_{Ph}$	Average phonon energy
f	Frequency

$\mathbf{F}$	Force
F_T	Bowing tension
f_D	Vibrational frequency of a dislocations
F_L	Drag force per unit length
G	Shear modulus
H	History function
h	Dislocation dipole height
$\hbar$	Reduced Planck constant
I	Intensity
K	Spring constant
k_B	Boltzman constant
L	Distance between pinning points in a dislocation forest
l	Length
$\mathbf{L}$	Local tangent vector
l_0	Initial Length
L_a, L_b	Slip band axes in slip plane
L_c	Slip band axis normal to slip plane
M	Taylor Factor
m	Mechanism dependent dislocation recovery sensitivity

m_D Dimension sensitivity in SOC relations

N Number of dislocations

N_p Number of planes adopted by a slip band

P Pressure

p, q Barrier shape parameters in MTS model

p_D Momentum of phonon at Debye energy

R Dislocation recovery function

r Specimen radius

r_0 Initial specimen radius

T Temperature

t Time

t_{pinned} Time dislocations spend pinned

t_{travel} Time dislocations spend travelling between pinning sites

$\mathbf{u}$ Displacement

U Potential energy/barrier

u_B Diameter of terminated slip band

U_η Normalised thermal barrier to recovery

V Voltage

$\bar{v}$ Drift velocity of a dislocation

$\mathbf{v}$	Unpinned dislocation velocity, drag limited
Δx_p	Separation between parallel slip planes
x, y, z	Cartesian co-ordinates
Z	Acoustic impedance

Greek Symbols

α_η	Fitting coefficient for plateau stress models
α_j	Taylor hardening coefficient in for a slip system denoted by j
α_T	Hardening coefficient in Taylor model
α_V	Strain gauge calibration coefficients
χ	Acoustic amplitude
$\dot{\varepsilon}$	Uniaxial true strain rate
$\dot{\varepsilon}_\phi$	Reference strain rate in instantaneous rate scalar models
ε	Uniaxial true strain
ε_{eng}	Engineering Strain
ε_η	Reference rate for recovery processes
ε_i	Strain at interrupt
Γ	Grüneisen parameter
γ	Local shear strain in a crystal lattice
γ_v	Lorentz factor for a speed of v

$\dot{\gamma}$	Local shear strain rate
κ	SOC Probability exponents
Λ	Dislocation generation/storage function
λ	Wavelength
η	Plateau stress
μ	Coefficient of friction
ν_p	Poisson's ratio
ω_D	Debye frequency
Φ	Wave phase
ϕ	Current condition stress scalar
Ψ_B	Volume fraction occupied by slip band
Ψ_O	Volume fraction of obstacles in a lattice
ρ	Planar dislocation density
ρ_a	Atomic density
ρ_M	Mass density
ρ_e	Edge dislocation density
ρ_i	Immobile (or forest) dislocation density
ρ_m	Mobile dislocation density
ρ_s	Screw dislocation density

Σ	Initial value of the mechanical threshold
σ_Y	Yield stress
σ_0	Athermal stress
σ_f	Flow stress
σ_R	Yield stress upon reloading
σ_p	Plastic stress / Mechanical threshold Stress
$\hat{\sigma}$	Thermal component of the flow stress
σ_{PN}	Peierls-Nabarro stress
τ	Local shear stress
Θ	Work hardening function, $\frac{\partial \sigma_p}{\partial \varepsilon}$
Θ_0	Initial (Stage II) work hardening rate
τ_p	Local shear value of the mechanical threshold
θ	Angle
θ_D	Debye temperature
θ_e	Effective angle between slip band and slip plane
ξ	Mean Free Path
ζ	Activation volume

Acronyms / Abbreviations

BCC Body Centered Cubic

DDD Discrete Dislocation Dynamics

DIHB Direct Impact Hopkinson Bar

FCC Face Centered Cubic

HCP Hexagonal Close Packed

PC Particular Condition

PCD Polycrystalline diamond

SC Standard Condition

SHPB Split Hopkinson Pressure Bar

SOC Self Organised Criticality

Chapter 1

Introduction

Material strength is of central importance to engineering, determining the point at which deformation changes from elastic to plastic, the rate of subsequent deformation, and influencing when, where and how failure occurs [1, 2]. The study of strength is a vast field, incorporating many different material types and mechanisms [3–5] . Metal strengths alone incorporate physical fields such as quantum mechanics, fluid dynamics, wave dynamics, thermodynamics, statistical mechanics and special relativity to name but a few.

The metrics used to quantify the mechanical behaviour of a material are stress, σ, and strain ε. Stress quantifies the internal forces that neighbouring particles in the material exert on each other, and has dimensions of pressure (Pa). Strain measures deformation by accounting for the displacement of points on a body from their initial positions, excluding rigid body motion, relative to their initial spacing, and is dimensionless. In the general 3D scenario, both quantities are described by second rank tensors, describing linear and shear components about three (usually orthogonal) axes. The removal of rigid body motion forces the requirement that both tensors be symmetric, with 6 independent components, corresponding to the linear and shear vales for each axis. Increments in stress and strain are

then linked through a "stiffness" tensor, **C**;

$$\mathrm{d}\sigma = \mathbf{C}\,\mathrm{d}\varepsilon, \tag{1.1}$$

that accounts for the general 3D response of the material [6].

All of the studies discussed and performed in this thesis will occur in a quasi-1D uniaxial stress geometry. In uniaxial loading, the *applied* stresses and strains are along a single axis, other strains do occur, due to effects such as volume conservation or the material's Poisson's ratio. In uniaxial loading, relation 1.1 can be reduced into a 1D expression, providing a more simple framework with which to empirically study material behaviour.

In uniaxial deformation the strain imposed upon a material axis can be defined purely as a function of the material length along the axis of the applied deformation;

$$d\varepsilon = \frac{dl}{l} \qquad \therefore \qquad \varepsilon = \ln\left(\frac{l}{l_0}\right). \tag{1.2}$$

Meanwhile the stress can be quantified by the pressure required to deform the material, which typically varies with an arbitrary number of other parameters depending on the material of study;

$$\sigma = \frac{F}{A}. \tag{1.3}$$

Here F is the applied load required to deform the material and A is some area depending on both the material type and geometry.

Mechanical Behaviour in Metals

At sufficiently low strains (typically $< 0.2\%$), metals behave elastically; imparted deformation is completely recovered upon unloading. Above a certain applied stress, the material yields and begins undergoing plastic deformation, which is not recovered upon unloading.

In a general 3D deformation, the limit of elasticity is defined by a surface (known as the yield surface), in a coordinate space formed by the three principal stresses of the system. The principal stresses correspond to the longitudinal stresses along each of the three axes in the configuration for which all shear stress components vanish. Whilst the 3-vector defined by the principle stresses remains within the yield surface, deformation remains elastic. In time independent deformation, when the principle stress vector reaches the yield surface, plastic deformation occurs and increments in strain can be determined by the geometry of both the principle stress vector and the yield surface [6]. In time (or temperature) dependent plasticity the relationship between the principle stress vector and yield surface becomes more complex. Depending on the conditions of deformation, models exist where the principle stress can either trigger yield before reaching the yield surface [7] or where it is required to extend past the yield surface [6]

In uniaxial deformation the applied stress is already a principal stress (with the other two being 0) and the quasi-1D nature makes the yield surface collapse to a single value known as the yield stress, σ_Y. Again, uniaxial deformation greatly simplifies the process of relating measurements to the underlying material behaviour. In 3D deformation there are a number of yield criteria (functions of the principal stresses that define the yield surface), which can be chosen, an ambiguity avoided in uniaxial deformation. The applied stress required to continue deformation past yield at a given set of conditions is then known as the flow stress.

Figure 1.1 shows a typical stress strain curve for a metal undergoing uniaxial deformation. The solid blue line corresponds to an experiment where a material is deformed to some strain ε then unloaded, the total strain before unloading is

$$\varepsilon = \varepsilon_E + \varepsilon_p = \frac{\sigma}{E} + \varepsilon_p. \tag{1.4}$$

Upon unloading the elastic strain ε_E is recovered but the plastic strain ε_p remains. The dotted line corresponds to a test that is conducted without termination, eventually the material succumbs to some form failure mechanism such as fracture.

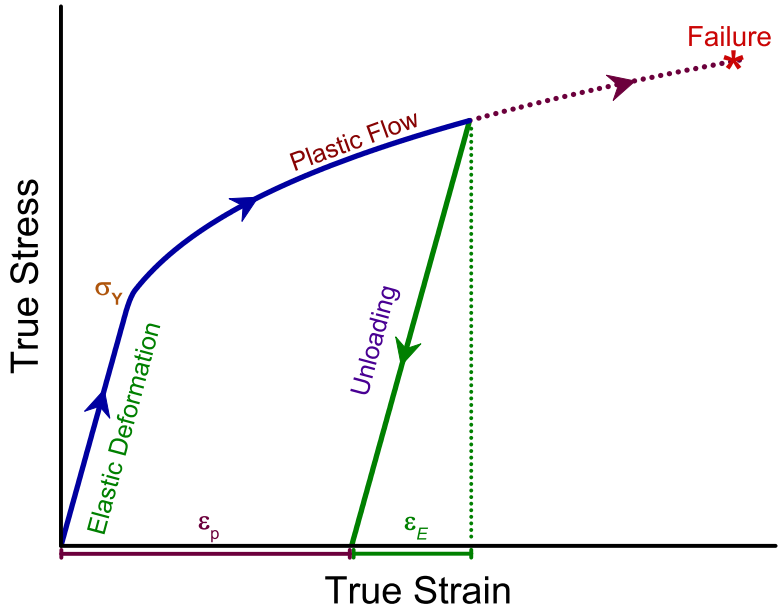

Fig. 1.1 A sketch of the stress-strain curve for a metal undergoing deformation at a fixed set of quasi-static conditions. The regions of the curve can broadly be separated into elastic behaviour, plastic behaviour and failure.

The onset of plastic deformation coincides with a substantial decrease in the gradient of the stress strain curve. The change arises from the main mechanism of imparting strain transitioning from the elastic deformation of atomic bonds to the creation and motion of crystal dislocations, discussed at length are discussed at length in chapters 2 and 3. The creation and motion of dislocations causes changes to occur in the metal's microstructure. Microstructural changes lead to work hardening; the increase in the flow stress with strain. Work hardening is retained, if a metal is deformed under a certain set of conditions to a certain flow stress, σ_f, then unloaded and subsequently reloaded under the same conditions, its yield stress, σ_Y will be close to the flow stress at the point of unloading.

In 3D work hardening is considered to correspond to changes in the yield surface. Depending on the material and loading geometry the general effects of work hardening are the

expansion of the yield surface (in isotropic or anisotropic hardening) and the translation of the yield surface (kinematic hardening) [6, 7]. Kinematic hardening is an important consideration as it can give rise to the Bauschinger effect [6]; where an increase in a material's compressive strength can be obtained at the expense of a decrease in tensile strength (and vice versa). For the purpose of this thesis all experiments will be performed in compression, reasons for this decision are discussed in chapter 4.

A large number of constitutive models (Appendix A) have been developed in attempts to describe the evolution of the yield surface under an arbitrary set of conditions. The aim of this thesis is to provide new insights that can be used improve the quality of constitutive models for FCC metals, known for their path dependent behaviour [8, 9], with a focus on strain rates in the range 10^4 to 10^5 s^{-1}.

History and Path Dependence

The response of all metals is dependent on their history. For example, the strength of a metal is dependent on its grain size [10, 11], which is dependent on its processing history (e.g. the rate at which it cooled during solidification). Path dependence refers to history effects that arise specifically due to plastic deformations of the material. FCC metals exhibit pronounced path dependent behaviour. The effects are less prominent in HCP, and almost entirely suppressed in BCC metals, the underlying reasons are discussed in chapter 2.

Figure 1.2 shows the effects of path dependence in an FCC metal by comparison to a BCC metal. For each metal, three low rate (which we will define as $\dot{\varepsilon} \leq 1$ s^{-1}) stress strain curves are shown. The two solid curves correspond to deformation at single strain rates, $\dot{\varepsilon}_2 > \dot{\varepsilon}_1$. The final dotted curve corresponds to loading that contains a "jump" in rate from the slow rate $\dot{\varepsilon}_1$ to the higher rate $\dot{\varepsilon}_2$. In all three scenarios deformation occurs at the same temperature, which remains constant throughout deformation. Within a lattice type, the specimens at the start of each experiment are completely identical. The key observation is

that after jumping to $\dot{\varepsilon}_2$, the path dependent FCC metal is softer than if it had always been deformed at $\dot{\varepsilon}_2$. Meanwhile the BCC metal, with suppressed path dependence, has a flow stress as if it had been deformed at $\dot{\varepsilon}_2$ since the start of the experiment. The difference in deformation conditions (loading path) has caused the two initially identical specimens to exhibit different subsequent behaviour.

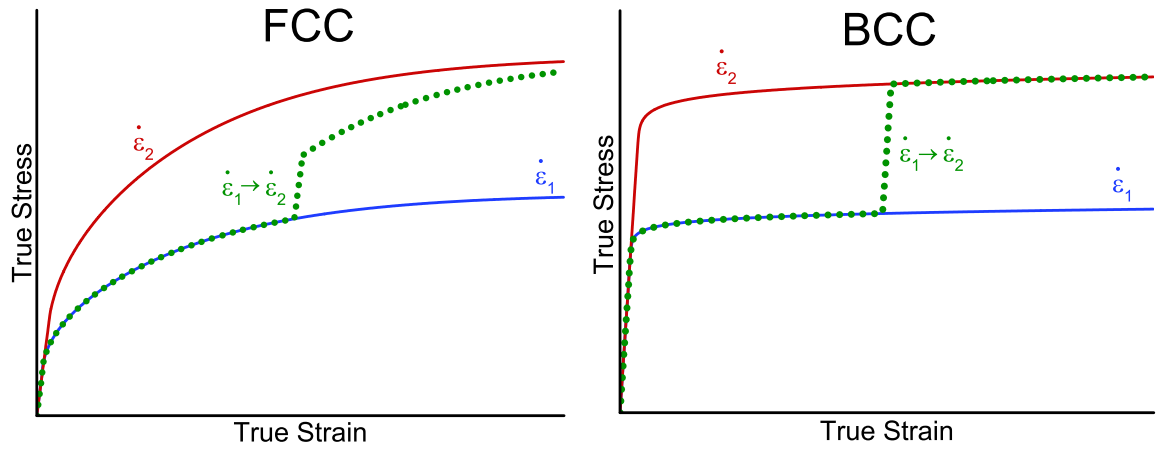

Fig. 1.2 Typical stress strain curves for FCC and BCC metals, intially identical for each lattice type, at different conditions. At low strains BCC metals exhibit neither strong path dependence or work hardening.

Path dependence arises due to the variations in the metal's rate of work hardening with the conditions (strain rate and temperature) under which the respective strain increment is imparted. In the case of a temperature jump during deformation, it is expected that being deformed at a higher temperatures leads to a lower strength in later deformation. Work hardening and path dependence are intricately tied to the metal's microstructure, their microscopic origins, as well as the subtleties of the stress strain curve are are the focus of discussion in chapter 2. It will become apparent in chapter 2 that the microstructural processes that give rise to path dependence occur in all metals, however, they are of specific interest in FCC metals as their relative contribution to strength is particularly high.

Interactions between instantaneous and path dependent contributions to strength leads to FCC metals having (under the current conditions of interest) more intricate material

behaviour than in BCC metals. Figure 1.3 shows an example of the edge profiles of FCC and BCC metals obtained from symmetric Taylor impact experiments performed at the Cavendish laboratory [12]. In symmetric Taylor impact, two identical cylinders collide head on, coaxially and at high speed ($\sim$100-300 ms^{-1}). In the non path-dependent BCC material, a smooth profile occurs at the specimen edge, caused by the monotonic decrease in strain rate with increasing distance from the impacted face. The FCC material exhibits a more complex profile; a 'bulge' is observed away from the impacted face and comparable in size to the largest features of the profile. Such a profile is not predicted by models that do not account for work hardening [12], and can only be accurately reproduced by models that account for path dependent work hardening.

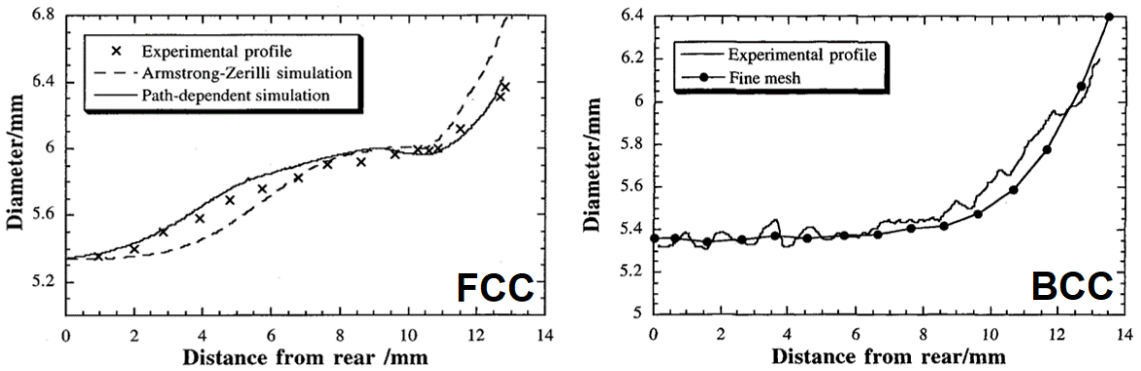

Fig. 1.3 The edge profiles of an FCC and BCC metal after Taylor impact experiments (outlined in the body text) at 200 ms^{-1}. The solid line on the FCC curve corresponds to the profile predicted by the path dependent Goldthorpe model [9] and the dashed line corresponds to a version of the Armstrong-Zerilli model [13] that models work hardening in a non path dependant manner. Both images are reproduced from Walley *et al.* [12].

Given the presence of such differences in a highly symmetric geometry such as Taylor impact, one can imagine the importance of correctly portraying the behaviour in real world scenarios. In practice, many commonly used metals adopt the FCC lattice structure, notably aluminium, copper, nickel, lead, silver, gold, platinum and iridium. The current study will focus on high purity metals, attempting to understand the fundamentals of the system in the absence of further complications, such as alloying or radiation damage.

Why 10^4 s^{-1}?

Low rate path dependence has been extensively studied by authors such as Klepackzo [8], Follansbee [14] and Gould [9]. Their studies have focused on experimentally separating instantaneous and path dependent contributions to strength, then in turn their influence on each other. These studies have led to a basic framework that is capable of faithfully reproducing the response of materials of arbitrary history at strain rates up to approximately 10^4 s^{-1}.

At rates close to 10^4 s^{-1} however, a sudden rapid increase in the flow strength of FCC metals is observed. The first observation of said increase was reported by Regazzoni, Kocks and Follansbee [16], the measurements of this seminal study are presented in figure 1.4. These measurements have been verified (with a large degree of scatter) by many authors, recently collated by Jordan *et al.* [17]. Despite the original observation of this phenomenon being decades old, the physical mechanisms underpinning the transition remain controversial [17–19].

A significant factor hindering the understanding of the nature of the strength transition (and the subsequent parametrisation of strength models) is the limited variaty in the nature

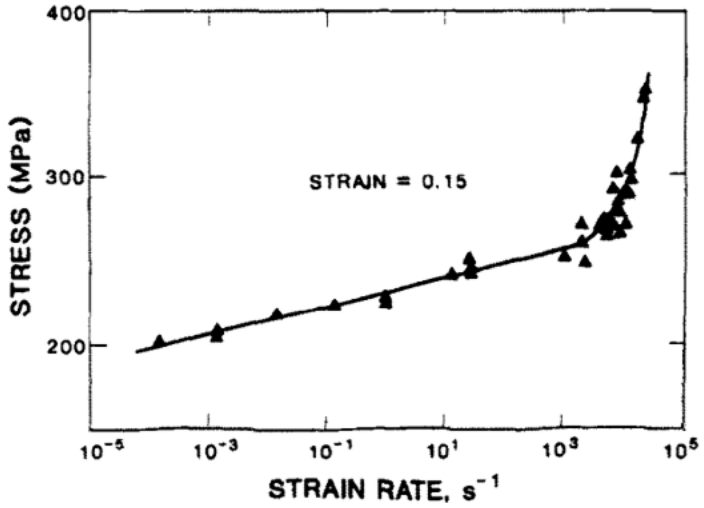

Fig. 1.4 The flow stress of an oxygen free high conductivity grade copper as a function of strain rate, reproduced from Follansbee et al [15].

of measurements available. Almost all measurements have performed been done so along a single path: a constant rate, and at room temperature, as evident from the review of Jordan *et al.* [17]. Importantly, there is a severe lack of any experimental work above 10^4 s^{-1} that attempts to separate instantaneous and path dependent effects in the same manner as Klepackzo [8], Gould [9] and Follansbee *et al.* [15] have below the transition. The significance of separating instantaneous and path dependent effects will become apparent in Chapter 3. A brief outline however is that of the two major mechanisms proposed for the increase in strength, one, termed 'phonon drag', predicts the increase in strength to occur only during the high rate deformation itself, whilst the other, which we will refer to as 'enhanced work hardening', predicts the increase in strength to be a more permanent, path dependent effect.

Thesis Overview

To summarise, the behaviour of FCC metals is defined by their path dependent nature. Currently this understanding breaks down at 10^4 s^{-1} due to a sudden, poorly characterised strength transition. Given the basic natures of the proposed mechanisms for this transition, a great improvement in understanding may be achieved by performing some kind of measurement that separates instantaneous and path dependent contributions to strength.

In Chapter 2, we begin by briefly outlining the fundamentals of metal plasticity, allowing us to understand why FCC metals exhibit such strong path dependence. We will expand from this basis to outline the almost universally adopted Orowan [20] and Taylor [21] models of metal strength in their most general forms. We will continue on to discuss more recent revelations, understanding flow as 'avalanche plasticity'. This is an area of research rarely discussed by the high rate metal strength community, despite realisations of an intimate relation between avalanche behaviour and work hardening, and thus path dependence.

In Chapter 3 we will begin by discussing the more established instantaneous rate effects below the transition, and continue on to outline the array of theoretical approaches used to attempt to model the transition itself.

Chapter 4 will outline two of the core experimental techniques used throughout both prior and current experimental studies: quasi-static experiments using Instron apparatus, and at higher rates split Hopkinson pressure bars [22]. Particular attention will be paid to sources and mitigation of experimental errors. Further emphasis will be on the introduction of photon Doppler velocity to the Cavnedish laboratory Hopkinson bar systems, a technique that enables the studies performed at higher impact velocities, and will prove invaluable in later work. Finally the material of study, a high purity copper, will be introduced and its fitness for purpose will be demonstrated. Particular focus is given to the specimen simultaneously being small enough to achieve high strain rates with minimal inertial effects, whilst simultaneously being representative of a true polycrystalline bulk.

In Chapter 5 we will present an initial set of experiments using a combination of the established methods. A miniaturised SHPB system will be used to study the deformation of the specimen material at elevated temperatures and strain rates above 10^4 s^{-1}. The study provides the first varying temperature measurements above the transition in the uniaxial stress geometry. Being the same geometry as the majority of literature studies in the range, the measurements are easily accessible for use in model calibration or verification. Rudimentary examination of the data will provide further justification for the remaining experimental work.

Chapter 6 will discuss experimental limitations that have prevented experimentalists from separating instantaneous and path dependent effects above 10^4 s^{-1} in the past. We will then build on direct impact Hopkinson pressure bar methods refined by Gorham, Field and Pope [23]. A novel application of photon Doppler velocimetry directly to the striker bar will provide key new measurements. The pressure wave in the striker will be measured, allowing

explicit verification of mechanical equilibrium, a requirement for obtaining valid strength measurements from Hopkinson bars. Furthermore, as the method enables measurement of the rise time of force at the impact specimen face, it will be used to ensure experiments can be performed that are a good approximation to a single condition path. These methods also show promise in studying a variety of other materials and potential future exploitation of the technique will be discussed.

Chapters 7 and 8 will present the core empirical results of the thesis. Using the newly established methodology, specimens will be deformed at strain rates between 10^4 and 1.5×10^5 s^{-1} and recovered at fixed strain, allowing for a subsequent path change. Reloading all of the specimens at 10^{-2} s^{-1} will present a basis for observing path dependent effects in the absence of instantaneous variations, allowing some separation of the effects. Key results obtained at ambient temperature will be presented in Chapter 7. Based on the observed behaviour, Chapter 8 will then expand measurements to a variety of temperatures and strains.

Chapter 9 will take a very different approach to the same problem. Based on observations made in Chapters 7 and 8, combined with observations for the literature, we will propose the beginnings of a model developed in collaboration with L.M. Brown [4]. The model will attempt to incorporate currently unaccounted-for avalanche plasticity effects into high rate metal deformation, focusing on the breakdown of self-organisation as deformation time-scales decrease.

Finally, Chapter 10 will draw together some of the more major results of the study. After a brief discussion of the conclusions and open questions, potential avenues and approaches for further work will be discussed.

Chapter 2

Path Dependence & Structural Evolution

In this chapter, we will outline the first of the two core metallurgical phenomena of study: path dependence. The path dependence of a metal is strongly linked to its structure across many potential length scales and has a complex influence on a metal's strength. The aim of this chapter is not to review every proposed model and mechanism in the literature, far too many exist. Instead the aim is to provide a simple basis from which most contemporary models build. The resulting picture will help to understand the motivation for, and models used in, the experimental work of later chapters. A collation of relevant models can be found in Appendix A.

The second phenomenon under study, (instantaneous) rate dependence, is outlined in Chapter 3. It should be noted that despite the separation, we will see that path dependence is itself rate dependent, and both phenomena are temperature dependent.

2.1 Three Term Framework

Before discussing the physical phenomena behind either instantaneous or history based strength mechanisms, we will outline the general framework in which these phenomena are typically modelled. In low rate deformation (below 10^4 s^{-1}) a three term model is typically used [9, 14, 24],

$$\sigma_f(T,\dot{\varepsilon},\mathbf{H}) = \sigma_0 + \phi(T,\dot{\varepsilon})\sigma_p(\mathbf{H}) = \sigma_0 + \hat{\sigma}. \tag{2.1}$$

Where **H** is a quasi-state parameter, signifying that a given term is path dependent.

The first term, σ_0, is known as the athermal term, accounting for all strengthening processes that are independent of, or negligibly dependent on rate, temperature and history [9]. One of the most notable contributions to this term is Hall-Petch behaviour [10, 11] in which decreasing the size of grains increases the strength of the metal. This mechanism is physically rationalised as grain boundaries impeding micro-scale deformation processes, discussed in more detail in section 2.3, and typically modelled using the empirical relationship

$$\sigma_0 = \sigma_{00} + \frac{\alpha_{HP}}{\sqrt{d}}, \tag{2.2}$$

where d is the average grain size of a metal and α_{HP} is an empirical fitting parameter. σ_{00} has many general contributions including impurities in lattice solution or precipitated phases [25]. As this contribution to strength is not observed to be strongly path or rate dependent, it is not an area of focus for the thesis. It does however have meaningful repercussions on the selection of material for study, which will be discussed later.

The second term in equation 2.1, $\phi(T,\dot{\varepsilon})$, deals purely with instantaneous effects [9, 14, 24], the focus of Chapter 3. It is a scaling factor that reflects the increase in applied stress required to deform a metal more rapidly, and the decrease in stress required if thermal energy is provided in the stead of mechanical work. This term will be outlined in detail in Chapter 3.

Alternatively, $\hat{\sigma} = \phi\sigma_p$ is used to denote the general instantaneous stress above the athermal term.

The final term, σ_p, is known as the 'plastic' [9, 24] or 'mechanical threshold' [14] stress and corresponds to the stress above the athermal term that is required to initiate slip at 0 K. This term therefore keeps a record of material strength dependent on history but not instantaneous conditions. All path dependence is imparted through the mechanical threshold term. In almost all models the history parameter (**H**) is abandoned at this point and the mechanical threshold itself becomes the history term.

Being a path dependent term, there is no general closed expression for σ_p. Instead it is assumed that one can express the derivative of σ_p with respect to some variable, for example strain, which must a function of both history and current conditions,

$$\frac{\partial\sigma_p}{\partial\varepsilon_p} = \Theta(T, \dot{\varepsilon}, \sigma_p), \tag{2.3}$$

a relationship known as a Voce hardening law [26]. Assuming Voce behaviour has a profound consequence; if any two specimens, through different deformation histories, reach the same value of σ_p, then given the same instantaneous conditions, both their behaviour and the evolution of that behaviour will be the same, despite different history. The mechanical threshold stress therefore acts in a manner similar to a thermodynamic state parameter, however, strictly it is not one. The use of a quasi-state parameter reduces a practically unsolvable problem, requiring the entire history of a specimen to be completely known, to a solvable one, only requiring measurement of the current value of σ_p.

In adopting this framework, we have already abandoned several prominent models. Notably, we abandon all variations of the Johnson-Cook model [27], which is prominently used in many areas of plasticity, but cannot describe path dependence.

2.2 Work Hardening & Empirical Voce Behaviour

Before progressing to physical modelling, we will briefly outline the (low rate) path dependent behaviour that physical theories seek to explain, a brief overview of which was provided in Chapter 1. The key phenomenon driving path dependence, 'work hardening', was touched on in the previous section. The most simple description of work hardening is any increase in a material's strength as it is deformed. Under certain conditions materials may also 'work soften'. In the three-term framework, work hardening is encapsulated in the increase of the mechanical threshold stress.

Work hardening is generally considered to occur in successive 'stages' [4], each with a characteristic rate of work hardening, $\frac{\partial \sigma_p}{\partial \varepsilon_p}$, depicted in Figure 2.1. Early 'Stage I' work hardening is known as easy glide, due to having a low level of work hardening. Stage I is typically not observed in polycrystals or at ambient temperatures.

Stage II work hardening is one of two stages of key significance to the studies of this thesis. Stage II is characterised by a constant rate of work hardening, Θ_0. The value of Θ_0 is very weakly dependent on strain rate, and the ratio $\frac{\Theta_0}{G}$, where G is the shear modulus of the material, has very weak temperature dependence. The emergence of such a stable rate of

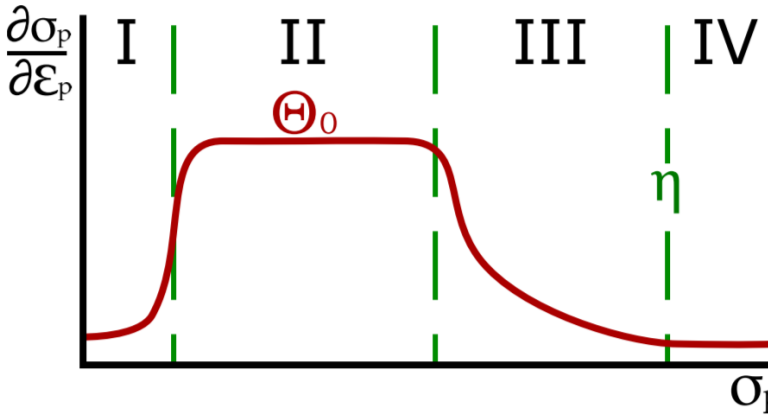

Fig. 2.1 A schematic of the rate of work hardening across each of the four successive stages of work hardening. Note that the transitions are typically better described by the stress thresholds rather than strain thresholds.

work hardening from rate and temperature dependent underlying processes is remarkable and remains an active area of research [4].

The second key stage is III, which is responsible for low rate path dependence. Without discussion of the controversial physical mechanisms (covered later), it manifests itself through the decrease of Θ to approximately zero at some rate and temperature dependent plateau stress, η. The rate of work hardening at arbitrary stress depends on how far the current mechanical threshold stress is from the plateau stress, and thus even at lower strains (or more importantly, mechanical threshold stresses), path dependence arises. Being saturative in nature, the reduction in Θ is more pronounced when the mechanical threshold stress is close to the plateau stress.

The appropriate regions of a stress strain curve corresponding to Θ_0 and η are shown in Figure 2.2. The figure also shows the typical nature of ambient temperature polycrystal curves; the effects of saturation begin very soon after yield, leading to a continuous rounding out rather than a well defined transition point.

Finally, Stage IV hardening is characterised by a low rate of work hardening, observed above the plateau ($\sigma_p > \eta$). This stage is outside the scope of current work and is typically

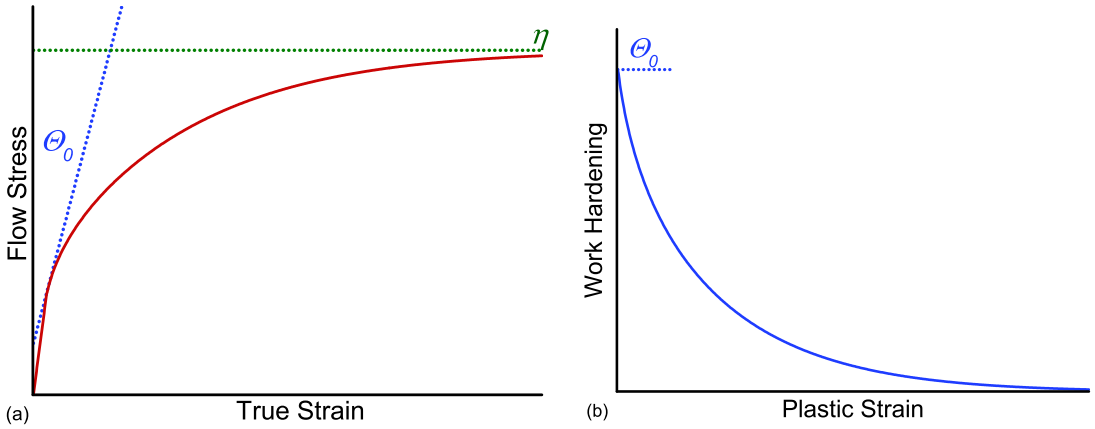

Fig. 2.2 Sketches showing (a) a typical single condition stress strain curve, saturating at some strength dependent on the current temperature and strain rate, (b) the rate of work hardening for a single condition up to the point of saturation.

neglected by many models. The existence of Stage IV should however be recognised when designing experiments and analysing measurements.

In empirical approaches, the key stages of work hardening (II and III) are typically modelled by fitting functions. Follansbee *et al.* [15] proposed the form

$$\frac{\partial \sigma_p}{\partial \varepsilon_p} = \Theta_0 \left[1 - \frac{\tanh\left(\alpha_\eta \frac{\sigma_p}{\eta}\right)}{\tanh\left(\alpha_\eta\right)} \right]. \tag{2.4}$$

A further widely used form is that proposed by Anand and Brown [24];

$$\frac{\partial \sigma_p}{\partial \varepsilon_p} = \Theta_0 \left(1 - \frac{\sigma_p}{\eta} \right)^{\alpha_\eta}, \qquad 1 \leq \alpha_\eta \leq 2. \tag{2.5}$$

In both cases, α_η is a dimensionless fitting parameter.

We will now address physical models of the origins of Θ_0 and η, beginning with the fundamental mechanisms on the atomic scale, progressing to discussion of the two most prevalent modelling approaches for work hardening.

2.3 Dislocations

In order to properly understand path and rate dependence, we must consider the underlying mechanisms that occur on the atomic scale. We will begin by imagining a perfect crystal lattice, in which all of the atoms are at energetic minima in positions defined by the properties of the constituent atoms. Typically metals adopt one of three Bravais lattice formations: 'face centered cubic' (FCC), 'body centered cubic' (BCC) or 'hexagonal close packed' (HCP).

All deformation, regardless of whether it is uniaxial compression, tension or shear actually arises from the motion of planes of atoms past each other on the crystal scale. The crystal planes with the lowest barrier to motion are known as 'slip planes'. Such movement is a shear deformation, all types of macro scale plasticity result from linear combinations of shears along multiple planes, with different orientations to the applied load.

Without specifying the underlying mechanism, we note that a single deformation event will split the metal into two regions - that which has moved or 'slipped' and that which has not. Unslipped regions are not defined as never having slipped, but as the region that does not slip in the current event. Volterra [28] originally observed that it is necessary that there must be some distortion, or interface between the two regions. In the interface region, atomic bonds will no longer be at energetically favourable lengths and some bonds may remain broken. Two examples of such an interface in a lattice are illustrated in Figure 2.3. The distorted region is raised to a higher energy than the lattice, with no immediate mechanism to remove the increase. These interfaces were coined 'dislocations' by G.I.Taylor in 1934 [29], and their behaviour underpins all of plasticity theory. It is much simpler to conceptualise and model dislocations than the multitude of atoms in the lattice. Furthermore, in practice dislocations move instead of atomic planes, simply due to the reduced number of atomic bonds that must be broken.

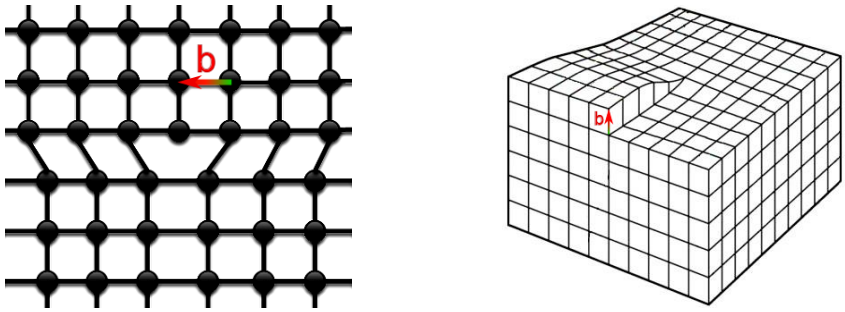

Fig. 2.3 Sketches of dislocations in an otherwise perfect simple lattice. On the left is an edge dislocation, caused by a bond mismatch leaving a line of bonds completely unpaired. On the right is a screw dislocation caused by an offset of part of a plane with reference to another, leading to a helical pattern of atom positions around the length of the interface. The different basic nature leads these two dislocations having different behaviour and mobility. Dislocations can be formed as a combination of the two states. The screw dislocation image was adapted from an original by Fernando et al [30]. similar images can be found in most dislocation textbooks.

The planar nature of slip allows us to determine two fundamental properties of dislocations. Firstly the dislocation, being the interface between two planar regions, must be a line defect. Secondly, a natural way to consider a dislocation population is the planar density, ρ, measured

in m^{-2} and interpreted as either the line length per unit volume or the number density of dislocations in a single plane.

If dislocations already exist in a lattice, the energetic barrier (and thus applied stress) required to move them between two adjacent sites, characterised by the Peierls stress [31], is typically orders of magnitude less than that required to move entire planes relative to each other. At low rates a majority of the strain is imparted by moving existing dislocations from site to site [20]. For a lone dislocation, we can describe strain due to through dislocation motion using the expression

$$\delta\gamma_{slip} = b\rho\bar{v}\delta t. \tag{2.6}$$

The scalar b corresponds to the length of the Burgers vector, **b**, depicted in figure 2.3 which denotes the direction and magnitude of the distortion to a lattice caused by a single dislocation and $\bar{v}$ corresponds to the average drift velocity of a dislocation [32].

The generation of a dislocation is in itself an introduction of strain into the lattice [20]. The strain introduced by creating dislocations can be expressed as

$$\delta\gamma_{gen} = b\Delta x_d \delta\rho, \tag{2.7}$$

where Δx_d is some small length scale corresponding to the displacement of a dislocation after nucleation [20, 33]

We have now expressed strain in two ways, the extensive uniaxial specimen strain, ε and the local shear on the atomic scale, γ. In a perfect polycrystal the macroscopic and microscopic values can be related by a constant, M, known as the Taylor factor [21]. The Taylor factor accounts for the averaging of the projection of the applied force onto each slip plane (individually known as Schmid factors [34]) for a single lattice orientation, then a subsequent averaging over all possible lattice orientations. The uniaxial and local strain are related through $\gamma = M\varepsilon$ and the uniaxial specimen stress, σ, and the local shear stress,

τ, are related through $\tau = \dfrac{\sigma}{M}$. For perfect polycrystalline copper, M has been measured as 3.06 [35].

At low rates, the motion of dislocations is considered to be the dominant contribution to strain, leading to an expression known as Orowan's law,

$$\dot{\gamma} = b\rho\bar{v}. \tag{2.8}$$

We should note that in a lattice with low dislocation density, the dislocations must travel at much greater speeds to achieve any given rate than if a larger dislocation density is present. Any metal in its soft or 'annealed' will not have a perfect crystal lattice within any of its grains, there will be some initial dislocation density typically, 10^{11} m^{-1} [36].

We shall make two final observations on the nature of individual dislocations before discussing emergent behaviour. Firstly, we should note that dislocations are capable of exerting a force on each other and thus acting as a barrier to dislocation motion [37]. If we consider a dislocation as a region of localised strain caused by broken bonds or altered bond lengths, these regions must be subject to some energetic penalty. In a simple elastic model, or by Taylor expansion with respect to the displacement of the atoms about their energetic minima, the energy penalty must be quasi-parabolic in displacement. The energetic penalty is lower if strain is spread out over some distance; the energy is lower for many bonds at low strain than one bond at the total strain. Secondly, we note that should these extended strain fields overlap such that the local strain is increased, the energy penalty will be greater than the sum of the individual dislocations in isolation, thus there will be a repulsive force between the two dislocations [3, 5]. Mathematically, the elastic energy stored in a dislocation is $\frac{1}{2}Gb^2$ per unit length, so the dislocations will repel if locally

$$\frac{1}{2}G(\mathbf{b}_1+\mathbf{b}_2)^2 > \frac{1}{2}G\mathbf{b}_1^2 + \frac{1}{2}G\mathbf{b}_2^2, \tag{2.9}$$

where the subscripts indicate two separate dislocations. The relation simplifies to the condition that $\mathbf{b}_1 \cdot \mathbf{b}_2 > 0$. Conversely, should the superposing strain fields negate each other ($\mathbf{b}_1 \cdot \mathbf{b}_2 < 0$), the interaction will be energetically favourable and will have an attractive effect.

The final observation is that the strain fields of two dislocations can also cancel out. Compatible dislocations under the right conditions ($\mathbf{b}_1 = -\mathbf{b}_2$) can annihilate [38]. Such processes are responsible for part of a phenomenon known as dynamic recovery [39], which in general corresponds to the removal of dislocation obstacles during deformation. Annihilation is clearly energetically favourable as it removes the elastic penalty for the existence of two dislocations. However in practice, the two dislocations may have to overcome some energetic barrier in order to annihilate, making the rate at which annihilation can occur dependent on specimen temperature and applied stress (or as a proxy, strain rate and mechanical threshold stress). Local but not complete annihilation can lead to 'foresting', an important strengthening mechanism discussed in section 2.4.

As an aside, dislocation motion enables us to better understand the Hall-Petch strengthening mechanism discussed in section 2.1. It is well known that different metallic grains correspond to different orientations of the crystal lattice [10]. For a dislocation to pass from one grain to another it must overcome a large energy barrier to migrate to the new orientation of the crystal plane. As the grains become smaller these barriers become more frequent, and thus the metal strengthens.

2.4 The Physical Origins of Path Dependence

2.4.1 The Peierls-Nabarro Stress

We have established that macro-scale deformation can be modelled as the motion of many atomic scale dislocations which can be created, annihilated and act as barriers for each other. The final concept we must discuss to understand why some metals are path dependent and others are not is the previously mentioned Peierls (or Peierls-Nabarro) stress. The Peierls-Nabarro stress, σ_{PN} is defined as the stress required to move a dislocation from one line of lattice site to the next in the absence of any other barriers [40]. In a pure metal it arises from a periodic potential caused by the motion of atoms about their energetic minima required to move the dislocation between two sites. In a pure metal, σ_{PN} is dependent on only the metallic element and fundamental geometry of the lattice, making it largely independent of sample history.

If we compare the geometry of the FCC and BCC lattices, we find the displacement due to a missing half plane (ie, the Burgers vector) is much larger in comparison to the inter-planar separation for BCC metals. This means that if a dislocation is to move between two sites, the surrounding atoms have to be pushed much closer to those in the neighbouring plane, and will thus feel stronger coulomb and 'hard-sphere' interactions. The Peierls stress of BCC metals is thus larger relative to other barriers than for an FCC metal [5]. Mathematically the geometry dependence of the Peierls stress is given by [40, 41]

$$\sigma_{PN} \propto \frac{G}{1-\nu_P} \exp\left(-2\frac{\pi}{1-\nu_P} \cdot \frac{\Delta x_P}{b}\right) \tag{2.10}$$

where Δx_P is the spacing between parallel glide planes and ν_P is the Poisson's ratio of the metal. Typical values of these parameters for FCC and BCC structures are [42]

	FCC	BCC
$\Delta x_P/b$	$\sqrt{2}$	$\sqrt{\frac{3}{4}}$
ν_P	0.35	0.29

Computing these values gives a Peierls stress, relative to the material's shear modulus, approximately 400 times greater in BCC metals should all other parameters be identical. The ratio has been experimentally confirmed [42].

2.4.2 Foresting

In FCC metals, the greatly reduced Peierls stress leads to the dominant structural strengthening mechanism being the interactions between dislocations. In principle there are many ways dislocations can interact. However, most physical models gather all interactions into a general foresting process. Dislocations only annihilate completely given the previously defined condition that $\mathbf{b}_1 = -\mathbf{b}_2$ along the entire dislocation. Given the array of possible Burgers vectors and slip planes, there is a significant probability this requirement will not be satisfied. However, dislocations can combine at any one point along their lengths if locally

$$\frac{1}{2}G(\mathbf{b}_1+\mathbf{b}_2)^2 < \frac{1}{2}G\mathbf{b}_1^2+\frac{1}{2}G\mathbf{b}_2^2. \tag{2.11}$$

Both dislocations are then 'pinned' in place if the Burgers vector at the junction does not lie in a permitted slip direction. The dislocation is then known as being 'sessile' [3]. In order to remobilise, the two dislocations must be separated to return them to permitted slip geometries. Wickhem *et al.* have shown point interactions to be responsible for the majority of foresting between two single dislocations [43].

Figure 2.4 depicts a dislocation trapped by two foresting partners, represented by two black circles and assumed to be orthogonal to the page. To determine the contribution of such a barrier to the material strength, we must determine the applied stress required to remobilise the dislocation, and will do so in the absence of any thermal effects.

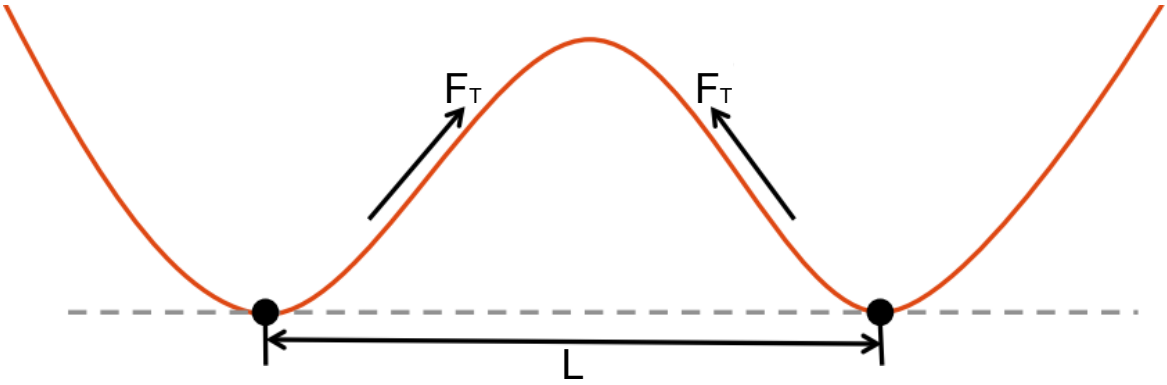

Fig. 2.4 A typical forest intersection. The originally moving dislocation is sessile at two points, stopping motion. External mechanical force is required to remobilise. The force acting on the dislocation will scale with the length that the applied stress is able to act on. The image has been adapted from an original by Hunter & Preston [19].

First we will account for the projection of an applied stress (σ in tensor form) onto a dislocation. If the dislocation has local tangent vector, $\delta\mathbf{L}$, then a force, $\delta\mathbf{F}$, is applied at each point along the length, according to the expression [44, 45]

$$\delta\mathbf{F} = (\sigma \cdot \mathbf{b}) \times \delta\mathbf{L}, \tag{2.12}$$

if the dislocation is straight and pure edge or screw in nature, the summation can be simplified to

$$F = \tau b L, \tag{2.13}$$

remembering τ is the local shear stress felt by the dislocation. For remobilisation, must exceed the back tension from the pinning points. As the dislocation breaks free it 'bows out', increasing in length. For a given bow out angle the arc length will always be proportional to the distance between the two pinning sites.

We define the line tension using the fact that that it must be equal to the energy stored per unit length in the created line length in the dislocation as it bows out, and thus is proportional to Gb^2.

Equating the two forces we find

$$\tau bL \propto Gb^2, \tag{2.14}$$

and thus the required applied stress [46]

$$\tau \propto \frac{Gb}{L}. \tag{2.15}$$

We can note at this point that BCC metals are still structurally history dependent as they generate dislocation based pinning barriers. However at low rates and strains work hardening is observed to be negligible, as the Peierls stress dominates.

We have now outlined the general mechanism of 'forest cutting' that is core to most models of work hardening. How models proceed from this concept however is a point of divergence. So, we will now separately discuss the specifics of the two most prominent approaches.

2.5 Taylor Theory

Arguably, the entire derivation of equation 2.15 is part of the Taylor model. However as previously stated it is also the result at which the Taylor model and other models part ways. Taylor's original model [29] proposes that for a regular arrangement of dislocations (known as the Taylor lattice) the length between any two pinning sites, L, is inversely proportional to the square root of the dislocation density,

$$L \propto \frac{1}{\sqrt{\rho}}. \tag{2.16}$$

Combining the relation 2.16 with equation 2.15 we obtain the Taylor relation;

$$\tau_p = \alpha_T bG(0)\sqrt{\rho}. \tag{2.17}$$

We should remember at this point that the mechanical threshold stress is defined at 0 K. α_T is a coefficient accounting for both of the proportionalities in equations 2.15 and 2.16 measured by Kocks and Mecking [35] as 0.048 for high purity copper. The Taylor relation forms the core of most physically based plasticity theories [15, 19, 24, 33, 35, 47–49].

At this point, the extensive history variable, σ_p is replaced with the intensive variable, ρ. More intricate models separate the total dislocation density into edge or screw dislocations ($\rho = \rho_e + \rho_s$) or mobile and immobile dislocations ($\rho = \rho_m + \rho_i$). Another common separation is into the many possible slip systems, which we will index as j, making $\rho = \Sigma(\rho_{m,j} + \rho_{i,j})$. If the distribution is separated by system the simple Taylor relation becomes dependent on the decomposition method used, but generally takes a form similar to [3, 4, 50],

$$\tau_p = G(0)b\sqrt{\sum_j \alpha_j \rho_{i,j}}. \tag{2.18}$$

The hardening coefficients, α_j, are typically studied and constrained using molecular dynamics, to prevent the models having an unmanageable number of free parameters. An important observation is that when separating the dislocations into mobile and immobile, only the mobile dislocations contribute to barriers. Such separations may be helpful in theoretical or computational modelling but are typically difficult to study experimentally during deformation. To simplify further discussion we will not separate by system.

The material strength is then modelled either by directly modelling the dislocation density and using the Taylor relation, or by converting dislocation evolution equations to a rate of work hardening. Using the chain rule;

$$\frac{\partial \tau}{\partial \gamma_p} = \frac{\partial \tau_p}{\partial \rho}\frac{\partial \rho}{\partial \gamma_p} = \frac{\alpha_T b G(0)}{2\sqrt{\rho}}\frac{\partial \rho}{\partial \gamma_p} = \frac{\alpha_T^2 b^2 G(0)^2}{2\sigma_p}\frac{\partial \rho}{\partial \gamma_p}. \tag{2.19}$$

The evolution of the dislocation density itself is separated into 'generation' and 'recovery' terms;

$$\frac{\partial \rho}{\partial \gamma_p} = \frac{\partial \rho_+}{\partial \gamma_p} - \frac{\partial \rho_-}{\partial \gamma_p}. \tag{2.20}$$

We can immediately identify our two key empirical parameters from this relation. Θ_0 must correspond to a pure generative regime, when so few dislocations exist that annihilation is negligible;

$$\Theta_0 = \frac{1}{M^2} \frac{\alpha_T b G(0)}{\sqrt{\rho}} \frac{\partial \rho_+}{\partial \gamma_p} \tag{2.21}$$

remembering that Θ_0 is defined as $\dfrac{\partial \sigma_p}{\partial \varepsilon_p}$, thus introducing two multiples of the Taylor factor. Empirical observations of Θ_0 are typically used to define the generation term, rearranging to

$$\frac{\partial \rho_+}{\partial \gamma_p} = \frac{2\Theta_0 M^2}{\alpha_T b G(0)} \sqrt{\rho}. \tag{2.22}$$

A more general form was proposed as a dislocation generation (or storage) function, $\Lambda(\rho)$ by Narutami [51];

$$\Lambda(\rho) \approx \Lambda_0 + \Lambda_1 \sqrt{\rho}, \tag{2.23}$$

who noted that the Λ_0 term corresponds to only a small correction to equation 2.22. Kocks and Mecking [35] developed physical rationalisations for the two Λ terms, relating the function not to dislocation creation, but to dislocation storage. They argued that the storage of dislocation length is the important factor in work hardening, not generation. Created dislocation length will recede back into its source after the applied load is removed, unless something prevents it. Therefore the only increase in dislocation length will arise from pinned dislocations or 'debris' that is created during slip [35]. The constant Λ_0 term is therefore interpreted as structurally constant pinning sites such as grain boundaries or impurities, meanwhile the dislocation dependent $\Lambda_1 \sqrt{\rho}$ term increasing corresponds to the spatial frequency of pinning sites.

The second parameter of interest, η, also arises simply from equation 2.20. It is the stress corresponding to the dislocation density at which the generation and recovery terms balance. The plateau therefore corresponds to some dislocation equilibrium. The equilibrium point is both rate and temperature dependent as whilst the generation term is generally considered athermal [14, 33] (below rates of 10^6 s^{-1} [52]) recovery is dependent on the applied stress and the current temperature.

We can begin describing recovery by introducing some general recovery rate

$$\frac{\partial \rho_-}{\partial t} = R(\dot{\gamma}, T, \rho) \tag{2.24}$$

where we note the derivative is with respect to time, as the process is limited by overcoming some annihilation barrier. We arrive at the general dislocation evolution relation

$$\frac{\partial \rho}{\partial \gamma_p} = \Lambda(\rho) - R(\dot{\gamma}, T, \rho)\frac{\partial t}{\partial \gamma_p} \approx \Lambda(\rho) - R(\dot{\gamma}, T, \rho)\frac{1}{\dot{\gamma}}. \tag{2.25}$$

The recovery term is controversial, having been modelled in several different ways by many authors (references [35, 39, 53–55] provide just a handful of examples). However, there is some agreement on the fundamental approach [56]. Recovery is modelled by analogy to the kinetics of chemical reactions, leading to a general relationship of

$$R(\dot{\gamma}, T, \rho) = R_0 f(\dot{\gamma}, T, \rho)\rho^m. \tag{2.26}$$

The function f corresponds to the frequency (inverse timescale) of a single recovery event and m is some power that depends on the sensitivity of a given recovery process to dislocation density. R_0 is a constant prefactor accounting for geometry effects both of the lattice and the statistical odds of any two dislocations being compatible for annihilation. The barrier to

annihilation arises from the fact that dislocations typically approach each other on different slip planes and must migrate to the same slip plane to annihilate.

Screw dislocations can move easily between planes through a process known as 'cross slip' and thus annihilate more readily [3]. Cross slip is possible because screw dislocations can slip on many planes, allowing them to move to other planes which intersect both their current plane and that of their annihilation partner. The dislocations cross slip again when they reach their partners plane. Therefore the frequency function f depends on overcoming the cross slip barrier, and the density sensitivity $m_s = 2$ as the ρ_s dislocations are attempting to interact with ρ_s dislocations.

Edge dislocations have a much more difficult time moving between planes and instead must move in a diffusive motion from one slip plane to the next parallel one. The process is known as 'climb' [3], and requires interaction with impurities or vacancies in the lattice. In this case the thermal barrier is now the barrier for climb, and the ρ_e edge dislocations are trying to interact with a number of impurities or vacancies which is independent of their density, thus $m_e = 1$.

The frequency function f is usually modelled in an Arrhenhius nature, typically using an Arrhenius or similar sinh law function. Kocks and Mecking [35] proposed a semi empirical form for an arbitrary recovery event, based on chemical reaction analogies:

$$\frac{\partial \rho_{-}}{\partial \gamma} = R_0 \rho^m \left(\frac{\dot{\gamma}}{\dot{\gamma}_R} \right)^{\alpha_R} e^{-\tau \zeta / Gb^3} \tag{2.27}$$

where ζ is a parameter equivalent to an activation volume and α_R is a constant.

Nix *et al.* [57] modelled cross-slip based recovery, resulting in the expression

$$\frac{\partial \rho_{-_s}}{\partial \gamma} = R_0 \rho_s \frac{f_0}{\dot{\gamma}} e^{-U_R / k_B T} \sinh \left[\frac{\zeta \tau}{k_B T} \right], \tag{2.28}$$

where U_R corresponds to the energetic barrier to recovery.

Finally, Kocks and Mecking [35] observed that forms such as those above provide an overly sharp nature to the stress strain curves. They instead opted for a Voce form for work hardening;

$$\Theta = \Theta_0 - R_d \frac{\sigma}{\dot{\varepsilon}^{1/n}}, \tag{2.29}$$

where both R_d and n are functions of temperature, but independent of stress and strain rate. The literature remains ambiguous as to any one definitive model.

To highlight the key points of Taylor modelling, the history variables are the densities of dislocation species in the specimen, ρ_j, the threshold strength is then proportional to $\sqrt{\sum \alpha_j \rho_j}$. Work hardening is proposed to arise from an athermal dislocation storage mechanism, whilst path dependence arises from the balancing athermal storage and thermal recovery processes.

Relation 2.17 is often treated as a fundamental physical law rather than the result of a well defined model [4, 5]. At this point we will emphasise some of the approximations made. The derivation of the model assumes a specific geometry (the Taylor lattice) and thus does not account for any effects due to intermediate patterning between the atomic and macro scale, or rearrangements under the applied load. Secondly, given the proposed lattice, multi-dislocation arrangements can exist for which the foresting barrier is zero [4, 5], leading to a negligible prediction of forest strengthening if the model is taken explicitly. Finally, the model assumes that dislocations overcome pinning barriers alone, and thus cannot account for any collective dislocation motion, a central point of discussion in later sections.

2.6 Dislocation Interactions in FCC Metals

Previous discussion of pinning has assumed a single simple mechanism. In FCC metals a variety of barriers can be formed as well as other dislocation structures that may enable slip. Each of which see varying levels of discussion in different material models. In this section we will briefly qualitatively introduce several prominent interactions, for the benefit of later discussion.

Node Junctions

In figure 2.4 we showed the simplest possible interaction to model, the interaction of two orthogonal dislocations travelling head on, resulting in a 'node junction', bound at a single point. The node junction is believed to be the most common interaction between two single dislocations [43].

Lomer-Cottrell Junctions

A similar scenario to the node junction, a Lomer-Cottrell junction, occurs when dislocations on two different planes attempt to simultaneously pass through the intersection of their planes. The result is that the two dislocations become sessile along an extended length rather than at a point [3]. The dislocations cannot remobilise by a process such as bow-out and instead must 'unzip' the junction by remobilising the sessile length from the ends in, ultimately removing it. Dislocations held in this barrier may act as a barrier to other dislocations, however screw dislocations can move round this barrier through cross slip.

Shotky Partials

A partial dislocation is when a dislocation decomposes itself into two dislocations. The new dislocations are confined by the rules that their total Burgers vector must be conserved and the elastic energy cannot increase; $(\mathbf{b}_1 + \mathbf{b}_2)^2 \leq \mathbf{b}_1^2 + \mathbf{b}_2^2$. A Shotky partial is when the

resultant dislocations remain in permitted slip directions. One then moves ahead of the other, creating an area between the two that is entirely offset from the crystal lattice by a constant vector. The offset of the atoms from the lattice is known as a 'stacking fault'. There is an energetic penalty arising from the upsetting of inter-planar bonds from their favourable lengths, known as a stacking fault energy, which scales with the area of the fault. Stacking faults and partials are capable of interaction with other stacking faults or single dislocations in the mechanisms already outlined.

Frank Partials

A Frank partial is similar to a Shotky partial; however the resultant dislocations are sessile and thus cannot move by slip [3]. The stacking fault therefore forms a stationary barrier for incident dislocations.

Pile-Ups

It is entirely possible for any barrier that the time taken to overcome the barrier will be longer than the time taken for another dislocation to arrive. In this scenario the dislocations will 'pile up' behind the first trapped dislocation. Their stress fields will apply a force to it. The front dislocation therefore feels a magnification of the applied stress, scaling with the number of dislocations in the pile up. A classic example of pile-ups is at grain boundaries, where they give rise to Hall-Petch behaviour [10, 11, 33]

Dipoles

A dislocation dipole is formed when two dislocations of opposing sign approach on different but parallel planes (sufficiently far apart that they do not annihilate etc). These paired dislocations share some parallels with electric dipoles in that they respond to gradients in stress and that their 'polarisation' scales with the magnitude of the applied stress [58]. The majority of dislocations produced in early strain adopt dipole arrangements [59], rather

than occurring as lone dislocations or pile-ups. They are also known to provide a major [60] contribution to structural evolution [61, 62], specifically in early or stage II work hardening. Finally, dislocations need not be simple line dislocations to form dipoles, loops can also form dipoles. Due to the importance of this particular interaction, and its absence from almost all Taylor based theories, despite its acknowledged impact on work hardening, we will outline a recent dipole based work hardening model in section 2.7.4.

2.7 Avalanche Plasticity

A range of contemporary plasticity studies (outlined in section 2.7.1) have revealed crystal plasticity on the nanoscale to occur in bursts of activity. Such observations are irreconcilable with plasticity models based on a combining Orowan's law (equation 2.8) and the Taylor picture of remobilising non-interacting pinned dislocations. The independent nature and large number of dislocations moving through the lattice predicts smooth deformation [63]. The general consensus is that the burst like nature of plasticity occurs due to some collective dislocation motion, often referred to as dislocation avalanches [4, 64–67] that are believed to exhibit self organised criticality (SOC) [68].

Both empirical and theoretical studies have led to the general conclusion that work hardening on the macroscale is fundamentally dependent on the underlying avalanche behaviour. However, there have been very few attempts to develop plasticity models based on SOC avalanche dynamics, especially in high rate deformation. Almost all of metal plasticity will likely have to account for the presence of (or justify the absence of) avalanche behaviour. Thus we will now review the experimental evidence, observed behaviour and models of avalanche plasticity.

2.7.1 Evidence of Dislocation Avalanches

High Resolution Extensiometry The earliest evidence of plasticity occurring in bursts was observed in tubular zinc monocrystals by Tinder and Trzil [69] who used a torsional

apparatus with strain resolution of 10^{-9}. The results of these seminal experiments are shown in Figure 2.5. At extremely high strain resolution, deformation was observed to occur in steps of varying size, with the largest strain increment observed to be 2×10^{-7}.

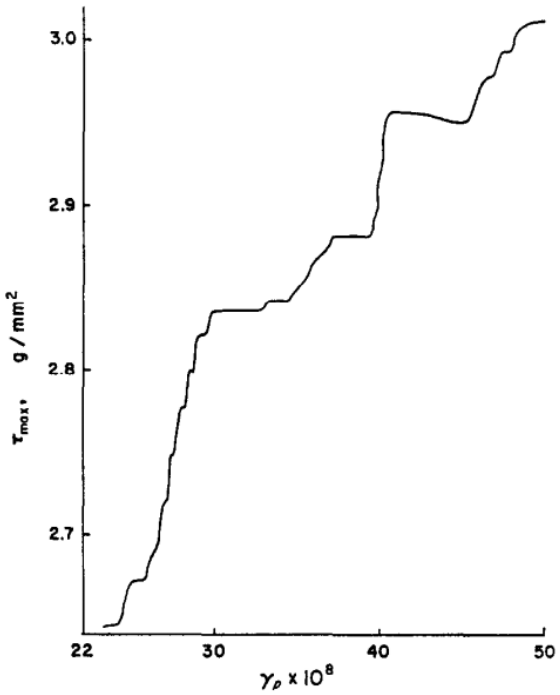

Fig. 2.5 Results reproduced from Tinder and Trzil [69] of the stress-strain relationship in the high resolution torsional deformation of tubular zinc monocrystals. Both stress and strain undergo step like increments.

Acoustic Emission Weiss *et al.* furthered the certainty of a plastic deformation occurring in bursts by performing compression experiments on single crystals of hexagonal ice [66, 70–72]. The specimens were fitted with an transducer that measured acoustic emissions from the specimen during deformation. An example of acoustic emission measurements is shown in Figure 2.6, the acoustic events were again observed to occur in bursts. Due to the transparency of the ice, micro-cracks could be excluded as an acoustic source, leaving dislocation motion as the only remaining source. The typical time between events is noted to be of the order of microseconds [4].

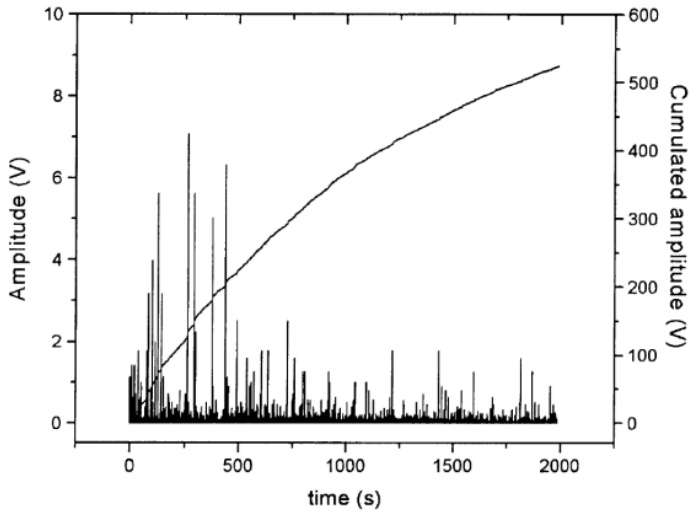

Fig. 2.6 Measurements of acoustic events in the compression of hexagonal ice, reproduced from Weiss *et al.* [71].

Subsequently, acoustic events in both ice and single crystal copper [66] were found to follow power law probability distributions;

$$P(\chi) \propto \chi^{-\kappa_\chi}, \tag{2.30}$$

for acoustic amplitude and

$$P(E) \propto E^{-\kappa_E}, \tag{2.31}$$

for energy. The exponents were measured to be $\kappa_\chi = 2.0 \pm 0.1$ and $\kappa_E = 1.5 \pm 0.1$. The largest avalanches are seen to depart from this distribution, typically accounted for by modulating the probability distribution by some general cut off function.

The relation between the observed power dependences in terms of acoustic amplitude and acoustic energy is simply solved [64]. Any region in the specimen that is not actively undergoing slip is elastic, therefore the relation between the radiating energy and wave amplitude is that of an elastic medium: $E \propto \chi^2$. Given the singular mapping of amplitude

and energy we can simply relate the probability distributions;

$$P(\chi)d\chi = P(E)dE, \tag{2.32}$$

which then gives

$$P(E) = P(\chi)\frac{d\chi}{dE} \propto \chi^{-(\kappa_\chi+1)} \propto E^{-\frac{1}{2}(\kappa_\chi+1)}. \tag{2.33}$$

Thus $\kappa_E = \frac{1}{2}(\kappa_\chi + 1)$, which is consistent with earlier experimental observations of $\kappa_\chi = 2 \pm 0.1$ and $\kappa_E = 1.5 \pm 0.1$.

Fractal Surface Patterning Sprůsil and Hnilica [73] observed that dislocation structures exhibited long range spatial correlations, exhibited as fractal step like patterning in the specimen surface. The combination of power law probability distributions and fractal patterning are typical hallmarks of self organised criticality [68], that commonly arises in 'slowly driven interaction dominated systems' that exhibit avalanche dynamics. Interestingly, no properties of the observed bulk dislocation structure after loading appear to be obviously linked to the step like surface profile.

Micropillar Plasticity Finally, avalanches have been imaged directly in the deformation of metallic micro-pillars [74, 75], when the specimens are reduced to the length scale of the avalanches. Figure 2.7 shows electron microscope images of micro-pillars that have undergone compression, as well as typical stress strain curves achieved in such experiments. Slip is observed to occur in a clearly localised and statistical manner, an effect that provides a major challenge in engineering at the micron scale.

A final basic observation, established by Weiss *et al.* [66] and visible in Figure 2.7, is that avalanches exhibit a lamellar (plate like) nature. The observation of avalanches being lamellar rather than planar is likely to be important in understanding the physical mechanisms

driving collective avalanches, notably that co-operation occurs across multiple parallel slip planes, that is typically not discussed by 2D models of avalanche plasticity [63].

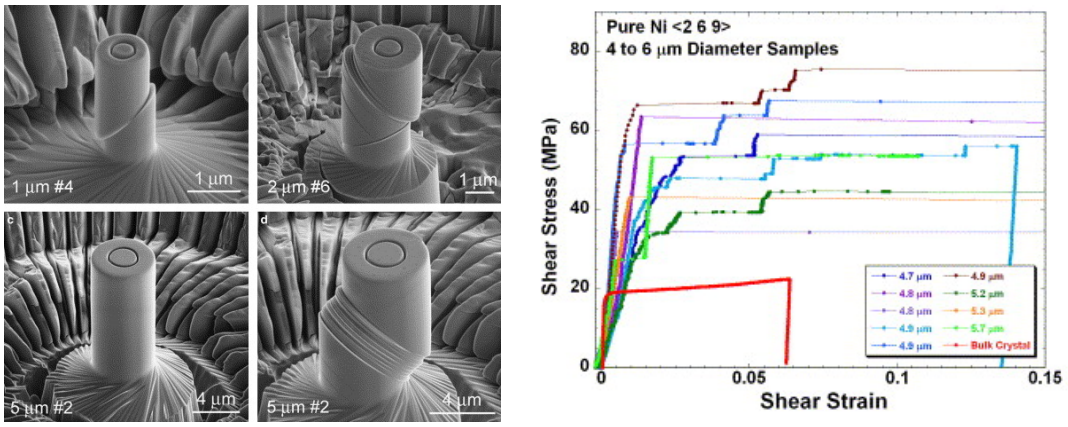

Fig. 2.7 Left: Electron microscope images showing micropillars of pure Ni that have undergone varying numbers of slip avalanches. Right: Stress strain curves for varying sizes of micropillar, the curves evolve in a clear step like manner.

2.7.2 Self Organised Criticality

Given that collective or avalanche plasticity is believed to obey self organised criticality, we will briefly outline what it is and how it arises. SOC is a physical picture of 'complexity', describing systems where the emergent behaviour cannot be trivially linked to the properties or dynamics of its individual elements.

Self organised criticality specifically deals with the slowly driven non-equilibrium motion of systems with many degrees of freedom and which are described as having a 'critical point' as an 'attractor,' [68]. That is, the system, despite being externally driven, will organise itself towards some fixed set of properties, that it will then fluctuate about for the remainder of the evolution. The dynamics about the attractor point are similar to the critical point of second order phase transitions, with the key difference that the system does not require the system conditions to be tuned to the correct values for the critical point.

The classic example of self organised criticality is the sand-pile, originally discussed by Bak [68]. If one starts with an empty finite surface, the edges of which are a sink (a practical

example could be a square table) and drops sand grains, one at a time, on to randomly selected locations on the table, a characteristic structure will emerge: the sandpile. Firstly the grains will simply sit on the table, however after the surface is completely covered, a pile forms and grows in height. As the pile grows, certain parts of the pile become so steep that gravity overcomes the friction between the grains; an avalanche event occurs. Multiple grains tumble at once, but the event is triggered by a single grain. Avalanches can lead to sand grains falling from the edge of the table, removing them from the system.

After sufficient time has passed, the global average slope of the sand pile adopts some maximum value. The global average will now remain approximately constant and any new grains added will eventually fall off the pile. This state is far from the energy minimum of the sandpile (being flat). As more grains are added, whilst we know avalanches will occur, when, where and with what size they occur cannot be determined. Many grains trigger no response, and then one grain triggers an avalanche that can vary wildly in size; the system is highly non-linear.

Importantly, as stated by Bak [68] in the original proposal of SOC; '*In the critical state, the sandpile is the functional unit, not the single grain of sand. No reductionist approach makes sense. The local units exist in their actual form, characterised for instance by the local slope, only because they are part of the whole. Studying the individual grains in a microscope doesn't give a clue as to what is going on in the whole sandpile. Nothing in the individual grains of sand suggests the emergent properties of the sandpile*.'

Similar behaviour is analogously found in a wide range of systems: earthquakes, solar flares, financial markets, extinction, epidemics and the original application of Bak; $\frac{1}{f}$ noise [68]. How then does the sandpile relate to dislocation dynamics? The grains of sand correspond to dislocations (however the number of grains in the pile need not correspond to the number density of dislocations). The pile is the overall material. The slope likely has multiple interpretations as a system may have multiple constant properties in the critical state.

The equivalent quantities for an FCC metal are not obvious, with stress, strain and dislocation density all undergoing a net increase. One potential quantity, proposed by Brown [4] is the volume fraction of the material filled with obstacles, Ψ_o. Avalanches may create obstacles in previously free space, increasing the volume fraction, but later avalanches sweep obstacles together retaining a constant average volume but increasing the density of the obstacle regions. The mean value of Ψ_o would then be determined by a geometric packing efficiency arising from the properties or geometry of the avalanches in the system.

The modelling of SOC inherits many of the behaviours of critical point dynamics in phase transitions, each verified by numerical simulations of toy systems [68]. The first of these, already observed in section 2.7.1, are power law relations between variables, across many orders of magnitude and not only between system properties, but also their probability of occurrence. The second major property arising from the critical state is fractal, specifically scale invariant, behaviour spatially and/or temporally. Scale free behaviour enables the constraining of relations between fluctuations of the system and their effects.

2.7.3 Elastic Interface Depinning & Discrete Dislocation Simulations

Elastic interface depinning [76] is a model basis in which the dislocation is treated as an interface between two physical phases (the moving and stationary regions of the lattice). The phases are separated by some unique critical stress τ_c above which the mean interface velocity is permanently non zero (τ_c is therefore a similar parameter to the mechanical threshold). Below this stress only avalanche motion occurs [63] and in this context plasticity is modelled similarly to a second-order phase transition. Several models exist using this basis in combination with stochastic equations to determine statistical relations from local fluctuations in the applied stresses. However, current models of this form remain largely mathematically abstract and as such have not been sufficiently developed to provide detailed testable rate dependent models of strength, let alone path dependence and as such will not

be discussed in detail. A mathematical outline of such models is present in the review of Papanikolaou *et al.* [63].

Discrete dislocation dynamics (DDD) simulations, in which dislocation lines are explicitly modelled in terms of length, position and strain field within an elastic continuum show flaws in elastic interface depinning models. Ispánovity *et al.* [78] performed 2D-DDD simulations revealing that a 2D model of the system (as is performed in elastic interface depinning) provides the wrong exponents in both power law distributions (finding $\kappa_E = 1$) and false behaviour in the cut-off size of avalanche distributions. Concluding that the 3D nature of crystal plasticity is critical to the underlying mechanisms.

Zaiser *et al.* studied avalanches in 2D-DDD and a separate explicit elastic continuum model. In both cases they found the maximum or cut-off avalanche size to be inversely proportional to the current rate of work hardening, shown by the results in Figure 2.8 where the truncated regions of the curve collapse if plotted in terms of $\Theta\Delta\gamma$. The collapse implies that the either mechanisms responsible for work hardening limit the maximum strain

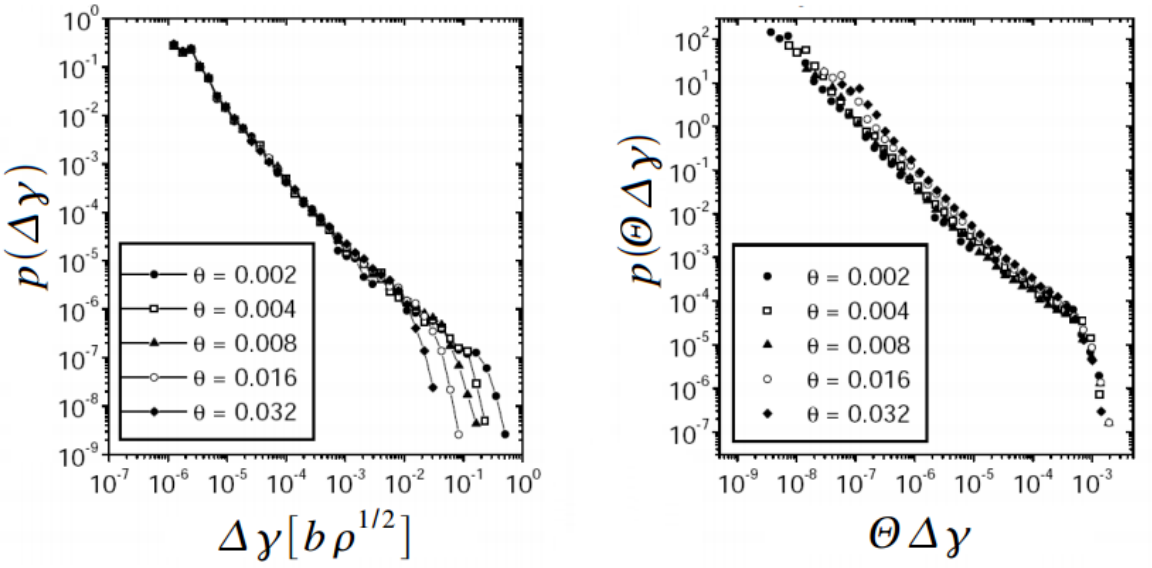

Fig. 2.8 The probability distribution functions for various stages if work hardening generated by two different 2D explicit dislocation dynamics simulations. The left graph presents unscaled distributions whilst the right presents scales strain increments with the rate of work hardening during the experiment. Reproduced from Csikor [77].

increment or the reverse; that the rate of work hardening is limited by the largest avalanches. The two are linked through the stress increment in a single avalanche being proportional to $\Theta\gamma$. It is unknown if this relation holds in 3D.

2.7.4 Elastic Inclusions as Avalanches

Brown[1] [79] has developed (to the authors knowledge) the only existing 3D analytical model of avalanche plasticity. Avalanches are modelled as elastic inclusions, finite 3D volumes containing the slipped lattice, contained within an interface of both edge and screw dislocations (referred to as 'primary' dislocations). The theory simultaneously provides an explanation of the influence of dipoles on early work hardening, avalanches, and provides a natural 3D extension of 2D pile up models, originally envisaged by Eshelby, Frank & Nabarro [80]. The dynamics and behaviour of elastic inclusions are largely determined by subtle consequences of geometric requirements at their interface.

2.7.4.1 Ellipsoidal Slip Bands & Stress Concentration

In 1957, Eshelby [81] proved that the stress field inside an ellipsoidal inclusion that has undergone a uniform strain throughout its volume must be uniform. The proof stands for any linearly elastic body, isotropic or anisotropic [82]. Decades later Markenscoff derived across a series of papers [83–86] that the inverse relation holds true. Any uniformly stressed inclusion surrounded by a body also under a uniform stress, must be ellipsoidal in shape.

Brown [79] developed a model for such an inclusion sketched in Figure 2.9, referred to as an ellipsoidal slip band. The band axes, with lengths L_a, L_b and L_c are indicated in the sketch. The slip band is effectively a series of N dislocations in adjacent planes, adopting either loops or dipole geometries. The avalanche then occurs as a co-operative lamellar expansion across those N neighbouring planes, most easily envisioned in the case of a stack of loops, all undergoing in plane radial expansion. The co-operative nature of the expansion

[1] Section 2.7.4 is largely a summary of work of LM Brown, for any uncited statements, refer to [4] and [64]

is driven by the requirement to maintain the included volume in an ellipsoidal shape. Any departure from the geometry creates a breakdown in stress uniformity that is rectified by the dislocation interface moving under the bias to return the uniform stress. A similar scenario to charge moving to eliminate an electric field in a conductor. After detailed study of the consequences of the restriction on interface geometry, Brown found that the requirement to maintain an ellipsoidal shape causes effects that 'concentrate' the applied stress.

The first is a stress concentration aids the overcoming of obstacles, arising from two sources. The first source is simple and present even in 2D pile up models [87]; if we have an avalanche of N dislocation loops or dipoles, each will feel a force from the externally applied stress. The stresses will be focused on the leading edge, and thus the force with which the avalanche overcomes any obstacles is magnified by N. The second effect causing a concentration of the obstruction clearing stress is more subtle; if we consider a slip event, which corresponds to the isotropic planar expansion of the dislocations slip band, slip obstacles only hinder the expansion of the band on one side, and likely hinder the expansion of one band axis more than the other. A one sided hindrance will clearly distort the band away from its ellipsoidal shape, so as the rest of the band expands freely, the departure from its ellipsoidal form amplifies the stress at the barrier. Brown derived the concentrated stress

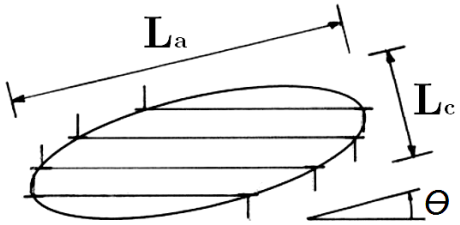

Fig. 2.9 A sketch of an ellipsoidal slip band showing the edge dislocation components of the interface between the slipped inclusion and the unslipped material. L_a and L_b correspond to the axes approximately in the slip plane whilst L_c is approximately normal to the slip plane ($N = \frac{L_c}{\Delta x_p}$). For simplicity and as most important effects arrise from cooperation between parallel planes, it is assumed that $L_a = L_b$ This image is modified from the original by Brown [4].

on obstacles, τ_{ob} to be

$$\tau_{ob} = \frac{\pi}{4}\frac{L_a}{L_c}N\tau. \tag{2.34}$$

We note that this stress clearly favours long "razor like" bands normal to the axis crossing the slip planes, corresponding to the lamellar shape of avalanches observed in experiment.

The second stress concentration is that felt by the external lattice in the neighbourhood of the band. The neighbourhood stress is also present in 2D pileup models and reveals a flaw in their 2D formulation; strain field calculations [88] show the stress imparted on the neighbourhood lattice, τ_n by the band to be

$$\tau_n(x) = \tau\sqrt{\frac{L_a}{2(L_a - x)}}, \tag{2.35}$$

where x is the distance from the center of the band. As the interface is approached ($x \to L_a$), the stress diverges, a clearly non physical prediction. In the slip band model, the 3D nature causes the stress to be constrained by the ability of the band to span multiple planes,

$$\tau_n(x \to 0) \to \frac{L_a}{2L_c}\tau. \tag{2.36}$$

The neighbourhood stress is important as it remains when an avalanche terminates. If the band's surroundings are not sufficiently strong, it will initiate another avalanche [4].

2.7.4.2 Slip Band Initiation, Propagation & Termination

We have already established a slip band avalanche as the expansion of dislocation loops or dipoles on adjacent planes. The avalanche is therefore initiated by the splitting of the loops or dipoles from their paired state, moving the adjacent dislocations in their planes to generate a shear motion across the slip band. This process is shown in Figure 2.10 (a). The

stress to separate an edge dipole in a linear elastic medium is

$$\tau(h) = \frac{1}{8(1-\nu)}\frac{Gb}{\pi h} \tag{2.37}$$

where h is dipole height; the distance separating the furthest two planes on the band is present [4]. For a screw dipole the factor of $8\pi(1-\nu)$ is replaced by a factor of 4π.

Importantly, dipoles of both types exist with a number distribution dependent on their height. The distribution is thought to result from a process in which passing dipoles interact if they overlap, trapping the overlapped region leaving two new shorter dipoles, both truncated to the edge of the overlapping region [79]. The resultant form is

$$N(h)dh \propto \frac{\delta h}{G(h-h_{min})^2} \qquad h_{max} > h > h_{min}. \tag{2.38}$$

The form of the distribution has been supported by evidence in cyclic plasticity studies in Ni and Cu [89–91]. The maximum dipole height h_{max} corresponds to some absolute spatial limit. The minimum dipole height h_{min} corresponds to the height at which the dipoles thermally break down, the breakdown mechanism for edge dipoles is controversial [4], however for screw dipoles it is likely to be due to dynamic recovery effects [92], such as annihilation by cross slip. Using our earlier relation between activation stress and height, we can convert the

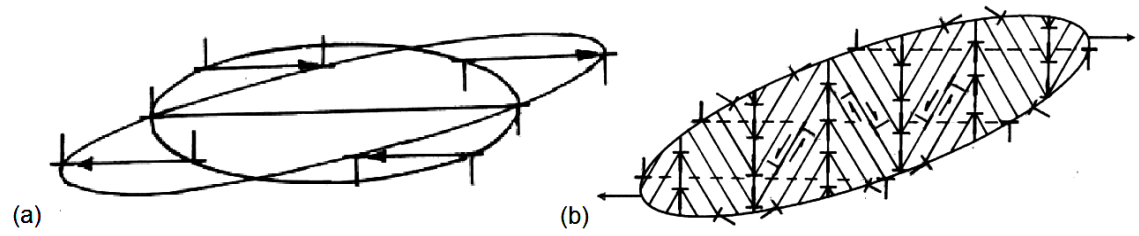

Fig. 2.10 The stages of slip after a band has been initiated. (a) The band undergoes a shear strain by expanding and moving loops or dipoles dislocations above its centre in the direction of the applied stress and those below against it. (b) As the band slips it rotates, projecting increasing stresses onto secondary slip planes. When a sufficient projected stress is reached secondary slip is triggered, anchoring the band. The image is modified from the original by Brown [4].

height distribution into the distribution of sources that activate at a certain stress;

$$N(\tau)d\tau \propto \frac{\delta\tau}{\left(1-\frac{\tau}{\tau_{max}}\right)^2} \tag{2.39}$$

where τ_{max} corresponds to the stress required to separate dipoles of height h_{min}.

As the interface is formed from a combination of edge and screw dislocations, it can tilt or roll about any of its axes during motion, typically by small angles due to the aspect ratio the band. Furthermore, as the slip is shear in nature the major axis of the band rotates by a small angle from the crystallographic plane. The rotation during slip causes the elastic stresses within the band to project onto secondary slip planes. Rotation therefore promotes the activation secondary slip systems, shown in Figure 2.10 (b), the secondary slip dislocations act to harden the band. After undergoing a sufficient level of shear the level of secondary slip stabilises the band, effectively anchoring the primary dislocations in a forest. Stabilising the band both terminates the propagation and prevents the band from retracting. Importantly at this point the band no longer exists, it instead forms a complex forest due to the secondary dislocations, that will be swept away as other slip bands pass through the same region. The transient nature of slip bands explains earlier observations of fractal steps on the specimen surface not being easily related to bulk dislocation patterning.

The activation of secondary slip will (excluding thermal effects) occur at a fixed stress. Given that the stress arises from a projection through some effective angle, θ_e, of the stress in the band, $2\tau L_c$, we find that when the band is anchored,

$$2\tau L_c \theta_e \propto constant. \tag{2.40}$$

If we then approximate the shear strain in a single band, γ_B, as being the opening angle between the band axis normal to the slip planes and the final radial expansion when anchored,

$$\gamma_B \approx \frac{u_B}{2L_c}, \tag{2.41}$$

where u_B is the final band diameter. We can combine the two expressions, and find

$$u_B \propto \frac{1}{\theta_e}\frac{\gamma}{\tau} \sim constant. \tag{2.42}$$

As the effective angle is approximately constant, limited by the packing ability of ellipsoids, and the ratio $\frac{\gamma}{\tau}$, given that the inclusion is elastic, is the reciprocal of the shear modulus. The relation is consistent with empirical evidence that suggests that in stage II the band height decreases with applied stress, whilst the slip displacement, **u** remains relatively constant [4]. Evidence that the bands are terminated by secondary slip anchoring rather than any obstacle in the lattice.

Having been anchored, the band will have imparted a bulk strain equivalent to strain in the band, scaled by the volume of the band relative to the specimen;

$$\Delta\gamma = \Psi_B\gamma_B = \Psi_B\frac{u_B}{2L_c}. \tag{2.43}$$

Ψ_f is the volume fraction of the band; the volume of the band divided by the volume filled by the lattice. Brown derived the band strain at which secondary slip occurs, accounting for the rotation of the band about its multiple axes during slip. The resulting expression is

$$\gamma_B \approx \frac{\tau}{\alpha_T(1-\alpha_T)G\theta_e}. \tag{2.44}$$

The effective angle, θ_e, accounts for the general two orthogonal angles through which the band can rotate, and is in practice due to their small values simply their quadrature sum. The

final form of the expression is not thoroughly surprising, it is to within some pre-factors accounting for projection and forest hardening in secondary slip, simply the definition of the shear modulus.

2.7.4.3 Slip Bands & Work Hardening

Stage I

In the ellipsoidal slip band picture, Stage I corresponds to the formation of dislocations and their arrangement into loops, dipoles and general avalanche precursors. As dislocations are just beginning to interact at this stage, no significant foresting occurs and the rate of work hardening is low. At the end of Stage I, dislocations begin to impede each other, as in the Taylor picture, it is at this point Stage II begins. Remembering the sandpile model, stage I corresponds to the grains landing on the empty table and building the pile to the critical slope, or in the current picture, maximum volume fraction of obstacles, Ψ_o.

Stage II

In Stage II, a sufficient number of dislocations have arranged and the system begins self organised avalanching. A distribution of potential source sizes and types are present. The self ordered critical nature is driven by the fact that the system is not yet at the stress required to mechanically activate any of the sources, fluctuations push sources to their required stress, initiating an avalanche. In this regime fluctuations in all quantities observe scale-free relationships, (i.e. fluctuations scale with the quantities they are fluctuating about). We can study work hardening through the relationship between stress fluctuations and fluctuations in some other parameter. Notably, when a band stabilises it causes a decrease in the obstacle free volume fraction of the crystal, $\Delta(1-\Psi_o)$ and a stress fluctuation (a stress release upon slipping, that is reapplied by the external load upon stabilisation) of $\Delta\tau$. SOC therefore gives

$$\frac{\Delta(1-\Psi_o)}{(1-\Psi_o)} = m_D \frac{\Delta\tau}{\tau}, \tag{2.45}$$

where m_D is a coefficient describing the dimensional sensitivity of the volume fraction to the stress, and for an unconstrained 3D band $m_D = 3$. However if the band manages to extend across the whole crystal in one dimension and becomes constrained m_D falls to 2, or 1 if it fills an entire cross section. The permanent increase in stress likely arises from the fact that whilst slip maintains a constant average obstacle volume, more and more obstacles are generated and then swept into said constant volume, reinforcing the obstacles that exist in said average volume.

Relation 2.45 is similar to a differential equation defining a power law relation, however it is physically incorrect to attempt to perform integration of it, the nature of the process is not smooth. We can however use it to combine relations 2.43 and 2.44 to arrive at a relation for the quantised increment in strain driven by SOC and the properties of the ellipsoidal inclusion;

$$\frac{\Delta\tau}{\Delta\gamma} = \frac{G\alpha_T(1-\alpha_T)\theta_e}{m_D(1-\Psi)} \tag{2.46}$$

Finally, we should observe that Ψ_o, whilst fluctuating, does so about a fixed value corresponding to a critical point. The value of the critical point is determined by the maximum efficiency with which ellipsoids can pack into a general volume. Extensive computational studies on the random packing of ellipsoids [93] have shown that the maximum packing efficiency is approximately 74%. As ellipsoids correspond to the elastic regions of the lattice, this means that the obstacles fluctuate about 26% of the lattice volume. Fluctuation is due to obstacles being generated in stabilisation and being swept away in slip. Packing efficiency is also likely to determine the maximum rotation angle of the ellipsoid about each of its axes during slip, and thus θ_e. Using these volume fractions to define the space available for the bands to rotate, Brown [64] concludes $\theta_e \approx 2.5^\circ$, matching experimental observation [94].

Before progressing on to Stage III, we should note the important result. The derived relation correctly predicts experimental measurements of Θ_0 [64] without any fitting parameters

(α_T, θ_e and Ψ are all fundamental geometrical constants of the lattice and ellipsoid packing respectively), and is the only such theory capable of calculating the term.

Stage III

Self organisation in Stage II required a complete range of band sizes, and the existence of both edge and screw dipoles to form a complete interface (and therefore an inclusion). At the beginning of Stage III, edge dipoles are no longer stable at any size, experimentally observed by Hirsch and Lally [95], who imaged the sudden disappearance of all screw dislocations in Mg above some critical stress. In the absence of screw dislocations, the inclusion boundary loses the ability to rotate about any of its axes as it slips. Some rotation does still occur as the deformation of the inclusion is a shear relative to the outside lattice but this does not induce secondary slip. Thus the band is no longer limited at a fixed strain by secondary slip.

The remaining edge dipoles now simply split into a pair of edge dislocations that run for some distance, limited by the dislocation structure remnant from Stage II, and is invariant of the properties of the remaining dipoles. This distance can be quantified in terms of a mean free path, ξ. Furthermore, the progressive increase in system stress due to work hardening begins to raise it high enough to activate bands in the absence of fluctuations. When the stress required to activate any source is reached, all of those sources will activate and slip will occur until they are depleted; Stage III is an exhaustive phase.

At any stress, $N(\tau)d\tau$ dipoles will break down, creating twice as many edge dislocations that then travel the mean free path. At any one value of stress, the strain increment is simply the integral of Orowan's law,

$$\delta\gamma = 2N(\tau)\xi b\delta\tau. \tag{2.47}$$

We have already established the distribution of edge dipoles, $N(\tau)$. Combining it with the imparted strain gives a work hardening gradient

$$\frac{\delta\tau}{\delta\gamma} \propto G\left(1-\frac{\tau}{\tau_{max}}\right)^2 \tag{2.48}$$

where we remember that τ_{max} corresponds to the stress required to separate the smallest dipoles. Comparing the relation to a traditional Voce law, τ_{max} is equivalent to η. The result is identical to the empirical power law form of the Voce relation, except the fitting parameter is now fixed at the physically meaningful value of 2, arising from the equilibrium distribution caused by dipole refinement interactions.

Stage IV is outside of the scope of this thesis, however we note that its onset is when all of the edge dipole sources have been exhausted. The remaining single edge dislocations then undergo some form of foresting.

2.8 Summary

In this chapter we reviewed the general approach for modelling path dependent materials, the fundamental origins of structural contributions to strength and then proceeded to discuss some of the most prominent models in more depth.

In the Taylor scenario, the specimen strength scales directly to the density of dislocations in the metal. At low rates, path dependence arises from the balance between athermal dislocation generation and thermal dislocation annihilation, which takes place over some finite time, creating rate dependence. The annihilation mechanism is dependent on the dislocation density through the probability of two compatible dislocations meeting and thus as the density increases annihilation decreases, balancing generation and annihilation at equilibrium point.

Meanwhile in avalanche pictures of plasticity, low rate path dependence is largely driven by a post SOC exhaustion phase in which edge dipoles of increasing strength are broken down. The smaller, stronger dipoles are more numerous and the average imparted slip for a single dipole is independent of its size. Thus as the stress increases more strain can be imparted before the sources are exhausted and a stress increment is required, creating saturation like behaviour.

At rates between 10^4 s^{-1} and shock deformation, little experimental data is available to inform any real theoretical picture, and as we will discuss in the next chapter remedying that is one of the key aims of this thesis. However, at this point we have only discussed the structural contributions to strength. In the next chapter we will discuss instantaneous contributions at low rates, then progress on to the variety of concerns and models present attempting to address the observed transition.

Chapter 3

Rate Dependence & Dislocation Dynamics

In the previous chapter we explored the concept of dislocations and the more static part of their interactions; pinning and consequent work hardening. We also established a framework with which to model metals, outlining the concept of the mechanical threshold stress that keeps track of specimen history and models its evolution. In this chapter we will discuss the more dynamic, rate dependent aspects of metal strength. Initially we will outline the more simple behaviour below 10^4 s^{-1} by exploring the arguments used to derive ϕ terms. We will then explore the variety of approaches used to explain the strength transition.

3.1 Quasi Static Rate Dependence

Rate dependence below 10^4 s^{-1} is intuitive behaviour. In order to make a substance deform more quickly one would expect to have to apply a greater stress from Newton's laws of motion alone. However, the exact relationships that are observed require more consideration. Given knowledge of dislocations and their pinning barriers, the expected quasi static dependence can be found quite quickly.

In section 2.1 we defined a three term model, including a structural 'mechanical threshold stress' σ_p accounting for dislocation pinning and some function, $\phi(\dot{\varepsilon}, T)$, that scales the structural stress depending on the instantaneous conditions with rate and temperature. We will now explain typical forms for ϕ. To begin, we will consider the time-scales involved in the movement of a dislocation. Dislocations have an effective mass close to that of a single line of atoms [96], which is small compared to the quasi-viscous processes that determine their terminal velocity, discussed later. Consequently, the acceleration time-scales of dislocations are very small ($\sim$10 ps). Therefore, the total time taken to travel from one pinning site to the next is approximately the sum of the time spent moving and the time spent pinned [14],

$$t_{motion} = t_{travel} + t_{pinned}. \tag{3.1}$$

The drift velocity, $\bar{v}$, used in Orowan's expression (Chapter 2) will then vary as $\frac{1}{t_{motion}}$. The drift velocity is much smaller than the speed of a 'free' dislocation, which is in principle reasonably close to the speed of sound, even at low rates (discussed in 3.2.1). In quasi static deformation, the time spent pinned is orders of magnitude greater than that in transit, so we shall currently approximate

$$t_{motion} \approx t_{pinned}. \tag{3.2}$$

In general, for a fixed structure with a constant number of mobile dislocations and distance between pinning points,

$$\dot{\varepsilon} \propto \bar{v} \propto \frac{1}{t_{motion}}. \tag{3.3}$$

The key to determining rate dependence in the quasi static regime is therefore to model the time taken to thermally climb the pinning barrier and remobilise the dislocation. We can make some progress, and in fact quite well describe deformation below 10^4 s^{-1}, by

describing the rate of pinning in an Arrhenius form

$$\frac{1}{t_{pinned}} = f_D \, exp\left[-\frac{U(\hat{\sigma})}{k_b T}\right], \tag{3.4}$$

where f_D is the vibrational frequency of the dislocation, that is taken to be the frequency with which the dislocation attempts to jump the pinning barrier. Being the motion of the large number of atoms around the distortion, the vibrational frequency of a dislocation is dependent on the dislocation length, but typically $\frac{1}{100}$ of the Debye frequency [97], a typical frequency in copper would be of the order of $\sim 10^{11}$ Hz. $U(\hat{\sigma})$ is the remaining thermal barrier after mechanical work. The exponential function results from the probability of a thermal equilibrium fluctuation being great enough to overcome the remaining barrier. There are several concerns with this approach, potentially causing the model to break down at higher rates, outlined in section 3.2.3.

Combining relationships 3.3 and 3.4, we can obtain

$$\frac{\dot{\varepsilon}}{\dot{\varepsilon}_\phi} = exp\left[-\frac{U(\hat{\sigma}) - U(\sigma_p)}{k_B T}\right]. \tag{3.5}$$

Where $\dot{\varepsilon}_\phi$ is some maximum strain rate obtained when the barrier is overcome on the first attempt, in practice the model will beak down before this rate is achieved as transit times will become important. By definition, if the applied stress $\hat{\sigma}$ equals σ_p the barrier is overcome by mechanical work alone, so $U(\sigma_p) = 0$. To achieve the desired final form ϕ, we will normalise the argument in the remaining barrier to the current mechanical threshold $U(\hat{\sigma}) \rightarrow U\left(\frac{\hat{\sigma}}{\sigma_p}\right) = U(\phi)$. We then have the relation

$$\frac{\dot{\varepsilon}}{\dot{\varepsilon}_\phi} = exp\left[-U\left(\frac{\hat{\sigma}}{\sigma_p}\right) \cdot \frac{1}{k_B T}\right], \tag{3.6}$$

that rearranges to

$$U\left(\frac{\hat{\sigma}}{\sigma_p}\right) = U(\phi) = k_B T \ln\left(\frac{\dot{\varepsilon}_0}{\dot{\varepsilon}}\right). \tag{3.7}$$

Thus if sufficient knowledge of the barrier geometry is available, we can determine the relationship between rate and strength.

To illustrate, we will begin with the simplest form available: a top hat with a height proportional to σ_p and width Δx_B. The energy required to overcome the barrier is $\int F(x)\mathrm{d}x$. The energy per unit dislocation length be considered in terms of a proportional stress integral, $\int \sigma(x)\mathrm{d}x$ (and $\int \tau(x)\mathrm{d}x$), as the force per unit dislocation length is τb ($\propto \sigma b$) shown by equation 2.12. With no applied stress in the top hat scenario, the initial energy required to climb the barrier can be described as $U_0 \propto \sigma_p \Delta x_B$. However if a constant stress is applied across the barrier, the remaining energy required is lowered to $U(\sigma_p, \hat{\sigma}) \propto \int \sigma(x) - \hat{\sigma}\mathrm{d}x = [\sigma_p - \hat{\sigma}]\Delta x_B$. By comparing the ratio of the barrier under the applied stress to the size of the barrier when no stress is applied, we find

$$U(\sigma_p, \hat{\sigma}) = \sigma_p \Delta x_B \left[1 - \frac{\hat{\sigma}}{\sigma_p}\right] = U_0 \left[1 - \frac{\hat{\sigma}}{\sigma_p}\right], \tag{3.8}$$

or, in terms of ϕ, $U(\phi) = U_0[1-\phi]$. Substituting this expression for U into relation 3.7 we arrive at the relationship

$$\phi = \left[1 - \frac{k_B T}{U_0} \ln\left(\frac{\dot{\varepsilon}_\phi}{\dot{\varepsilon}}\right)\right], \tag{3.9}$$

and therefore a rudimentary prediction of material strength,

$$\sigma_f = \sigma_0 + \sigma_p \left[1 - \frac{k_B T}{U_0} \ln\left(\frac{\dot{\varepsilon}_\phi}{\dot{\varepsilon}}\right)\right]. \tag{3.10}$$

Even with the most basic barrier scenario we have established two important relationships; the relation between strength and temperature occurs on approximately linear scaling, whilst rate dependencies occur on a logarithmic scale. Furthermore, the barrier magnitude, U_0 arises

from internal stresses, which depend on the materials shear modulus, and will be altered by its variation with temperature. The shear modulus can be extracted from U_0, describing it as

$$U_0 = U_\phi G(T) b^3 \tag{3.11}$$

where U_ϕ is now dimensionless and approximated to be a constant describing the dimensions of the barrier, such as Δx_b relative to b [14]. We should note that despite its approximation as a constant, U_ϕ, has some variation with the mechanical threshold, which has been observed experimentally [14].

The next logical step would to be to consider the barrier as parabolic; having established the energies involved with pinning to be quadratic in displacement. Manipulating non rectangular barriers is more complicated as there is now liable to be some region of the barrier instantly overcome by the applied force on the dislocation. Said regions are no longer rate limiting and thus will no contribute to the force integral. To find the remaining energy, U(ϕ), the general procedure becomes integrating vertically from the applied stress σ up to the top of the barrier, rather than across the barrier width. The derived expression can then be compared to the barrier integral with zero ap plied stress, to find U(ϕ) as a scaling of U_0, exemplified in expression 3.8.

True dislocation barriers are further complicated by the fact their elastic fields extend significant distances, important in correctly modelling material response under low applied stresses. The force profile, $F(x)$ of the real barrier id not easily derived from first principled, and is more easily considered phenomenologically. Kocks proposed a profile to account for a quadratic barrier with tails [97]. Integrating the expression to find the remaining energy required as a function of ϕ, resulted in the expression

$$U(\phi) = U_0 (1 - \phi^p)^q = U_\phi G(0) b^3 (1 - \phi^p)^q . \tag{3.12}$$

The profile of force barrier as a function of position (i.e. the function integrated to find U(ϕ)) is shown for a number of potential values of the parameters p and q in figure 3.1. The parameter q corresponds to the shape of the short range barrier, for a quasi-parabolic barrier, q must be somewhere in the range $1 \leq q \leq 2$. The parameter p accounts for the slower decay of the field at long distances, a value of 1 corresponds to a no alteration, and a value in the region $0 < p \leq 1$ corresponds to U decaying slowly at extended distances. In the mechanical threshold stress model, for which this expression was arrived, the values the values p= $\frac{2}{3}$ and q= 1 were adopted [15], however these parameters can be fit to data within their accepted ranges. More recently, the values of p=$\frac{1}{2}$ and q=$\frac{3}{2}$ have been adopted due to being considered more physically realistic [98].

The resultant barrier rearranges to the expression

$$\phi(\dot{\varepsilon}, T) = \left\{ 1 - \left[\frac{k_B T}{U_\phi G b^3} \ln \left(\frac{\dot{\varepsilon}_0}{\dot{\varepsilon}} \right) \right]^{\frac{1}{q}} \right\}^{\frac{1}{p}} \tag{3.13}$$

which is the rate scalar in the MTS model [14]. The approach adopted in this section is specifically that used in deriving the mechanical threshold stress model. However, a variety

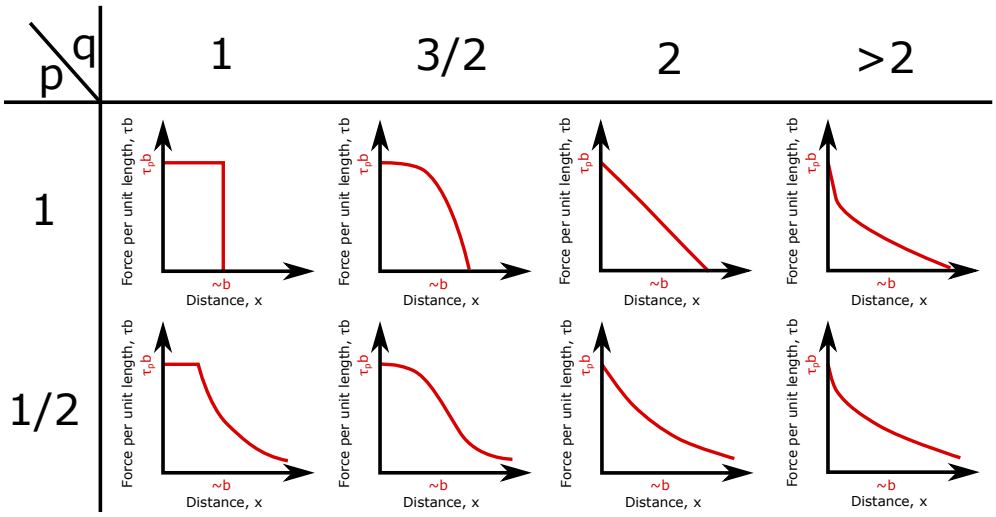

Fig. 3.1 The variation of the energy landscape modelled by expression 3.12 with parameters p and q. For values close to $p = \frac{2}{3}$ and $q = 1$ the barrier decreases in a parabolic manner close to the center, but slowly at greater distances. Image edited from original by Kocks [97].

of models exist, in each case the approach however is generally the same, using an Arrhenius like relation to relate some internal depinning barrier to describe the average time-scale any one dislocation spends pinned. Notable similar models are the Zerilli-Armstrong model [13] and the similar Goldthorpe model [9], a tabulation of other models is included in Appendix A.

Models based on the scaling of a mechanical threshold, σ_p, using a current condition scaler, ϕ, with the mathematical forms outlined in this section and the previous chapter perform very well below 10^4 s^{-1}. Examples of their success can be seen in the work of Gould [9] and the modelling of Taylor impact shown in figure 1.3 of Chapter 1. However, as we introduced in Chapter 1, at 10^4 s^{-1} a sudden upturn in strength is observed. We will now continue our discussion by examining the variety of approaches that have been applied to modelling this transition.

3.2 Enhanced Rate Dependence

Above strain rates of 10^4 s^{-1} an upturn is seen in the flow strength of many FCC metals. This phenomenon was initially observed by Follansbee *et al.* [99], their measurements are shown in figure 3.2 (a). Since this original observation, many similar measurements have been performed by a variety of authors and have been collated by Jordan et al. [17], shown

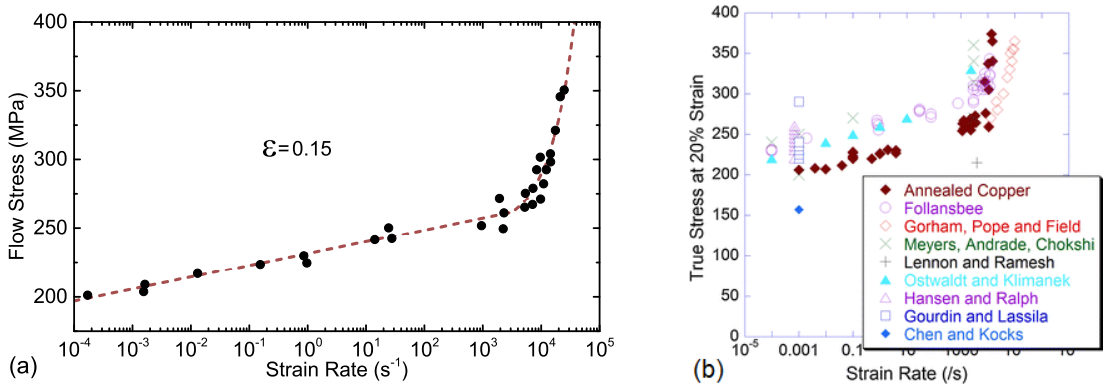

Fig. 3.2 (a) The initial measurements showing the upturn of flow stress at 10^4 s^{-1}, by Follansbee et al [99], the dashed line is to guide the eye. (b) Equivalent subsequent measurements by a collection of authors at 0.2 true strain, compiled by Jordan et al. [17]

in figure 3.2 (b). A large amount of scatter is observed in the collated data, and comes from a large number of sources; grain structure, specimen purity, specimen size and prior deformations all affect measurements.

All models composed from the forms currently discussed fail to capture this upturn, instead continuing the approximately log-linear relation observed below 10^4 s^{-1}. An early observation made when analysing the transition was that the post transition strength appears to have an approximately linear behaviour with strain rate. The linear relation is visible in figure 3.3, where the measurements of Gorham, Field and Pope [100] are replotted on a linear axis. The approximately linear nature of strength immediately above the transition has led to the region being known as the 'viscous regime'. An observation that has led to the common use of drag based theories, which will be discussed in section 3.2.1.

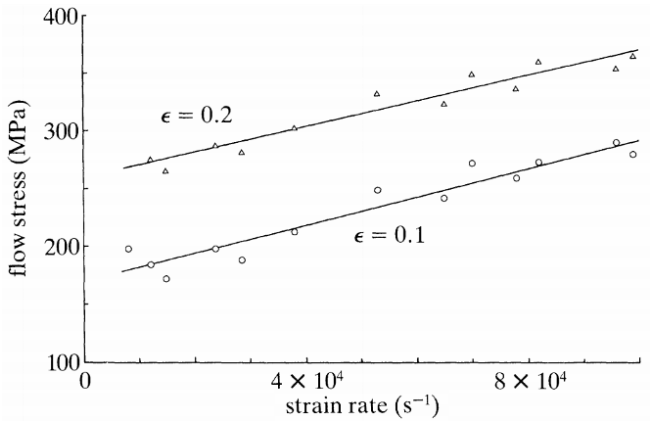

Fig. 3.3 The measurements of Gorham, Field and Pope [100], presented against strain rate instead of log strain rate. The data appears to fit two approximately parallel straight lines, with higher gradient at lower strain and slight quasi-parabolic residue pattern.

There are several phenomena that are believed to occur simultaneously, causing the measurement of flow stress to increase with rate. The level of effect of these phenomena as well as the level of confidence to which the physical theories have been tested vary dramatically. In this section we will outline the main theories used, the justification for them, and the flaws in the current state of each model.

3.2.1 Phonon Drag & Relativistic Effects

Early evidence of a viscous force acting on moving dislocations was found by Gilman [101], who used 'etch pit' techniques on LiF crystals. Dislocations, being areas of strained material and thus areas of stored elastic energy, etch more easily than unstrained regions, creating pits. Gilman was capable of imaging the location of a dislocation based on the centre of a pit, then moving the dislocation by applying a stress pulse of known duration and amplitude. Re-etching the specimen revealed the new position of the dislocation, allowing the displacement to be measured, allowing a relation to be drawn between drift velocity and the applied stress. An approximately linear relationship was observed between the applied stress and derived dislocation velocity was observed.

Etch pit methods were applied to aluminium by Parameswaran [102], shown in figure 3.4, where again a quasi linear relationship between applied stress and dislocation velocity

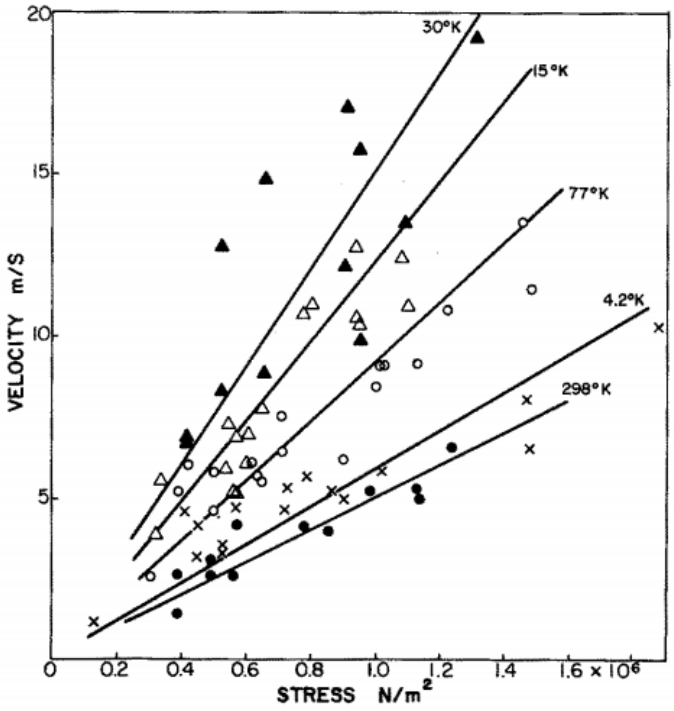

Fig. 3.4 The speeds of dislocations in annealed aluminium with respect to applied stress, measured by Parameswaran. The measurement was a two point one with time resolution of the order of 10 μs. Image from Parameswaran [102].

was found. Pulse durations of the order of 10 μs were applied, no measurement of strain rate was given. However the crystals were annealed, leading to typical dislocation densities of 10^{10} m^{-2} and from Orowan's law for a single crystal we would infer a shear strain rate of 150 s^{-1}. Furthermore, the applied stress pulses were of the order of 1 MPa, making them well below typical values mechanical threshold, as such pinning was likely to be affecting the dislocations, an unknown amount of time was spent pinned.

Based on the apparent linear relation between dislocation velocity and applied stress, a viscous drag force per unit dislocation length was proposed [1],

$$\mathbf{F}_L = -B(T,v)\mathbf{v}, \tag{3.14}$$

where B is the drag coefficient, a material property that is both temperature and strain rate dependent. We can consider this force in two regimes; either as a small to equal contribution to material strength, or as a dominant one. By far the simplest is the dominant scenario; balancing the local drag force with the applied force on a dislocation (equation 2.12) we find

$$\frac{\hat{\sigma}}{M}b = Bv, \tag{3.15}$$

and using Orowan's law (assuming at such rates it holds) we obtain

$$\hat{\sigma} = \frac{M^2 B(T,\dot{\varepsilon})}{\rho_m b^2}\dot{\varepsilon}. \tag{3.16}$$

In this limit we note that the proportionality between stress and strain rate only holds for a fixed mobile dislocation density, any increase in dislocation generation (seen in section 2.4) will suppress the viscous effect. Several other discrepancies arise in the $10^4 - 10^5$ s^{-1} region when attempting to use this form under the assumption of constant structure. The viscous limit is however well suited to scenarios such as when the applied stress exceeds

the mechanical threshold or at temperatures close to melt, where dislocations cease being stopped by pinning barriers.

The more complex scenario, and the most likely immediately above 10^4 s^{-1}, is when drag is not a dominant contribution; when pinning still occurs and is comparable in duration to the travel time between sites. Early models attempted to introduce drag in this scenario in a rudimentary manner [103, 104] by adding a '$B\dot{\varepsilon}$' drag stress to models used below 10^4 s^{-1} and fitting the value of B to the rise in stress.;

$$\sigma_f \rightarrow \sigma_0 + \phi(T,\dot{\varepsilon})\sigma_p + B\dot{\varepsilon} \tag{3.17}$$

Applying the to experimental data can provide a good fit for a single strain and temperature, however it breaks down upon varying either. The physical reason to expect such a construction to fail is simple; the dislocation explicitly experiences one force or the other, a rapidly moving dislocation is not pinned and thus will not feel a pinning stress.

We must then construct a more physical picture, again, we will use the arguments of Follansbee [99]; whilst this does not provide the most complete picture, it outlines the standard methodology and many of the same results as more complex models.

We will begin by remembering that acceleration time scales are negligible, allowing a simple expression for the drift velocity of a dislocation;

$$\bar{v} = \frac{\xi}{t_{travel} + t_{pinned}} \tag{3.18}$$

where ξ is the 'mean free path', effectively the average distance between any two pinning sites, which we will initially treat as a constant, but is likely to vary with dislocation structure. The pinning time we will assume unchanged from below the transition. The transit time we

can calculate form the viscous relation and the mean free path;

$$t_{travel} = \frac{\xi}{v} = \frac{MB\xi}{\hat{\sigma}b}. \tag{3.19}$$

we then arrive at a relation for where the two forces act only in their respective scenarios;

$$\dot{\varepsilon} = \frac{1}{M}\rho_m b\bar{v} = \frac{\rho_m b}{M}\frac{\xi}{\frac{MB\xi}{b\hat{\sigma}} + \frac{1}{f_D}exp\left[U(\hat{\sigma})/k_B T\right]}. \tag{3.20}$$

We now have a general relation in which there are two time scales. The pining time scale, whilst initially being large decays exponentially with the pinning barrier as the mechanical threshold is approached, allowing for orders of magnitude decrease in pinning time for very little increase in stress. When this term reaches a low enough value, the travel time, that decays much more slowly with stress ($\hat{\sigma}^{-1}$) becomes the limiting time scale. Unlike the ϕ relations derived for below 10^4 s^{-1}, high rate relations tend not to be analytically invertible to a ϕ like expression, due to the flow stress appearing both linearly in the first term and in the exponent of the second.

An iteration to the model was proposed using a similar basis to the Taylor model of pinning: the travel distance between pinning sites would be expected to be approximately $\frac{1}{\sqrt{\rho_i}}$ [14, 19], incorporating this approximation we obtain

$$\dot{\varepsilon} = \frac{\frac{1}{M}b\rho_m}{\frac{MB}{\hat{\sigma}b} + \frac{\sqrt{\rho_i}}{f_D}exp\left[U(\hat{\sigma})/k_B T\right]} \tag{3.21}$$

Using this scaling, we can see, as we would expect from Orowan's rule, that drag will not only be active at extremely high rates, but it will also play a part for low dislocation densities, potentially affecting the early stages of deformation in an annealed metal.

Having established how a viscous term is incorporated, we will now discuss the physical effects proposed to be behind the viscous force, to infer the temperature and velocity

dependence of the force. In general, the viscous term is composed of three parts

$$B = B_{Ph} + B_{e^-} + B_{Imp} \tag{3.22}$$

summing forces from interactions between phonons, electrons and impurities. At low temperatures ($T < \theta_D$, where θ_D is the Debye temperature of the metal) electron viscosity is the dominant source of drag. However, this rapidly falls with temperature [103]. Impurity drag is only significant if the dislocation is moving at speeds of below 0.1 ms^{-1} [105]. We will therefore simplify the relation to $B \approx B_{Ph}$, and consider the viscous nature of phonon interactions.

3.2.1.1 Phonon Drag

The main source of drag at ambient and raised temperatures is due to a moving dislocation scattering from of phonons. The earliest estimate of this value was performed by Leibfried [106] and similarly by Hirth [107] and Lothe [108], resulting in the expression

$$B \approx \frac{\alpha_L \varsigma_{Ph}}{C_s}, \tag{3.23}$$

where α_L is a statistical constant to cover the projection, into the movement direction, of all potential scattering angles over which the phonons can interact, that is approximately 1/10. C_S is the shear wave speed of the medium. ς_{Ph} is the thermal energy density of the system, which is defined as

$$\varsigma_{Ph} = 3\frac{\bar{E}_{Ph}}{b^3}. \tag{3.24}$$

where $\bar{E}_{Ph}$ is the average energy contained in in any single polarisation, and the factor of 3 accounts for the three polarisations available to the phonons. The average energy can be

obtained from the Bose-Einstein statistics of the phonons [108], in the high temperature limit

$$\bar{E} = \frac{\hbar\omega}{e^{\hbar\omega/k_BT} - 1} \to k_BT. \tag{3.25}$$

where ω is the angular frequency of the phonon and $\hbar$ is the reduced Planck constant. Thus a first estimate of B (above the Debye temperature) is then

$$B \approx \frac{3k_BT}{10C_sb^3}, \tag{3.26}$$

and this estimate is close to most subsequent attempts [109]

We will use more complex models to discuss the physical mechanisms that give rise to viscous drag. These mechanisms separate motion of the dislocation into that of a rigid body and that due to flexibility. The flexibility mechanism is known as fluttering [110], and involves phonons exciting vibrations within the dislocation line itself, that are subsequently re-radiated around the phonon cylindrically. If the phonon is moving, there is a scattering bias for phonons travelling in the opposite direction to motion. The scattering bias creates a bias in the imparted momenta, and thus a force against dislocation motion [110]. Furthermore, the motion creates an asymmetry in the re-radiation, also biased against the motion of the dislocation [108], that becomes increasingly important at high velocities.

Applying time dependent perturbation theory to the relevant dislocation and phonon momentum states gives a value of the fluttering drag term in the low velocity limit of [110]

$$B^0_{flut} = \frac{k_BT\,\omega_D^2}{\pi^2C_s^3} \qquad \text{for } T \geq \theta_D. \tag{3.27}$$

where ω_D is the Debye frequency, corresponding to the highest allowed frequency in the Debye model.

$$\omega_D = \left(\frac{3\rho_a}{4\pi}\right)^{1/3} C \tag{3.28}$$

where ρ_a is the atomic density of the metal, and C is the average sound speed of the relevant phonon polarisation. The Debye frequency also defines the Debye temperature,

$$\theta_D = \frac{\hbar\omega_D}{k_B} \tag{3.29}$$

We note that in this term, the original temperature dependence predicted by Leibfried [106] is retained.

The terms accounting for rigid interactions of the dislocation are known as the 'phonon wind' and the 'slow phonon' terms. The wind term accounts for the fact that extremely close to the core of a dislocation, the strain system is too extreme to obey linear elasticity. Thus any phonons passing through the dislocation must deviate from their behaviour as a harmonic oscillator, scattering and imparting momentum into the dislocation core [108, 111–113]. Expressions for this effect have been derived by Brailsford [112], again in the low velocity limit,

$$B^0_{wind} = \frac{96\Gamma^2 P_D \hbar}{b^3}\left(\frac{C_s}{C_l}\right)^4\left(\frac{b}{2\pi}\right)^5\frac{T}{\theta_D} \qquad \text{for} \quad T \geq \theta_D. \tag{3.30}$$

P_D is the magnitude of the momentum of a phonon at the Debye energy and Γ is the Grüneisen parameter, that describes the change of vibrational properties of a lattice due to a change in volume.

The final phonon term is known as the slow phonon term, and is a correction of the phonon wind term for phonons close to the edge of the Brilloin zone, where the Debye assumption that group velocity, $\frac{\partial\omega}{\partial k} = C$ breaks down (k is the magnitude of the wave vector). In fact $\frac{\partial\omega}{\partial k}$ decreases as the edge of the Brilloin zone is approached, the group velocity of these phonons is much slower than in the simple linear theory. The 'slow' motion leads to a

different anharmonic interaction, corrected for by Al'shits and Indenbom [111];

$$B^0_{slow} = \frac{\Gamma \hbar b^2 P_D^4}{8\pi^5 r_D} \qquad \text{for } T \gg \theta_D \tag{3.31}$$

where r_D is the radius of the dislocation core, approximately b. The effect is only notable when a significant fraction of phonons are at the Debye energy and thus close to the Brillouin zone boundary. In practice, B^0_{slow} is smaller than B^0_{flut} in FCC metals [105] but is importantly independent of temperature when active.

A final effect exists, for large temperatures ($T \gg \theta_D$) involving thermoelastic effects. As a dislocation moves, the compressed and rarerified regions either side of the dislocation must move with it. The motion of these regions will cause adiabatic heating and cooling of either side of the dislocation. The required heat flow will excite additional phonons. Thermoelastic effects are often neglected due to only occurring at very high temperatures and due to ease of heat flow in metals [108, 112], but are accepted to vary as T^2 and thus may become important in deformation at very high temperatures.

We can therefore, to leading order and using the terms given above to calculate the coefficients, define some total B^0, which has the high ($T > \theta_D$) temperature relation

$$B^0 = B^0_0 + B^0_1 T + B^0_2 T^2 \tag{3.32}$$

where $B^0_1 > B^0_0 \gg B^0_2$. The linear temperature dependent term arising from phonon wind and fluttering, the temperature independent term from 'slow' phonons and the quadratic term from thermoelastic effects. These expressions, were however derived in the low velocity limit, denoted by the 0 superscripts. We will now expand them to general velocities.

3.2.1.2 Relativistic Dislocation Motion & Phonon Drag

The fundamental equations of elasticity are mathematically equivalent to those of other physical phenomena, such as electromagnetism and diffusion. Using a parallel to

electromagnetism, many authors [1, 114–118] have noted that the dynamics of a dislocation can be mapped onto that of a stationary dislocation through a Lorentz transform, with the characteristic maximum velocity being the shear wave speed of the medium.

We can begin with Newton's second law in a continuum,

$$\nabla \cdot \sigma = \rho_M \frac{\partial^2 \mathbf{u}}{\partial t^2}, \tag{3.33}$$

where $\mathbf{u}(\mathbf{x})$ is the vector displacement field of the solid. Noting the definition of shear modulus as $\sigma = G\nabla\mathbf{u}$ we can obtain

$$\frac{G}{\rho_M}\nabla^2\mathbf{u} = \frac{\partial^2 \mathbf{u}}{\partial t^2} \tag{3.34}$$

which is the travelling wave equation for shear wave speed $\sqrt{\frac{G}{\rho_M}}$. Thus the strain fields of a dislocation propagate as elastic waves at the shear wave speed. We note, as with electromagnetism, that the strain field of a dislocation moving at uniform speed v in the x direction can be mapped onto that of a stationary dislocation (i.e. the time derivative term is removed) if we apply the transform [1]

$$x' = \frac{x - vt}{\sqrt{1 - \frac{v^2}{C_s^2}}}, \qquad y' = y, \qquad z' = z. \tag{3.35}$$

We map onto the solution for a stationary dislocation, Laplace's equation

$$\nabla^2\mathbf{u} = 0 \tag{3.36}$$

leading to, in some effective form, many of the effects documented in special relativity.

Here we will focus on length contraction. In the rest frame of the crystal lattice, the strain field of the fast moving dislocation is compressed in the direction of travel, exemplified in

figure 3.5. Two effects arise, firstly, the strain field will become more severe as it is localised, causing more severe scattering with incident phonons. Secondly, as discussed previously, the motion of the dislocation also affects the re-radiation of the absorbed phonon energy; biasing it to impart a net momentum against dislocation motion, in the relativistic limit, this re-radiation effect bias will become more severe.

From here, the most common approach of authors is to use a relativistic mass term to try and describe the behaviour in velocities approaching the shear wave speed. However, deriving a relativistic theory by substitution of an effective mass into a classical relation is controversial at best. Furthermore, the effective mass of a dislocation was noted to be velocity invariant by Gilman [119]. Finally, relativistic mass methods make little sense when the final result of the derivation, and the empirical observation is the amplification of a viscous force, inertial mass having no effect in a viscous (low Reynolds) regime.

Instead we will apply a more standard relativistic approach to the problem, transforming into the rest frame of the phonon scattering events, ie, that of the dislocation, as shown in figure 3.6. We can then deal with the much simpler transform effects on the phonons. The drag coefficient is proportional to the product of the momentum imparted by a single phonon and the rate at which phonons scatter.

In the rest frame of the dislocation, it is the x direction of the lattice that length contracts by γ_v. The contraction has two effects, firstly the phonon wavevector in the x direction increases as the wavelength contracts, increasing the x-momentum imparted by the phonons into the dislocation per collision. We note that this is by just the Lorentz factor, rather than the traditional relativistic Doppler shift formula, as the phonons are not being generated by a source that our dislocation is moving relative to, they are simply present throughout the lattice, in what is termed the phonon gas. The rate of scattering from the dislocation is proportional to the density of the phonon gas. In the rest frame of the dislocation, the phonon gas as a whole must be moving with speed v and thus also length contracts, increasing in

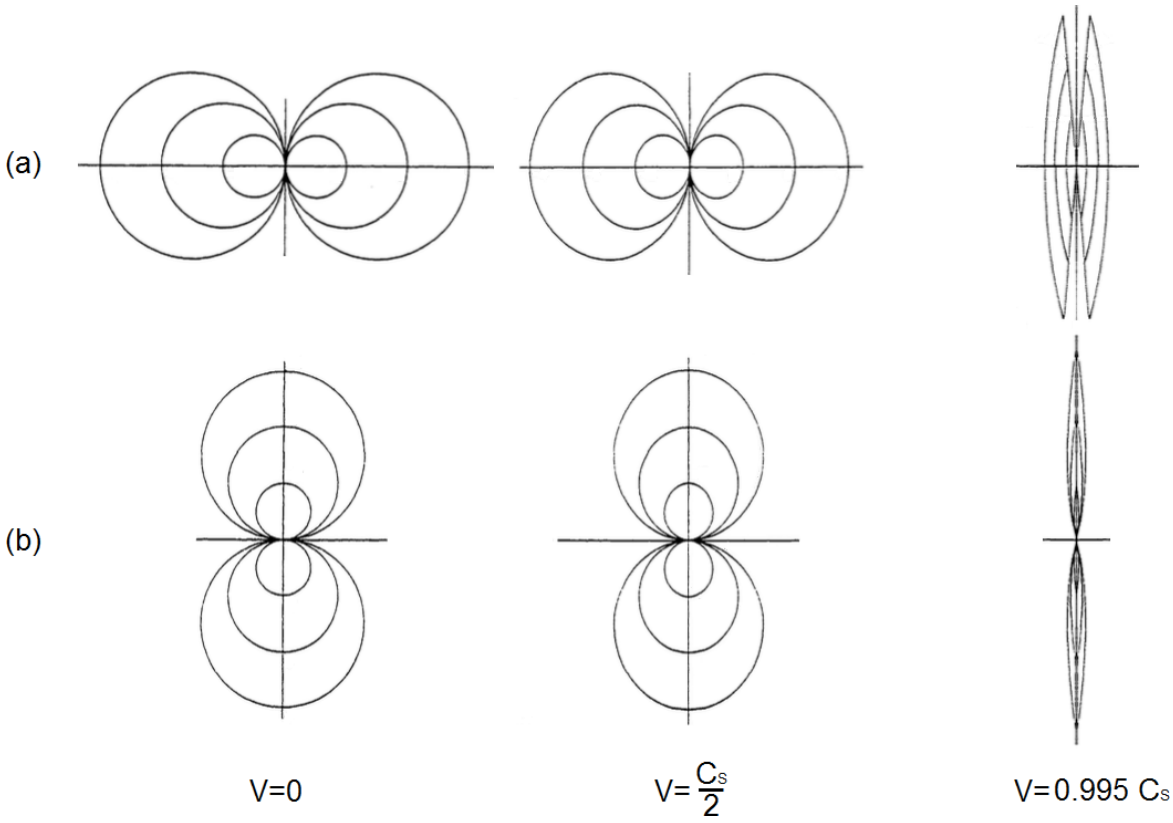

Fig. 3.5 The Lorentz contraction of dislocations travelling from left to right with respect to the page (a) in the direction of travel (b) orthogonal to the direction of travel for several speeds. Image adapted from Meyer [1] and by Pelton and Rebenberg.

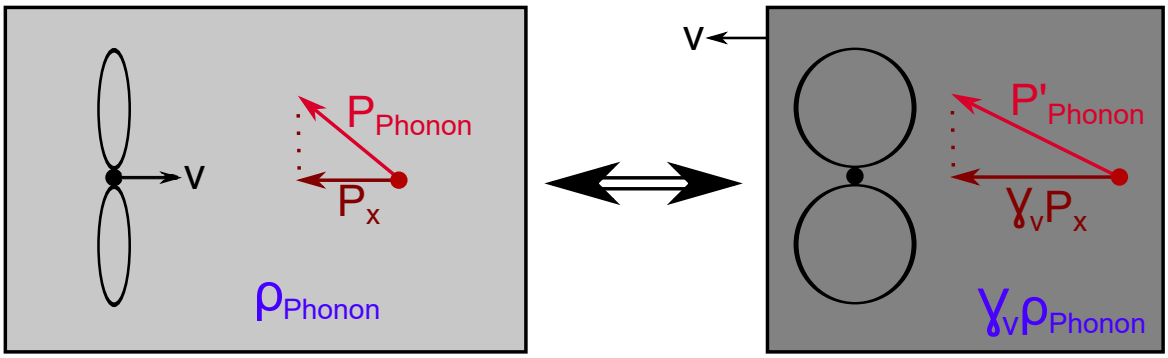

Fig. 3.6 A sketch of the transform between the rest frame of the lattice (left) and the rest frame of the dislocation (right). In the rest frame of the dislocation, and importantly the scattering events, the momentum of phonons increases as their wavelength contracts, and the density of the phonon cloud increases as it contracts.

phonon density by γ_v, therefore increasing the scattering rate by a Lorentz factor. The result is that we observe an increased viscous force for a fast moving dislocation of factor γ_v^2. This rise, being based on the momentum states, is typically attributed to the flutter term, that will dominate at high speeds, so

$$B(v_{travel}) \rightarrow \gamma_v^2 B^0_{flut} = \frac{B^0_{flut}}{1-\frac{v^2_{travel}}{C_s^2}}. \tag{3.37}$$

The picture presented is, of course, simplified. However it is consistent with empirical observations [118], and is likely to be sufficient outside of shock loading. A more complete derivation of the phenomenon is provided by Roos [105], using time dependent scattering theory.

The new form for drag gives a different relation between $\hat{\sigma}$ and v for high speeds,

$$v_{travel} \rightarrow \frac{MB^0_{flut}C^2}{2\hat{\sigma}b}\left[\sqrt{1+\left(\frac{2\hat{\sigma}b}{MB^0_{flut}C}\right)^2}-1\right], \tag{3.38}$$

and, as in order to reach relativistic speeds, a dislocation will be under stresses well above the mechanical threshold. the rate can be expressed as

$$\dot{\varepsilon} \rightarrow \frac{1}{M}\rho_m \frac{MB^0_{flut}C^2}{2\hat{\sigma}}\left[\sqrt{1+\left(\frac{2\hat{\sigma}b}{MB^0_{flut}C}\right)^2}-1\right]. \tag{3.39}$$

The complete relation between applied stress and dislocation drift velocity (proportional to strain rate for a constant mobile dislocation density) is shown in figure 3.7. Below yield the dislocations are stationary, above some stress the dislocations overcome the pinning barrier, rapidly increasing their drift velocity and thus the imparted strain rate. Eventually the de-pinning time becomes significantly short enough that drag becomes an effect, limiting the rise of the dislocation velocity with stress. Above the mechanical threshold, the dislocations

enter a pure drag scenario which continues until they reach relativistic speeds, where increased scattering and re-radiation effects limit their velocity to the sound speed of the medium.

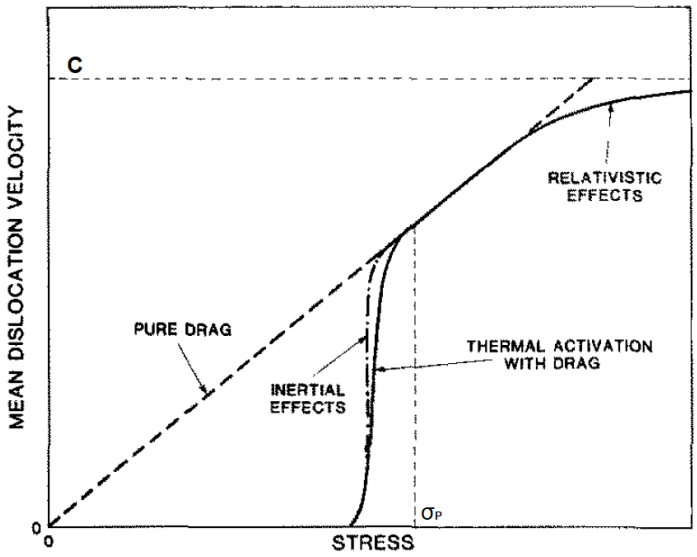

Fig. 3.7 The picture of dislocation drift velocity as a function of the applied stress at fixed structure. The relative regions are outlined in the body text. Image from Follansbee [14].

There are several flaws with such a theory, as outlined by Gilman [120]. Firstly, slip motion is a shear, and thus has an angular component that will also become relativistic, yet is disregarded. Secondly, a lower maximum velocity would be expected where the elastic energy at the dislocation core causes bond failure in the lattice. The results of such a failure are unknown, however they could involve the spontaneous nucleation of a second dislocation.

3.2.1.3 Phonon Drag as a Strengthening Mechanism

Dislocation drag is proposed to provide an increased strength to a metal in high rate deformation by limiting the velocity of unpinned dislocations depending on the applied stress. As the mechanism limits dislocation velocity, it cannot easily be defined as directly proportional to rate, instead the two must be linked through dislocation density, that increases by orders of magnitude during plastic deformation. The coupling of strain rate to structural evolution is theorised to suppress drag effects for applied stresses below the mechanical threshold [121]. Furthermore, for applied stresses below the mechanical threshold, the

inclusion of the pinning timescale in dislocation dynamics prevents any simple analytical inversion at all.

However, studying the underlying phonon mechanisms and their relative contribution has revealed an interesting change in the expected temperature dependence of a metal if it becomes phonon limited. The dominant contribution to viscosity is expected to be linearly proportional to temperature above θ_D, with smaller constant and quadratic terms. It could therefore be predicted that at very high rates the thermal softening of metals reverses to thermal strengthening, if phonon drag provides a limiting mechanism [122–126].

Molecular dynamics simulations of moving dislocations have observed such inverted behaviour on the atomic scale. The simulations of Olmsted [127] have shown that dislocation velocities for both edge and screw dislocations can be described well by the single parameter $\frac{\hat{\sigma}}{T}$. However above approximately half of the shear wave speed, screw dislocations were observed to lose the temperature dependence, resulting in a velocity that depends only on $\hat{\sigma}$, presumably due to the re-radiation of the phonon energy becoming more important as relativistic effects become large. Current studies do not expect to achieve relativistic dislocation velocities.

Early measurements performed to test dislocation drag theories in the $10^3 - 10^4$ regime did not observed any proposed relations except for a linear stress-rate dependence. Most notably Kumar [103] noted no apparent rise in material strength, or reduction in thermal softening at rates below 10^4 s^{-1}. Given that this is when the observed upturn is only just beginning, it is potentially because drag effects are too small to usefully extract their temperature dependence. Similarly, pure copper was observed to decrease in strength with temperature for shear strain rates as high as 10^6 s^{-1} [128, 129], however the shear nature of deformation makes both the experimental stress and strain rates difficult to compare to the experimental data. In chapter 5 we shall perform similar raised temperature experiments

at rates above 10^4 s^{-1} in the a uniaxial compression configuration to search for a change in behaviour in a more comparable scenario.

However, whilst experiments performed close to the transition appear to show now obvious change in thermal behaviour, there are scenarios where the inversion of thermal softening is observed. The first of these is in high rate deformation at temperatures close to melt. Grunschel [130] performed measurements, shown in figure 3.8 (a) of pure aluminium at shear strain rates of approximately 1.45×10^6 s^{-1} and at a shear strain of 0.8, specimens deforming at 1000 K were observed to be softer than those measured at 1100 K. The authors predicted an upturn in strength to occur at approximately 600 K for their shear strain rate.

Further evidence was provided in the work of Kanel [122–124] and later Gurrutxaga-Lerma *et. al* [125, 131]. Experimental data form the latter is shown in figure 3.8 (b) which depicts Hugoniot elastic limit (HEL) measurements, that correspond to the elastic plastic transition in shock deformation and is identified on each trace in figure by black squares. In their shock geometry, the applied stress is well in excess of the mechanical threshold, and the dislocations are purely drag limited. The specimen strength as defined by the HEL can be seen to increase with increasing temperature for the entirety of the range. Unlike the measurements of Grunschel, where pinning was progressively removed by thermal activation,

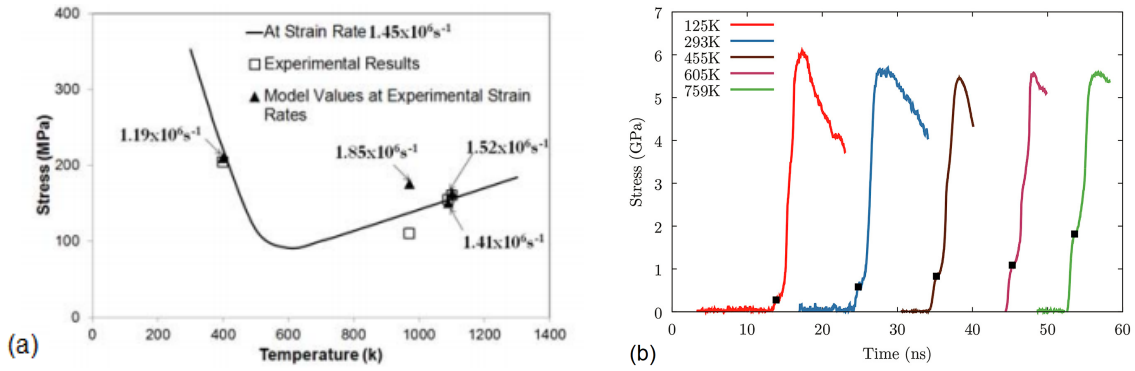

Fig. 3.8 The variation in the strength of high purity FCC metals with temperature for (a) high rate shear loading, measured by and reproduced from Grunschel [130], (b) laser shock, measured by and reproduced from Gurrutxaga-Lerma *et. al* [125]. In figure (b) each trace is offset by an arbitrary amount of time for visibility.

no thermal softening is observed, as the mechanical threshold is always completely overcome by the applied stress.

The experiments discussed provide strong evidence for the existence and behaviour of phonon drag on dislocations. However, it does not prove that the mechanism is dominant or in fact significant in the $10^4 - 10^5$ s^{-1} regime, and thus does not prove that it is responsible for the observed transition. Hunter and Preston [19] calculate that given the respective terms in the denominator of equation 3.21 that at a dislocation density of 10^{13} m^{-2}, typical of early stage plastic deformation, and at a rate of 10^6 s^{-1}, the timescale predicted due to drag limited dislocation transit is 1% of that related to pinning. Therefore, given currently measured values of the various constants dislocation drag should negligible as a rate limiting mechanism. Hunter and Preston also note that models attempting to use dislocation drag either physically or in a constitutive form become progressively less accurate with increasing rate.

The phonon drag mechanisms discussed are largely only concerned with the terminal velocity of free dislocations. The onset of such rate limiting behaviour would cause much of the intricate path-dependent behaviour of FCC metals to be suppressed above the transition. However, phonon drag is not the only mechanism proposed to be responsible for this transition, and indeed the main alternative mechanism makes quite the opposite prediction; instead of predicting that path dependence in the material strength becoming negligible, it predicts that path dependent effects become much greater.

3.2.2 Rate Sensitivity in early Structural Evolution

The specifics of interactions between strain rate and early structural evolution have seen much less study than viscous drag, experimentally theoretically and computationally. However, a number of authors, including Follansbee [14], Granato [109], Austin [126] and (under the right conditions) Armstrong [33] have proposed that above 10^4 s^{-1} some change occurs in the evolution of dislocation structure. Unlike in studies of phonon drag where

different approaches are taken to modelling the same set of physical mechanisms, theories modelling changes in structural evolution each model different underlying mechanisms.

There are two key differences between theories which predict changes in dislocation structure and those that use phonon drag. Firstly, as drag does not become the dominant mechanism, dislocation evolution theories do not necessarily predict any change in thermal behaviour (relative to the mechanical threshold) from low rate theories. Secondly, structural strength corresponds to the materials mechanical threshold, σ_p, and if any changes cause an increase in the threshold, the increase will be present permanently (to within the effects of saturative effects). Unlike drag effects which cease if the high strain rate is removed, structural changes increase the specimen strength in later loading, even if it is at substantially lower rates.

3.2.2.1 Rate Sensitivity in the Mechanical Threshold Stress Model

The concept of rate sensitive structural evolution was initially raised by Follansbee [15]. They performed a series of 'jump test' experiments on high purity copper specimens that were deformed to a fixed strain of 0.15 at a variety of initial rates between 10^{-4} and 10^{4} s^{-1}. The low strain was chosen kept the effects of saturation small. After the fixed strain, specimens were reloaded at room temperature and a fixed rate of 10^{-3} s^{-1}. One can easily argue the results of the experiment using the three term framework, however the results can be considered in an much more intuitive manner. As the metal strength is a function of the instantaneous conditions and the material structure and the specimens are reloaded at fixed conditions, any variation in the reload strength of the specimens is attributed to some change in dislocation structure.

The results of these experiments are depicted in figure 3.9 (a) with a broken vertical axis and (b) without. A small variation is seen in the range 10^{-4} and 10^{3} s^{-1}, which is attributed to a combination of saturation effects not being negligible and slight (logarithmic) rate dependence in the nature of work hardening, relating to the line tensions involved in

pinning. Between 10^3 and 10^4 s^{-1} however the beginnings of a more significant upturn are seen, the reload yield increases by the same degree between 10^3 and 10^4 s^{-1} as it had in the prior seven orders of magnitude.

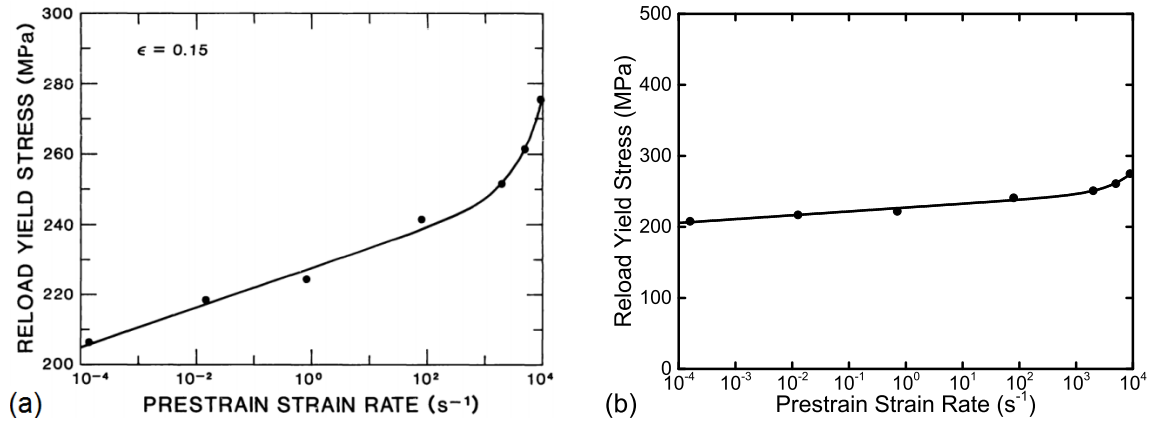

Fig. 3.9 (a) The yield stress of a 0.99999 Cu at 10^{-4} s^{-1} when reloaded after 0.15 plastic strain at varying rates, (b) the same data plotted without a broken axis to show the relative sizes of the upturn and absolute value. Image (a) from Follansbee & Kocks [15]

Based on this observation, Follansbee *et al.* added a linear rate dependence to their expression for stage II work hardening

$$\Theta_0(\dot{\varepsilon}) = \Theta_{00} + \Theta_{01} \ln \dot{\varepsilon} + \Theta_{02} \dot{\varepsilon}. \tag{3.40}$$

Subsequently fitting the form, combined with a Voce law, to their reload measurements to obtain coefficients for each term. Using this form they generated a set of mechanical thresholds for a variety of strains, strain rates and temperatures.

The data set was then compared to Hopkinson pressure bar experiments, performed in the same study [14]. However, rather than comparing constant strains, the strain at which a certain mechanical threshold was expected was calculated for each experiment, and the data was compared as a function of rate at constant mechanical threshold [14], plotted in figure 3.10. When the data was gathered by mechanical threshold rather than strain, the upturn

appeared not to occur, therefore, if changes in structural evolution were accounted for, then no change appeared to be needed in the dynamical considerations.

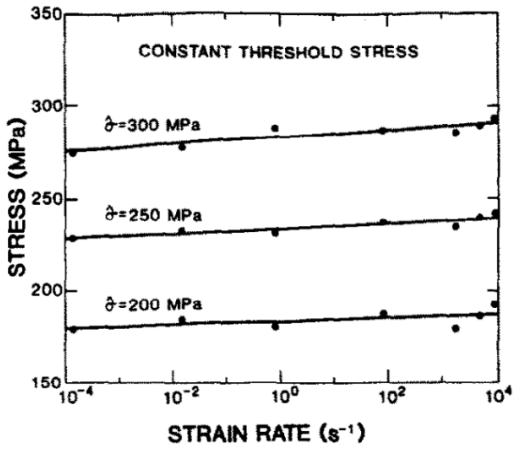

Fig. 3.10 Follansbee's observation of flow stress as a function of rate rate for fixed mechanical threshold stress instead of fixed strain. The values of the mechanical threashold at each rate were computed using a constitutive model [14] as a function of strain for each experiment. The flow stress values in different experiments were then compared at the point the mechanical threshold was predicted to be the same, rather than the strain. As a consequence of comparing the at constant mechanical threshold rather than strain, the upturn became less visible in the range of the experiment. A consistent linear deviation from the fit still remains above 10^3 s^{-1} for all mechanical threshold stresses. Image from Follansbee [14].

Follansbee attributed the changes to the decrease in the timescale available for slip with rate, arguing that as the timescale available decreases, dislocations would expect to move less far from their sources or original pinning sites [17]. The argument however would appear to be inconsistent with Orowan's law, that states the rate and dislocation velocity are proportional, thus the increase in drift velocity would be expected to balance the decrease in time available for slip.

Whilst the model appears promising, there are several large flaws that remain to this day. Firstly, jump tests have only been performed with pre-jump strain rates up to 10^4 s^{-1}. The application of the model to the upturn that is almost entirely above this value requires a large degree extrapolation. Extrapolation is compounded by the fact that the reload measurements do not extend into the post transition regime, and therefore the linear dependence is effectively

a guess. Figure 3.10 shows a constant linear residue between the experimental measurements between 10^3 and 10^4 s^{-1} and predicted curve, a potential artefact of an incorrect form for Θ_0.

A major hindrance to the current understanding of the strength transition is the lack of reload measurements such as those performed by Follansbee *et al.* above the transition region (ie, in the 10^4 to 10^5 s^{-1} rate range). The only available reload measurements at higher strain rates are those performed by Follansbee and Gray [132] on shock deformed metals. However, in shock deformation the dislocation dynamics and expected structural evolution are both significantly different due to homogeneous nucleation at the shock front [133].

3.2.2.2 Enhanced dislocation generation due to phonon scattering

Huang et al [47] proposed a model for rate dependent structural evolution arising from phonon scattering events. After forming a thermodynamic framework they propose a mechanism where scattering with a phonon causes a moving dislocation to lose energy to the surrounding lattice, that in turn excites the growth of dislocation line length. They therefore proposed a modification of dislocation generation (outlined in section 2.5);

$$\frac{\partial \rho_+}{\partial \varepsilon} \propto \alpha_T M G b \sqrt{\rho} + \left[B^0_{wind} + \frac{B^0_{flutter}}{1-(\dot{\varepsilon}/Mb\rho_m C_s)^2} \right] \frac{T}{\theta_D} \frac{\dot{\varepsilon}}{Mb^2\rho_m}. \tag{3.41}$$

An example of the predictions of the model are shown in figure 3.11, compared to the measurements of Follansbee [14]. The increase in dislocation density due to drag is mapped using the Taylor relation to an increase in material strength. The plateau seen at approximately 2×10^5 s^{-1} is due to the use of an old expression for viscosity that is subsequently abandoned in favour of more recent expressions quoted.

Whilst the mechanism is novel, there are serious concerns that should be raised regarding the model. The most major is that it relies on the use of a 'back stress' to define the rate of dislocation generation. The result of the model's thermodynamic formulation is to state that

the generation of dislocations is proportional to said back stress defined opposing dislocation motion. The application of a back stress formulations are often unrigorous. In this scenario we see that the back stress used corresponds to the sum of the stress required to overcome the Taylor pinning barrier, and the nominal drag stress acting on a dislocation at its expected terminal velocity given the strain rate, $\dot{\varepsilon}$. The model therefore exhibits the same flaw as early models explored by Kumar [103, 104]; a dislocation does not experience pinning and drag (for its terminal velocity) simultaneously, the two resistive forces are mutually exclusive.

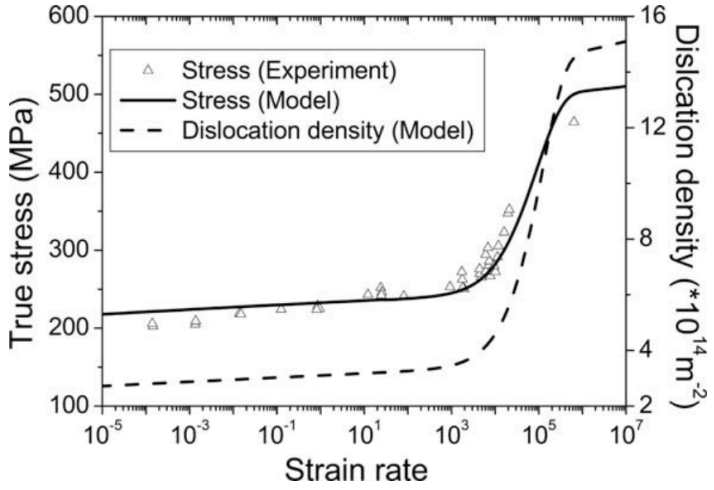

Fig. 3.11 The predictions of the irreversible thermodynamic model of Huang et al. the dislocation density increases by an order of magnitude between 10^3 and 2×10^5 and then plateaus. Figure from Huang et al [47].

3.2.3 The Breakdown of Approximations at High Rates

Having studied the two major mechanisms proposed for the strength transition; phonon drag and enhanced structural evolution (or work hardening), we will now turn our attention to a series of less prominent but important concerns, largely centred around the approximations typically used in the derivation of most constitutive models.

Arrhenius relationships have long been known to be unfit for describing barrier jumping in dislocation systems [134]. Originally intended for chemical reactions of independent point like particles, an Arrhenius relation has no ability to account for the fact that dislocations

are extended bodies with a limiting speed with which the two ends can communicate [120]. Dislocation systems are clearly different from the intended systems for Arrhenius kinetics, developing large correlations both along the length of a single dislocation, and between groups of many dislocations.

Arrhenius kinetics, being based in equilibrium dynamics, assume that after each transition the system has enough time to completely rethermalise. An assumption that cannot be not valid to arbitrarily high rates. Furthermore, the applied force for deformation is assumed to be a perturbation, much less than the barrier (requiring both $U(0) \gg k_B T$ and $U(\hat{\sigma}) \gg k_B T$). If the applied force is large, the Boltzmann distribution cannot be as the applied force will significantly disturb the energy states of the system. These criteria are shown to be broken in high rate deformation by Hunter and Preston [19], who show that for an annealed metal and a rate just above 10^5 s^{-1}, $U(\hat{\sigma}) \approx k_B T$.

At still higher rates, Hunter [19] raises concerns that pinning time scales are short enough to be of the order of the coherence time of thermal noise. Accounting for applied stresses, thermal fluctuations, their correlations and dislocation motion against the applied load, they derived a new expression for the average time taken to remobilise a dislocation;

$$t_{pinned} = \frac{t_0}{2}\sqrt{\frac{\pi k_B T}{U_0(\rho)}} exp\left(\frac{U_0(\rho)}{k_B T}\right)\frac{\sigma_p}{\hat{\sigma}}, \tag{3.42}$$

where $U_0(\rho)$ is the height of the pinning barrier at $\hat{\sigma} = 0$. The new expression is then combined with the drag time to create a kinetic equation such as 3.21, in the place of the classic pinning term.

The authors [19] comment, as we saw earlier in discussions of the same form, the kinetic equation is impossible to invert analytically, nor is it trivial to invert numerically. They do however provide more detailed solutions for the limiting rates. In the low limit;

$$\ln\left(\frac{\hat{\sigma}}{\sigma_p}\right) \approx \frac{k_B T}{U_0(\rho)}\left[\ln\left(\frac{\dot{\varepsilon}}{1\text{s}^{-1}}\right) - \ln\left(\frac{b\rho_m}{\sqrt{\rho_i}t_0 \cdot \text{s}^{-1}}\right)\right] \tag{3.43}$$

or

$$\hat{\sigma} = \sigma_p \left(\frac{\dot{\varepsilon} t_0 \sqrt{\rho_i}}{b\rho_m} \right)^{\frac{k_B T}{U_o(\rho)}} \tag{3.44}$$

and in the high limit

$$\hat{\sigma} = \sigma_p \frac{\dot{\varepsilon}}{b\rho_m} \left(\sqrt{\rho_i} t_B + \frac{B}{b\sigma_p} \right) \tag{3.45}$$

where t_B is the minimum time required for a pinned dislocation to bow out and escape;

$$t_B = \frac{16B}{5\pi b^2 \rho G \ln\left(\frac{1}{b\sqrt{\rho}}\right)}. \tag{3.46}$$

Whilst not dependent on the applied stress, it is dependent on the dislocation density and drag. The Hunter and Preston model views the upturn in high rate plastic strength to be due to the required time scale for depinning approaching this value. Finally, we should acknowledge a previous model in common use by Preston and co-authors, known as the Preston-Tonks-Wallace model [135], we have preferentially summarised the most recent model by the author.

3.3 Discussion

In the current and previous chapter, we have outlined a wide range of interconnecting phenomena that give rise to the bulk behaviour of FCC metals. The phenomena can broadly be broken into the evolution of material structure, the mobilisation of pinned dislocations at a given structure, and the drag limited transit of unpinned dislocations. The complete picture shows a much more complex problem than initial observations of the upturn in flow strength would imply.

Correctly identifying the nature of the transition is key to predicting both instantaneous behaviour under a general set of conditions and path dependent effects in subsequent deformation. Generally, phonon drag models are expected to decrease and eventually reverse thermal softening. Meanwhile, in an enhanced work hardening scenario the effects

of thermal softening would be expected to scale with the increasing mechanical threshold. Furthermore, many (but not all) dislocation drag pictures predict relatively little change to the mechanical threshold during deformation, whilst enhanced work hardening theories predict large increases in subsequent material strength at all rates. Finally, we will remind the reader of a statement made in chapter 2, that no consideration of avalanche dynamics is present in the standard framework of high rate plasticity.

How then do we progress the current physical understanding, in order to create a more solid basis with which to develop material models? There is currently a lack of experimental measurements immediately above the transition, except for largely repeated fixed rate, room temperature experiments, collated by Jordan [17]. To improve understanding we aim to fill these gaps, initially providing measurements immediately above the transition at a variety of temperatures, to provide insight into predicted changes in the temperature response of FCC metals. We will then progress on to perform a set of strain limited tests, such as those of Follansbee (shown in section 3.2.2.1) that will extend above the transition, into the rate range 10^4-10^5 s^{-1}.

To do so, we will have to establish an experimental scheme in which we can accurately control temperature, strain rate and strain in extremely high strain rate deformation. Furthermore, we will have to achieve this in bulk representative specimens without resorting to techniques that cause shock deformation.

The required range for study sits at the upper limit of Hopkinson pressure bars, the highest rate uniaxial apparatus capable of achieving uniform deformation (strain and strain rate) across a specimen. We will therefore tailor Hopkinson bar methods to perform the required controlled testing, tailoring the methods appropriately. We will begin outlining the Instron and split Hopkinson pressure bar methods used for the majority of the desired strain rates in Chapter 4, with the relevant alterations. We will introduce one final method, of particular importance to good high rate interruption, in Chapter 6

Chapter 4

Methods & Materials

In the previous chapters we established a set of experimental requirements to better understand FCC metal behaviour above 10^4 s^{-1}. An ideal experiment is one where we can separately control strain, strain rate and temperature, whilst providing an accurate measurement of a specimen's response. A further concern, not yet explicitly stated, is that we wish for the strain, strain rate and temperature to also be constant throughout the specimen volume, otherwise the experiment will not be a test at a well defined condition, and will be more like the Taylor impact experiments discussed in Chapter 1. For the same reason, we would ideally want for the strain rate and temperature to remain constant as a function of time and therefore at fixed strain rate, strain. Variations in temperature throughout strain are unavoidable above 10^2 s^1 as the deformation becomes adiabatic, instead we will have to seek to minimise and account for temperature changes.

The two experimental apparatus we will discuss in this chapter are the most commonly adopted arrangements for quasi-static and dynamic strength measurements: Instron and split Hopkinson pressure bar systems. In this chapter we will introduce the fundamentals of, and experimental concerns accounted for in each system. Any experiment specific additions of modifications to the systems can be found in the relevant chapters. Refinement of another system, direct impact Hopkinson pressure bars, corresponds to a significant fraction of the

work presented in this thesis that will be discussed in Chapter 6, closer to studies in which it is used.

The highest rate tests performed in this thesis (outlined in Chapter 6) are only possible in a compressive geometry. For consistency, we will avoid effects caused by varying deformation geometry [136], performing all tests in uni-axial compression. The general scheme of a test is to apply an axial compressive load in a cylindrical system, with a specimen held between two solid, elastic bulks. The two connecting solids allow the specimen to equilibrate its deformation, a concern in dynamic testing where it will be discussed extensively. In each scheme some method is used to track the positions of the specimen faces, generating a strain measurement, and the normal reaction force from the specimen, generating a stress measurement.

4.1 Quasi-Static Loading

Quasi-static deformation was performed using a model 5566 Instron universal testing machine [137]. The device is designed to smoothly compress a specimen between two cylindrical anvils by moving a screw (Cavendish apparatus) or hydraulically driven vertical cross head according to a pre-programmed control routine in the machine's 'Bluehill' software. The extension of the cross-head is measured and related back to a change in specimen thickness and therefore generate strain measurements, outlined in section 4.1.1. The reaction force from the specimen is measured using a load cell above the top anvil and related back to the specimen flow stress, as described in section 4.1.2.

4.1.1 Measuring Strain & Strain Rate

The system is capable of sophisticated load or displacement dependent instruction sets, however the control used in these experiments was simply to maintain a constant cross head speed throughout an individual experiment. The cross head is capable of moving at speeds between 10^{-7} and 10^{-2} m s^{-1}. For an arbitrary sample the speed can be approximately

related to the engineering strain rate (which is also the initial value of the true strain rate) through

$$\dot{\varepsilon}_{eng} \approx \frac{v_{Instron}}{l_0}, \tag{4.1}$$

where l_0 is the initial sample thickness. Relation 4.1 was used to set the appropriate cross-head speed for the desired strain rate. For large strains relation 4.1 can be calculated as a function of strain and therefore time or cross-head position to provide a velocity profile maintaining an exact value of strain rate. Most of the Instron work only involve measuring yield stresses, modulation was not required.

After the cross-head has moved some distance $\Delta x_{Instron}$, then outside of experimental error, the specimen, having the lowest yield point in the system, must have plastically deformed to thickness $l(t) = l_0 - \Delta x_{Instron}$ where l_0 is the initial thickness. We can then calculate the true strain using the relation

$$\varepsilon(t) = \ln\left(\frac{l(t)}{l_0}\right). \tag{4.2}$$

The resultant strain is negative for compressive strains, throughout this study however we will plot compressive strains as positive in figures, as they are the only type under study. We can then plot the imparted strain against time, checking that the rate appears constant, and extracting an experimental rate with error using linear regression.

4.1.1.1 Punching & Compliance

In order to provide a good measurement of strain, and as will be shown in section 4.1.2, stress, we wish to remove any sources of error in our displacement measurement, $\Delta x_{Instron}$. The two most significant sources of error arise from the fact that the specimen length is inferred from a measurement at the cross-head, however the two are separated by the steel anvils of the Instron, that are elastic themselves.

Firstly, as both the anvils and the sample materials are metal, specimens undergoing plastic flow are likely strong enough to cause significant "punching" into the anvils. The specimen elastically indents only the central portion of the larger diameter anvil, causing it to bow round the specimen. Punching will make the cross-head measure a greater extension than has actually occurred, shown in figure 4.1 (a). Punching is mitigated experimentally by placing spacers between the Instron anvils and the specimen, made of polycrystalline diamond (PCD). The typical elastic modulus of PCDs is 1 TPa, compared with 200 GPa in a steel. The spacers then spread the load more evenly across the steel anvils, as shown in figure 4.1 (b).

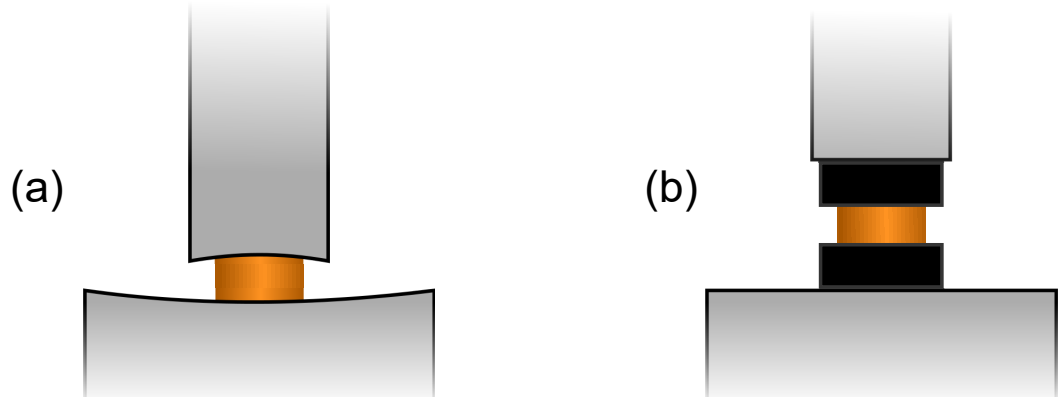

Fig. 4.1 (a) The sample anvil interface in an Instron, (b) the interface with PCD anvils added between the sample and Instron. Punching is reduced due to increased elastic modulus in the PCD.

The second source of error, known as compliance, again arises from the fact that the test system itself has finite elastic modulus. Even without punching, the anvils themselves will elastically compress along their length as force propagates to the load cell, again overestimating $\Delta x_{instron}$. The elastic nature leads to a simple relation where the overestimation is linearly proportional to the specimen reaction force. It can be calibrated out using the correction

$$\Delta x_{Instron} \rightarrow \Delta x_{Instron} - k_I F_{reaction} \tag{4.3}$$

where k_I is the compliance of the Instron, and can be found by running a compression test with no sample present, as shown in figure 4.2 (a).

The compliance curve reveals another practical complication; there is a repeatable tail up to approximately 0.005 mm or about 700 N, which also affect the stress strain curves, if only a simple linear correction is applied. In practice a 6^{th} order polynomial is fit to the compliance curve to also account for the tail allowing interpolation throughout the entire range available to the load cell. The total extension of the system at the limit of the load cell was found to be 500 μm, which is a large fraction of a Hopkinson bar specimens thickness, equal in size to the smallest specimens used in this study. The correction is therefore vitally important when generating strain data. However, in the vast majority of measurements throughout this study however, the Instron is used to reload samples to find the new yield point, allowing the plastic strain to be measured accurately using a micrometer between each step in testing. Figure 4.2 (b) shows the effects of the applications of these corrections for a 2 mm thick, 6 mm diameter copper specimen. The tail is removed by the correction and instead an approximately linear elastic region arises, the entire curve becomes steeper and

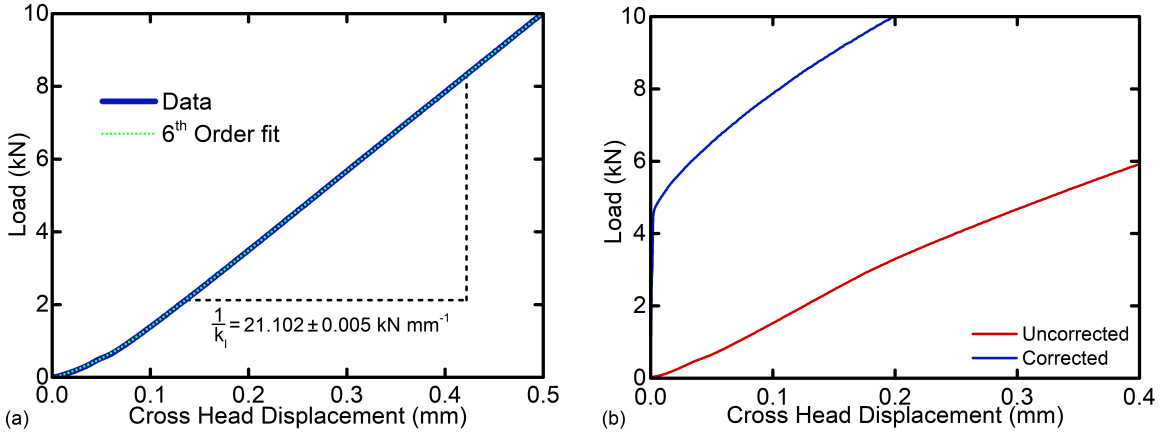

Fig. 4.2 (a) The calibration curve for the Cavendish 10 kN load cell, a compression test with no specimen. Both first order and a 6^{th} order polynomial correction are shown. (b) The origional force-extencion curve for a 2 mm copper specimen before and after the application of the corrections as described in the body text.

importantly the yield point becomes much more apparent as a ‘corner’ in the data set rather than a gradual change.

4.1.2 Measuring Flow Stress

We have established the specimen reaction force as a function of time, $F(t)$, measured by the Instron throughout deformation. The results can be mapped onto the true stress using the relation

$$\sigma(t) = \frac{F(t)}{A(t)}, \tag{4.4}$$

where $A(t)$ is the specimen area as a function of time. To a good approximation, plastic deformation conserves volume [100]. We can therefore calculate the specimen area from the extension data by approximating the product of thickness and area to be invariant,

$$A(t) = \frac{A_0 l_0}{l(t)}, \tag{4.5}$$

where A_0 is the initial specimen area. Given no other experimental effects this would provide all information required to generate a stress strain trace.

4.1.2.1 Friction

During compression, the sample expands out sideways to conserve volume. There must be a frictional force between the specimen faces as they move against the anvils, scaling with the reaction force of the specimen.

Friction complicates the loading conditions, changing the scenario from the ideal 1D loading to a triaxial stress state [138]. Furthermore the frictional force can cause "barrelling" where the centre of a sample expands more than the edges, by an amount dependent on the magnitude of the frictional effect.

Barrelling is akin to necking in tension, except for the very important difference that for low friction and in the absence of internal voiding (unlikely for small strains), it is a

self negating process. In necking, the reduced area focuses the transmitted force to a higher stress and causes preferential flow, a positive feedback scenario. In barrelling, the reverse happens and barrelled areas are unlikely to flow until those at the interface have caught up to a level dictated by the level of friction, suppressing the problem. For a more comprehensive discussion of effects in friction, the reader is referred to Walley [139].

An expression for the ratio of metal flow and measured stress was derived by Male [140], and empirically found by Walley [141]. A variety of pre-factors are placed before the friction coefficient in different models, that will not matter as the model form itself will be used to calibrate our correction. We will use the same form as Gorham [23]

$$\sigma_{fric}(t) = \sigma_f(t)\left(1+\mu\frac{2r(t)}{3l(t)}\right). \tag{4.6}$$

Where μ is the coefficient of friction, which we must experimentally calibrate.

If we take two samples of the same material, both bulk representative (discussed in section 4.3), but of different initial aspect ratios $\left(\frac{r_0}{l_0}\right)$, then the measured stress including friction as a function of strain for each specimen, will from the conservation of volume be

$$\sigma_{fric}(\varepsilon) = \sigma_f(\varepsilon)\left(1+\mu\frac{2r_0}{3l_0}e^{\frac{3}{2}\varepsilon}\right), \tag{4.7}$$

by taking the ratio of these two values, $\sigma_{\frac{1}{2}} = \frac{\sigma_{fric\,1}}{\sigma_{fric\,2}}$, we can eliminate unknown specimen strength and rearrange to

$$e^{\frac{3}{2}\varepsilon} = \frac{3}{2\mu}\cdot\frac{\sigma_{\frac{1}{2}}(\varepsilon)-1}{\frac{r_{01}}{l_{01}}-\frac{r_{02}}{l_{02}}\sigma_{\frac{1}{2}}(\varepsilon)}\,. \tag{4.8}$$

Regression can be performed on the two sides of this expression to extract a measurement of μ and associated error, performed across multiple aspect ratios for verification.

Before any attempt to calibrate out friction, everything possible should be done to experimentally minimise friction. Polishing specimens mechanically is not advised as this

imparts unwanted work hardening to the sample. The main minimisation of friction in both quasi-static and dynamic experiments is from lubrication. Available data on high temperature lubricants [142] would suggest powdered graphite to perform best both in terms of consistency and minimisation of μ at room temperature, whilst boron-nitride performs best at very high temperatures in a vacuum. In air, both have limited lifespans at temperatures of 350 °C, which is below the temperatures where boron-nitride is preferable. Powdered graphite was used to minimise friction in all Instron tests performed in this thesis.

Exemplar stress strain curves and resultant calibration plot for our samples, anvils and lubricant are shown in figure 4.3. The friction between the specimen faces and polycrystalline diamond anvils was found to be $\mu = 0.08 \pm 0.002$, where the error was obtained from the standard deviation between several independent tests performed such that no sample curve used twice and no experiment had the same pair of starting aspect ratios. The error generated is notably much larger than the error in the regression gradient of single calibration, better accounting for the variability between experiments that is likely to be larger than that during a single one. The variability, however, is small, being approximately 5% of the already small absolute value.

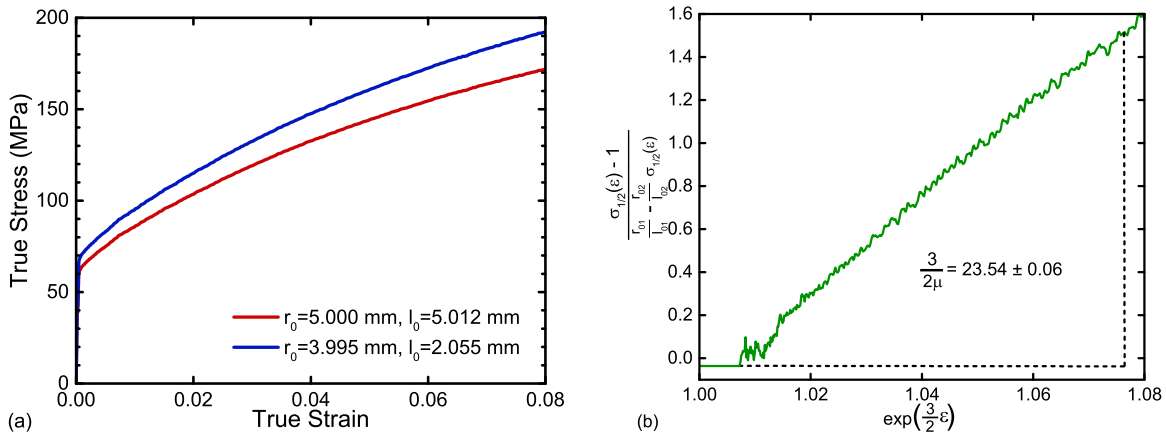

Fig. 4.3 (a) A pair of compliance but not friction corrected stress-strain curves for the copper specimen of study. (b) A regression plot based on equation 4.8 and using the two specimens from a data from (a).

Finally, figure 4.4 depicts the effects of the two steps of correction for a 2mm specimen. The compliance correction is clearly the greater of the two, but friction has a significant effect on the final stress strain trace, largely because for the thin specimens required to achieve high strain rates (see equation 4.1) the resultant aspect ratio rises above unity.

We should also note that for very large strains, friction becomes much more complicated [139]. Material flow complicates friction and lubrication. Part of the reason the linear fitting in figure 4.3 (b) works so well is because the strains over which calibrations were performed were small. All major testing to be performed will be at small strains, on the 0.1 level. To the author's knowledge, this method of friction calibration is new, with the typical approach being iteratively applying the correction to stress strain curves until they collapse to a single value.

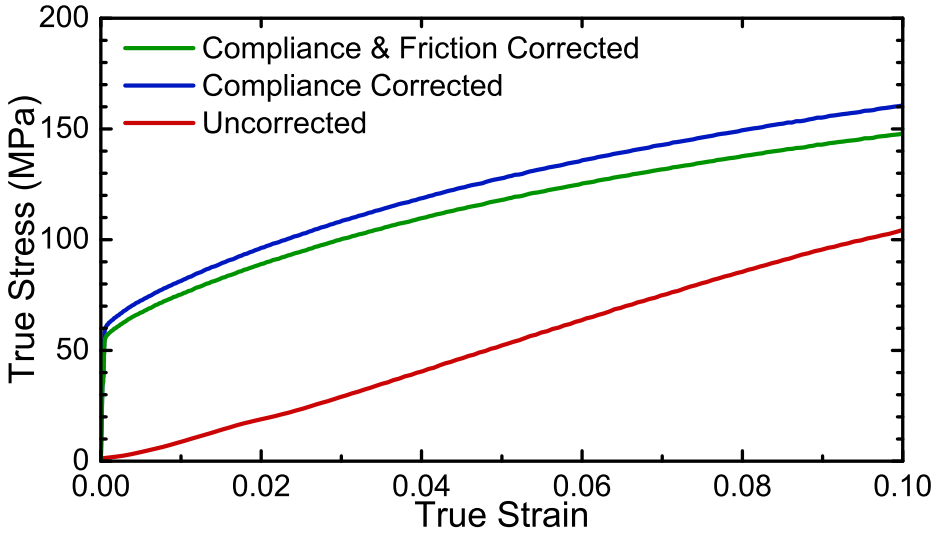

Fig. 4.4 The effects of applying compliance and friction corrections on the stress strain curve of the 2.055 mm thick specimen from figure 4.3 (a).

4.2 Split Hopkinson Pressure Bars

In order to begin testing at rates above unity, Instron like systems are replaced with projectile or prestrain driven dynamic loading apparatus. Dynamic loading is a very different regime to that of quasi static, as the specimen deformation time-scale becomes comparable to that of the travel time of the waves which propagate applied forces. In an Instron experiment, we assume due to Newton's third law that the force measured at the load cell was the force at every point along the experiment. In dynamic loading, this is no longer valid. We must instead observe the propagation of the applied force as a pressure wave throughout the experimental apparatus.

The wave nature of the loading forces leads to several complications that will be discussed in section 4.2.3 and also sets the fundamental limit on the velocities and thus rates with split bar systems. As we cannot measure the force directly, we must infer it from particle velocities or strain gradients in the system. In order to do so accurately, the experimental apparatus must remain perfectly elastic. In the scenario that any of the bars begin flowing plastically, the experimental data is no longer valid, and more importantly, the apparatus is damaged. Elasticity is however a powerful constraint on the system, allowing many variables to be constrained using different linear combinations of a single set of measurements. Both deformation and force histories can be recorded from as few as two measurement probes.

The Hopkinson pressure bar was initially developed by Bertram Hopkinson in 1941 [143]. He devised a two bar system in which one bar near an event acted as a waveguide, carrying away any pressure incident upon it. The waveguide bar transmitted the pressure to a second momentum trapping bar that flew into a capture box attached to a pendulum. Using the height swung by the pendulum and a variety of different length rods, the shapes of the stress pulses of various phenomena could be measured.

The arrangement we will use was developed by Kolsky [22, 144] and later Davies [145] and is shown in figure 4.5. They expanded the two bar system to one in which the sample is

placed between a pair of bars, allowing measurements of both sides of a specimen. Again, a momentum trap was placed at the end but now only to protect the experiment. A stimulus is applied through varying means to the input bar, that causes deformation of the specimen as it propagates through the system.

In the Cavendish arrangement the striker bar is projected using a gas gun into the input bar. At this point the propagating stimulus can be measured, known as the input pulse. The wave travels to, and interacts with the specimen. A reflected wave forms at the boundary between the input bar and the specimen, dependent initially on the relative elastic properties of the two sides of the interface, but later determined by the specimen strength. The reflected pulse travels back down the input bar and can be measured by the same probe as the input pulse. A third wave is generated at the output bar by the force transmitted through the specimen, which is again initially dependent on the relative elastic properties of the two bars and the specimen, but later becomes defined by the specimen strength. This 'output' wave is measured as it travels along the output bar. Finally, the output pulse is contained in the momentum trap, that travels off as in the original arrangement by Hopkinson, however now it is into a rag tube, to arrest the projectile.

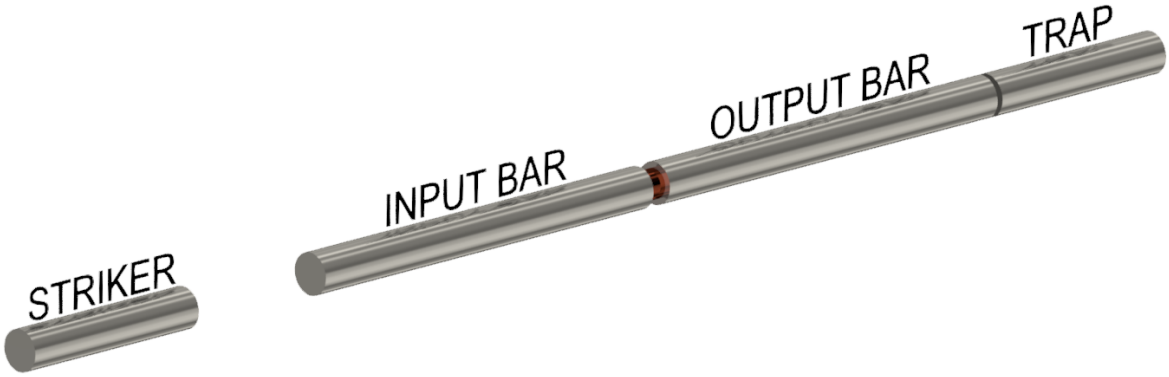

Fig. 4.5 A typical split Hopksinson pressure bar arrangement. A test specimen is sandwiched between two bars which act both to apply a deforming load and carry away the specimen response.

4.2.1 Experimental Measurement of Pressure Waves

If the bars remain elastic, then at any point along the length of the bar the stress, strain and local particle velocity are all proportional. If assume an arbitrary 1D wave in the bar, causing a displacement $u(x \pm C_{bar}t)$, we can find the stress, $\sigma_{bar}(x \pm C_{bar}t)$, strain $\varepsilon_{bar}(x \pm C_{bar}t)$ and particle velocity, $v_{particle}(x \pm C_{bar}t)$ given knowledge of any one of the three and its travel direction;

$$\sigma_{bar}(x \pm C_{bar}t) = -\rho_{bar}C_{bar}^2 \frac{\partial u(x \pm C_{bar}t)}{\partial x} = -\rho_{bar}C_{bar}^2 u'(x \pm C_{bar}t),$$

$$v_{particle}(x \pm C_{bar}t) = \frac{\partial u(x \pm C_{bar}t)}{\partial t} = \pm C_{bar}u'(x \pm C_{bar}t), \tag{4.9}$$

$$\sigma_{bar}(x \pm C_{bar}t) = \pm\rho_{bar}C_{bar}v_{particle}(x \mp C_{bar}t) = \mp Z_{bar}v_{particle}(x \pm C_{bar}t).$$

Where ρ_{bar} is the mass density of the bar and Z_{bar} is the *specific* acoustic impedance of the bar. Importantly, the relative direction between the force and particle velocity depends on the travel direction of the wave. The wave travelling in the 'positive' direction, denoted by the argument $(x - C_{bar}t)$, has particle velocity and stress in the same direction. A final note should be that due to the nature of elasticity, the stress waves in the bar obey the principle of superposition.

What we can now see is that although we cannot easily probe the stress in the bar directly, we can measure it by proxy, either through local strain or local particle velocity. Such measurements, however, are only easily performed at the surface of the bar, introducing an experimental constraint known as Saint-Venant's principle [146–148]. If the specimen is smaller than the bar ends, which our experiments it will be, to allow radial expansion in deformation, then the stress field at the bar ends is localised in the centre of the bar.

Over some propagation distance the higher order radial modes will decay, leaving a stress field that is uniform across the bar. It is only at this point that surface measurements are representative of entire bar. Thus, there is a minimum distance from the specimen at which we can infer bulk deformation using a surface measurement. The quotation of this number varies between sources, however the generally accepted value is 10 bar diameters from the specimen, [149–153].

4.2.1.1 Strain Gauges

Strain gauges were not used in any of the results presented in this study. They were however the state of the art at the beginning of the study and thus shall be summarised to better understand the migration to photon Doppler velocity based measurements outlined in the next section, and indeed when to revert back. For a thorough discussion of gauge based methods the reader is referred to Siviour [149] and for more recent refinements, Taylor [154].

Strain gauges were first applied to Hopkinson bars by Lindholm [155]. Two general types see widespread use; foil and semiconductor. The latter are preferentially used in the Cavendish SHPB due to higher sensitivities and smaller sizes. Time resolution is limited as gauges average strain over their length, leading to a time resolution of $\frac{l_{gauge}}{C_{bar}}$, typical gauge lengths are 5 mm in foil and 0.5 mm in semiconductor gauges.

Regardless of type, strain gauges work as an electric component with a resistance that varies, approximately linearly, with strain. Generally the resistance of the component increases in tension and decreases in compression. The strain gauge is placed in a potential divider circuit with another fixed resistance and a stable voltage source. The fixed resistance is probed and recorded using an AC coupled digitiser. An example of a voltage trace is shown in figure 4.6. Initially a rise in voltage is seen as the input wave compresses the gauge, decreasing its resistance and creating an increase in the voltage across the reference resistor. Subsequently and with a time delay depending on the relative travel distance in each case, a

negative voltage is seen due to the tensile wave returning in the bar and a positive is seen in the output bar.

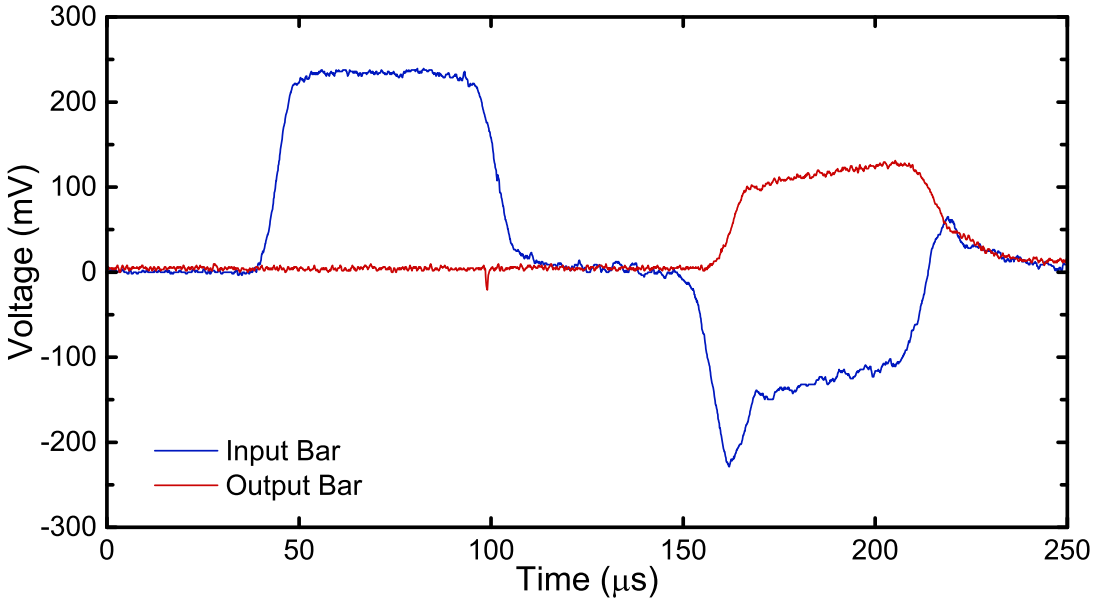

Fig. 4.6 Example voltage traces for semiconductor gauges, the reflected wave is tensile and thus inverted with respect to the other two.

The relationship between the voltage and stress in the Cavendish SHPB bar is observed to be approximately linear [149], and to better than 1% accuracy taking the form

$$\sigma(V) = \alpha_{V1} V \left(1 + \alpha_{V2} V\right). \tag{4.10}$$

The input pulse arises as the third law pair of the impulse bringing the striker, with an initial of momentum $\rho_{bar} A_{bar} l_{str} v_{str}$ to rest in a time of $2\frac{l_{str}}{C_{bar}}$. Therefore, for a known striker velocity, we can compare the time integral of the voltage to the impulse to calibrate the stress coefficients

$$\int \sigma(V) dt \approx \frac{2 l_{str}}{C_{bar}} \alpha_{V1} \bar{V} \left(1 + \alpha_{V2} \bar{V}\right) = \rho_{bar} l_{str} v_{str} \tag{4.11}$$

where the approximate equality is possible due to the small value of α_{V2} [149].

Performing shots at a variety of speeds and measuring $\bar{V}$ in the input pulse for each allows the two calibration parameters, α_{V1} and V_{V2} to be obtained by fitting. In this scenario the velocity of the striker bar is measured by a set of light gates, and is subject to errors caused by the width of the beam in the gates and a systematic error due to any deceleration of the bar after the point of measurement. The gauges are tension calibrated by leaving the end of the bar free, causing a perfect tensile reflection to pass by the gauges.

4.2.1.2 Photon Doppler Velocimetry

In this study, we aim to make reaching the strain rate limit of Hopkinson bar systems routine. Strain gauges, whilst certainly used at these rates [23, 150, 156], are susceptible to damage and can fail, usually due to spall at the solder contacts to the bars, typically due to the inertia of the attached wiring. Measures can be taken to minimise the occurrence of damage, but not to prevent it completely.

For this purpose, as well as for benefits at high temperatures and key applications discussed in Chapter 6, the gauges were replaced with non-contact, and thus non vulnerable, photon Doppler velocimetry (PDV) probes. Probes were initially applied to Hopkinson bars in the split arrangement by Avinadav [157]. The present thesis is the first time PDV has been applied to the direct arrangement [158, 159], that will be discussed in detail in Chapter 6.

The PDV principle was originally developed by Strand [160], and the variation in use at the Cavendish is shown in figure 4.7. A 1550 nm infra-red laser is split into multiple channels (the Cavendish currently has access to 5 channels, not all from the same laser source), passed through a circulation device to the PDV probes shown in figure 4.8.

The probes used for the Hopkinson bar systems simply consisted of 8 μm fibres, cleaved normal to their axis at the end, providing a transmission interface which also partially reflects some of the incident light, creating a reference signal. The fibre mounting system can be seen in figure 4.9. The ends of the fibres were run along tracks with fixed angles to the axis of the bar system. The tracks were mounted on a pair of orthogonal optical stages to allow

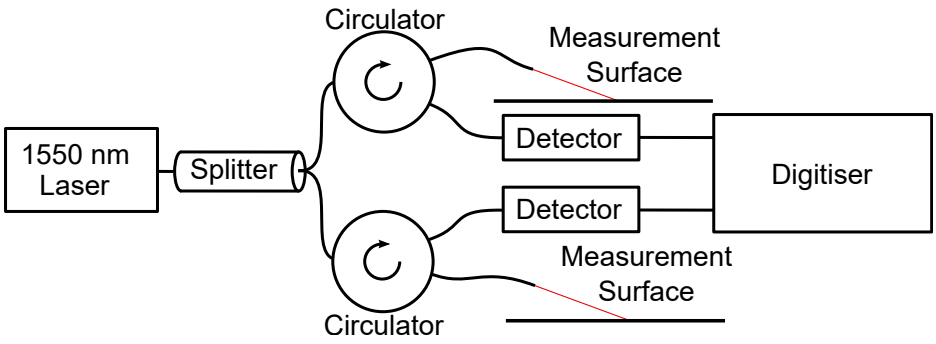

Fig. 4.7 A schematic of the Cavendish PDV interferometer. Light is passed through the circulator to the measurement surface, and then from the surface to GHz response photodiodes, that output an intensity proportional voltage. Interferometer probes were orientated as shown in Figure 4.8. Image taken from author's previous work [158].

fine adjustment of the vertical and horizontal position of the fibre. The angle between the fibre and the experiment was controlled by slotting into one of several pre-machined holes in the stage mounts, the standard angles for the system are 10°, 20°, 30° and 45°. The light reflects of the surface off the bars, aided by a retro-reflective coating, a layer of small glass beads, that converts a diffuse reflection into one directed back up the source fibre.

The signal which reflects off of the bar surface is Doppler shifted due to the projection of the motion of the bar at the probing point,

$$\Delta f_{PDV}(t) = \frac{2v_{particle}\cos\theta}{\lambda}, \tag{4.12}$$

where λ is the laser wavelength. Note the angle based error will vary as $\sin\theta$, and is small for small angles. The unshifted reflection from the cleaved fibre end and shifted bar reflection interfere to give a product with a beat frequency dependent on the Doppler shift,

$$I(t) = I_0 + I_1\cos(2\pi\Delta f_{PDV}\,t). \tag{4.13}$$

The product is passed by the circulator to a GHz response photodiode and converted to a proportional voltage that can be recorded. The entire pattern is also modulated by a much higher frequency component which is averaged out during measurement. I_0 and I_1 are

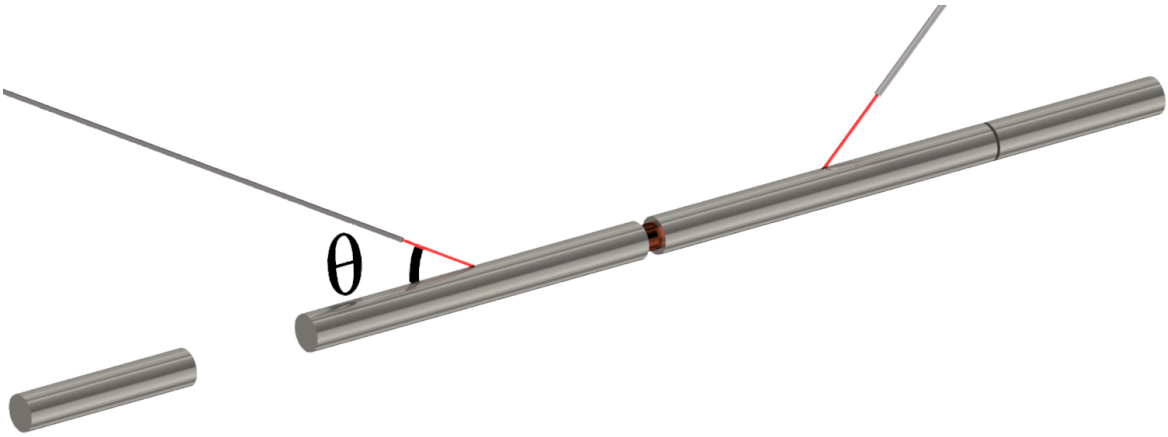

Fig. 4.8 Typical laser probe arrangement in the SHPB assembly, the typical incident angle on both bars (θ_{IP}, θ_{OP}) is 10°, allowed by the use of retro-reflective paint. Whilst the probes are shown at the middle of the bars here, they can be moved anywhere within the limits of Saint-Venant's principle allowing for much more experimental flexibility than strain gauges.

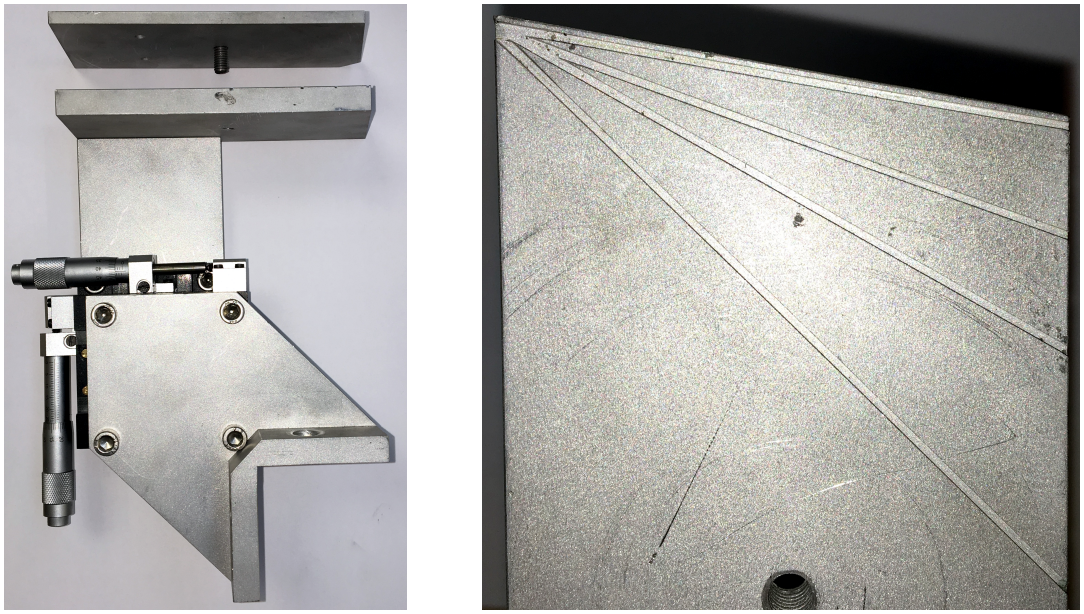

Fig. 4.9 The mount of optical stages used to precisely position the optical fibres near the bar surface. The fibres run down one of a number of grooves at different angles to the axis of the bar system. The fibres are held in place by screwing down a top plate that grips onto the cladding of the unstripped fibres.

dependent on many variables including the incident intensity of the laser and the reflectivity of the surface. However they are unimportant, as all required information is encoded in the frequency of the pattern. Frequency based measurement makes the technique resilient to typical laboratory noise. It does however mean that there is no well defined starting edge to the measured waveform, and thus an external trigger must be used, which is a single light gate placed immediately before the input bar. Typically a pair are still used to provide a rough estimate of striker velocity as a check for later measurement processing.

The interference pattern is then extracted from the PDV data using a standard procedure [160]. Each interference pattern, exemplified by the inset in Figure 4.10 (a) is split into a series of overlapping time windows which are then fast Fourier transformed, creating a series of spectra depicted in Figure 4.10 (a). Each vertical slice is the spectrum of a single window.

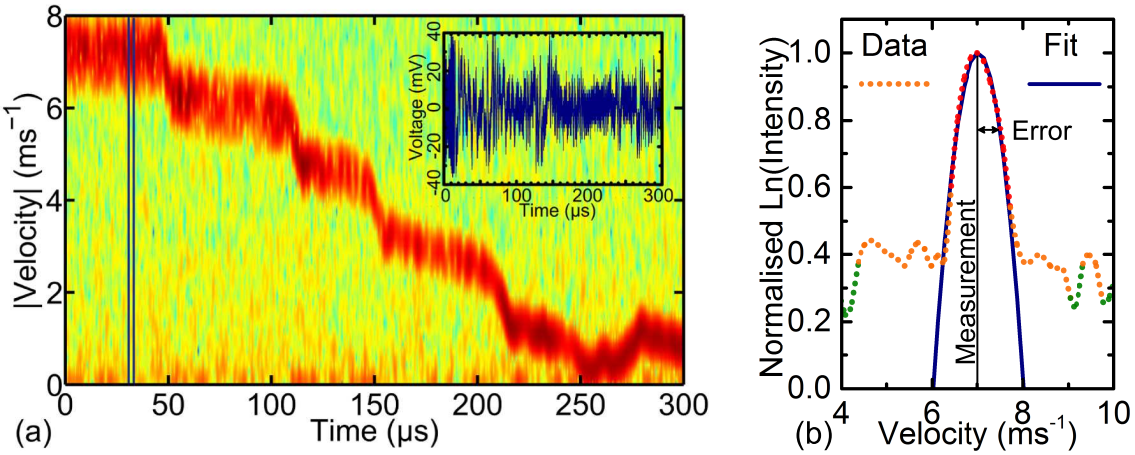

Fig. 4.10 (a) A map of the velocities obtained from Fourier transforming the inset interference pattern, as described in the body text. The step like pattern in the velocity measurement is due to the measurement being performed on the striker of a direct impact experiment, whilst the trace is different the extraction process is the same. (b) The velocity and error at each time step is found by fitting a Gaussian curve to the spectrum. Note that the vertical axis is logarithmic, so the Gaussian curve appears as a parabola. This figure is taken directly from a prior publication by the author [158].

An example of a single window's spectrum is shown in Figure 4.10 (b) compared to the marked region in Figure 4.10 (a). Velocities are obtained by fitting a Gaussian curve to the peak in each spectrum, as shown in Figure 4.10 (b). The centre value of the peak is taken

as the velocity, and its standard deviation as the error. The example trace was measured on the striker during a direct impact bar experiment, rather than either of the bars of a split bar system. Note that this is the projection of the measurement and the measurement from the spectrum must be divided by $\cos\theta$ to give the true longitudinal velocity.

A strong background signal near zero velocity, visible in Figure 4.10 (a), is caused by imperfections in the optical components, that along with any other background signals are both removed and avoided during fitting. Subtraction is performed by measuring the background spectra of the lab immediately before the experiment occurs and subtracting the measured background intensities. Particularly monochromatic sources of noise are avoided by selecting regions of interest in the data before performing the fitting procedure.

Interpolation is used to prevent errors due to loss of light. The window lengths for fitting vary depending on the speed of measurement, since earlier publication of the method [158], improvements to the apparatus have allowed a time resolution of approximately 100 ns, due to achieving stronger signals and performing experiments at higher velocities, far from the main background signal. The conversion of spectra to velocity measurements is performed using a MATLAB script and associated GUI written by Dr. Nick Taylor of the SMF group at the Cavendish [161].

At this point we have managed to extract a measurement of the particle velocity of the bar at the probing point, directly comparable to the strain measured using gauges through the relationships depicted in equation 4.2.1. There is however a final complication at the highest testing speeds. The PDV probes perform Eulerian measurements, whilst the gauges perform Lagrangian ones, arising from the fact the gauges are mounted on the bars themselves whilst the PDV probes are not.

As a result of the measurement type, the gauges give a true measurement of the shape of the pulse, but a PDV probe gives one that is either compressed or stretched in time as the probe moves towards or away from the source of the pressure wave. Providing we do

not have to solve any problems involving overlapped waves, the resultant effect equivalent to a classical Doppler shift in the sampling frequency of the velocity trace after all Fourier transforms and fitting have been performed.

If we consider the input wave, and imagine two points on the stress pulse forming at the striker input interface, some time Δt apart then between the arrival of the first part and the second, the probe has moved towards the source by a distance $v_{particle}(t)\Delta t$. The second part of the pulse therefore does not have to travel that distance, and the travel time of the second part of the pulse is reduced

$$\Delta t \rightarrow \Delta t - \frac{v_{particle}(t)\,\Delta t}{C_s} = \Delta t \left(1 - \frac{v_{particle}(t)}{C_s}\right). \tag{4.14}$$

Thus, if we make our measurements at the probe at Δt_{meas} apart, then these measurements actually correspond to a separation time at the source of the pulse of

$$\Delta t_{true} = \frac{\Delta t_{meas}}{1 - \frac{v_{particle}(t)}{C_s}}. \tag{4.15}$$

The relation holds true for the output bar as well, as the source of the pressure wave will also be travelling towards the probe. In the reflected wave however, the source is travelling away and thus the required transform is

$$\Delta t_{true} = \frac{\Delta t_{meas}}{1 + \frac{v_{particle}(t)}{C_s}}. \tag{4.16}$$

We should note that all of these corrections are of order $\frac{v_{particle}}{C_s}$, which, in the absolute highest velocity split bar tests (100 m s^{-1} on 350 maraging steel) the ratio is $\sim 2\%$ (typically to avoid damaging the bars shots remain below 70 m s^{-1}). Figure 4.11 shows the effect on an input trace at this maximum speed, and a trace for the inaccessibly high speed of 0.2 C_s to better illustrate the effect.

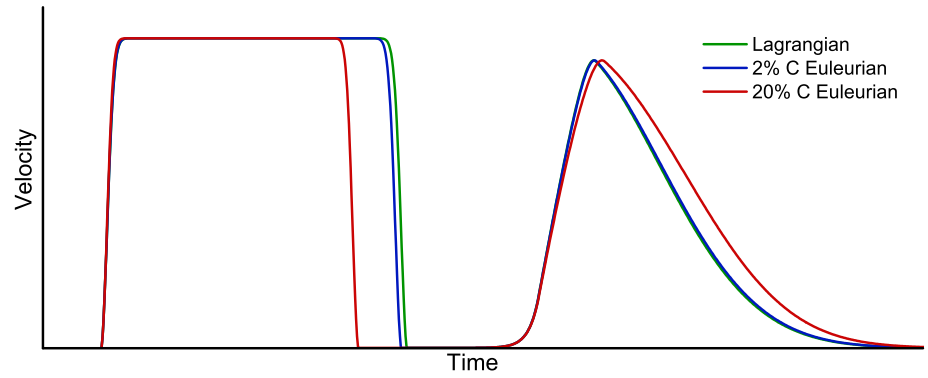

Fig. 4.11 The effects of having a probe moving relative to the bars on the measured traces. The input pulse is contracted compared to a Lagrangian measurement as the probe moves towards the source, meanwhile the reflection source moves away so the pulse is extended. The blue line shows the highest velocity achievable in a real experiment, whilst the red line in an exaggeration to illustrate the effect.

4.2.1.3 Comparison

Having introduced both gauge and PDV based measurements, we will briefly compare the two systems. As we have already discussed, PDV based methods are far more resilient than gauge circuitry, making the technique more suitable for repeated use in high velocity Hopkinson bar experiments. We have also discussed how not being mounted on the bars requires a small correction due to the changing co-ordinate system of the measurements, which is readily solved in postprocessing.

A major concern is whether or not the measurement system is susceptible to temperature changes. Even in experiments where the specimen is heated far away from the probes (which is not the case on the output bar, we place the probe as close as possible to minimise dispersion, discussed later) there will still be some conduction, and the temperature of the probed point may change by a few tens of degrees. The PDV, being non contact and based on the Doppler effect will not vary with the temperature at the measurement point, as long as the elastic constants do not vary significantly. Semiconductor strain gauges however are temperature sensitive [149]. The unstrained resistance of a semiconductor strain gauge increases linearly by between 1 and 12% per 10 °C [162]. The effect of temperature variation

in gauge response can be calibrated for, however it requires a bar temperature measurement at the gauge position and requires a much greater set of calibration data.

Time resolution is another area of comparison, here we must first consider the limiting factor in each scenario. For strain gauges we have discussed that whilst the measurements of the gauge can be recorded as fast as the attached digitiser samples, the true time resolution is dependent on how long it takes a wave to pass through the gauge. For typical 500 μm gauges and a bar sound speed of 5 km s^{-1}, the time resolution is 100 ns. In comparison, the PDV probe width is ideally 8 μm, however after shallow projection and spreading of the beam from the fibre end the laser spot size on the side of the bar will be in the region of 100-500 μm. The lower diameters requiring collimation. The fundamental limits of PDV time resolution are therefore similar to that in gauges. In a PDV measurement however, another resolution limitation arises from the time period required to provide an accurate enough Fourier transform to resolve the signal. The slower a velocity, the lower the beat frequency and the longer window required to observe it. Typical PDV applications are usually in the km s^{-1} range and as such long window widths may be required. In the experiments shown in this thesis, sampled at 2 GHz, a 1024 sample window is required to properly extract the traces. The time step between output measurements is $\frac{1}{8}$ of the window width, arising from the use of Gabor window modulation [163]. The step size is therefore approximately 60 ns. In practice the spot size on the bars is the limiting factor for time resolution. We note that in the majority of PDV applications the laser is normal to the measurement surface, meaning that the spot size limitation to time resolution is not present.

There is however a range of slow velocity measurement where gauges vastly outperform PDV, which for the Cavendish apparatus would appear to be below 1 m s^{-1}. The measurement floor is due to the strong signal near zero, visible in figure 4.10, that is caused by imperfections in optical components and stationary objects in the probe field of view. The low velocity noise is typically avoided by confining the analysis to a region of interest that excludes the

lowest velocities. However when trying to measure exceptionally low speeds, the Gaussian peak of the measurement spectrum overlaps with this region, making the measured velocity appear to be zero.

Furthermore, if the peak overlaps the origin to a significant enough degree it is impossible to discern the measurement from zero. The error occurs because the beat pattern is a cosine, it is not sensitive to whether the measurement light was up shifted or down shifted. We therefore effectively measure the magnitude of the velocity. This is problematic as if any part of the Gaussian crosses zero, it reflects back, creating an even greater intensity at zero, and quickly making the measurement indistinguishable from zero even in the absence of any background signal. In more complex PDV systems two lasers can be used, one as a measurement source and one as a reference laser. The two can then be tuned apart creating a fixed frequency beat pattern corresponding to zero velocity. The frequency in the beat pattern can then shift up or down depending on the direction of the velocity. As the Cavendish PDV uses back reflected light from the fibre as its reference signal, there is no directional information.

Without the use of more complex optics the Cavendish system has a minimum practically digitizable velocity of approximately 1 m s^{-1} or if optimised (large fitting windows, long time steps), 0.3 m s^{-1}. To put into context, in Duralmin (aluminium alloy) bars and with a specimen diameter 70 % that of the bars, this corresponds to a minimum stress measurement of approximately 3 MPa, low enough for metallic foams and polymers, shown in 6.1, but not for softer biological materials.

The experimental uncertainty between the two measurements is also largely similar. In a gauged system it is defined by the ratio of the voltage noise to the pulse height, and the error in the calibration constants for a gauged system. In a PDV system an example of an error measurement is shown in figure 4.10, the uncertainty is characterised by the difference between the velocities at which the intensity is maximal and that at which it has halved. The

PDV measurement error is larger for exceptionally low velocities, as discussed. Gauges suffer from a systematic error from calibration, notably that from the deceleration of the striker between the light gates and the calibrated bar. The deceleration can be partially accounted for by adding further light gates to approximate the rate of deceleration. The PDV does not require any calibration outside of a precision measurement of the laser wavelength, typically provided with the laser.

Finally, the two systems have largely similar performance regarding bending in the bars. Whilst bending is unwanted and always minimised before an experiment, some small level is inevitable. Gauges are normally placed on bars in pairs on opposite sides of the same point to attempt to cancel out any bending effects. Meanwhile PDV probes can shone at glancing angles (very low θ). For a small bend the bending velocity will be normal to the bar axis and thus will project very weakly on to a shallow angle probe. The PDV probes also provide the advantage of being adjustable, such that they can be arranged to probe just the bending in a system, allowing for quantitative evidence that a bar system is well aligned.

4.2.2 Data Analysis

Upon measuring the forms of the input, reflected and output waves, the stress strain history of a specimen can be evaluated. The first thing we will note is that the three waves are not recorded at the specimen face. The input wave is measured before the experiment whilst the others are measured after. We must time shift the experimental measurements to the time when they were at the specimen face. If the probes are Lagrangian in nature and distance Δx_{probe} from the source, the transform would be $+\frac{\Delta x_{probe}}{C_s}$ for the input wave and $-\frac{\Delta x_{probe}}{C_s}$ for the reflected and transmitted waves. For a moving probe the procedure is more complex due to the relative motion between the bar and probe frames. However, the time-step correction provided in section 4.2.1 maps PDV measurement onto this scenario.

In PDV analysis the resultant measured quantity is velocity so we will analyse our data in terms of that value. At this point we remind the reader of the relationships between wave

travel and force/particle velocity discussed in section 4.2.1. The directions of all of the relevant forces and velocities an SHPB experiment are shown in figure 4.12.

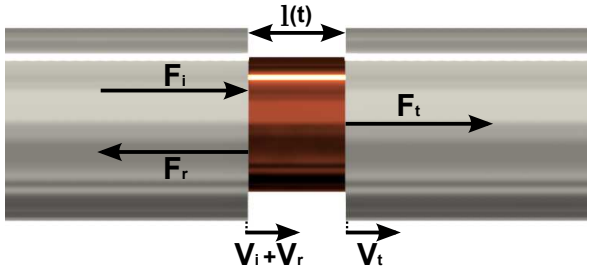

Fig. 4.12 The directions of the velocity and force contributions due to the input, reflected and transmitted waves.

In terms of the movement of the interface, all three waves, v_i, v_r and v_t are in the same direction as the striker bar is propelled. Therefore we note the relative velocity of the specimen faces to be $v_i + v_r$ and v_t, where all $v(t)$ terms are those after being correctly time shifted to the specimen face. The specimen length therefore evolves as

$$\frac{\partial l(t)}{\partial (t)} = v_t(t) - [v_i(t) + v_r(t)] \tag{4.17}$$

or

$$l(t) = l_0 - \int v_i(t) + v_r(t) - v_t(t)\, dt \tag{4.18}$$

which, as with quasi static experiments allows for a measurement of true strain through

$$\varepsilon(t) = \ln\left(\frac{l(t)}{l_0}\right) \tag{4.19}$$

and strain rate through either regression between time and strain or through the relationship

$$\dot{\varepsilon} = \frac{1}{l(t)} \frac{\partial l(t)}{\partial (t)} = \frac{v_t(t) - [v_i(t) + v_r(t)]}{l(t)} \tag{4.20}$$

All that then remains is a measurement of the specimen strength throughout deformation, a dynamic but equivalent case to the Instron. We will measure the reaction force of the specimen to the applied load. The simplest way of measuring this phenomenon would be through the transmitted pulse, that corresponds to the reaction force of the specimen alone. For a complete experiment however, we should also measure the force at the input face, reasons for this will be discussed in section 4.2.3.

At the impact face, we can simply turn our velocity measurement into a force measurement using the relations given in equation 4.2.1,

$$F_t(t) = A_{bar}\sigma_t(t) = A_{bar}\rho_{bar}C_{bar}v_t(t) = A_{bar}Z_{bar}v_t(t). \tag{4.21}$$

Which is converted to a stress measurement in the specimen through

$$\sigma_f(t) = \frac{F_t(t)}{A(t)} = \frac{A_{bar}}{A(t)}Z_{bar}v_t(t), \tag{4.22}$$

where $A(t)$ is the specimen area and again found from approximating volume conservation

$$A(t) = \frac{l_0}{l(t)}A_0. \tag{4.23}$$

The equivalent measurement at the input face can be seen from figure 4.12 to be

$$\sigma_f(t) = \frac{F_i(t) - F_r(t)}{A(t)} = \frac{A_{bar}}{A(t)}Z_{bar}\left[v_i(t) - v_r(t)\right] \tag{4.24}$$

4.2.3 Dynamic Effects

Whilst in some areas the SHPB experiment can be considered in a largely analogous manner to an Instron measurement after waves have been properly shifted to the specimen

face, there are two large differences that arise on dynamic time-scales we must discuss; equilibration and dispersion.

4.2.3.1 Force Equilibrium

Clearly if we wish to make a measurement of deformation effects at any given strain rate and strain, then the specimen must be at the same value of said variables throughout its entire volume. This is one of the great strengths of Hopkinson compression bars, the free moving interface on both sides of the specimen allows mechanical (or force) equilibrium.

Hopkinson bars reach force equilibrium through a phenomenon known as "ring up", which arises due to the fact that either side of the specimen presents an acoustic transmission barrier. The fact the bar faces are free to move with the specimen allows it to define the transmission properties. Initially, when the input wave reaches the specimen its transmission into the specimen and its reflection depend on the mismatch between the input bar's and specimen's acoustic impedances (ZA, not specific impedance, Z). The same scenario occurs at the output face, where some of the pulse in the specimen transmits out into the output bar, whilst some reflects back into the input bar. Clearly the situation gives rise to the initial condition that the force and deformation are not the same throughout the specimen volume, caused by the finite force propagation velocity. However, after an amount of time on the specimen wave speed and impedance mismatch, a specimen wide equilibrium is obtained. A system that allows force equilibrium to occur also allows sample wide deformation at the same rate.

The ability to achieve mechanical equilibrium makes the SHPB favourable for our intended studies. If we compare SHPB to experiments such as laser shock or Taylor impact, the impacted face deforms at higher rates, greater strains and different temperatures to the surrounding material. A non uniform deformation profile makes post-mortem testing of the flow stress extremely dependent on the specific area tested. The extraction of said region of the specimen requires putting in unwanted mechanical work between the two tests.

Furthermore the typical approach to analyse said experiments is computer modelling, thus making the measurement irrevocably dependent on both the simulation method and the input material model. SHPB experiments allow us to make measurements and observations in the absence of any assumed material model.

The standard test for equilibrium is to probe the forces at the front and back faces of the specimen. The onset of force equilibrium is observed as when the two forces settle to the same value, that is when $F_i(t) - F_r(t) = F_t(t)$. An example of this is shown in figure 4.13, where the input force, depicted in the purple line, is initially much greater than the output force, the green line, which has yet to propagate through the specimen. The forces quickly converge however upon the specimen yield, at approximately 20 μs in the figure. The time between yield and equilibrium is of the order of 1 μs, which at a rate of 10^4 s^{-1} corresponds to of the order of 0.01 true strain.

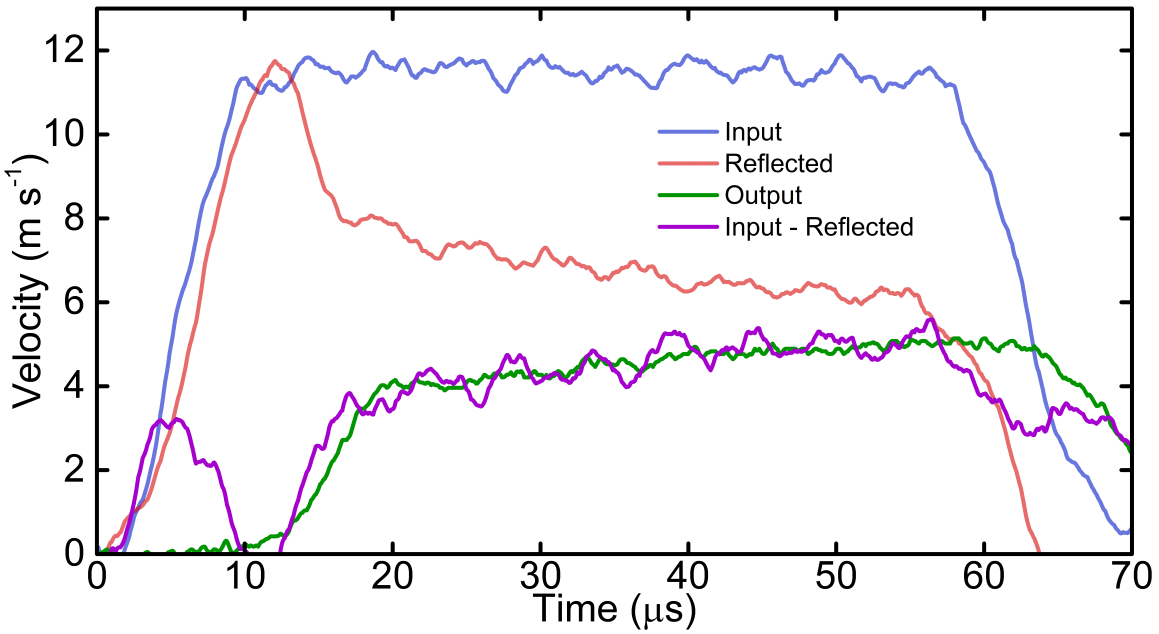

Fig. 4.13 The input, reflected and output velocities for a high purity aluminium speicmen impacted at approximately 25 m s^{-1}. The input face force is the difference between the input and reflected waves. Oscillations of the input force about the output force are due to dispersion occurring in the force measurement, discussed in the next section.

In a split Hopkinson pressure bar system, it is generally accepted that ductile metals equilibrate in three wave passes [164]. Typically only one transit occurs after yield, carrying the equilibrated force. Initially concerns may arise due to equilibrating wave potentially being a plastic wave, which is expected to have a speed much slower than that of an elastic wave. However, empirical studies of post-yield equilibration have found the post yield propagation of force through a specimen to occur at velocities close to the elastic wave speed [164]. The time for a specimen to reach force equilibrium can often be shorter than the rise time of the applied load (input wave), caused by dispersion, discussed later. The time taken to reach a target rate throughout the specimen is therefore not just determined by force propagation and mechanical equilibrium, but the profile of the loading itself.

Force equilibrium and the fact that it typically occurs at small strains in yielding specimens is often exploited [165]. If a specimen is in force equilibrium, we add yet another constraint to our already well determined system,

$$F_i(t) - F_r(t) = F_t(t) \qquad \therefore \qquad v_i(t) - v(r)_t = v_t(t) \tag{4.25}$$

that allows us to simplify equation 4.17,

$$\frac{\partial l(t)}{\partial t} = v_i - v_r - [v_i + v_r] = -2v_r \tag{4.26}$$

meaning if force equilibrium is assumed to occur throughout the experiment, specimen strength can be derived from the output wave alone, and deformation history from the reflected wave alone.

An equivalent approximation is in heavy use in direct impact arrangements, discussed in section 6.1. However the reliance on this approximation leaves the DIHB lacking in several areas, notably the ability experimentally verify force equilibrium. In section 6.1, we will

discuss work performed restore direct measurements of force equilibrium to the direct impact geometry.

4.2.3.2 Dispersion

The second major difference between quasi static and dynamic loading is that as force propagation time scales become important, effects arise due to the variation between the speeds of the frequency components in the pressure waves. In a 1D, dispersion free scenario, no extra complications arise due to dispersion. However in the true 3D nature of the experiment they do. As we have noted, the purpose of the input and output bars in the system is to act as a wave-guide, to make sure the waves travel to the specimen. The waves are guided by the bars because the edge of a bar is a free surface and thus perfectly reflects any waves indecent on it back towards the centre of the bar.

We have a scenario where, as for all free faces in elastic media, we force a zero traction boundary condition, effectively forcing standing waves radially across the bar. The standing wave constraint means only small quantised fractions of the pulse wavevector can be projected in radial directions, requiring the remainder of the wavevector, and thus travel, to be down the bar.

Figure 4.14 shows the furthest from axial paths that can be taken by two waves in a 2D wave guide. A node must be at each corner, due to the free boundary, therefore the line length between each corner is fixed at half of the wavelength. The longer wave shown by the green line must make a smaller angle to the bar axis than the shorter dashed red line. A greater component of longer wavelengths is therefore forced to be in the axial direction, and the axial projection of their velocity is greater. One immediately apparent way to mitigate this effect is to ‘miniaturise’ the system - reducing either the diameter to constrain all waves closer to the axis, or reducing the length of the bars to reduce the distance over which the waves can spread apart.

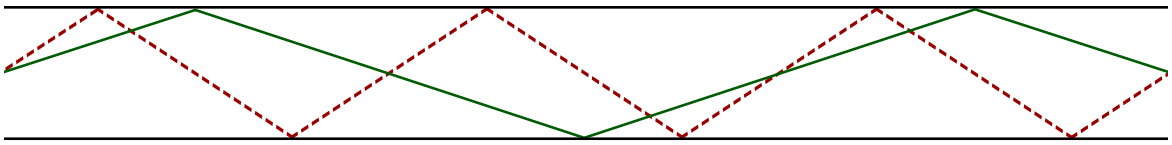

Fig. 4.14 A sketch of possible wave paths for two different wavelengths in a 2D rectangular waveguide. The longer wavelength (solid line) is better constrained down the bar due to the zero pressure boundary condition at the edge of the guide.

Real pressure waves in the bar system are a Fourier superposition of a range of wavelengths. The different speed of these wavelengths means that if we assume the wave imparted by the striker into the input bar is a perfect top hat, then as the wave propagates the different frequencies will disperse into and the top hat will evolve into some other shape. An example of dispersion is shown in the input wave of figure 4.13, the original top hat has begun to break down and oscillations are now visible. Importantly, the edges of the pulse shallow as the frequencies separate.

Dispersion means that if a probe is a significant distance from the specimen, the measured waveform at the probe will not be the same as that at the specimen. The input pulse will undergo more dispersion between being measured and reaching the specimen, meanwhile the reflected and transmitted traces will have undergone dispersion between leaving the sample and being measured.

There are three general approaches to reducing or removing dispersion effects. The first, and simplest is to minimise the distance between the specimen and probe whilst satisfying Saint-Venant's principle [146]. The input probe distance is limited by wave overlap if it is closer to the specimen than the length of the striker bar. The output bar however does not suffer from this issue and can be placed much closer to the specimen. The second approach is known as pulse shaping, and involves placing an extra piece of material between the striker and input bars to attenuate the shorter wavelength components, reducing dispersion but shallowing the input pulse significantly.

The final approach is more complex, the measurement wave is decomposed into its Fourier components, that are then phase shifted to add or remove the resultant difference

due to the difference in sound speed and the travel distance [99]. The required phase can be determined in one of two ways. The first approach is theoretically based, analytical expressions for wave velocity in a cylindrical wave-guide have been found by Pochhammer [166] and Chree [167]. Given the axial sound speed as a function of wavelength $C_z(\lambda)$, the change in phase, Φ per unit distance is

$$\frac{\Delta\Phi(\lambda)}{\Delta x} = \frac{2\pi}{\lambda}\left(\frac{C_s}{C_z(\lambda)} - 1\right), \tag{4.27}$$

or, since the pulse is measured as a function of time and thus it is easier to use the expression in terms of frequency,

$$\frac{\Delta\Phi(f)}{\Delta x} = 2\pi f\left(\frac{1}{C_z(f)} - \frac{1}{C_s}\right) \tag{4.28}$$

where $f = \dfrac{C_s}{\lambda}$.

The second potential way to determine $\dfrac{\Delta\Phi}{\Delta x}$ is experimentally, by probing a wave at two points along the bar, and measuring the relative phase between the fundamental frequency and each other frequency, f, at both points. The change in the phase difference between the two points gives $\Delta\Phi$ which can be normalised to the difference between the two probing sites to give $\dfrac{\Delta\Phi}{\Delta x}$ for that frequency.

In this study, the approach taken was to physically minimise dispersion rather than correcting for it in post-processing. The method use was to minimise the bar diameters and travel distances involved in the experiments. In the output bar this simply corresponded to using the smallest diameter bars possible and probing as close to the specimen as permitted by Saint-Venant's principle [146]. The input bar requires the probe point to be in the middle of the bar to properly separate the waves. Furthermore, regardless of the probe position the waves must travel the full bar length to reach the sample. We can therefore only reduce dispersion effects in the input wave by using short bars with a small diameter. This will present concerns at very high rates that will be addressed in Chapter 6. Finally, many of

the experiments performed will involve interrupting and recovering the specimen, and will allow strain to be generated using micrometer readings of the recovered specimen, bypassing dynamic errors in SHPB analysis.

The output trace importantly provides the measurement used to derive the flow stress of the specimen. We should therefore point out that in figure 4.13, which corresponds to the longest and largest diameter bars used in this thesis, no dispersion oscillations are visible.

4.2.4 Inertia

Inertia arises from two sources, in the case of simple 1D deformation, we would ideally measure the specimen strength under purely stationary conditions with respect to the lab frame. If the specimen is not stationary or is accelerating, some of the applied force is not being used to physically deform the specimen, and thus is not actually due to specimen strength, this amount must be accounted for.

In the initial ring up (section 4.2.3.1) period of dynamic loading the forces on the specimen faces are imbalanced, leading to a bulk velocity that remains when mechanical equilibrium is achieved. The real world situation is shown in figure 4.15 (a), where both the front (input) and back (output) faces of the specimen are moving, however as the input face is moving faster there is a net deformation of the specimen. In this scenario part of both the input force and normal reaction of the specimen are actually due to bulk acceleration. The ideal scenario is shown in (b), where there is no net translation of the sample during its compression.

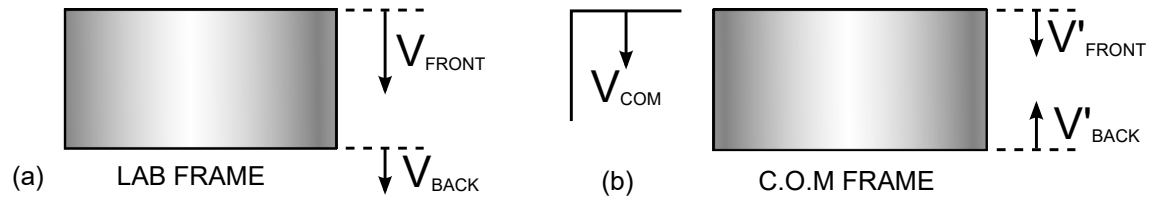

Fig. 4.15 The true impacted face velocities in a quasi-1D loading experiment and the desired velocities in the center of mass frame. The 'front' of the specimen is the face under which any deforming force is applied under non hydrostatic conditions. The relationship between the different velocities must be $v_{COM} = \frac{1}{2}[v_{Front} + v_{Back}]$ and $v'_{Front} = v'_{Back}$.

Secondly, a further inertial term exists due to the true 3D nature of the deformation. Any specimen plastically deformed in one direction must expand in others. Whilst in elastic deformation this expansion is defined by Poison's ratio, in plastic deformation the mechanism of dislocation movement rather than long range bond stretching makes deformation, to a good approximation, volume conserving. Therefore as the specimen is compressed, it must expand in the plane perpendicular to compression, at a velocity dictated by the rate of deformation, as shown in figure 4.16.

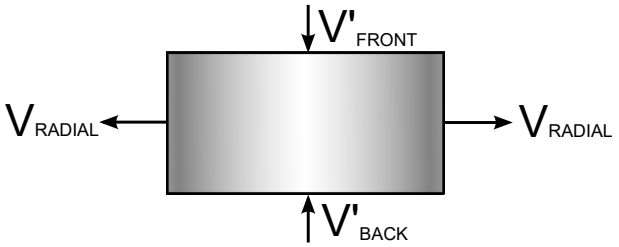

Fig. 4.16 The radial expansion of a specimen due to uniaxial compression. The radial velocity can be constrained to the strain rate due to conservation of volume in the specimen.

Several iterations of approximations have been made to these terms. The most successful attempts were performed by Samanta [168], who solved to first order the scenario $V_{Back} = 0$ m s^{-1}, and for a cylinder. Samanta's expression was then expanded to the general scenario of where both faces can move by Gorham [169].

The solutions for the relative pressures on the front and back faces of the specimen were found to be

$$P_{Front} = \sigma_f + \rho_M \left[\left(\frac{r^2}{8} + \frac{l^2}{3} \right) \ddot{\varepsilon} + \left(\frac{r^2}{16} - \frac{l^2}{3} \right) \dot{\varepsilon}^2 + \frac{l \dot{v}_{Back}}{2} \right] \tag{4.29}$$

$$P_{Back} = \sigma_f + \rho_M \left[\left(\frac{r^2}{8} - \frac{l^2}{6} \right) \ddot{\varepsilon} + \left(\frac{r^2}{16} + \frac{l^2}{6} \right) \dot{\varepsilon}^2 - \frac{l \dot{v}_{Back}}{2} \right] \tag{4.30}$$

where ρ_M is the mass density of the metal, r is the radius of the specimen, and l is the sample length or thickness. These are first order expressions, ignoring material inhomogeneities arising due to wave propagation and inertial effects themselves [23]. However, they are

accurate enough to give an order of magnitude estimate of the effect and inform specimen design.

4.2.5 Temperature Effects & Control

As outlined in chapters 2 and 3, we will want to perform tests at varying temperatures. Temperature variation adds another set of complications to performing a bar experiment, namely how to control and measure temperature and what effects it will have at the point of measurement. We remind the reader further concerns would arise if strain gauges were used to measure the waves in the bars, however PDV measurement removes said concern.

4.2.5.1 Control and Measurement

In order to obtain a good temperature range, we will want to perform tests as close as we can to the annealing temperatures of our specimen material. For copper, this is typically considered to be in the region of 350 °C. At this point thermal recovery and recrystallisation begin occurring on a sub-hour time-scale in the absence of any applied force. We therefore want to provide a heating profile that is slow enough to ensure the entire specimen is at the same temperature, but fast enough to prevent any recrystallisation. Combined with the fact that required temperatures are above 100 °C we cannot use methods such as hot air guns [149], and a furnace enclosure is extremely difficult to apply to a bar system due to fast moving components involved.

Here the method used was induction heating. A TR1 model induction heater made by Cheltenham induction heating Ltd. was used to pass a high frequency alternating current to a solenoid coil which was placed around the specimen and bar ends, shown in figure 4.17. This generates a uniform alternating magnetic field, inducing eddy currents in the specimen and bar ends, that impart heat through the internal resistance of the metal.

A sample was placed in the bars with a thin thermocouple attached to its side with silver dag. Measurements were taken of temperature during heating both at the specimen

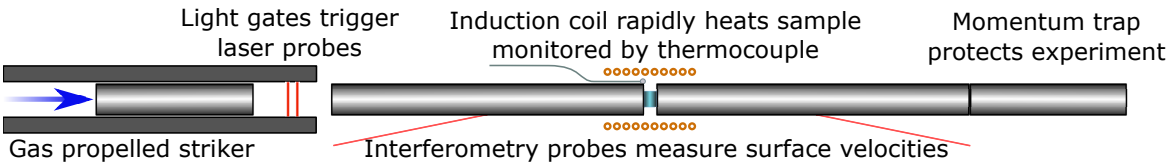

Fig. 4.17 The complete experimental arrangement for a raised temperature SHPB experiment.

thermocouple, and a second one also attached to the corner of the bar with a lightweight symmetric clamp. These thermocouples were used to find a heating rate fast enough to avoid recrystallisation but slow enough to ensure measurements made by the bar mounted thermocouples represented the specimen temperature well. A ramp time of between 60 and 90 seconds was found to maintain the specimen and the bars at the same temperature throughout. The thermocouple instrumented specimen was then replaced with an unmodified specimen and the heating was performed with reference to the bar thermocouple alone, preventing the specimen thermocouple or silver dag interfering with the experiment.

The rate of temperature rise in induction heating, combined with the significant electrical noise generated by the heater prevented experiments being accurately performed while the heater was on. Instead, the specimens were slightly overheated, typically by 10 °C. The induction heater was then turned off and striker fired as the temperature passed back down through the desired value. The finite thermal conductivity of the specimen and the human error present in triggering the experiment give rise to an approximate variation about the target temperature at the beginning of the experiment of 5 °C. The absolute error is worse than prior methods [149], however it is acceptable given the much greater temperature increases achieved ($\sim$ 300 K), and is approximately 1% of the absolute temperature.

Upon initiation of the experiment, deformation rates above 100 s^{-1}, the specimens deform too rapidly for the generated heat to leave the specimen [23, 29]. It has been observed by Taylor [29] and later by Walley [170] that approximately 90% of the mechanical work is converted into heat, we can therefore describe the temperature as a function of strain as

$$T(\varepsilon) \approx T(0) + \frac{0.9}{c_p \rho_m} \int_0^{\varepsilon} \sigma_f d\varepsilon \tag{4.31}$$

where ρ_m is the mass density and c_p the specific heat capacity of the sample. Given typical values for copper and a flow stress of 500 MPa, the highest observed in figure 3.2, there is a temperature change of 130 K per unit strain, assuming no work hardening. The temperature change at unit strain is large, however at a strain of 0.1, the change is typically less than 10 K, typically $2-3\%$ of the absolute temperature. Figure 4.18 depicts the full time temperature curve during an experiment, including an extra quenching step in the case of interrupted specimens, to be discussed in 8.

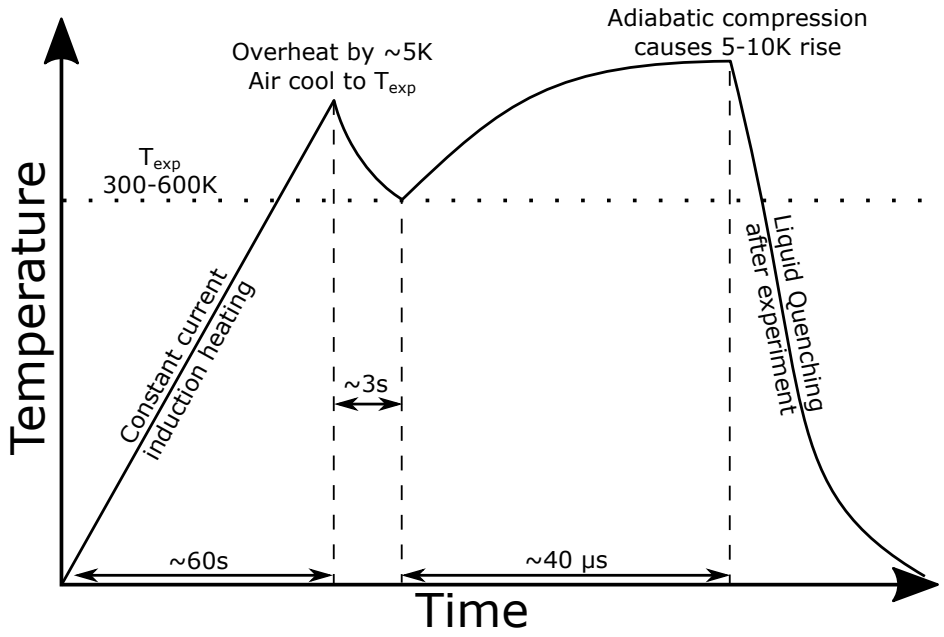

Fig. 4.18 The typical time temperature profile relative to room temperature for an experiment arrested at 0.1 true strain. The time axis passes through the temperature axis at room temperature.

4.2.5.2 Temperature Effects on the Bars

The induction heater not only heats the specimen but the bars as well. It is therefore important to make sure varying the temperature of the apparatus does not significantly effect our measurements. As noted in section 4.2.1, strain gauges can be extremely temperature sensitive, this issue was bypassed due to PDV measurement. What remains then is the acoustic properties of the bars themselves.

Heating a bar is likely to change the elastic properties and density of the bar, altering the impedance, and causing two unwanted effect. Firstly the impedance is the constant of proportionality between the measured velocity and the inferred flow stress, thus making stress measurements inaccurate. Secondly, as the bar is only heated at one end, the temperature profile and thus impedance is liable to vary along the bar length, generating a gradual transmission-reflection boundary effect (like that between the bar and specimen) along the bar length. Such boundaries will partially distort the wave as it partially reflects during transit.

A number of approaches have been used to overcome the impedance variation; altering the cross section of the bars along their length [171, 172], using insulating end caps on the bars [173], holding the bars away from the heated specimen until milliseconds before impact [174] and calculating or measuring the temperature and impedence change and correcting the experiments theoretically [175].

The approach used in this study was to use bars made of Inconel 718 alloy, which has elastic properties with a very weak temperature dependence [176]. Experiments by Walley [177] have shown no observable wave reflection in Inconel 718 when regions of the bar are heated as high as 550 °C or cooled as low as -150 °C. This material, whilst setting a lower limit on the maximum striker velocity at non ambient temperatures, allows experiments to be performed without corrections for thermal effects.

4.2.6 Alignment

An important factor to performing a good bar experiment, is proper alignment of the system. This is a process which must be done at every interface along the bars, most importantly the two on either end of the input bar.

At the striker-input interface, the alignment of the bars and thus the match between their end faces, determines the rising edge of the input pulse. In order to obtain early force equilibrium in the highest rate experiments, a sharp rising edge is required for the input pulse.

There is a limit to how steep alignment can make the rising edge, however, due to the input pulse shallowing with dispersion.

In deformation well below the plastic limit of the bars, good striker-input alignment can be obtained by placing the end of the input bar inside the striker barrel. Sliding the input bar into the barrel ensures the two have been aligned before the test and prevents the typical source of misalignment, the striker bar rising due to uplift as it leaves the barrel. Barrels contain air vents in the side to prevent pressure build up in front of the striker affecting the experiment in this arrangement.

The most important alignment boundary is arguably that between the input and output bar. Any misalignment may break down the uniformity of deformation, and will certainly affect the pulses formed between the two faces and the specimen during deformation, creating erroneous measurements. This alignment however is easily tested, the system is set up with no specimen in place and a test is performed. If the system is well aligned, there will be little to no reflection at the input output interface.

Alignment between the bars and the entire system can be well tested using a pair of PDV probes on each bar. If probes are placed at equal angles to the bar axis, on opposite sides of the same point along the length of a bar, the measurements made by the two probes are

$$v_{Probe_1} = v_{axial}\cos\theta + v_{bend}\sin\theta, \tag{4.32}$$

and

$$v_{Probe_2} = v_{axial}\cos\theta - v_{bend}\sin\theta. \tag{4.33}$$

We can therefore find the axial (desired) velocity by adding the two probe measurements;

$$v_{axial} = \frac{v_{probe_1} + v_{probe_2}}{2\cos\theta}, \tag{4.34}$$

and the bending velocity from the difference in same set of measurements;

$$v_{bend} = \frac{v_{Probe_1} - v_{Probe_2}}{2\sin\theta}. \tag{4.35}$$

Allowing a quantitative analysis of the ratio of axial to bending motion, assuming that the bend is small.

4.2.7 Cavendish SHPB Systems & Rod Materials

At the beginning of this study, the only SHPB dimensions available in the Cavendish laboratory were bars of 12.7 mm diameter and 0.5 m length. However, a wide variety of bar materials were available, ranging from low impedance materials such as Magnesium and Duralmin, to high velocity limit metals such as 350 maraging steel, and high temperature metals such as Inconel 718 alloy.

Such a system was not suitable for performing measurements at rates of 10^5 s^{-1}, requiring large diameter specimens and thus large inertial and frictional effects. Miniaturised bar systems were reintroduced, varying in diameter depending on the experimental requirement, a change greatly simplified by the use of PDV. Of note, for interrupted testing at the highest rates, 6.35 mm systems were made in 350 maraging steel and Inconel 718 alloys. These bars were mounted on the same system as the half inch bars, and low impedance polymer sabots were used to propel the strikers. A variety of different striker bar lengths were used in the miniaturised system to ease the controlling of the strain imparted.

We can also note that along with sensitivity, defined by the specific acoustic impedance, and the temperature performance of the material, we are also aware of the limiting velocity available to any given bar material. The striker is bought to rest through the pass of two waves, a compressional wave and its tensile reflection, each wave therefore corresponds to a particle velocity of $\frac{1}{2}v_{str}$, and thus a stress of $\frac{1}{2}Z_{bar}v_{str}$, thus to remain elastic the system

must not exceed a striker velocity of

$$v_{max} = \frac{2\sigma_Y}{Z_{bar}} \tag{4.36}$$

where σ_Y is the yield stress of the bar. Some stronger bars may fail before this velocity in a brittle manner. We therefore find a fundamental limit on SHPB test strain rates, however the limit can be overcome in the direct impact arrangement, discussed in Chapter 6.

Friction calibrations were performed for each bar set using the methodology outlined in section 4.1.2.1. The typical effective friction coefficient for the bars was found to be $\mu = 0.08 \pm 0.01$, higher than the polished diamond anvils used for Instron experiments. Graphite grease was also calibrated and found to have a coefficient of $\mu = 0.06 \pm 0.01$. Experimentally important values for typical Cavendish bar metals are summarised in table 4.1 below.

	v_{max} (m s^{-1})	σ_Y (MPa)	Z (MRayl)	C_s (m s^{-1})	Temp. Range (°C)
Dural	50	345	13.67	5050	RT
Inconel 718	50	1090	41.18	4980	−55 to 550
350 Maraging Steel	120	2400	39.48	4882	RT
Magnesium AZM	30	130	8.83	4917	RT
Titanium 318	90	990	21.38	4840	RT
Tungsten	14	550	75.28	4406	RT

Table 4.1 *The key elastic constants and strength limits of the most commonly used bars in the Cavendish laboratory compression bar systems. The strength of Inconel 718 is quoted at 350°C, the maximum experimental temperature it will be used at. The Rayleigh (Rayl) has dimensions of* kg m^{-2} s^{-1}

4.3 Specimen Material & Design

To maintain consistency with the majority of the surrounding literature [8, 9, 16, 17, 33, 103, 178] the studies in this thesis will be performed on a high purity polycrystalline material, a decision which has implications that both simplify and constrain experiments. In this chapter we introduce the high purity copper studied in all later experiments. We will discuss each of the concerns relating to its polycrystalline nature one by one, explicitly verifying the material as a fit candidate for experimental study. In doing so we will be able to approximate some of the initial material properties for use in the analysis of later experiments.

4.3.1 C103 Copper & Specimen Design

The metal studied in this thesis is a C103 grade oxygen free copper, grade C103 copper has a purity of greater than 99.95 wt% and the majority of the impurities remaining are lead at approximately 0.03 wt% Assuming all of the impurities to be lead returns an atomic purity of 99.98%. The material was received the form of a heat treated plate.

Due to the cylindrical symmetry in all of the experimental methods used, the specimens themselves were cut into right cylinders using spark erosion (often referred to as EDM). Spark erosion was chosen as a forming method as due to the low applied pressures in the cutting process, the specimens will not be significantly work hardened during their forming, furthermore the technique is well suited to precisely forming of small specimens.

An important consideration for specimen machining in compression is friction, outlined in section 4.1.2.1. Recalling from section 4.1.2.1 the expression for frictional effects found by Male [140] and Walley [141];

$$\sigma_{fric}(t) = \sigma_f(t)\left(1+\mu\frac{3r(t)}{2l(t)}\right). \tag{4.37}$$

Now, if we consider two specimens of different size but same initial aspect ratio, equation 4.7 shows that if both specimens undergo the same level of uni-axial strain, they will still have the same aspect ratio. Therefore, for any two specimens of equal initial aspect ratio, throughout the entirety of their stress strain curve frictional effects are reduced to a common pre-factor. Constant specimen aspect ratios can therefore be used to remove the need to separate frictional effects from those caused by deformation conditions.

4.3.2 Grain Statistics & Specimen Behaviour

Grain statistics are exceptionally important when determining poly-crystal specimen sizes, ultimately defining the minimum specimen size and therefore the maximum rate. We can understand why relatively simply; if we have a single crystal of metal, its strength varies in a very well defined way depending on the angle of the applied load to the various slip planes. If we add a second crystal (i.e. a second grain) in a random orientation, the behaviour will now become dependent on the relative orientation of the two crystals. Furthermore, as the orientation of the second grain is random, then it is extremely unlikely that any two specimens will provide a consistent response to the same load and angle. If however, we add a sufficient number of randomly oriented grains, eventually we will have a large enough set to approximately sample all angles, something greatly aided by the symmetries of the crystal lattice. At this point, known as a bulk, an ideal material will give the same response regardless of the directionality of the applied load (in practice this will vary depending on specimen shape) and, importantly, will have repeatable behaviour.

It is therefore of key importance that we have a sufficient number of randomly oriented grains that the specimens behave as an ideal polycrystalline bulk. No experimental measurements can be conclusive if the specimen to specimen variation is large and unpredictable. Armstrong [179] determined a criterion that a material should ideally have 100 grains in any cross section to be considered as a bulk. We therefore find that our specimen thickness, typically the smallest dimension, should be at least 10 grain diameters.

To determine the grain characteristics, a combination of scanning electron microscopy (SEM) and electron backscatter diffraction (EBSD) [180] mapping was performed on the specimen material. An example of an SEM micrograph and its corresponding EBSD map are shown in Figure 4.19, the final data set is generated from many of such image tiled together. The grains were measured to have an average axis of 16 ± 3 μm, with a longer axis in the direction of the final rolling of the plate, for the majority of the grains the aspect ratio remained less than 1.5.

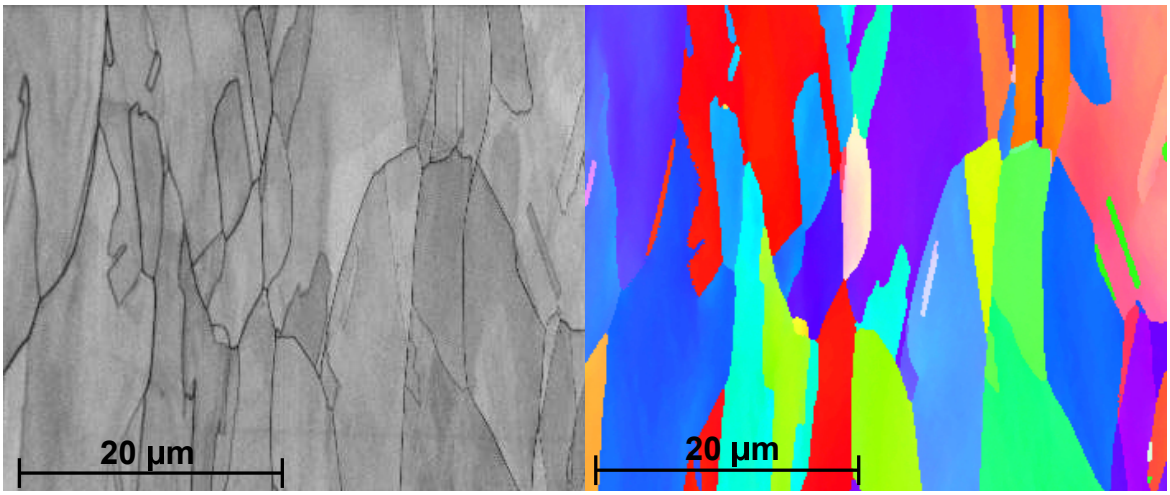

Fig. 4.19 Typical micrographs of a copper specimen, imaged using a Phillips XL30 SEM. The grains are of typical size 16 ± 3 μm, with some grains having longer axes in the plane of the plate, presumably caused by the rolling procedure. EBSD maps showed no strong bias in lattice orientation.

However, whilst imaging can provide a guide as to what minimum specimen size can be used, it does not guarantee that grain statistics will not affect the repeatability of the specimens. We will therefore explicitly demonstrate the consistency in a set of simple quasi-static tests. Based on the average long axis of the grains at approximately 20 μm a potential minimum specimen thickness could be 200 μm. To ensure bulk behaviour and to simplify experimental aspects such as specimen recovery, a larger thickness of 500 μm was adopted. Figure 4.20 shows the stress-strain curves generated for 5 specimens of 500 μm

thickness and 2 mm diameter, and a single curve for a specimen of 3 mm thickness and 12 mm diameter.

The scatter on the specimens is small, approximately 2% of the absolute value, implying the specimens are repeatable. Furthermore, the curves prove a good match to the 3 mm thick specimen, which contains a number of grains several orders of magnitude above the threshold.

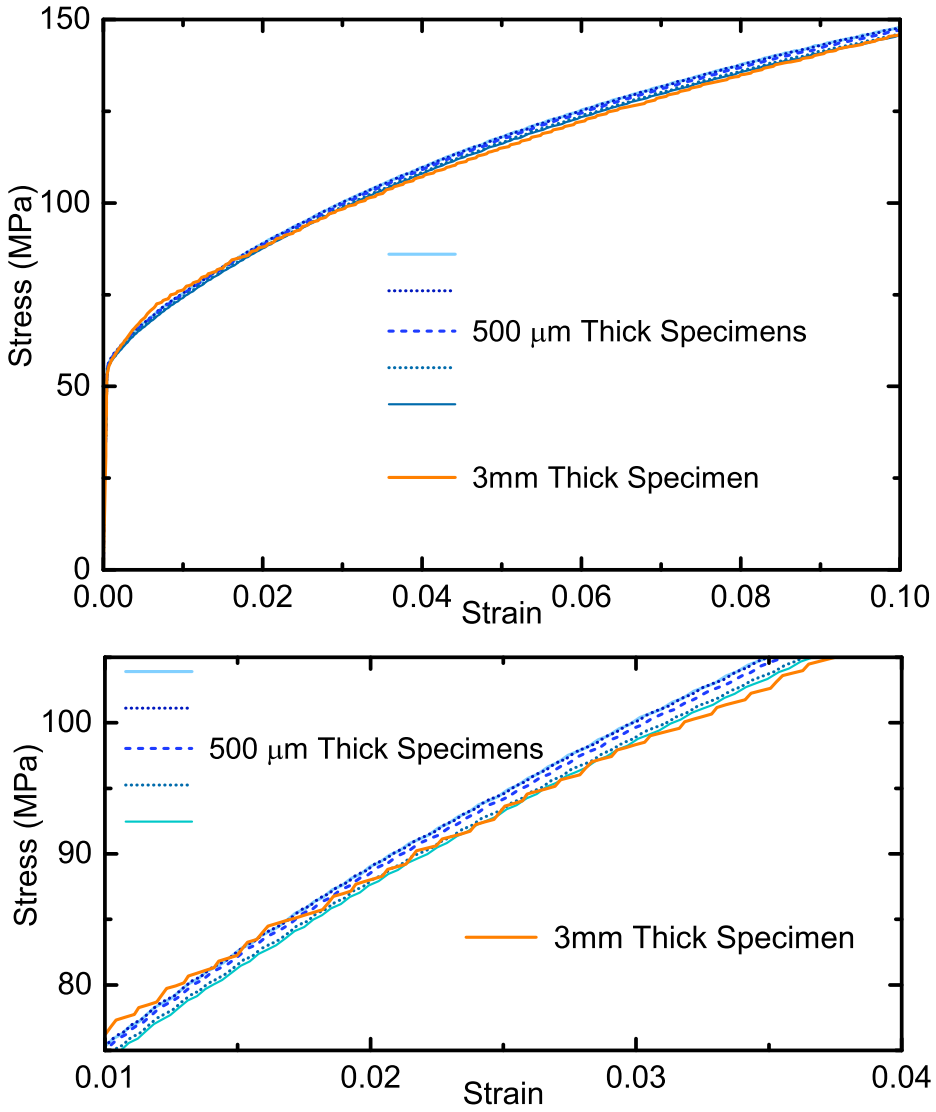

Fig. 4.20 The stress strain curves recorded from a set of C103 copper specimens, five of the curves (blue) correspond to small specimens, 500 μm thick, whereas the orange curve corresponds to a larger 3 mm by 12 mm specimen. The step like pattern observed on the larger specimen is believed to be due to the nature of the screw driven loading in the Instron, rather than a material behaviour.

It therefore appears that the smallest specimens not only behave consistently within their own size, but also do not suffer from any major size effects. We can therefore use multiple specimen sizes to expand the testable strain rates in each piece of equipment.

4.4 Summary

In this chapter we have outlined the most common methods of both quasi-static and dynamic testing. We have discussed sources of error, in both cases friction plays a significant part and specimens have been designed to attempt to make friction a constant pre-factor in most studies. We have discussed experimental errors due to the elastic properties of both systems, notably deformation of the apparatus in quasi-static testing, and wave transmission in dynamic testing. Finally, we introduced the specimens and performed a set of rudimentary tests to show that they have repeatable behaviour at all specimen sizes. We will now progress on to a piece of experimental work, studying the temperature dependence of the specimen material at strain rates above 10^4 s^{-1} and temperatures between ambient and the static annealing temperature, 350 °C.

Chapter 5

High Rate Deformation at Elevated Temperatures

In chapter 3, we established a generally accepted picture of a transfer from an Arrhenius or Krammer type pinning scenario to a viscous phonon drag limited one. We did note however that their use in the $10^3 - 10^6$ s^{-1} regime is subject to heavy criticism, and thus their responsibility for the strength transition. Hunter and Preston have shown that given etch pit measurements of drag coefficients, dislocation transit times are not expected to become rate limiting until approximately 10^6 s^{-1} [19]. Meanwhile finite element simulations based on phonon drag theories provide poor predictions of verification experiments such as Taylor impact experiments, typically significantly under predicting the strain to occur. Such observations have led authors such as Couque [181], to search for additional phenomena to explain the discrepancy in strain. Similarly, Armstrong [33] has noted phonon drag theories fail to account for observations of increases in ductility at high rates. In order to progress the understanding of the level of responsibility of phonon viscosity for the strength transition, we will seek to test one of the core predictions of drag based strength models. Ideally we want to test a prediction that is universal, rather than the product of any particular material model.

Such a prediction is the reversal of thermal behaviour in a drag limited regime [111]. If the rate limiting mechanism transitions from thermally activated barrier escape to a phonon damping effect, the behaviour of a metal will transition from thermal softening to thermal strengthening, discussed in Chapter 3 and section 5.1. Such an effect should begin to be visible in a series of uniaxial, single condition Hopkinson bar experiments above the transition.

In this chapter, we will describe a series of measurements performed at the limits of the capabilities of split Hopkinson bar systems, ensuring measurements are well above the strength transition. We will study temperature variations between room temperature and 300 $^{\circ}C$, refraining from higher temperatures to avoid crossing the static annealing temperature of the metal, which is approximately 350°C [182, 183].

5.1 Thermal Sensitivity in the Phonon Drag Regime

The theory presented in this section is largely a summary of the relevant parts of chapter 3, which should be referred to for complete discussion. The general rate equation developed by Follansbee,

$$\dot{\varepsilon} = \frac{\frac{1}{M} b \rho}{\frac{MB}{\hat{\sigma} b} + \sqrt{\rho} t_0 \, exp\left[U(\hat{\sigma})/k_B T\right]}, \tag{5.1}$$

that cannot be analytically inverted [19]. The low and high rate limits are simpler and will be used to outline general qualitative behaviour. At low rates the pinning term dominates

$$\dot{\varepsilon} \approx \dot{\varepsilon}_0 \, exp\left[-U(\hat{\sigma})/k_B T\right] \qquad \therefore \qquad \hat{\sigma} = \phi(\dot{\varepsilon}, T)\sigma_p. \tag{5.2}$$

The remobilisation of pinned dislocations is thermally assisted. At fixed rate and structure, if the temperature is increased, less mechanical work, $\hat{\sigma}$, is required to lower the barrier, $U(\hat{\sigma})$, to allow thermal escape. The strength of the metal therefore decreases with increasing temperature.

If, however, deformation becomes limited by a dislocation drag mechanism, ignoring inertial effects which are small [19], and in the high rate limit, the flow stress is predicted to follow the form

$$\hat{\sigma} \approx \frac{M^2}{\rho b^2} B(T)\dot{\varepsilon}. \tag{5.3}$$

The flow stress is then proportional to the viscosity constant, $B(T)$, that, as discussed in section 3.2.1, increases with the energy of the phonon gas, taking the form

$$B(T) = B_0 + B_1 T + B_2 T^2 \approx B_1 T. \tag{5.4}$$

Combining standard values for copper with analytical expressions for each term gives $B_0 \approx B_1 T/10$ in the 300 - 600 K range, and the $B_2 T^2$ term remains negligible until very high temperatures. We therefore expect, given a constant structure, that as deformation enters a drag limited scenario, the fixed rate response of a metal to increased temperature will change from softening to strengthening. Figure 5.1, shows a sketch of the predicted variation of flow stress with rate at two temperatures, $T_2 > T_1$, based on phonon drag mechanisms. The sketch assumes the dislocation structure remains constant at all conditions.

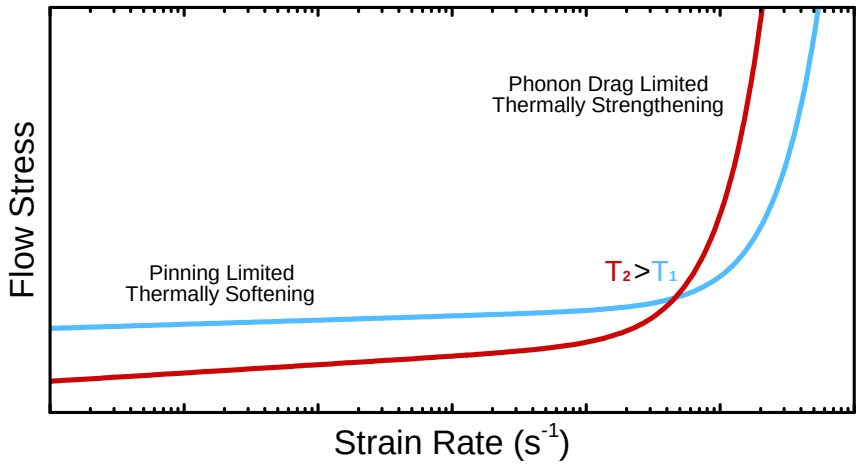

Fig. 5.1 The predicted variation of flow stress with rate for low true strains in a model which uses a combination of thermal escape from barriers and phonon drag as a physical basis. The higher temperature is expected to begin its upturn in flow stress at a lower rate, and at high rates greatly exceed the flow stress at lower temperatures.

The inversion of thermal softening has been observed in flow stress measurements by Clifton [130], and in Hugoniot elastic limit measurements by Kanel [122, 123] and Gurrutxaga-Lerma [125]. Experimental confirmation of the inversion provides strong evidence that phonon drag is a real mechanism and that it behaves consistently with phonon gas theory. However, all of these studies were either performed at stresses well in excess of the mechanical threshold (several GPa) , or at temperatures close to the melt point of the material. The studies therefore correspond to a scenario where pinning no longer occurs. However, the observed transition occurs at stresses in the hundreds of MPa, and temperatures away from melt, where structural barriers cannot be ruled out. We therefore cannot used the results of high stress of near melt experiments to make conclusive statements about the 10^4 to 10^5 s^{-1} regime.

Kumar and Kumble [103, 104], Ferguson [178] and Khan [136] have all performed tests in the $10^3 - 10^4$ s^{-1} regime, in which no inversion in strength or reduction in thermal softening was observed. However, these studies, being at or below 10^4 s^{-1} are either before, or on the cusp of the transition, and therefore difficult to draw solid conclusions from. Finally, Clifton [129] has performed pressure-shear experiments at strain rates of 10^6 s^{-1} in which thermal softening was retained. However, the differing measurements of shear stress and shear strain makes pressure-shear makes the measurements difficult to compare to uniaxial stress studies [136], that make up the bulk of the available data [17, 184].

A beneficial study, helping to complete the picture, would be one that extends uniaxial stress measurements to above the transition to varying temperatures. Doing so will provide a more readily usable data set that is directly comparable to the bulk of the currently available data, and therefore be more accessible for the development, parametrisation and verification of both physical and constitutive models that cross the transition.

5.2 Method

This section is largely based on methods outlined in more detail in Chapter 4. Miniaturised Hopkinson bar apparatus allow the study of non-shock deformation at rates above 10^4. Specimens were tested in a 6.4 mm diameter Inconel 718 split bar system, the bar surfaces were probed with PDV interferometry (outlined in section 4.2.1.2) as shown in Figure 5.2. The laser probes were placed at the middle of the input bar and as close as permitted by St-Venants principle on the output bar. Inconel 718 was chosen due to the consistent elastic properties throughout the temperature range (section 4.2.5). PDV probes were used for two reasons. Firstly, they are impervious to spall which wired gauges suffer from in the severe impact conditions of the test. Secondly, PDV measurements are temperature independent, compared to the strongly temperature dependent response of semiconductor gauges. Stress, strain and strain rate were measured and force equilibrium was verified for every test using methods outlined in chapter 4.

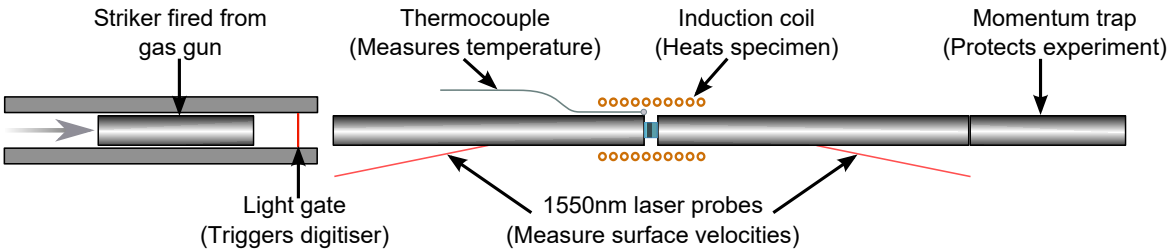

Fig. 5.2 A schematic of the miniaturised 718 Inconel SHPB system used to test specimens at high rates and temperatures, outlined in the body text.

Raised temperatures require the use of a compatible and thermally consistent lubricant. Dry graphite powder (described in section 4.1.2.1) was chosen over other lubricants such as graphite grease due to its more consistent performance at raised temperatures. Dry powder lubricants lack the adhesive qualities present in some wet lubricants [139, 177]. Due to the lack of strain arresting (present in later chapters) the rise time of the miniaturised system, that was found to be approximately 1 μs was considered to be acceptable. Using the split

system however limited the maximum strain rate to 8×10^4 s^{-1} due to the yield strength of the Inconel 718 alloy at raised temperatures. The maximum achievable rate is still expected to be well above the strength transition, and mechanical equilibrium will still have been achieved by 10% strain in all experiments.

Temperature was varied using an induction heater, outlined in section 4.2.5. A schematic time temperature curve for the experiments performed is shown in figure 5.3. The specimen is heated over a period of approximately one minute, which was determined using dummy specimens with thermocouples attatched, to be slow enough for a thermocouple mounted on the corner of the output bar to accurately measure the specimen temperature. The time also remains well below the timescales required to statically anneal a specimen [182, 183]. The specimens (presented in Chapter 4) were heated to approximately 10 K above the target temperature, and then the induction heater was turned off to reduce electrical noise, the experiment was triggered when the specimen temperature passed back through the target temperature, the typical temperature error from this method was estimated to be 5 K.

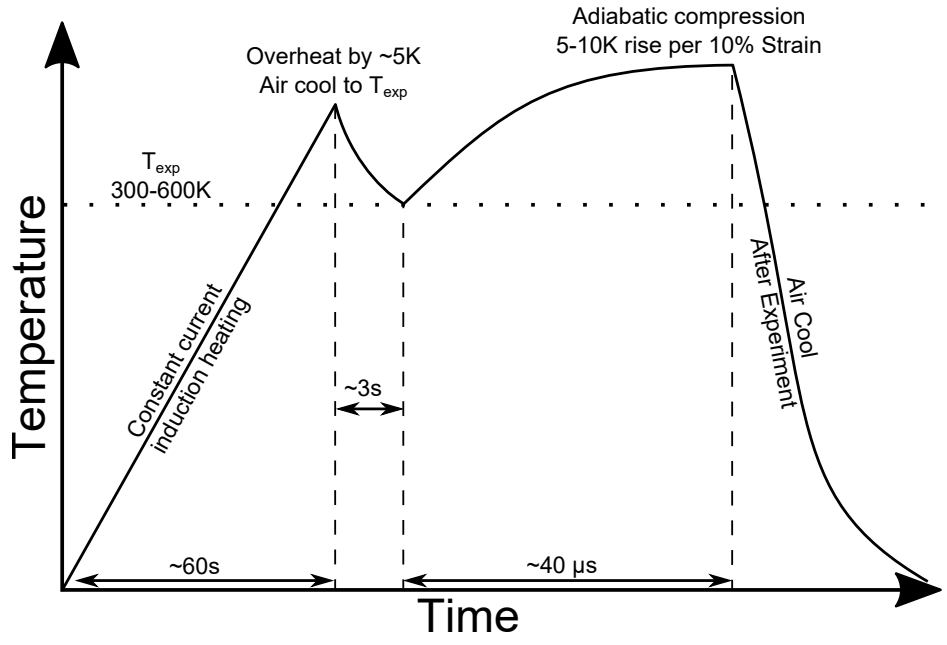

Fig. 5.3 The time temperature curve of specimens in an induction heated SHPB experiment. Due to the vast difference in the timecales of the varios stages of the experiment, no relative scale can be inferred from the lines in the diagram.

The specimen temperature unavoidably varies throughout the test, caused by the work done in compression and the adiabatic nature of deformation above 100 s^{-1}. Based on typical specimen strengths the temperature rise during the experiment will occurs at a rate of approximately 100 K per unit true strain, proportional to the flow stress of the specimen [23]. The change from the test temperature will be smallest early in the experiment and the rate of change increases if specimens work harden. Including the consideration of temperature dependent saturation in work hardening, comparisons are most valid at small strains.

The specimens themselves were right cylinders wire eroded from a plate of C103 grade oxygen free copper, with nominal purity greater than 99.95%. Micrography and EBSD study showed the grains to be of size 16-20 μm. Instron testing of five specimens gave repeatable results. The cylinders were 3 mm in diameter and 500 μm thick. The high strain rates involved in these experiments will lead to a significant inertial stress being superposed on top of the specimen strength measured by the output bar. General terms for inertia in compression have been derived by Gorham [169], and in the highest strain rate experiments the effect is expected to be approximately 10 MPa, small compared to the expected specimen strengths.

Powdered graphite was used to lubricate the bar ends, minimising frictional effects from radial expansion as the specimen compresses. The lubricant was chosen due to its consistent behaviour between ambient temperature and 600 K. Furthermore, as all specimens have the same aspect ratio, at low strains frictional effects reduce to a strain dependent pre-factor that is the same in every experiment.

5.3 Results & Discussion

A preliminary set of experiments were performed in both split and direct impact geometries to determine at what rate the specimen material underwent the strength transition, as this is likely to be affected by grain size and purity. Figure 5.4 shows the flow stress of the C103

copper used in this study as a function of rate, as measured at 0.1 true strain. The transition appears to occur at approximately 10^4 s^{-1}.

Based the measurements in figure 5.4, three target rates were chosen. Firstly, close to the transition at 2×10^4 s^{-1}, where both structural and viscous thermal effects would be expected to cause intricate thermal behaviour. The second rate selected was 4×10^4 s^{-1}, twice the transition rate and approaching twice the stress of the transition. At 4×10^4 s^{-1} viscous forces should be approximately balanced with structural and strengthening should have begin. Finally, the maximum feasible rate available, given the experimental apparatus and temperature range, is 8×10^4 s^{-1}, well above twice the transition strength - viscous forces should be dominant at this rate.

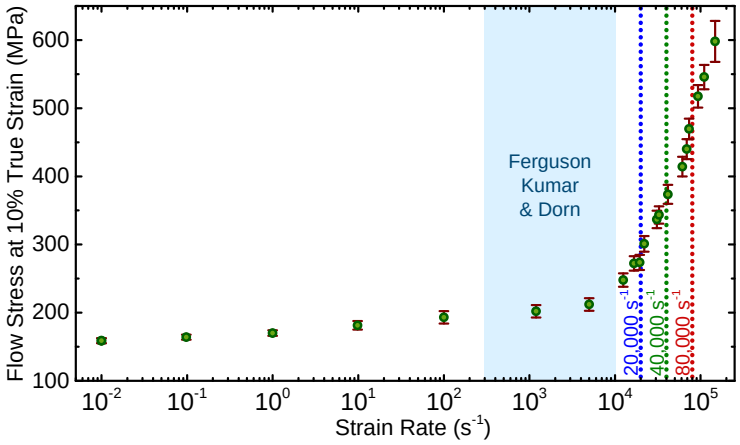

Fig. 5.4 The flow stress at 0.1 true strain as a function of rate for the copper specimens in this study. The dotted lines signify the rates selected for study, discussed in the body text. The shaded region shows the range of rates previously studied by Kumar in copper [103, 104] and Ferguson in aluminium [178].

Figure 5.5 shows the flow stresses measured as a function of strain and starting temperature for the achieved rates: 2.2×10^4 s^{-1}, 4.4×10^4 s^{-1} and 7.9×10^4 s^{-1}. Each condition was tested in triplicate, the solid line presented for each set of conditions corresponds to the average flow stress measured for that strain, whilst the shaded region corresponds to the standard deviation in flow stress. The periodic nature of the standard deviation reflects the uncertainty being largely due to dispersion in the output wave. Despite measuring at the

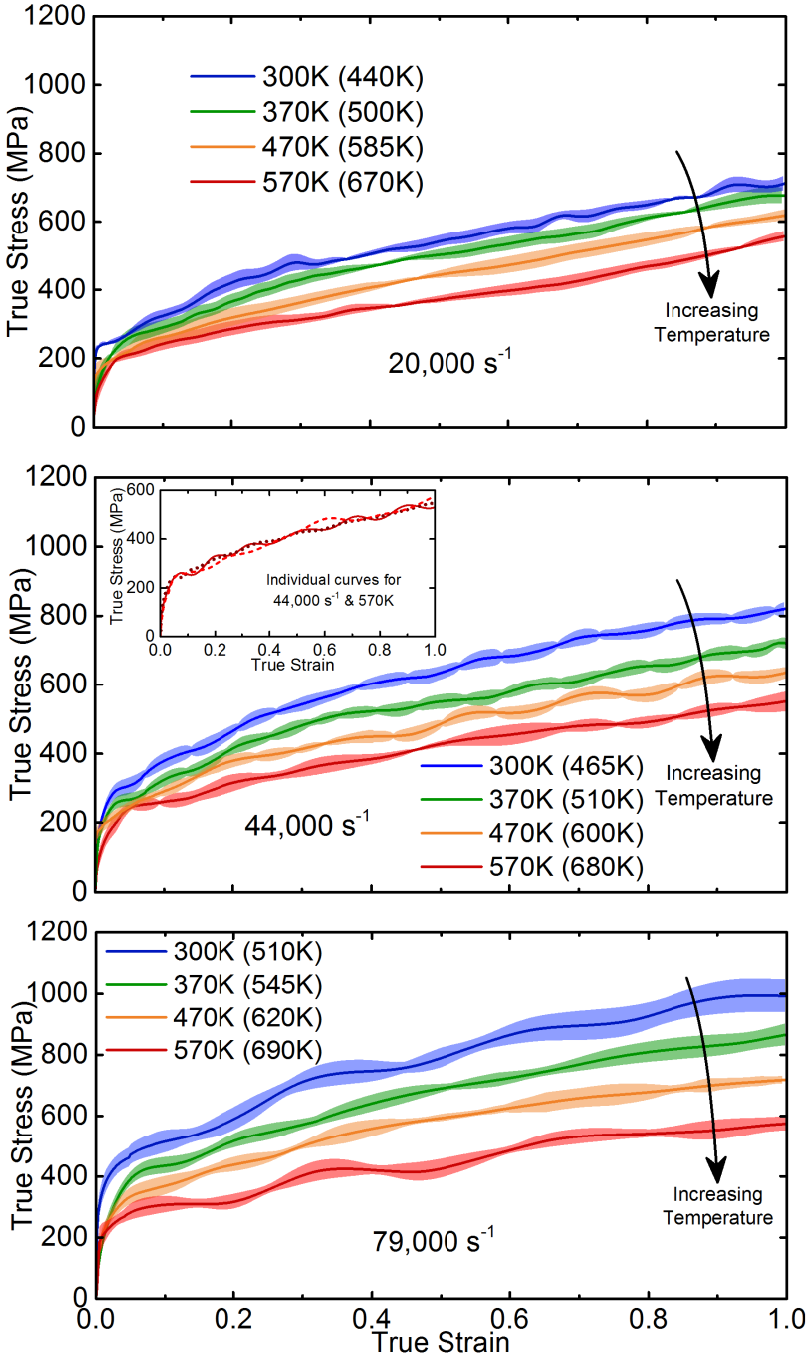

Fig. 5.5 The flow stress of the OF copper described in the body text, as a function of strain for four temperatures and three strain rates. All of which are at or above the strength transition. Despite being well into the proposed viscous drag regime, the curves still monotonically decrease in strength with increasing temperature.

minimum distance permitted for a valid surface measurement the effects remain a significant source of error. A typical triplicate of individual results is shown as an inset.

It is immediately apparent from the stress-strain curves presented in figure 5.5 that at no point (up to 7.9×10^4 s^{-1}) does the temperature dependency of the flow strength reverse. The curves monotonically decrease in strength with increasing starting temperature. Such results strongly contradict the concept that thermal phonon damping is the dominant strength mechanism at these rates, and therefore contradict that it is responsible for the strength transition.

Continued thermal softening above the transition implies that despite the increase in flow strength, structural barriers remain the dominant strengthening mechanism. The thermal behaviour observed is more consistent with increasing strain rate affecting the evolution of dislocation structures within the material, resulting in an increased value of the threshold stress, σ_p. Physical models to such extent have been proposed by Follansbee [14], Armstrong [33], and Huang [47].

If we attempt to process the data using the relationship described in equation 5.2, and a rate dependent threshold stress, discrepancies remain. For the purpose of illustration we will use the form (and parameters) of ϕ proposed by Kocks [97];

$$\phi(\dot{\varepsilon}, T) = \frac{G(T)}{G(0\ \mathrm{K})}\left[1 - \frac{k_B T}{U_\phi G b^3}\ln\left(\frac{\dot{\varepsilon}_0}{\dot{\varepsilon}}\right)\right]^{3/2} \tag{5.5}$$

where U_ϕ is a dimensionless material constant [14], $\dot{\varepsilon}_0$ is some limiting strain rate taken to be 10^7 s^{-1} [14] and G is the shear modulus. The relation is derived using a phenomenological form of $U(\hat{\tau}, \tau_p)$ which describes a quadratic remobilisation barrier with extended tails, accounting for the strain's far field [97]. Other expressions exist for ϕ like terms, notably those by Zerilli and Armstrong [13] and Hunter and Preston [19], also predict qualitatively similar interdependence between rate and temperature effects.

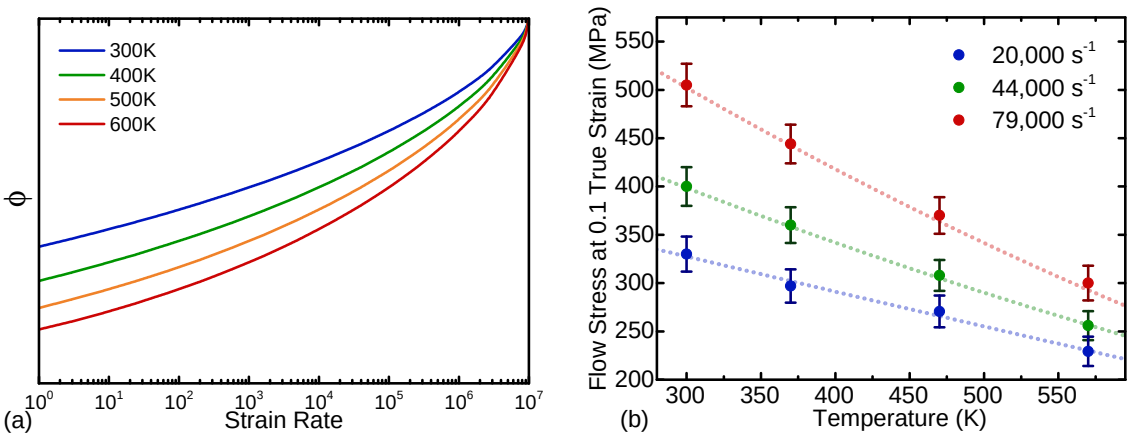

Fig. 5.6 (a) A sketch of $\phi(\dot{\varepsilon},T)$ as a function of rate for varying temperatures above ambient, as predicted by the model by Follansbee *et al.* [14]. (b) The measured flow stress for each condition at 0.1 true strain as a function of temperature. The dotted lines on the graph are to guide the eye.

Equation 5.5 is sketched in Figure 5.6 (a), as the rate increases the various temperature curves converge, corresponding to a prediction of decreasing thermal softening with rate. Physically the behaviour can be rationalised from the fact that with increasing rates $\hat{\tau}$ approaches τ_p, reducing the remaining barrier for thermal activation, and in turn the temperature sensitivity. Eventually when $\hat{\tau}=\tau_p$, the barrier is mechanically overcome and the temperature dependence owing to ϕ vanishes. This behaviour is not directly observable in the stress-strain curves. Without any processing of the data it would appear that the 7.9×10^4 s^{-1} specimens undergo greater absolute thermal softening than those at 2×10^4 s^{-1}. This is shown in Figure 5.6 (b) which plots the flow stress at 0.1 true strain for each rate as a function of initial temperature, the higher rate measurements show a steeper thermal softening gradients.

The increased thermal softening behaviour can partially be explained in models proposing increased work hardening with rate, as increasing σ_p may lead to greater absolute softening even for reduced variations in ϕ. We will initially assume we are observing some increase in work hardening due to strain rate alone, and that our measurements are at low enough strains that recovery effects [8, 35] for all specimens are the same. Under these approximations, the value of σ_p at fixed strain is purely a function of rate.

If σ_p is purely a function of rate, we can remove σ_p effects by grouping the measurements by rate and then normalising each group to the corresponding ambient temperature measurement (an arbitrary choice), removing σ_p as a common factor;

$$\frac{\phi(\dot{\varepsilon},T)}{\phi(\dot{\varepsilon},300\text{ K})} = \frac{\hat{\sigma}(\dot{\varepsilon},T)}{\hat{\sigma}(\dot{\varepsilon},300\text{ K})}. \tag{5.6}$$

We can then compare the normalised behaviour to typical model predictions of ϕ.

Normalising ϕ to the 300 K measurement for each rate, we expect to see the curves shown in Figure 5.7 (a). The normalisation causes all curves to begin at unity, however the lower rates decrease more quickly, due to their higher temperature sensitivity. Thus, if the experimentally observed strength increase is due to some general, purely rate dependent increase in work hardening, we expect the level of thermal softening, normalised to that rates ambient temperature flow stress, to decrease with increasing rate. Figure 5.7 (b) shows the measurements taken at 0.1 true strain (presented earlier in Figure 5.6 (b)) normalised to each rates ambient temperature measurement. We see that even after normalisation, the 7.9×10^4 s^{-1} specimens still show the greatest levels of softening. The highest rates undergo the most thermal softening both in absolute and relative terms.

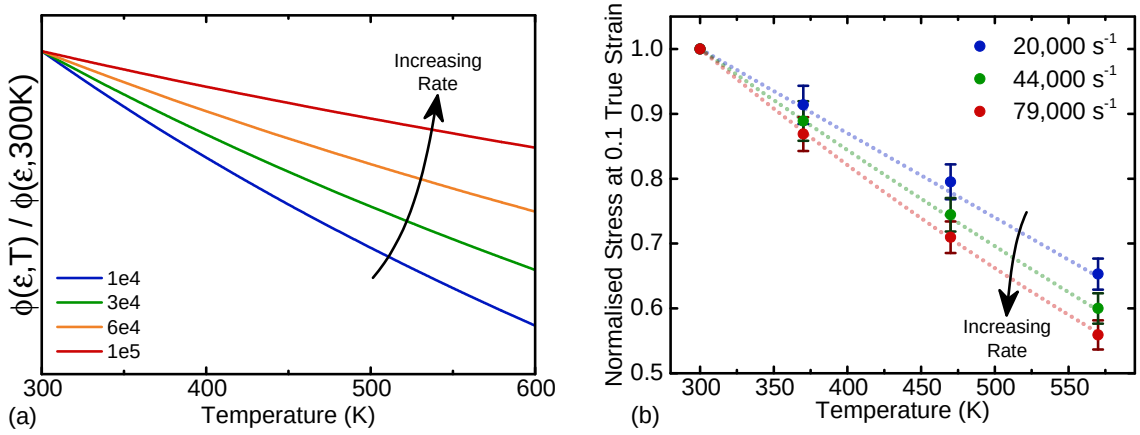

Fig. 5.7 (a) A sketch predicted variation in ϕ with temperature normalised to the value of ϕ at room temperature for a variety of rates between 10^4 s^{-1} and 10^5 s^{-1}, based on the form of Follansbee *et al.* [14]. (b) The ratio of the flow stress at each rate and temperature, relative to the ambient temperature strength for that rate, after the removal of the athermal term (σ_0).

There are three potential sources for such a discrepancy. Firstly, current models for ϕ may be inaccurate above the transition. There may be a phenomenological change in how structural barriers are surpassed, leading to an increasing temperature sensitivity ϕ with rate.

Secondly, whilst it is yet unknown what process is responsible for the transition, many strain rate dependent processes in metals exhibit ‘time-temperature superposition" effects. Typically, increasing the specimen temperature has effects similar to decreasing the applied strain rate. If the specimen strength increases due to a rate dependent increase in work hardening, increasing temperature may affect the underlying process in a way analogous to performing work hardening at a lower rate.

Thirdly, if the strength increase arises from an increased rate of work hardening, higher rate specimens may experience an earlier onset of ‘stage III’ work hardening [8, 14, 64], in which recovery effects reduce the rate of work hardening to a small fraction of that in stage II. The stress at which work hardening transfers to stage III decreases with temperature. If higher rate specimens undergo greater initial work hardening, then at a fixed strain they are likely to be more greatly affected by temperature dependent saturative effects. The threshold stress itself would therefore be expected decrease with temperature as the plateau stress lowers. It should be noted that this scenario is already predicted by many state-variable based models [14, 98].

In order to fully understand the observed increase in thermal softening, and indeed the strength transition itself, measurements are required that separate instantaneous (ϕ) and structural (σ_p) effects to allow detailed studies of the individual mechanisms, rather than their combined effects. The results of the present study emphasise the importance of the threshold stress as a quasi-state variable in FCC metal deformation, and the need to properly understand its behaviour in the absence of dynamic effects.

5.4 Conclusions

A series of oxygen free copper specimens were tested at elevated temperatures and rates well above the onset of the materials proposed viscous transition. The inversion of thermal behaviour predicted by phonon drag models was not observed, instead the level of both absolute and relative thermal softening increased with rate. The data contradicts the predicted behaviour in a phonon driven transition, as informed by phonon gas theory and experiments in pure drag regimes. Models based on increasing levels of work hardening above the transition provide better qualitative agreement with the data. However, there were still lesser qualitative disagreements with the measurements at 10% true strain, for which several potential sources exist.

In order to properly understand the behaviour of the materials and gain insight to the physical mechanisms involved, experiments are required to separate instantaneous (ϕ) and structural (σ_p) effects. In Chapter 7 will will aim to separate these effects, to both provide general insight to the mechanisms causing the strength transition, and to provide a strong test for the use of state variable models above the transition, as we did for phonon drag in this chapter. To provide a faithful study of the two separated effects, we will introduce and develop a new experimental method; direct impact Hopkinson pressure bars.

Chapter 6

Application of Photon Doppler Velocimetey to Direct Impact Hopkinson Pressure Bars

Based on the results of the previous chapter, it is clear we must attempt to separate structural and instantaneous effects. Both our own results and historical measurements [14] would indicate that the phenomena of interest is early stage work hardening.

In order to properly access this range we will require a third experimental apparatus, known as a direct impact Hopkinson bar system. Developments made to this system to ensure the accuracy of later experiments in this study also created a technique providing opportunities in the testing of many other materials. In this chapter we will outline the method developed, and as an aside discuss its potential application to a variety of material types.

6.1 Motivation & Direct Impact Bars

There are two major limitations in SHPB apparatus which make it unsuitable for testing close to 10^5 s^{-1}. Firstly, as outlined in section 4.2.7, there is a maximum velocity that striker

bars can be fired at in an SHPB system before yielding occurs at the striker-input interface;

$$v_{max} = \frac{2\sigma_Y}{Z_{bar}}. \tag{6.1}$$

Where σ_Y is the yield strength of the bar material and Z_{bar} is its specific acoustic impedance. Given the 500 μm sample thickness and 350 Maraging steel bars, this limit would correspond to a strain rate of approximately 2×10^5 s^{-1} and is therefore not a major drawback in the current study.

However, dispersion during wave travel in the input bar creates a more major limitation. Even in the miniaturised split system, with the least dispersion, the rise time of the pulse inferred from probing the bar end was in the region 0.5-1 μs. If we consider an experiment deforming a specimen to 0.1 true strain (as we seek to impart relatively low strains), the entire experiment duration is approximately 1 μs. This is approximately equal to the rise time in the split bar system. Instead of performing an experiment at 10^5 s^{-1} we would in fact have performed an experiment in which the strain rate continuously and significantly increased throughout. The split system therefore cannot be used for history experiments where we wish to maintain a single deformation condition in the initial stage of the loading. A single condition is required if we wish to make relatively simple statements of the interplay between early stage work hardening and rate, rather than model the more complex load path. We therefore seek to perform experiments where the majority (we will aim for >90%) of the load path is an approximately constant strain rate.

Both of these problems have, nominally, been addressed in an alternative loading geometry known as a direct impact Hopkinson pressure bar (DIHB) arrangement. The DIHB geometry is shown in figure 6.1, the name is derived from the fact that the input bar is removed, and the sample is impacted directly by the striker.

In a DIHB experiment the striker decelerates more slowly as it continues moving with the deforming sample, and does so for multiple passes of the wave, meaning the peak and

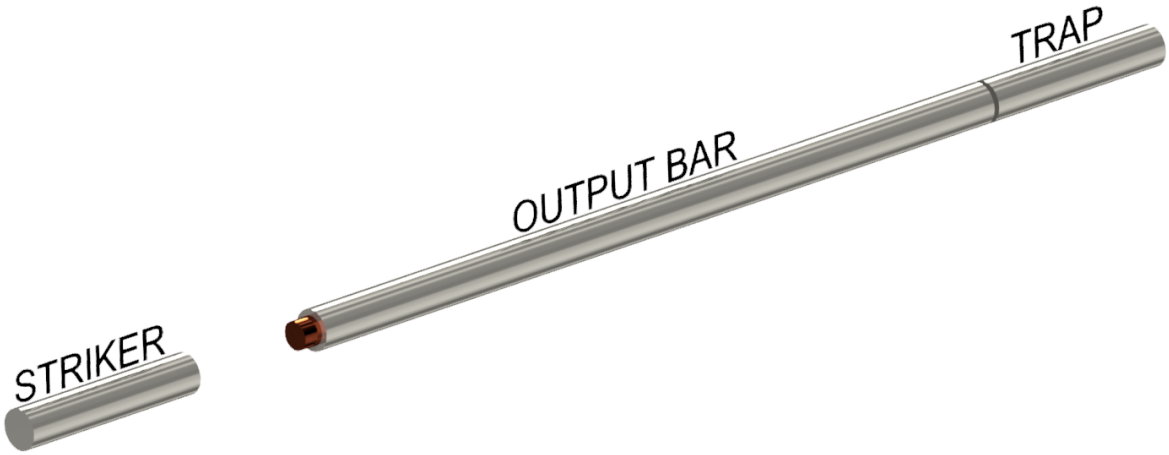

Fig. 6.1 A typical direct impact Hopksinson bar arrangement. Unlike in an SHPB the input bar is removed leaving the specimen attatched to the front face of the output bar as the impact target.

average stresses experienced by the striker bar for a given velocity are lower, and hence higher shot velocities can be used given the same bar material. The velocity limit in a direct arrangement is then when either the specimens flow stress exceeds the bar yield. A further potential limit arises if the specimen or any apparatus perfectly transmits the striker load, returning limit to that a striker-input interface.

The geometry also removes the Pochhammer-Chree dispersion that occurs as the pulse travels though the input bar [185] to reach the sample. Some specimen types may reach force equilibrium faster in a DIHB setup as removing dispersion makes the rising edge of the stress pulse steeper. However, equilibrium is still dominated by the properties of the specimen.

Currently, the advantages gained from a direct impact setup come at significant cost. Removing the input bar removes all gauge information about the input face, meaning approximations have to be made about the striker face velocity and therefore strain and strain rate. Similarly, the achievement of stress equilibrium in a sample cannot be experimentally verified. Consequently, even in materials that equilibrate quickly (such as fully dense metals) DIHB data are generally less reliable than SHPB data. In materials slow to reach force equilibrium, and materials that undergo compaction such as foams or cellular materials, DIHB methods are often unusable.

Importantly, a major uncertainty is posed for our desired use of the apparatus. We know that in an ideal picture the method should alleviate any problems in the rise time, reducing the time to the force equilibration of the specimen, exceptionally short ($<$100 ns) in our small metal samples. However, what is the rise time in a real, imperfect system? If we have no measurement of the impacted face we cannot tell.

Since the earliest direct impact experiments, high speed photography and streak methods have been available to measure the velocity of the striker bar [185]. However, these methods provide no information about the force at the striker face, are of limited resolution and are time consuming. Work done by Govender and Curry at the same time as this study used applied strain gauges to instrument striker bars [186]. This method is certainly useful, and recommended for experiments with extremely low striker velocities ($<$1 m s^{-1}), which may be affected by the PDV noise floor. however, gauges remain highly susceptible to damage and require heavily modified barrels for circuitry. These methods make DIHB experiments much less convenient to perform, both during the experiment and in post-processing, sacrificing one of the main attractions of bar techniques.

As we outlined in section 4.2.1, non contact measurements can be made using PDV probes, that can be converted to all required measurements. For this probe type, a striker bar is no different to any of the other bars in an arrangement, the surface velocity of the striker bar can be probed with ease.

6.2 Instrumentation & Velocity Measurement

The proof of principal for our PDV system was performed before miniaturised systems were developed [158, 159]. The bars used in this study were made of Dural alloy, and used in sizes of 25.4 mm and 12.7 mm. The sample of interest was attached to the face of the output bar using graphite grease. The lack of an input bar required adhesive lubricants to hold the specimens to the system. For comparison we also performed tests on a 12.7 mm

diameter Dural split system was used for comparison. The same system was used to perform the measurements presented in section 6.3.

PDV probes were placed on the output bar as in the split system and at the position the desired probing point on the striker will reach as it impacts the specimen, shown in figure 6.2. Output bar measurements are performed exactly as in a split bar system.

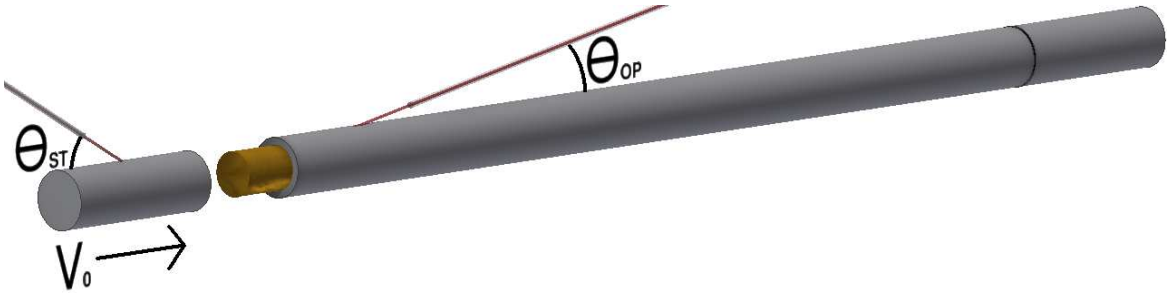

Fig. 6.2 An illustration of the DIHB experimental geometry. The incidence angles between the probing lasers and the bar axis in a DIHB system. The spot probing the striker bar is positioned based on the location of the bar at the moment of impact.

6.2.1 Striker Bar Measurements

As the striker bar is repeatedly fired from the barrel, it is not coated in any kind of reflective or retro reflective paint. The fibre was still shone at a shallow angle (10°) unless background noise was too large, in which case an angle of 30° was used to increase the diffuse return. Despite the absence of any paint, a signal was still collectable with the fibre placed 5 mm or closer to the bar surface. An example a direct impact bar trace was shown in figure 4.10, also explaining the analysis stages. Increasing the projection angle had no large effect on the influence of bending modes that are still negligibly small due to the reduced moments in direct impact, as any bending forces, small due to proper alignment, are limited to the specimen radius.

For the purposes of this discussion the laser probe will be placed at the mid point of the bar, 12.5 cm from the sample, firstly to satisfy Saint-Venant's principle, but also to aid in more simply visualising wave separation, discussed in section 6.2.3. The probe can be

placed anywhere further than the Saint-Venant's limit, including the back face of the bar. The location of this probe alters the offset times involved in performing wave separation, however these times can be calculated using the relevant travel paths and sound speeds in the bar, discussed in sections 4.2.1.2 and 6.2.6.

The free face of the striker bar was not chosen as either the striker bar would have to leave the barrel by a significant distance to allow it to be properly probed, overcomplicating system alignment, or significant changes to a typical Hopkinson bar set-up would have to be made in order to allow the fibre to enter the barrel at a shallow angle. The method we propose requires no bar or barrel modifications to implement the PDV.

The basics of extracting a trace are the same as for a split bar. The probe interferes due to a Doppler shift, causing an interference pattern that is converted into a velocity history. At this point though the measurement is different for two reasons, firstly it is the sum of the particle velocity at the probe and the "bulk" velocity (the velocity of the bar as a whole). Secondly, due to the nature and timescale of the unloading in the striker bar, measurements of the sample face velocity will usually be superimposed with the tensile wave reflections of compressional waves returning from the free end of the striker bar. We must separate these in post-processing.

The velocity measured by the probe is the combination of three separate components,

$$v_{probe} = v_{bulk} + v_{compressive} + v_{tensile}. \tag{6.2}$$

In order to obtain the force and velocity history of the sample face, these profiles must be correctly separated and time shifted. Separation is possible as the initial bulk velocity is measurable, and the initial tensile velocity is zero.

Figure 6.3 depicts the complete path of one wave in the striker. The compression wave is formed at the sample, (a), at t_1 and passes by the measurement probe (b) at t_2. It then reaches the back surface (c) where the free end boundary condition forces it to be reflected into a

tensile wave. The tensile wave passes back past the measurement probe at (d) at a time t_3 and contributes a further change in the velocity at that point, equal to the compression wave at (b). After passing as a reflected wave, the tensile wave returns to the sample at (e) after which any effects of the wave can be considered as part of the motion at the sample face, and do not require separating and correcting.

The velocity at the struck face of the specimen is the signal in the absence of the reflected trace, as that is the only velocity not to originate from the sample. If the experiment is being performed to reach high rates (as opposed to high strains at a low rate, for which the DIHB is also an improvement on a split arrangement) then just the trace before the arrival of the reflected wave can be used, and reflection no correction is required at all.

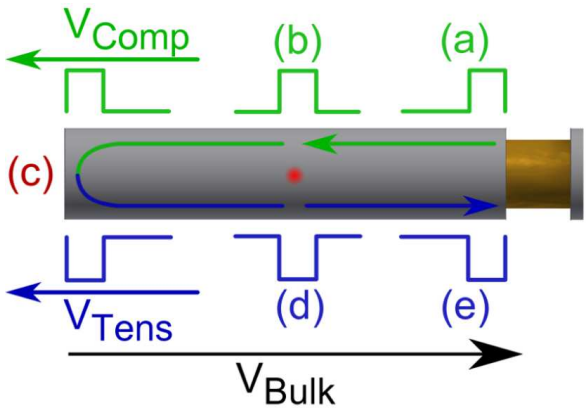

Fig. 6.3 The complete path of a compression wave from the sample to the free face and back as a tensile wave, passing the measurement probe each way. Also labelled outside the bar are the directions of the contributions to local particle velocity from each pulse relative to the bulk velocity. Note that the tensile wave further decelerates the striker bar due to the inversion of both wave type and travel direction.

The corrected trace for the impacted face velocity is

$$v_{st}(t_1) = v_{probe}(t_2) - v_{tensile}(t_2), \tag{6.3}$$

where v_{st} is the velocity of the struck face of the sample, and time shifting from t_2 to t_1 is applied as discussed above. As the back end of the bar is a free surface. It perfectly reflects

incoming compressional waves into tensile ones, the inversion of both wave type and travel direction at the striker free end means the velocity change due to the tensile component is the same as that of the equivalent earlier compressive component,

$$v_{tensile}(t_2) = v_{compressive}(t_3). \tag{6.4}$$

6.2.2 Trace Recovery Simulations

We generally wish to obtain v_{st} and v_{comp}, to enable the deformation and force histories to be extracted. Whilst simulations are not required for any of the experimental analysis, to illustrate and confirm the correction procedure, we used a simple 1D simulation shown schematically in Figure 6.4. A 50 long chain of unit masses were connected by springs of equal spring constant, K_1, to represent an elastic striker bar. These were set to an initial speed, v_0, of 100 m s^{-1} and connected to a 5 long chain of equal masses with restoring force dictated by a Kelvin-Voigt viscoelastic material model representing a sample. For a mass in the middle of the sample the force experienced took the functional form

$$F_i(t) = K_2 \left[x_{i-1}(t) + x_{I+1}(t) - 2x_i(t)\right] + \eta \left[v_{i-1}(t) + v_{I+1}(t) - 2v_i(t)\right], \tag{6.5}$$

where x_i(t) and $v(t)_i$ are the position and velocity of mass i as a function of time. After the sample chain was a 445 long chain of unit masses, of spring strength equal to the striker bar, modelling the output bar and preventing the output wave reflecting back within the time scale of the simulation.

Values of K_2 and η were chosen to provide a complex velocity history, with steps between complete transits of the compressional wave, not always observed in real samples. These extra steps provide more complex features to check the fidelity of our reflection correction procedure.

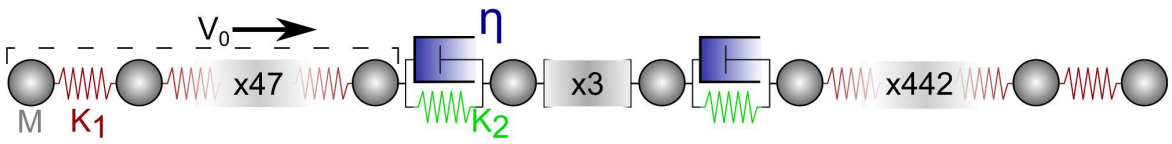

Fig. 6.4 A sketch of the simulation setup. A 50 mass elastic striker with initial velocity $v_0 = 100$ m s^{-1} impacts a 5 mass viscoelastic sample connected to another 445 mass output bar. The sample uses a Kelvin-Vöigt parallel spring and dashpot model. Tensile forces were turned off at the interface atoms.

Velocity histories were obtained by extracting the average velocity of the mass of interest and two masses either side, to simulate the broadness of a real PDV probe and remove high frequency oscillations of individual masses about their net motion. The probes were placed with their centres in the middle of the striker bar, and on the striker side face of the sample. It should be emphasised at this point that such a measurement of the struck face of the sample is not possible in 2D as Saint-Venant's principle shows surface measurements at this point unrepresentative of the bulk. The results of these two extractions are shown in Figure 6.5, and discussed in the next section. The probe measurement (solid line) has been time shifted onto the sample face measurement (dotted line).

We should note before further discussion that such simulations can be dispersive and may not be the best general model, instead a one dimensional continuum model is likely preferred. The model described was chosen for the simplicity with which probe positions can be moved and material parameters altered, allowing for fast verification of the wave modelling in multiple scenarios.

6.2.3 Reflection Correction Procedure

For the purpose of discussing the correction procedure simply, we define a dimensionless time, $\hat{t}$, such that one unit is the time taken for a sound wave to travel one length of the striker bar,

$$\hat{t}_i = \frac{C_{str}}{L_{str}} t_i \, . \tag{6.6}$$

where C_{str} is the sound speed and L_{str} is the length of the striker bar.

For a probe at the midpoint of the striker bar, the dimensionless time between $\hat{t}_1$ and $\hat{t}_2$ is 0.5 and between $\hat{t}_2$ and $\hat{t}_3$ is 1 ($t_2 > t_1 > t_3$). For a probe on the free end of the bar $\hat{t}_3$=$\hat{t}_2$=$\hat{t}_1$+1. We will now continue outlining the correction procedure for the scenario where the probe is at the midpoint of the striker bar.

Due to the reflections taking one unit of dimensionless time to return, we know that for $\hat{t} < 1$ our trace does not require correction, this is depicted in Region I of Figure 6.5. In this region, given the initial velocity from either light gate or pre-impact PDV measurements, we can extract the compression velocity from the difference between the initial and measured velocity, as shown by the blue down pointing arrows in Region I.

We now know the tensile velocity that returns to the probe and can correct the probe trace by subtracting that velocity from the probe measurement, as shown by the same blue arrows from Region I, inverted one unit of $\hat{t}$ later in region II. At this point the trace in Region II is correct, and the process can be repeated to correct Region III. However during this time the bulk velocity of the striker bar is likely to have decreased due to a deceleration step making a complete transit of the bar. The bulk velocity for any region is that of the most recently completed velocity step before that region. In Region I we observe two velocities, approximately 76 and 59 m s^{-1}. Whilst the 59 m s^{-1} is the more recently reported velocity, as its step continues into Region II it cannot have completed decelerating the entire bar, making the new bulk velocity 76 m s^{-1} as labelled in Figure 6.5. Such steps in the middle of a wave pass are unlikely in a real experiment and are the consequence of our simulation parameters. However, in a real experiment the shallow regions are not perfectly flat, in which case the same argument holds, the bulk velocity will correspond to the highest point of the final step, as the sloped region has yet to pass through the entire bar.

Time shifting for the compressional waves can be performed more reliably in the case of striker reflections than reflections in the input bar in an SHPB, as the shifting takes place

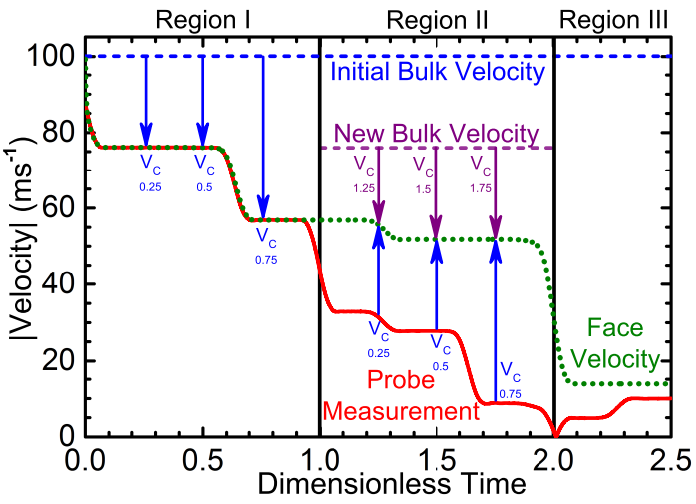

Fig. 6.5 A graph depicting the stages of the reflection correction procedure to convert the probe measurement (solid line) to the true striker sample face velocity (dotted line), outlined in the bulk text. At $\hat{t}$ =2 the striker bar velocity passes through zero and becomes negative, however it appears positive as PDV measurements are direction insensitive.

between parts of the same monotonically decreasing wave; any incorrect shifting produces obvious spikes in the recovered velocity.

As an aside, in the studies performed in later chapters, the strain rate is so high that the experimental duration is much shorter than the time required for the wave to return. This methodology mostly applies to the application of the DIHB to very high strains.

6.2.4 Sample Deformation Calculation

Once measurements have been made of the front, or striker impact face, V_{st}, and the back, or output bar face, V_{op}, the sample length as a function of time is determined by the difference between these two velocities

$$\frac{\partial l(t)}{\partial t} = v_{op} - v_{st} \ , \tag{6.7}$$

and

$$\varepsilon(t) = \ln\left(\frac{l(t)}{l(0)}\right) \ , \tag{6.8}$$

where compressive strains are considered positive. The stress history of the sample is measured as per a classic DIPB test, using the elastic relation

$$\sigma(t) = Z_{op}\frac{A_{op}}{A_{sa}(t)}\, v_{op}(t)\ , \tag{6.9}$$

where Z_{op} is the acoustic impedance of the output bar and A_{op} and A_{sa} are the cross sectional areas of the output bar and sample respectively. For fully solid samples the area is calculated using the approximation of constant volume during plastic deformation

$$l(t)A_{sa}(t) = l(0)A_{sa}(0). \tag{6.10}$$

6.2.5 Force Measurements and Equilibrium

The force at the output face can be found directly from the measured velocity

$$F_{op}(t) = Z_{op}\, A_{op}\, v_{op}(t)\ , \tag{6.11}$$

the same relationship holds true for the striker bar. However, the only velocity component due to the force from the sample is the compressive wave

$$F_{st}(t) = Z_{str}\, A_{str}\, v_{compressive}(t)\ . \tag{6.12}$$

These measurements allow force equilibrium analysis to be performed in exactly the same way as classic split bar tests. It should be noted that bars of equal acoustic impedance and area, a compressional velocity comparison is equivalent to a force comparison.

6.2.6 Experimental errors

We have already discussed the general sources of experimental error in Hopkinson bar apparatus in section 4.2. There are however two phenomena that are more complex in a

DIHB arrangement, Eulerian measurement errors and dispersion effects. Both of these were shown to be small for the Cavendish system.

Eulerian measurement errors and dispersion effects become more complicated because of the different nature of wave separation in the striker bar. Our correction procedure assumes that the probe does not move and that the waves returning are completely unaltered reflections. In reality the waves will disperse on their round trip and the travel distance between the two passes varies throughout the experiment.

Dealing with probe motion along the striker bar therefore requires a stepwise analysis of the waves in the bar, although the effects of probe motion were shown to be small in section 4.2.1.2, so this can often be neglected. A more complex issue arises in that the wave which passed the probe travelling to the free end of the bar may have undergone significant dispersion upon its return. Again, in a miniaturised system and given the short length of a typical striker bar, the effects of dispersion are likely small. As stated earlier; in the high strain rate studies of this thesis the time scale is sufficiently short that reflection and bulk velocity changes are not important.

At this point we should emphasise that the most significant benefit of PDV instrumentation in a DIHB is we can faithfully measure the interface behaviour of a specimen that has not yet reached force equilibrium. The benefits of this refinement to the technique are therefore likely to be large for slowly equilibrating materials such as polymers, and those which only equilibrate after key processes have already occurred, such as cell collapse in metallic foams.

6.3 Applications for Foams & Cellular Materials

The brief study presented in this section is based on work performed with Dr, C. Braithwaite and C. Gurnham in 2016 and T. Cowie in 2017.

In foams and cellular materials, collapse of the internal structure leads to the localisation of deformation [187] and alters local properties such as the mechanical impedance. Localised

processes affect the relationship between the forces on the sample faces in a way that is not only dependant on the sample, but is also time varying and dependant on the conditions and type of impact. Furthermore, the largely empty structure in metallic foams leads to a reduced force transmission along the sample that is not only much slower relative to the sound speed of the metal, but also more variable due to the large number of different paths through which the force can propagate.

The result is that throughout all deformation before full densification, the forces at the impacted and output faces are not related by any simple means. Thus, direct measurement of the impacted and output faces at the same time provides a strong basis for the verification of a mechanical model. In an SHPB system the dispersion oscillations along the input bar create oscillations in the input force measurement that obscure any of the more sensitive features in the input force. Meanwhile in a classic DIHB arrangement there is no measurement. Attempts have been made at replacing the measurement for a DIHB scenario, by firing the foam as a projectile into an output bar [188]. Firing the specimen only records the information from one face in any given test, and provides a different loading arrangement to the DIHB measurement used to provide the measurement of the output face, with a free face in the case of the foam projectile, and both faces in contact with bars in the DIHB.

Applying PDV to a striker bar allows the problem to be solved simply, as both sides can be measured simultaneously in one experiment, and the probes can be placed close enough to the faces of the specimen to reduce dispersion to negligible levels. Figure 6.6 shows an example of such an experiment. Disk samples of 5 mm thickness and 10 mm diameter of an aluminium foam were compressed in a Dural DIHB arrangement of of 12.5 mm diameter. The foam was open celled with an average cell size of approximately 130 μm. Figure 6.6 shows an example spectrum, noting that even the soft ($\approx$ 10 MPa) compaction region can be clearly resolved for the output bar. Figure 6.6 (b), shows a comparison of the force measurements for the impacted face and output face. The impacted face has the same

average force as the output face however also present are quasi-periodic spiked oscillations, that coincide with much smaller spikes at the same point on the output trace.

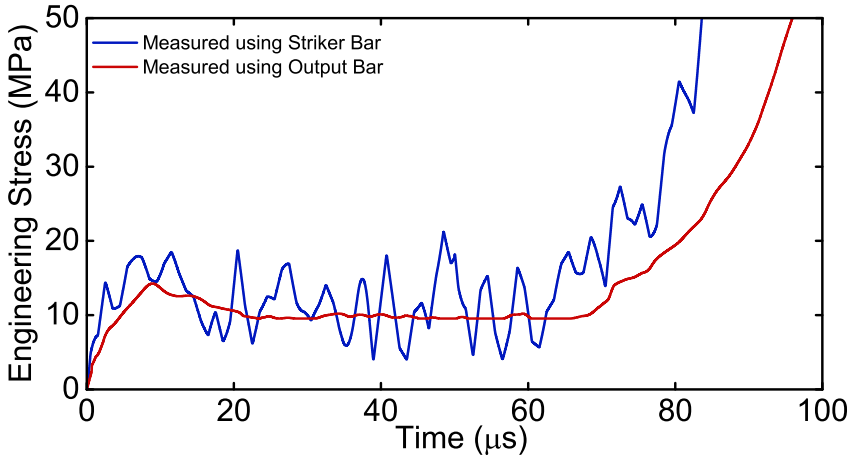

Fig. 6.6 The engineering stress measured at the input and output faces of a metallic foam specimen that was impacted at 32 m s^{-1}, undergoing deformation at an engineering strain rate of 6,400 s^{-1}.

These spikes are often seen in foam materials, and arise from the cell by cell failure being quasi-brittle in manner [189]. The spikes on the output trace have a periodicity (4 μs) which is a good match the average cell size over the striker velocity. It is plausible that the spikes seen on the input trace correspond to the engineering stress required to break cells, previously smeared by propagation through the foam or lost in Pochammer-Chree oscillations in the input bar of an SHPB. If the spikes are linked to cell collapse, they provide previously unavailable verification data for the mechanical modelling of foams.

6.4 Summary

In this chapter, we have presented a new method for directly measuring the velocities and forces at the impacted face of a specimen in a DIHB experiment. Analysis of the data was demonstrated including the recovery of the sample face trace in the presence of free end striker reflections. We expect the technique to be of wide applicability, potentially allowing

access to previously untested strain regimes. Potential was shown for the system to provide novel measurements of certain material types such as metallic foams.

Regarding the current study, the falling edge of the striker velocity will provide a measurement for the rise time of our experiment. Furthermore, the ability to extract the reaction force at the input face provides explicit verification of mechanical equilibrium. We therefore have an experimental scheme in which we are capable of providing confidence in our high rate, low strain experiments, the focus of the next two chapters.

Chapter 7

High Rate Structural Evolution

In the Chapter 5, the reversal of thermal softening, one of the most fundamental predictions of phonon viscosity models, was shown not to occur in uniaxial deformation for strain rates between 10^4 and 10^5 s^{-1}. In fact, specimens exhibited much greater thermal softening at high rates than expected by simple implementations of most existing theories. Such observations bring into question the relevance of phonon drag as the driving force behind the increase in rate sensitivity observed above 10^4 s^{-1}.

The retention of Arrhenius like behaviour above the sensitivity transition gives credence to the concept that the increase in sensitivity is not an instantaneous viscous effect, but rather a more permanent structural one. A transition in structural evolution could be responsible for creating a greater potential barrier to dislocation motion and thus the mechanical threshold. Increases in the mechanical threshold stress would then lead to the observed increases in thermal softening. Such behaviour would have to occur at the start of deformation, effectively acting as an increase in stage II work hardening.

Thus follows the aim of this chapter; to experimentally search for explicit evidence of enhanced structural evolution through its effects on work hardening. This will be achieved through experimental measurements designed to separate instantaneous (ϕ) and structural

(σ_p) effects. If such behaviour is found, a quantitative study of the relative contributions of instantaneous and structural effects can be performed.

7.1 Low Rate Path Dependence

We will briefly summarise relevant parts of chapter 2, in which the reader will find a more complete discussion.

The low rate expression for a specimens flow strength (outlined in section 2.1) is

$$\sigma_f(\dot{\varepsilon},T,H) = \sigma_0 + \phi(\dot{\varepsilon},T)\sigma_p(H), \tag{7.1}$$

Structural strengths are described through a 'plastic' or 'mechanical threshold stress' term, σ_p that encapsulates strength imparted by the loading history of the metal, considered to be some arbitrary function, H. Physically the term corresponds to the stress required to deform the material at 0 K [15]. Instantaneous effects of rate and temperature are gathered into a single scaling function, ϕ, that reduces the required stress below the mechanical threshold to account for thermal activation effects, and also introduces rate dependence.

In chapter 2, we noted the presence of several interpretations of path dependence. For the purpose of experimental design, we can describe the evolution of σ_p without making any assumptions of the underlying mechanisms using a Voce law [26]

$$\frac{\partial \sigma_p}{\partial \varepsilon_p} = \Theta(\dot{\varepsilon},T,\sigma_p) = \Theta_0 \left(1 - \frac{\sigma_p}{\eta}\right)^{\alpha_\eta} \tag{7.2}$$

outlined in more detail in section 2.2. The key components of this behaviour are the initial or 'Stage II' rate of work hardening, Θ_0 and the plateau stress, η. At low rates, Θ_0 is weakly dependent on rate [4, 15], and $\frac{\Theta_0}{G(T)}$ is weakly dependent temperature [64]. Low rate path dependence is imparted through variations in saturation effects and therefore, η.

7.2 Enhanced Structural Evolution at High Rates

The results of chapter 5 appear to be more consistent with a large increase in σ_p, especially at low strains. The presence of the strength increase at low strains would require a rapid, rate dependent increase in Θ_0 above 10^4 s^{-1}. If any rate dependence in Θ_0 is observed, underlying dependent process may involve thermal activation, leading to an onset of thermal dependence in Θ_0 above the transition. Potential mechanisms that could drive such a transition are outlined in section 3.2.2 and will be discussed in light of experimental data in Chapter 9.

Follansbee et al. [15] empirically observed what is interpreted as the onset of such a transition, their measurements are shown in Figure 7.1. The figure depicts the results of a set of experiments known as jump tests [9, 15] in which the specimens are loaded to 0.15 strain at a variety of strain rates between 10^{-4} to 10^4 s^{-1}, at which point the specimens were recovered and reloaded to yield at 10^{-3} s^{-1}. As we will show in section 7.3, if a set of specimens with different histories are reloaded at a fixed set of conditions, any variation in their yield stress corresponds to variations in σ_p and thus intermediate work hardening. A slow variation is seen in the reload strength between 10^{-4} and 10^3 s^{-1}, where a more rapid upturn begins. Unfortunately, no non-shock measurements are available above 10^4 s^{-1}, which is at or below the strength transition. All subsequent models that propose variations in Θ_0 do so based on this evidence, requiring unsound levels of extrapolation to be made. No experimental studies (to the authors knowledge) have been performed between 10^4 s^{-1} and the shock regime, in which the dislocation dynamics change substantially [33]. In order to establish or disprove that changes in work hardening are responsible for the strength transition, we require measurements that can remove uncertainties arising from potential changes in instantaneous effects above 10^4 s^{-1}.

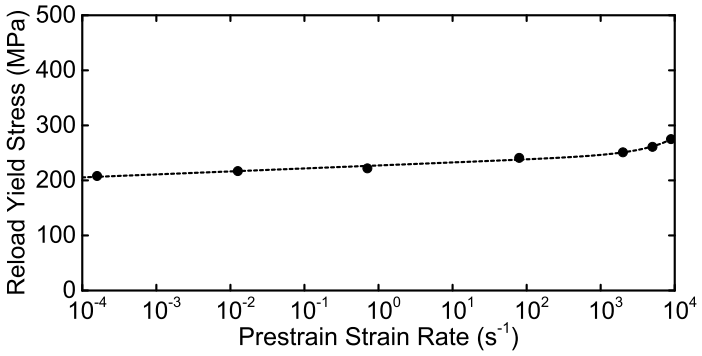

Fig. 7.1 The yield strength of a series of specimens deformed to a constant strain at varied initial rates. The vertical axes extend to zero to show the relative magnitude of the observed change. This image is created from the data of Follansbee et al [15]

7.3 Jump Tests

In order to simplify discussion of the current work, we will define two terms. The first is the 'particular condition' (PC), which corresponds to the rate and temperature that is varied throughout a set of experiments. For example, in Figure 7.1 the particular conditions for Follansbee's experiments were 300 K and rates varying between 10^{-4} and 10^{4} s^{-1}. The second term is the 'standard condition' (SC), which for the entirety of this thesis is 300 K and 10^{-2} s^{-1}. The standard condition is used to provide a fixed value of the instantaneous rate scalar, $\phi(300\text{ K},10^{-2}\text{s}^{-1}) = \phi_{SC}$. Fixing the value of the instantaneous rate scalar allows the comparison of structural contributions to strength in the absence of instantaneous effects.

A jump test is any deformation experiment involving a sudden (approximatable to instantaneous) change in any of the experimental conditions (in the present case, strain rate or temperature). The purpose of a test varies depending on the order of the conditions in the jump. As the aim of this study is to measure variations in structure, we will perform jumps from the particular condition to the standard condition after a fixed amount of strain is imparted. The strain at which the jump occurs will ideally be low to minimise the influence of saturation effects on the measurements. Compromises will have to be made with experimental limitations, discussed in chapter 4. The target interrupt strain chosen for this study was set at 0.1 this provides a measurement further from saturation than the study of by Follansbee et

al. for which the interrupt strain was 0.15, allowing the data to be discussed more clearly without analysis for saturative effects and providing important low strain data points for subsequent mathematical analysis.

After 0.1 true strain, the specimens will be reloaded to yield at the standard condition, at which the yield upon reload is at a stress of

$$\sigma_R(H) = \sigma_0 + \phi_{SC}\sigma_p(H) \tag{7.3}$$

in which all of the terms except $\sigma_p(H)$ are constant, thus variations in the yield upon reload directly reflect structural changes. Furthermore, the flow stress at the particular condition can be used to make empirical measurements of the scaling parameter,

$$\phi(\dot{\varepsilon},T) = \phi_{SC}\frac{\sigma_f(\dot{\varepsilon},T,H) - \sigma_0}{\sigma_R(SC,H) - \sigma_0}. \tag{7.4}$$

Grade C103 is known to have an athermal stress, $\sigma_0 \approx 50$ MPa [190]. Jumping from the particular condition to the standard condition therefore allows for direct extraction of $\phi_{SC}\sigma_p(H)$ and $\phi(\dot{\varepsilon},T)/\phi_{SC}$. In both cases the measurements retain some factor of ϕ_{SC}, an artefact of the arbitrary choice of standard condition. Determining the value of ϕ_{SC} requires the assumption of a particular model form and currently serves little purpose - we are searching for sudden changes in behaviour that will be unaffected by a constant prefactor.

The outlined set of jump tests, combined with expressions 7.3 and 7.4 provides a platform to separately test instantaneous and structural transitions which are typically inseparable in single condition tests. Doing so will allow determination of the relative contribution of each type of mechanism to the strength transition. What is now required is an experimental framework that can accomplish jumps in strain rate from 10^5 to 10^{-2} s^{-1}.

7.4 Arrested Strain Methods

The method used to perform loading at the particular condition will vary depending on strain rate. For rates below 10 s^{-1} a universal testing machine (Instron) will be used, described in Section 4.1. For rates up to 2×10^4 s^{-1} split bar arrangements (Section 4.2) and finally we will progress to the direct impact Hopkinson bar arrangement outlined in the previous chapter to achieve the novel 10^4-10^5 s^{-1} conditions with a fast rise time. At the SHPB to DIHB swap we will perform measurements in both geometries covering the region 10^4 s^{-1} to 2×10^4 s^{-1}, to check for consistency between the methods.

In bar experiments, interruption is performed using a 'strain limiting ring', shown in Figure 7.2. A piece of stronger material that is placed around the specimen and bears the deformation load when the has deformed to match its thickness, terminating the experiment. In previous Cavendish arrangements [191] strain limiting rings have been made from Duralmin alloy and had relatively thin walls, due to being used to interrupt lower rate polymer experiments. Expanding the system to high rate metal deformation requires a new approach to ring design.

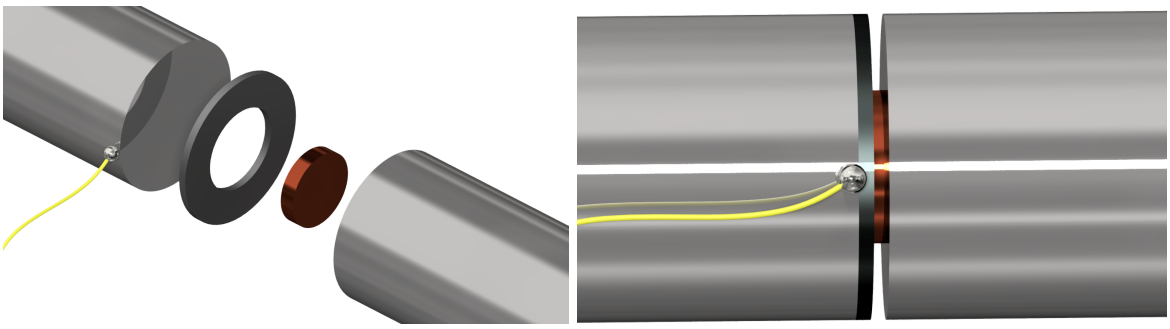

Fig. 7.2 The experimental arrangement for the split configuration. The ring is attatched to the output bar in both split and direct configurations.

Importantly we note that when bearing the load, the ring is liable to deform itself. In Instron experiments we can note an upturn in reaction force and terminate the experiment before any further strain is imparted. However, in Hopkinson bar experiments the experimental

duration is fixed (to within varying the length of the striker bar). Our aim is therefore to minimise the dynamic elastic deformation of the ring during the remaining loading, after the required strain is reached.

We must use a material that has high yield strength to prevent plastic flow, and high acoustic impedance, maximised through both high specific impedance and maximising ring area, to minimise elastic deformation. A combination of tungsten carbide and Densimet 176 alloy was used to make the rings, with tungsten carbide being used for rates above 3×10^4 s^{-1} and Densimet below (as the WC rings tend to shatter on release even in low rate experiments). The external diameter of the ring was matched to the loading system. The internal diameter was machined to be 1.15 that of the specimen starting diameter, maximising the area of the ring whilst allowing safe room for the predicted 5% radial expansion.

We can calculate the various outcomes for a given ring. Firstly, we should note that if the ring bears the entire load (which is an over estimation but beneficial for ensuring the system remains elastic), the stress originally spread throughout the entire bar area, A_{Bar}, becomes localised to the ring, area A_{Ring}. The localisation of force in the system magnifies the stress at the interface between the ring and the output bar to

$$\sigma_{Ring} = \sigma_{in}\frac{A_{Bar}}{A_{Ring}} = Z_{Bar}\frac{A_{Bar}}{A_{Ring}}v_{in} \tag{7.5}$$

where the pre-magnification stress is $V_{in}Z_{Bar}$ as no reflected wave will be present when strain has been interrupted. This expression gives a decreased maximum striker velocity if the system is to remain elastic,

$$v_{max} = \frac{2Y_{Bar}}{Z_{Bar}}\frac{A_{Ring}}{A_{Bar}}. \tag{7.6}$$

As the bar faces are not physically bound to the ring or specimen, the interfaces cannot support tension, therefore the reflection coefficient,

$$\frac{v_{ref}}{v_{in}} = \frac{A_{Bar}Z_{Bar} - A_{Ring}Z_{Ring}}{A_{Bar}Z_{Bar} + A_{Ring}Z_{Ring}} \tag{7.7}$$

remains fixed at zero in the scenario $A_{Ring}Z_{Ring} > A_{Bar}Z_{Bar}$. We therefore expect a fast interruption for the condition

$$A_{Ring} \geq A_{Bar}\frac{Z_{Bar}}{A_{Ring}} \tag{7.8}$$

given typical values for 350 maraging steel ($Z_{M350} \approx 40$ MRayls) and tungsten carbide ($Z_{WC} \approx 90$ MRayls), the ring area should be at least 45% of the bar area.

We showed in section 4.2 that the deformation rate of a specimen in force equilibrium can be calculated from the reflected pulse alone

$$\frac{\partial L(t)}{\partial t} = -2v_{ref} \tag{7.9}$$

in an SHPB system good interruption can be checked by the apparent disappearance of this wave. The true quality of interruption is measured using wave measurements in the bars and micrometre measurements of the specimens after interruption.

The most significant concern arises during experiments above 10^4 s^{-1}. As we established in the previous chapter, the shortest achieved rise time on input pulse of the miniaturised split bar system is 1 μs. At 0.1 true strain and 10^4 s^{-1} the total experimental time is 10 μs, making the rise time 10% of the overall experimental duration, by 10^5 s^{-1} the pulse rise time is equal to the experimental duration. The rise time of the input wave is important to our strain path, to make any simple statements about the data, we wish for the initial strain path to be a single set of conditions. We therefore need to set some minimum fraction of our experiment that must be spent at the target rate to allow us to approximate it as being a

single condition. For the purpose of the current work we attempt to make this 90% of the experiment.

We therefore need to bypass the limiting rise time from the input pulse. As discussed in the previous chapter this can be done by changing the impact geometry to a direct impact Hopkinson bar system. The rise time in a DIHB is not dependent on dispersion ramping of the input wave, but instead solely on the impedance mismatch at the bar sample interface. In metals, after yield this elastic behaviour is replaced with specimen equilibration in the next wave pass. Equivalently, the ramp up condition simply becomes the next wave pass after specimen yield. Given the sound speed of copper and specimen dimensions of 500 μm this corresponds to a time close to 0.1 μs. Therefore the minimum experimental duration before the rise time becomes significant is 1 μs and, above strain rates of 10^5 s^{-1}, the single loading path approximation requires experiments to be performed to strains greater than or equal to 0.1.

Idealised analytical expressions aid in planning such experiments, however they do not provide evidence that the required time scales have been achieved. We must therefore measure the ramp and equilibration times in each experiment. An example of an extracted striker trace for a 500 μm specimen and a tungsten carbide interrupting ring is shown in figure 7.3 (a) and the inferred wave component of the velocity is shown in (b). The yield point typically corresponds to the slight overshoot in the compression wave of the striker, that settles back as the plastic nature begins, the two 'force' traces have converged within two measurements of the peak of the overshoot, corresponding to approximately a 100 ns equilibration time, in line with the expected values.

Similarly it would appear that we can use the method to ensure that the interrupt is working as intended. At the end of the plastic region, corresponding to approximately 2 μs in figure 7.3 (a) we observe that the striker velocity rapidly drops over approximately 150 ns to half of its original velocity, meanwhile the output bar rises up to the same velocity, visible

in (b). The fact the two faces are travelling at the same velocity implies the specimen is no longer deforming, but instead undergoing translational motion with the system. Furthermore, the fact that the striker trace drops to approximately half of its initial value can be thought of as the interrupting ring bypassing the specimen and connecting the striker directly to the output bar, making the velocity profile behave as one would expect in a striker bar as it impacts the input bar of a split system.

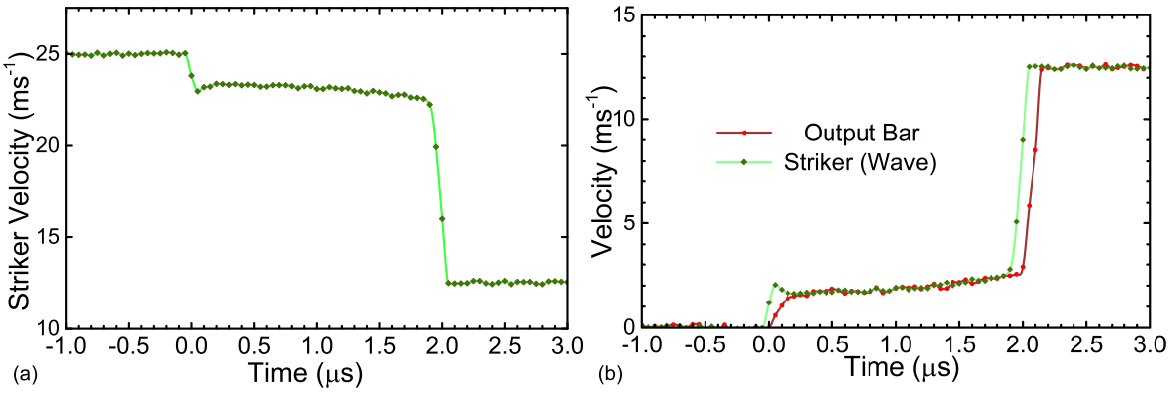

Fig. 7.3 (a) The striker velocity for a typical interrupted experiment. (b) The compressive wave velocity calculated in the striker bar compared to the velocity of the output wave, deformation equilibrium is reached approximately 100 ns after yield. The measurements are derived from PDV spectra collected at 2 GHz using a 1024 bin widths with a 7/8 overlap, meaning that the time between each data point is approximately 60 ns. The time step between each point is both close to the limit imposed by the finite laser spot size and the expected time scale of the ramp.

7.4.1 Measuring Stress and Strain

The core methods for both Instron and Bar loading are outlined in Chapter 4. However, in the case of the point of interrupt, several simplifications can be made that will serve to remove some experimental errors in particular condition measurements. For example, no deformation data is required at the particular condition to generate the strain at interrupt, it can be measured directly using a micrometre between the two conditions.

If we assume, as we already have in the standard Instron and bar analysis, that the elastic strain at yield is small, we can also assume that the change in area upon unloading is also

small. Given that we can accurately measure the area between the two experiments, using micrometre measurements or calculation from photographs, all we need to measure is the force at the point of interrupt, and yield on reload. Only requiring the force measurement reduces the influence of errors such as dispersion in high rate loading, and compliance in quasi static loading, both of which are likely to be much greater than the area change in elastic expansion.

If the subscript i denotes the value of a measurement at the point of interrupt, we note that plastic strain is found from

$$\varepsilon_{p,i} = \ln\left(\frac{L_0}{L_i}\right) \tag{7.10}$$

the particular condition flow stress is found from the output bar velocity, v_i, as

$$\sigma_f(PC) = Z_B \frac{A_B}{A_i} v_i, \tag{7.11}$$

and the standard condition yield is found from the Instron force at yield,

$$\sigma_f(SC) = \frac{F}{A_i}. \tag{7.12}$$

The yield in an Instron measurement, especially of a work hardened metal, is typically sharp, as shown in Figure 4.4, and thus can be extracted easily with low error. Measurements of the output velocity however are more complicated because, as seen in Figure 7.4, there is a rounding out as the strain limiter begins to transmit the applied load, caused by the superposition of the reaction forces from the specimen and the ring, both of which are deforming. To extract a consistent result, a correction scheme was developed, shown in Figure 7.4. The linear rise due to the interrupter was found as a function of time using regression and subtracted from the trace before interrupt to approximate the force transmitted by the specimen. The maximum measured velocity after this first order correction was

used as v_i. To ensure the accuracy of the extraction method, a number of non-interrupted experiments were performed and analysed as outlined in Chapter 4.

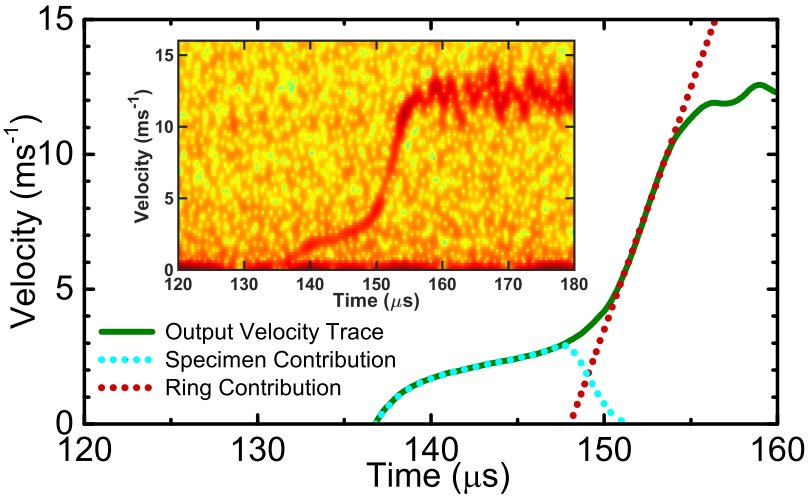

Fig. 7.4 An example of an output trace in a strain arrested experiment. The linear rise is due to the elastic deformation of the specimen as it begins to take up the deforming load. This region was fit to, providing a first order correction for the contribution of the ring to earlier parts of the output wave. This image was generated using titanium bars and a titanium interrupting ring from an early iteration of the experiments and is used as it shows clear rounding, for an example of a true experimental trace with a tungsten carbide interrupting ring see Figure 7.3.

7.5 Results & Discussion

7.5.1 Structural Strengthening

Figure 7.5 shows the processed measurements of both flow stress at interrupt for the particular condition and the yield stress at reload in the standard condition against both linear and logarithmic rate axes. It is instantly apparent that the characteristic upturn in flow strength at the particular condition is met by a similar upturn at the standard condition. Before even performing any analysis on functional forms, we can see qualitatively the proposal of Follansbee, that the upturn in flow strength above 10^4 s^{-1} is significantly structurally based, appears to be correct. Furthermore, as in the previous chapter, the observations are at odds with most phonon viscosity theories, that do not predict the increase in strength to be retained

at the standard condition. The inset of Figure 7.5 shows the flow and reload stresses against a linear axis. We note that by 8×10^4 s^{-1} the linear dependence typically referred to as viscous behaviour has ceased, the curves rise at a slower rate with increasing strain rate. The seeming plateau in reload strength may however arise from the time spent ramping up and down during deformation becoming increasingly significant at 10^5 s^{-1}.

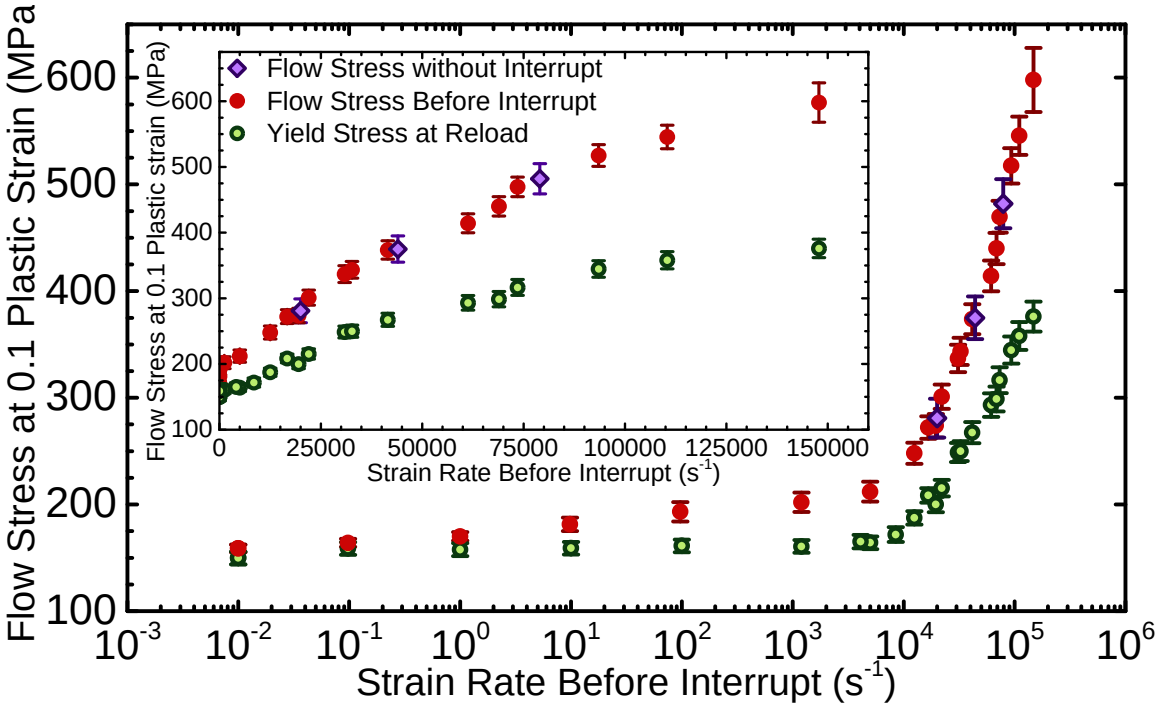

Fig. 7.5 Measurements of the flow stress at interrupt, and yield upon standard condition reload for a series of jump test specimens as a function of initial strain rate.

Observations of the reload stress at fixed strain allow us to draw important, but limited conclusions. It is clear that some form of structural evolution must play a large part in high rate behaviour, and that some change in structural evolution must occur at 10^4 s^{-1}. What is yet unknown is how to model the underlying mechanisms.

At this point several potential theories are available (outlined in more detail in section 3.2.2), however none can be applied with confidence. Follansbee e al. [15] proposed that the effect is due to the decreasing time available for slip in high rate deformation, as the time available is inversely proportional to strain rate. They argue the decreasing time causes

dislocations to spread out less from their source, increasing the forest density. We note however that this proposal is inconsistent with the use of Orowan's law [20],

$$\dot{\gamma} = b\rho_m \bar{v}, \tag{7.13}$$

in their model. As the drift velocity is proportional to strain rate and the time for slip inversely proportional, the two cancel out (as one would expect for fixed strain). Follansbee's mechanism can only work if Orowan's law breaks down.

If Orowan's law breaks down, we arrive the model of Armstrong [33], who argues that when dislocations reach some limiting velocity, any strain that is not imparted by moving dislocations (or damage effects such as creating voids or spall) must be imparted by creating more dislocations. Typically the limiting velocity of a dislocation is the speed of sound in the medium (Chapter 3), at which point one expects extremely viscous behaviour such as temperature inversion, as observed by Kanel [124] and Gurrutxaga-Lerma [125]. However some other criterion may decide the transition, such as the relative work required generate a certain amount of strain through either mechanism.

A third theory for changing structural evolution is the work of Huang [47], who proposes that phonons encourage increases in dislocation length when they scatter from moving dislocations. Scattering events give off energy in their locality and Huang proposed that it that excites the generation of dislocation length in the vicinity. This would increase the structural strength with increases in the drag coefficient (and thus temperature), making it difficult to reconcile with the observations of Chapter 5.

As a final observation, we will note that the structural strength is greatly increased at the highest rates, and this may drastically effect the level to which high rate specimens are affected by saturative effects. This is something that will need to be accounted for to gain a complete picture of the material's behaviour.

7.5.2 Instantaneous Strengthening

Having verified a large increase in structural strength, we will now turn our attention to variations in the instantaneous contributions, ϕ. Figure 7.6 presents two sets of measurements, the first depicts the results of processing the measurements using equation 7.4, and the second set where the same manipulation is performed on the measurements after the predicted inertial stress (outlined in section 4.2.4) has been subtracted from the particular condition data.

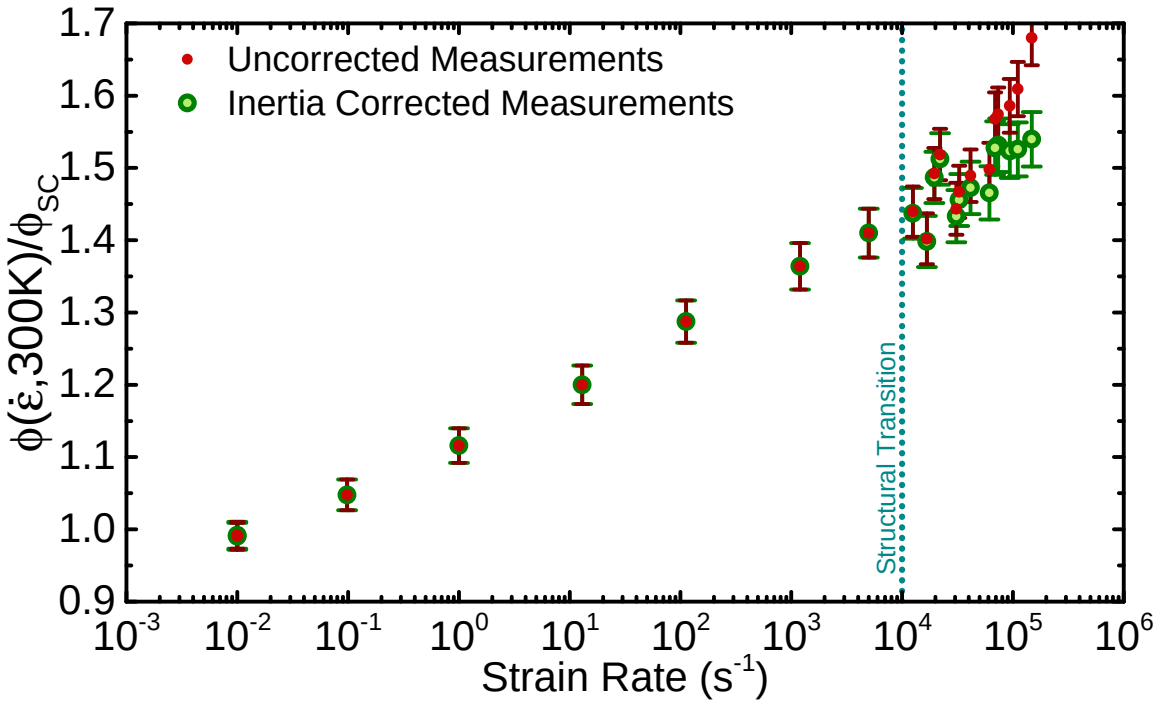

Fig. 7.6 The instantaneous rate scalar, to within the constant prefactor $1/\phi_{SC}$ calculated with and without corrections for inertia at the particular condition.

We note an up-turn is visible in the un-corrected data, however this occurs at 10^5 s^{-1} which is firstly significantly above the transition rate, and secondly when for the given sample size, inertial effects are likely to become significant. After a theoretical correction is applied to account for specimen inertia, the data returns to a consistent curve across the entire data set.

The apparent behaviour of the data would imply that whilst the material structure undergoes a change at 10^4 s^{-1}, the way in which the structural barriers are overcome remains unchanged.

Both sets of values can be reasonably fit to typical models for ϕ, for example, using the relation derived for the MTS model [14],

$$\frac{\phi(\dot{\varepsilon},T)}{\phi_{SC}} = \frac{1}{\phi_{SC}}\frac{G(T)}{G(0\text{ K})}\left\{1-\left[\frac{k_B T}{U_\phi G b^3}\ln\left(\frac{\dot{\varepsilon}_\phi}{\dot{\varepsilon}}\right)\right]^{2/3}\right\}^2 \tag{7.14}$$

$\dot{\varepsilon} \approx 10^7$ s^{-1} is defined as a constant in the model, leaving only U_ϕ and for our specific data set, ϕ_{SC} as unknowns. Regression was performed on both data sets to extract these parameters, the fit to the data is shown in Figure 7.7.

The parameter values extracted are shown in the table below, including the values obtained by Follansbee for OFHC copper [15]. The values of U_ϕ generated from direct measurements are significantly lower than those measured by Follansbee et al, implying given the form outlined in equation 7.14 that the observed rate sensitivity is greater than previously assumed. Using the extracted value of ϕ_{SC} we can reverse engineer the true change in σ_p during work hardening. Given that the initial yield of an undeformed specimen at the standard condition is 70 MPa (Chapter 4) we can approximate a value of $\Theta_0 \approx 1650$ MPa below the transition, if we assume no saturation has occurred making the value clearly an under-approximation. The extracted value of Θ_0 is low compared to that measured for OFHC copper by Follansbee et al [15], however it is greater than that measured for gilding copper by Gould and Goldthorpe [9]. The parameters clearly depend on the micro-structure and purity.

	No Correction	Inertia Correction	Follansbee [15]
U_ϕ	0.74 ± 0.02	0.80 ± 0.02	1.6
ϕ_{SC}	$0.552 \pm .01$	$0.535 \pm .002$	N/A

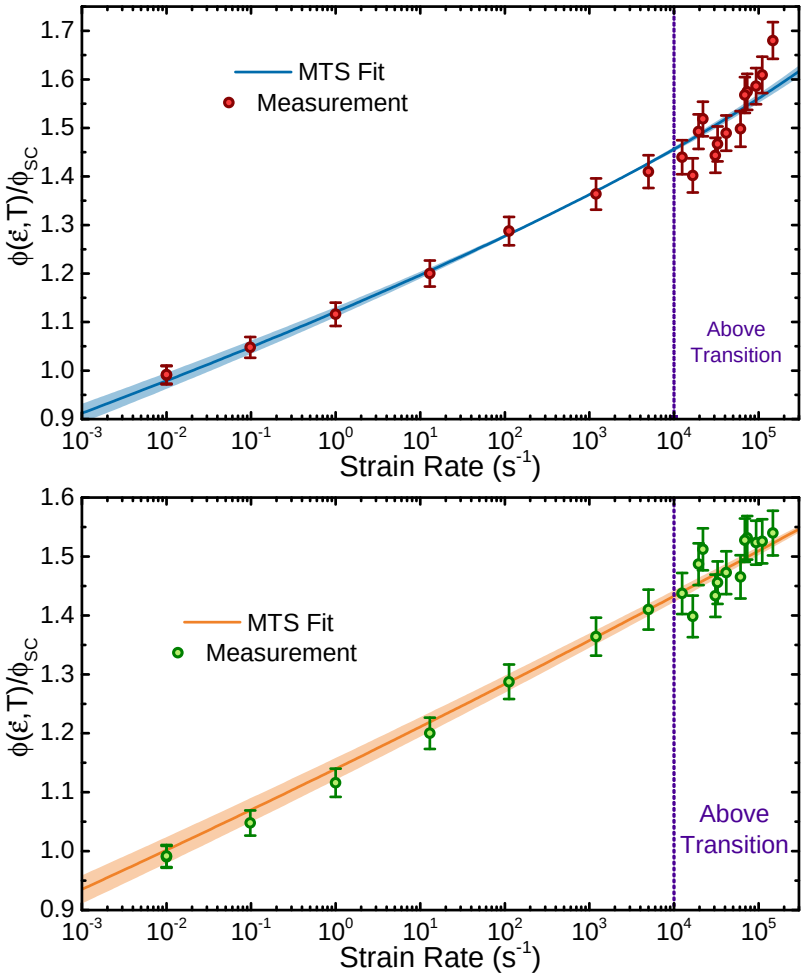

Fig. 7.7 Regression plots showing the optimal fit of the MTS form for ϕ to inertia the uncorrected (top) and corrected (bottom) data sets including the associated error regions.

If a power law approach is taken, $\frac{\phi}{\phi_{SC}}$ fitting finds an exponent phi to be proportional to $\dot{\varepsilon}^{0.026}$ at room temperature.

7.6 Summary

After the observations of the Chapter 5, there was a clear need to separate and individually consider the structural and instantaneous contributions to material strength. In this chapter we reviewed jump tests, an experimental scheme designed to separate the two effects, and detailed a way to use them to explicitly extract structural effects, and thus allowing for the subsequent analysis of instantaneous effects.

A substantial increase was found in the mechanical threshold at 0.1 strain for specimens deformed at rates above 10^4 s^{-1}. This phenomenon combined with the results of the previous chapter is not easily described by any current theories predicting a change in mechanical threshold. The yield stresses measured upon reload increased more slowly than the linear rate predicted by Follansbee [14] and more quickly than the square root relation predicted by Goto [98]. However, reload measurements include saturation effects, themselves dependent on the initial rate of work hardening. Saturation effects must be accounted for before more conclusive statements are made. Alternatively the slower than linear increase in reload yield may be due to the increasing significance of the rise time in the experiments at high rates.

Instantaneous effects appeared (after the approximate corrections for inertia) to remain consistent above the threshold, implying that whilst the structural barriers are changing, the (thermal) manner in which they are overcome is unchanged. Extracting approximate parameters by fitting the MTS model form for ϕ showed significantly different values of some of the key parameters, U_ϕ and the pre transition value of Θ_0, the former is likely due to the different microstructure and composition of the OF copper compared to OFHC copper, meanwhile the variation in Θ_0 is likely to be a combination of composition and the fact that it was obtained from a two point measurement.

To better investigate the change in work hardening, allowing the groundwork to form a good physical understanding of the mechanisms involved, we will now study the interaction of enhanced work hardening with both temperature and saturation.

Chapter 8

Thermal Effects & Saturation in High Rate Structural Evolution

The results of the empirical studies presented in previous chapters have led to a reasonably clear picture in which the increase in FCC metal strength above 10^4 s^{-1} is driven by a change in the nature of work hardening. The picture is however incomplete, with two main outstanding questions; what is the physical mechanism behind the change, and how does the increase in work hardening interact with saturation effects? The former of these questions will not be solved with experimental data alone, we shall discuss a potential mechanism in the next chapter. However, studying the interaction between the observed increase in work hardening and saturation effects provides a good avenue for a final set of empirical work. Notably, saturation effects, having relatively strong temperature dependence, would appear to be the prime candidate for explaining the abnormal increase in thermal softening observed in Chapter 5.

In this chapter, we will combine the methodologies of the previous two chapters, performing jump tests which will now include temperature variation at the particular condition. Furthermore, the jump strain will be varied in an attempt to understand saturation mechanisms above the strength transition. These experiments will also serve to provide

a comprehensive data set encompassing separated variations in strain, strain rate and temperature in the $10^4 - 10^5$ s^{-1} range. We will use the data obtained to provide a more robust parameterisation of the mechanical threshold stress model [14] for high purity copper.

8.1 Enhanced Work Hardening and Saturation

Taylor and Voce models for work hardening present different pictures of the interaction between early stage work hardening and the saturation strength, η. We will begin with the Taylor picture, for simplicity only working in one slip system;

$$\sigma_p = \alpha_T bMG(0)\sqrt{\rho}\ . \tag{8.1}$$

As outlined in Chapter 2 the evolution of strength is then defined by the evolution of dislocation density;

$$\frac{\partial \sigma_p}{\partial \varepsilon_p} = \frac{\alpha_T bMG(0)}{2\sqrt{\rho}} \frac{\partial \rho}{\partial \varepsilon_p}. \tag{8.2}$$

Furthermore, dislocation evolution can be split into generation and annihilation terms,

$$\frac{\partial \rho}{\partial \varepsilon_p} = \frac{\partial \rho_+}{\partial \varepsilon_p} - \frac{\partial \rho_-}{\partial \varepsilon_p}. \tag{8.3}$$

At low mechanical threshold, too few dislocations exist to annihilate at any rate meaningfully close to their athermal generation. Therefore, we can state a relation between the initial rate of work hardening, Θ_0 and the generation term;

$$\frac{\partial \rho_+}{\partial \varepsilon_p} \propto \Theta_0 \sqrt{\rho}. \tag{8.4}$$

As we observed in the previous chapter, a rapid increase in Θ_0 must occur above 10^4 s^{-1}. In the Taylor picture, this corresponds directly to an increase in dislocation generation. There is however, no evidence suggesting annihilation processes will undergo any significant

change. If only generation undergoes a dramatic increase, the equilibrium dislocation density will also be expected to abruptly increase above 10^4 s^{-1}, and in turn so should the saturation stress, η.

A different prediction is made by the Voce form. Again, to illustrate we will recall the form obtained by Brown [4] arising from the exhaustion of avalanche sources;

$$\frac{\partial \sigma_p}{\partial \varepsilon_p} = \Theta_0 \left(1 - \frac{\sigma_p}{\eta}\right)^2. \tag{8.5}$$

The Voce form saturates at η regardless of the value of Θ_0. Instead of predicting a change in the behaviour of η, the Voce form simply predicts that the system more quickly approaches saturation.

We can study these two predictions in the same manner as we did for ϕ in the previous chapter. We sample above the transition for the variations in the plateau, and see if they are consistent with the values below.

8.2 Dislocation Generation Through Phonon Scattering

Before we begin to study saturation itself, we will first address one of the outlying theories discussed in Chapter 7. Huang *et al.* [47] proposed a model (outlined in Section 3.2.2.2) in which dislocation generation is enhanced by phonon scattering, arguing that the dissipation of energy during scattering may create new dislocations in the neighbourhood of the scattering event. The model therefore predicts that phonon drag not only effects the instantaneous strength, but would also increase the (permanent) reload strength. They propose the dislocation generation rate to become

$$\frac{\partial \rho_+}{\partial \gamma_p} \propto \alpha_T G(T) b \sqrt{\rho} + \left[B^0_{wind} + \frac{B^0_{flutter}}{1 - [\dot{\gamma}/(b\rho_m C_t)]^2} \right] \frac{T}{\theta_D} \frac{M\dot{\varepsilon}}{b^2 \rho_m}. \tag{8.6}$$

Where the second term in the sum is proposed to account for phonons increasing dislocation generation. Huang's theory may remain consistent with the thermal softening seen in Chapter 5. If drag effects are mostly exhibited through changes in the mechanical threshold stress, shown to be the dominant in Chapter 7, then the system may still thermally soften as the mechanical threshold stress increases, maintaining a structurally limited regime. The best way to test such a mechanism can be seen in equation 8.6. The first term decreases slowly with temperature (due to the shear modulus), however the second term has a more rapid linear temperature dependence. If the two terms are comparable in size, that would be expected somewhere between $10^4 - 10^5$ s^{-1}, then the term would be expected to undergo a net increase with increasing temperature. We assume here that the material is not close to the melting point of the metal, where the temperature sensitivity of the shear modulus changes more rapidly. The simplest way to test Huang's form is similar to the tests performed in Chapter 5, we perform jump tests with range of temperatures during particular condition and then examine the temperature ordering of the reload stresses at the standard condition. If phonon viscosity is causing the generation of dislocations adjacent to scattering events, we will see raised temperature experiments undergo greater rates of early stage work hardening.

8.3 Methods

The methods used in this Chapter have been given in detail on a system level in Chapter 4, with respect to temperature variation in Chapter 5, and strain limitation in Chapter 7. In this chapter we will combine the methodologies. Particular condition to standard condition jumps will again be performed, however the particular condition will now include varying temperatures, and the strain at which interruption is performed.

With increasing interruption strains, the stress magnification effects at the limiting ring will become more severe, as the area of the ring must decrease to accommodate radial expansion of the specimen. As approximated in Chapter 7, the limiting velocity of an

experiment is

$$v_{max} \approx 2\frac{Y_{Bar}}{Z_{Bar}}\frac{A_{Ring}}{A_{Bar}}. \tag{8.7}$$

Given that the area of a specimen increases with strain as

$$A_{Sample} = A_0 e^{\varepsilon_p}, \tag{8.8}$$

we can express our limiting velocity (given the extra 5% radius put into all inner ring diameters to prevent the ring and specimen interacting) as

$$v_{max} \approx 2\frac{Y_{Bar}}{Z_{Bar}}\frac{A_{Bar} - 1.1A_{sample}e^{\varepsilon_p}}{A_{Bar}}. \tag{8.9}$$

Given that the specimens have a fixed initial area and the elastic constants of 350 Maraging steel and Inconel 718 are known, we can calculate a safe limiting velocity, and then a safe maximum rate as $\dot{\varepsilon}_{max} \approx \frac{v_{max}}{l_{sample}}$. The values from these calculations are shown in Figure 8.1, that shows the maximum recommended strain rate for a given strain and thus given ring dimensions. Increasing the interruption strain rapidly decreases the maximum

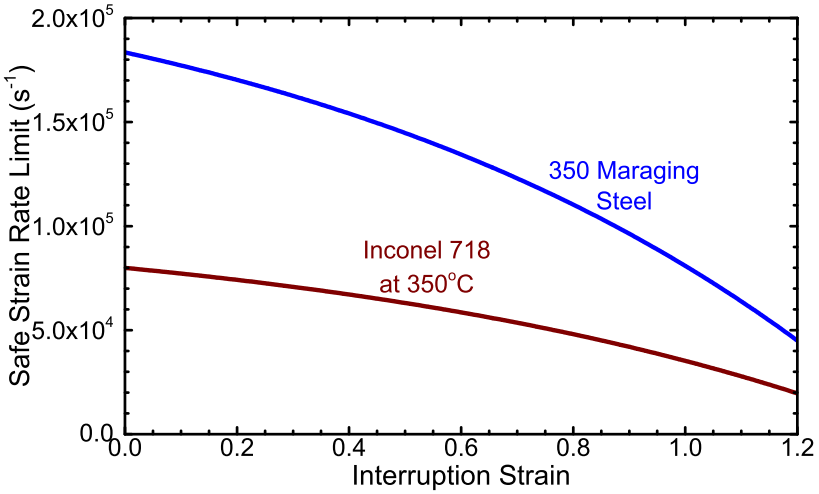

Fig. 8.1 The absolute upper limit in strain rate achievable for a the experimental system given the dimensions used in these studies. Note that typically the impact velocity and thus strain rate should be about 80% of these values to ensure the system remains undamaged.

achievable velocity, and by approximately unit strain we find the practical limit to be approximately 5×10^4 s^{-1}, hence the use of said rate in earlier discussion. For raised temperature experiments, the maximum strain rate falls even lower, limited to approximately 2×10^4 s^{-1}. This rate is close to the transition, and thus the inferences made from varying temperature measurements may be limited.

A second effect arising due to strain variation is friction. Previously all specimens were of fixed aspect ratio at interrupt and were only deformed to a small degree (sometimes referred to upsetting). Now that strain will be varied, we must account for variations in friction due to varying , using the expression;

$$\sigma_f = \frac{\sigma_{measured}}{1 + \mu \frac{2r(\varepsilon)}{3l(\varepsilon)}}. \tag{8.10}$$

Where $\mu = 0.08 \pm 0.01$ is the coefficient of friction for the reload system, which was determined in Chapter 4

8.3.1 Direct Impact at Elevated Temperatures

In experiments where $\frac{\varepsilon}{\dot{\varepsilon}} \geq 10\mu$s, the SHPB rise time is sufficiently fast to ensure that 90% of the experiment is at the required rate. In this scenario the split system was used as the inability to use adhesive lubricants at high temperatures made the approach most practical. However, for low strain or very high rate data, where $\frac{\varepsilon}{\dot{\varepsilon}} < 10\mu$s, a direct impact arrangement was used. Due to the lack of high temperature lubricants, the specimen was held in place using a low density polymer foam, placed between the specimen and the arresting ring. No changes were observed in the radial expansion of the recovered specimen due to the presence of the foam.

8.4 Results

8.4.1 Temperature Dependence in Early Stage Work Hardening

Firstly, we shall test the predictions of Huang *et al.* [47], as discussed in sections 3.2.2.2 and 8.2. We have established that a core prediction of this model is an increase in early stage work hardening with temperature, that itself becomes more prominent with rate. Figure 8.2 presents the results of a series of jump tests to 10% strain, where the particular condition has variations in both rate and temperature. Throughout the data set, the reload stress increases with rate for any given temperature and decreases with temperature at any given rate. There is no apparent convergence or crossing of the high and low temperature curves signalling an apparent onset of reversing thermal behaviour. It is unlikely that dislocation generation is enhanced by phonon drag mechanisms at the studied rates and temperatures.

There are two possible interpretations of the data shown in Figure 8.2, firstly the increase in work hardening may be due to the freezing out of some thermal mechanism, and thus decreasing the temperature shifts the transition point to higher rates. The second possibility is the scenario observed below the transition; the increase in temperature is lowering the

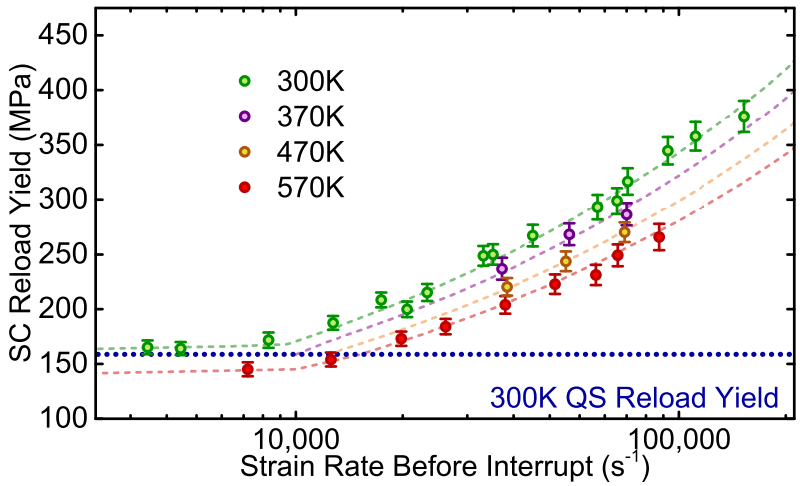

Fig. 8.2 The reload yield at standard condition after 10% true strain at a variety of rates and temperatures. The dashed lines are to guide the eye.

rate of work hardening through saturation. Such an affect is almost certainly why the specimen below the transition at 7×10^3 s^{-1} at 570 K is slightly softer than a quasi-statically deformed specimen at 300 K. As it is below the transition, the strength is purely dependent on saturation.

Saturation may be the mechanism separating the curves, and with increasing rates of work hardening, it will become much more significant at low strains with increasing rate. We therefore need to study this effect to ensure we properly account for the effects of saturation in reload data such as presented in the previous chapter, and in deformation at general strains. We will therefore perform a brief empirical study to attempt to confine the currently unknown level of saturation that is occurring.

8.4.2 Quantifying Saturation Effects

In order to obtain useful quantitative measurements of early stage work hardening, we must account for saturation effects. Accounting for saturation is complicated by the controversial nature of structural evolution, as discussed in Chapter 2. There are two very different approaches to modelling structural evolution; combining the Taylor model with dislocation density models, and avalanche plasticity models, both discussed in Chapter 2, with the relevant forms reiterated in section 8.1.

The two theories have an important distinction that may be used to determine which provides a better approach to model saturation. Dislocation density theories predict an increase in early work hardening through an increase in dislocation generation. The increase in generation then predicts a relatively sharp increase in the plateau stress above the transition, as the equilibrium dislocation density is disturbed. Avalanche theories, specifically those outlined for 3D elastic inclusions discussed by Brown [4], explain saturation as exhaustion rather than equilibrium. Such theories predict that η will be largely independent of Θ_0, and thus will behave consistently across the transition.

As stated earlier, we will employ the same approach as used for ϕ in the previous chapter; we will attempt to characterise the trend in η above the transition, and see if the behaviour is consistent with that below the transition. The standard condition reload measurements for a variety of particular conditions and strains are shown in figure 8.3, along with a single condition curve entirely at the specific condition. Being the most readily applied form, we will extract both the saturation stress, η and the initial rate of work hardening, Θ_0 using Brown's version of the Voce law, equation 8.5.

Given the low strain sampling of our measurements, in order to compare to the reload data we must integrate equation 8.5, which has been performed by Gould [9];

$$\sigma_p = \eta \left\{ 1 - \left[\Theta_0 \frac{\varepsilon_p}{\eta} + \left(1 - \frac{\Sigma}{\eta} \right)^{-1} \right]^{-1} \right\} \tag{8.11}$$

where Σ is the value of the mechanical threshold stress at the start of the experiment and can be inferred from measurements Chapters 4 ($\phi_{SC}\Sigma \approx 15$ MPa) and 7 ($\phi_{SC} \approx 0.54$). Using

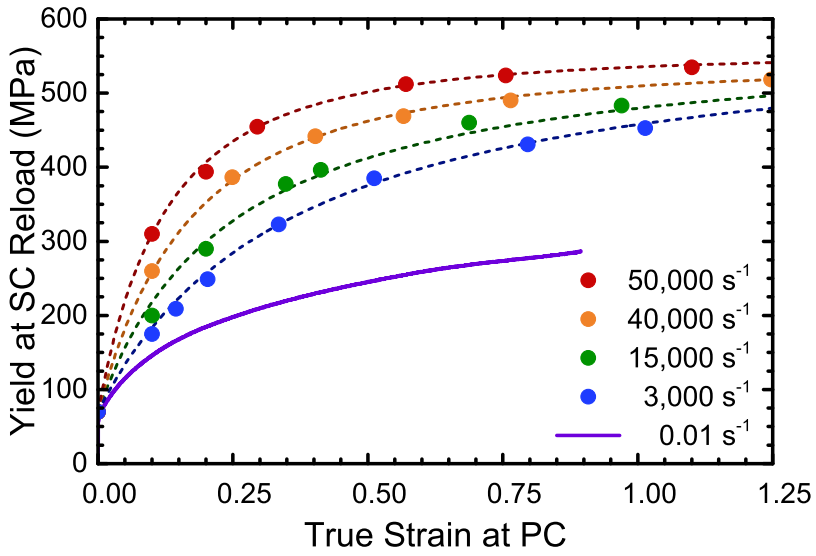

Fig. 8.3 The reload yield stress of specimens deformed to varying strains at a variety of strain rates, after a theoretical correction (equation 8.9) has been applied for friction. A single condition curve is included at the particular condition to show the plateau at that rate. The dashed lines correspond to an optimal fit to the form $\sigma_0 + \phi_{SC}\sigma_p$ where σ_p is defined by equation 8.11.

this form and the relation $\sigma_R = \sigma_0 + \phi_{SC}\sigma_p$, values of Θ_0 and η were extracted by numerical fitting to the data set. The integral assumes the plateau stress remains constant. A more accurate approach, if the variation in η was already known would be to perform stepwise calculations of all model components.

The extracted values of Θ_0 are depicted in Figure 8.4 (a), along with the values of Θ_0 that would be obtained from the reload measurements of Chapter 7 under the assumption that no saturation has occurred. These highlight the importance of saturation effects even at low strains. It is clear that saturation acts to a significant degree even in low rate specimens,

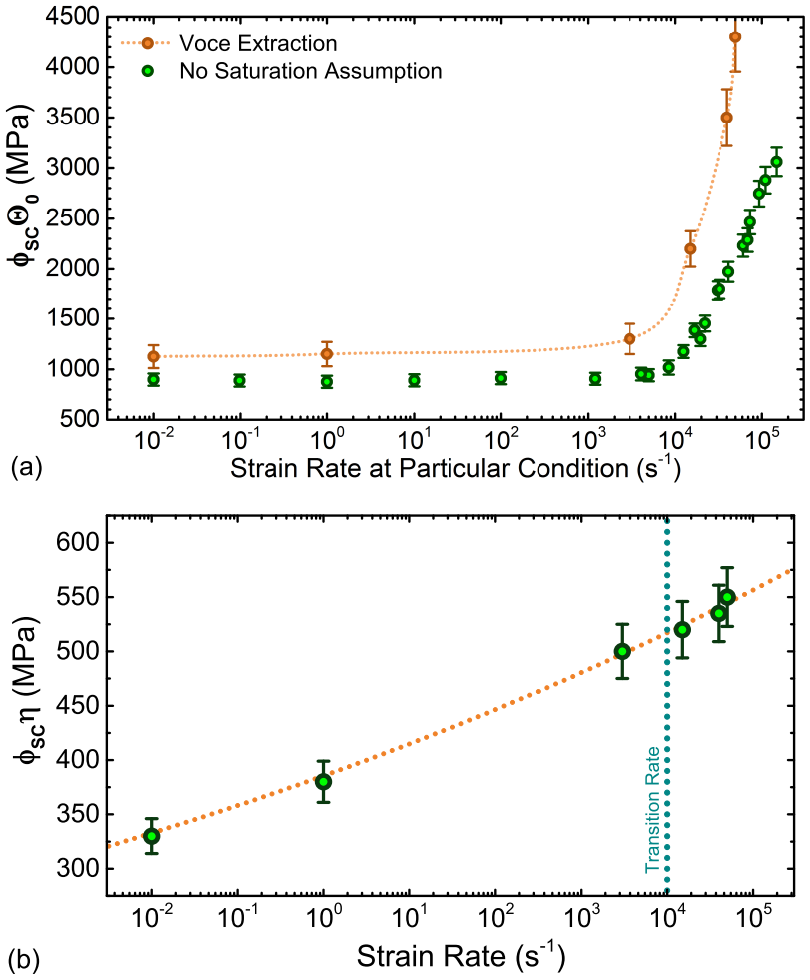

Fig. 8.4 The extracted values of (a) Θ_0 from full Voce fitting compared to those that would be generated from the measurements in Chapter 7 under the assumption no saturation occurs, (b) η extracted from full Voce fitting. In both images the orange dotted line is to guide the eye.

however above the transition the effects of saturation become even more severe. The reload stress at fixed strain becomes less representative of changes in Θ_0. The change reflects saturation naturally being a function of σ_p rather than strain ε. Figure 8.4 (b) shows the extracted values of the plateau stress as a function of rate above and below the transition. Much like the behaviour of ϕ, η appears to behave relatively consistently across the transition. These measurements were sadly limited by the quantity of material available.

Given the significant effect of saturation on work hardening, even at 0.1 true strain, it seems likely that the decrease in threshold strength seen in Figure 8.2 is likely due to the decrease in saturation strength. The simplest way to determine this would be to compare the predictions of equation 8.11 with completely parameterised functions of η and Θ_0 to the data set. To provide a better parametrisation and understanding of η, we will now attempt a brief study of the temperature dependence of saturation.

8.4.3 Temperature Effects in Saturation

There is a major assumption in the previous sections that should be addressed; the adiabatic deformation of the specimens will lead to temperature increases during deformation . Furthermore, different specimen strengths will lead to different temperature rises. In this section we will attempt to approximate the variations in the plateau stress with both temperature and strain rate by direct measurement rather than Voce fitting, given that varying strain will also correspond to varying temperature. The data set produced will then be capable of completely parametrising forms for η above the transition.

A series of specimens were deformed to 1.25 strain at varying initial temperatures. They were then reloaded to form an estimate of the plateau stress as a function of both initial and inferred final temperature. Figure 8.5 (a) shows estimated plateau stresses at the standard condition for the range of rates as a function of initial temperatures. Figure 8.5 (b) shows the data mapped to the approximate temperature at saturation by accounting for the work

done [23, 29]

$$\Delta T \approx \frac{0.9}{\rho_M c_p} \int_0^{\varepsilon} \sigma_f \, d\varepsilon. \tag{8.12}$$

Where ρ_M is the mass density of the material and c_p is the heat capacity at constant pressure. c_p is treated as a constant as the order of variation in the parameter is approximately 1% per 10 GPa [192], and therefore in our experimental range will undergo fractional changes of the order of 10^{-4}. In the temperature corrected data we see the plateau stress variation with temperature can be considered approximately linear and the curves appear close to parallel in the regime tested. Approximating the variation in this range as linear we see a decrease of approximately 0.65 MPa K^{-1}, the saturation point clearly decreases significantly with temperature.

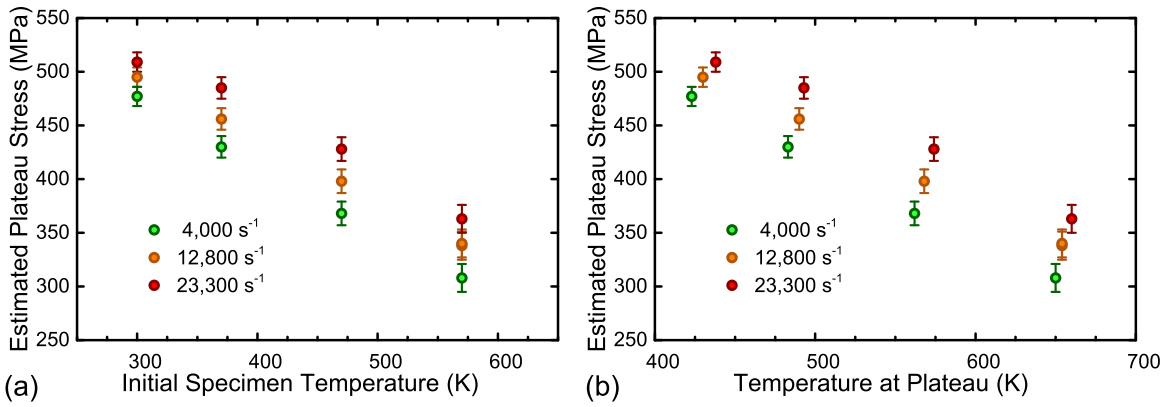

Fig. 8.5 The plateau stress estimated from Voce fitting to standard condition reload data for a variety of rates as a function of (a) the specimen temperature at the start of deformation and (b) the estimated specimen temperature at the plateau.

Whilst we cannot directly account for adiabatic temperature variations in our experiments, data such as that shown in 8.5 (b), combined with the right choice of physical model, can allow corrections for such effects during intermediate modelling. As the saturation stress would appear to be unaffected by any enhanced levels of dislocation generation, we will apply a density insensitive thermal recovery model, of the kind employed by Follansbee *et*

al. [15] and Gould [9];

$$\eta = \eta_0 \left(\frac{\dot{\varepsilon}}{\dot{\varepsilon}_\eta} \right)^{\frac{k_B T}{G(T) b^3 U_\eta}}, \tag{8.13}$$

which is a semi-empirical relation describing the general thermal climb of any given barrier to recovery. As with thermal remobilisation models, $\dot{\varepsilon}_\eta$ is some reference rate and U_η describes the thermal barrier normalised to $G(t)b^3$. The relation can be manipulated for linear regression against experimental data;

$$\ln \eta = \ln \eta_0 + \frac{k_B T}{G(T) b^3 U_\eta} \left(\ln \dot{\varepsilon} - \ln \dot{\varepsilon}_\eta \right). \tag{8.14}$$

The linearised form allows temperature regression in $\ln(\phi_{SC}\eta)$ to find $\phi_{SC}\eta_0$ and further regression of the extracted gradients against $\ln \dot{\varepsilon}$ to find $\dot{\varepsilon}_\eta$ and U_η. The extracted parameters are shown in the table 8.1. The saturation stress at 0 K, η_0, and the reference rate, $\dot{\varepsilon}_\eta$, appear to be consistent with measurements on OFHC copper by Follansbee *et al.*, and lower than the values for gilding copper as measured by Gould [9].

	η_0 (MPa)	$\dot{\varepsilon}_\eta$ $\left(\mathrm{s}^{-1}\right)$	U_η
This study	900±30	$1.00 \pm 0.13 \times 10^{11}$	0.206 ± 0.006
Follansbee *et al.* [15]	900	6.2×10^{10}	0.312
Gould [9]	1475	2.4×10^{11}	0.344

Table 8.1 *The extracted parameters for the saturation stress combined with two prior literature studies.*

Finally, U_η appears to be lower than the measurements of both prior studies. In the previous chapter the normalised activation parameter, U_ϕ, was also measured to be smaller than that measured by Follansbee *et al.* U_η again represents a normalised activation volume, with both terms taking the same place in their respective relations. U_η is however much closer to previously measured values than U_ϕ. terms were. Potentially, the variations may be due to some structural or chemical variation, affecting both barriers to similar levels, arising

for example from the different purities of the two coppers. The values do however remain within the same order of magnitude. The reduced value of both normalised barrier parameters implies greater rate sensitivity in the material. Another explanation for the result may simply be that the measurements of this study were purely empirical, reload measurements, whereas the measurements of Follansbee *et al.* used their assumed forms for Θ_0 and ϕ (Chapter 3) to assume values of the mechanical threshold.

8.4.4 Instantaneous Temperature Effects

The majority of the current and previous chapters, being studies of work hardening, have focused on the mechanical threshold. However, the data accumulated, now at varying strains and temperatures, provides an opportunity to compare to models for instantaneous strengthening. Therefore as a final study, we will compare our data to the predicted trend in the mechanical threshold stress model [14] form for $\phi(\dot{\varepsilon},T)$;

$$\frac{\phi(\dot{\varepsilon},T)}{\phi_{SC}} = \frac{1}{\phi_{SC}}\frac{G(T)}{G(0\mathrm{K})}\left\{1-\left[\frac{k_B T}{U_\phi G b^3}\ln\left(\frac{\dot{\varepsilon}_\phi}{\dot{\varepsilon}}\right)\right]^{2/3}\right\}^2. \tag{8.15}$$

A key feature we could not test in the previous chapter, and is present in all Arrhenius based models, is that after corrections for variations in the shear modulus with temperature, instantaneous strengthening is predicted to be some function of the single argument $\frac{T}{G(T)}\ln\left(\frac{\dot{\varepsilon}_\phi}{\dot{\varepsilon}}\right)$. Variations in the shear modulus will be calculated based on the measurements of Nadal and Poac [193].

As outlined in Chapter 7, it is possible to separate the instantaneous contributions from structural ones, including saturation;

$$\frac{\phi(\dot{\varepsilon},T)}{\phi_{SC}} = \frac{\sigma_f(\dot{\varepsilon},T)-\sigma_0}{\sigma_R(\dot{\varepsilon},T)-\sigma_0}. \tag{8.16}$$

For varying temperature data however, we must account for variations of the shear modulus.

Jump tests presented earlier in this Chapter already contain information on temperature effects, we now simply need to extract them. Due to adiabatic deformation, the specimens presented in Figure 8.3 increase by as much as 170 K whilst at the particular condition. The data set simultaneously provides measurements of $\frac{\phi}{\phi_{SC}}$ for a variety of rates, temperatures and strains (that are assumed not to effect ϕ, behaviour which should also be tested).

We can therefore calculate the value of ϕ by comparing the flow stress before interrupt and the reload stress at the standard condition, using expression 8.16. The rate is already known, so the only unknown left to constrain is the temperature, which we can calculate using the mechanical work of deformation, previously outlined in equation 8.12.

Figure 8.6 (a) shows the ratio of the flow and reload stresses, and therefore contains the combined effects of the Arhennius like effects, but also further softening due to variations in the shear modulus. Generally, the higher rate specimens are stronger and the rate of thermal softening appears to increase with temperature, but little more is obvious.

After the shear modulus is accounted for, the data is plotted as a function of the proposed single argument, $\frac{T}{G(T)} \ln\left(\frac{\dot{\varepsilon}_\phi}{\dot{\varepsilon}}\right)$, in figure 8.6 (b). Also plotted is the curve the curve predicted by the fitting to room temperature measurements that were performed in Chapter 7. The data appears to collapse reasonably well onto the single curve, however some of the highest strain measurements for each curve deviate from the fit, most easily seen towards the right of the graph. The same observation was made by Follansbee *et al.* even below the transition. The discrepancy was attributed to a changing of the dislocation structure during work hardening decreasing the normalised activation parameter U_ϕ. Interestingly from their more expansive study, it would appear that U_ϕ was approximately inversely proportional to σ_p. Better understanding this variation would appear to be an immediate avenue for further theoretical and experimental work.

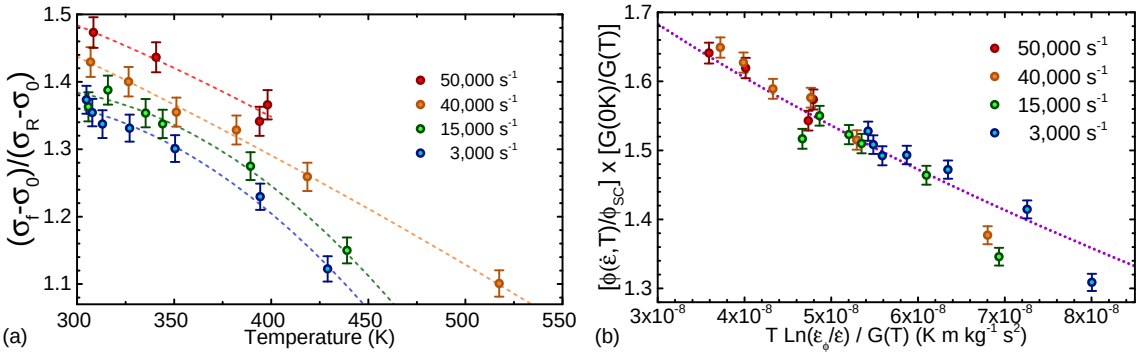

Fig. 8.6 (a) The measurements extracted from calculating the temperature change occurring in the experiments depicted in Figure 8.3, the dashed lines are to guide the eye. (b) The processed data for comparison to the form of 8.15, where the dotted line corresponds to the curve predicted by the measurements in Chapter 7.

8.5 Summary

In this Chapter, methodologies for temperature variation and strain arresting were combined within limits dictated by bar material yield. In doing so the effects of temperature and saturation were studied independently by once again separating instantaneous and structural factors, which has not, to the authors knowledge, been accomplished in the $10^4 - 10^5$ s^{-1} range before.

Saturation was found to behave consistently across the transition, bringing into question either the nature of enhanced work hardening as an increase in dislocation generation or saturation models that mimic the kinetics of chemical reactions. The behaviour of η remains similar to that described by an exhaustive or dislocation density insensitive recovery mechanism. Density based models may be made consistent with the results, but would require the introduction of extra mechanisms to do so.

After accounting for a Voce like saturation, the extracted values of $\Theta_0(\dot{\varepsilon})$ were found to be significantly larger than those that would be extracted from the measurements performed in Chapter 7 assuming negligible saturation. The sum of the previous two chapters leads to arguably the most important observation of the current study; not only does work hardening rapidly increase above the transition, but the increase in mechanical threshold stress rapidly

couples to recovery effects, meaning that above the transition the importance of path dependence is greatly increased. In the modelling of macroscopic material behaviour, path dependent models are often overlooked in favour of those with simpler expressions, such as the Johnson-Cook model [27], that allow faster computation. Given the results obtained, non path dependent models are expected to provide progressively worse predictions above 10^4 s^{-1}.

Finally, the instantaneous effects of temperature were found to behave semi-consistently with typical thermal barrier escape models for ϕ. Notably, jump tests revealed that the lower rate curves do in fact undergo greater levels of thermal softening. The anomalous softening behaviour observed in Chapter 5 is most likely explained by recovery effects decreasing the plateau stress with temperature. As we now know, increased rates of work hardening above the transition make the specimens interact more strongly with recovery effects at low strains. Experimental measurements of ϕ collapse reasonably well onto a universal curve as predicted by the mechanical threshold stress model, however the highest strain results for each condition diverge from the universal curve, an effect observed by Follansbee *et al.* even below the transition. The divergence with increasing strain is thought to be due to changes in the nature of the barrier or barrier climbing, and provide an avenue for further study.

Given the data presented in Chapters 5, 7 and 8, we will now study a potential mechanism for the increase of Θ_0 above 10^4 s^{-1}.

Chapter 9

A Model for the Breakdown of Avalanche Plasticity at High Rates

In previous chapters, the separation and explicit measurement of the plastic strengths generated in deformation at rates above 10^4 s^{-1} has lead to three qualitative conclusions;

1. The increase in material strength observed above 10^4 s^{-1} remains even if the high deformation rate is removed, implying the strengthening mechanism at true strains greater than 0.1 is structural.

2. The plateau stress, η, appears to not to exhibit any discontinuous behaviour, unlike that shown by the initial rate of work hardening, Θ_0. The lack of an obvious upturn in η would make it appear not to be the result of a simple generation - annihilation balance, as an increase in Θ_0 would correspond to an increase in generation, disturbing the equilibrium point.

3. No obvious increase in the temperature dependence of Θ_0 arises above the threshold. Temperature variations in the reload stress at lower strains would appear to be consistent with observed variations in η using a Voce law. However, due to adiabatic deformation, a better picture may be obtainable from modelling the entirety of a stress strain curve.

Having established a major contribution to the observed transition as being structural, we will review a set of established observations of high rate dislocation structures. We will then propose and test the early stages of a model based on the combined insights of the literature, and our own developments. Initially we will describe qualitatively the expected change in behaviours from the model and will then progress on to a rudimentary analytical form.

9.1 High Rate Dislocation Structure

Decrease in Activation Area

Armstrong has performed a substantial body of work [18, 33, 194] studying the results of many different experiments across between strain rates of 10^{-4} and 10^{10} s^{-1}. The resultant picture from his work is that above 10^4 s^{-1}, some increase in dislocation generation occurs, a picture compatible with the observations of our study, given the right recovery mechanisms.

One of the key pieces of evidence used by Armstrong to reach this conclusion is illustrated in Figure 9.1. In analysing the experimental data of Follansbee *et al.* [16] using the Zerilli-Armstrong model [13] that contains an 'activation volume' parameter for slip, Armstrong proposes that said parameter undergoes a change at 10^4 s^{-1}, decreasing from a volume $\sim 1000b^2$ to an asymptotic value of $\sim b^2$, where b is the length of the Burgers

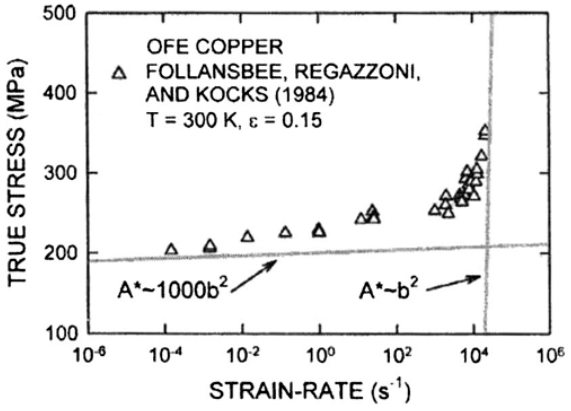

Fig. 9.1 A graph from Armstrong [33] depicting the two activation regions in the Zerilli-Armstrong model as fit to SHPB data, the low rate region has an activation volume of $\sim 1000b^2$ and the high rate asymptotes to $\sim b^2$.

vector. Armstrong attributes this change in behaviour to a change in the length scale of the slip process, the larger corresponding to remobilisation and dislocation motion, and the asymptote value to a highly localised process of dislocation generation. This observation may be related to the observation of Follansbee *et al.* that their normalised barrier, U_ϕ, also decreases with increasing mechanical threshold [16].

Rate Variations in Dislocation Cells

In his 2012 review [195], Gray summarises several major changes that occur to dislocation structure with increasing strain rate for FCC metals;

1. More uniform dislocation distributions arise at the same level of strain.
2. Discrete dislocation cell formation is hindered.
3. Dislocation cell size decreases.
4. More dislocations are found within the interiors of dislocation cells.

We should note that some of these observations, notably those relating to cell size, have been found by Kiritani *et al.* to occur abruptly and at approximately the transition rate [196].

Avalanche Plasticity and Slowly Driven Systems

At the end of his extensive work on elastic inclusions as dislocation avalanches, Brown [64] discusses avalanche behaviour as being that of a 'slowly driven interaction dominated threshold system'. One key aspect of such a system is that the ongoing extensive process must occur on a longer timescale than each individual avalanche event, the system will cease to be 'slowly driven'. Based on the strain in the band, calculated from a combination of theoretical and microstructural observations [4], and the formation time of bands, measured as the time between avalanches, Brown concludes the avalanche dynamics should cease being slowly driven at approximately 10^4 s^{-1}. Above 10^4 s^{-1} the most likely outcome is that

avalanches cease being able to form. Formation is assumed to be the limiting timescale as the time between any two avalanches (typically several μs) is typically much longer than the avalanche duration [4]. The formation mechanism is yet unknown, however when it begins to fail, the consequence is that the system will be forced to adapt a finer regime of slip.

9.2 Breakdown in Avalanche Formation

High rate plasticity does not incorporate avalanche behaviour outside of the use of pile-ups [33], typically only considered at grain boundaries, used to justify Hall-Petch behaviour. More general collective motion such as avalanches have not been considered as a major mechanism for slip at high rates, despite the large body of evidence now present at low rates for such a mechanism. Incorporating avalanche behaviour into high rate theories is important, given the influence it has on overcoming slip obstacles and work hardening, discussed in Chapter 2.

Current high rate models are completely disconnected from the modem understanding of avalanche plasticity. One of two things must be true; either avalanche plasticity still occurs at extremely high rates (including shock), significantly effecting the dislocation dynamics and modelling requirements, or, avalanche behaviour must break down at some rate, leading to some kind of behavioural transition. Given the observations of Brown regarding avalanche behaviour breaking down at 10^4 s^{-1}, the latter option appears most likely.

We do not yet understand what causes the rate threshold, however Brown [4, 64] refers to the scenario as being limited by some communication mechanism required to organise individual dislocations into an avalanche. Any formulation mechanism is likely to take longer to form larger avalanche precursors, and thus larger avalanches. Acoustic emission [66, 70, 71] and high resolution extensometery [69] both show that avalanches occur across several orders of magnitude in size; at least 3.5 orders of magnitude in amplitude can be observed

experimentally [66]. Thus, a large range of formation timescales may be expected. It is therefore likely that any breakdown in avalanche behaviour will happen progressively.

Figure 9.2 shows a sketch of a probability distribution for the length of any of the axes in an avalanche precursor. As the avalanche dynamics of the system cause it to adopt self organised critical (SOC) behaviour [64] (outlined in Chapter 2), the system adopts 'scale free' (fractal) geometry. Therefore a consequence of SOC is that all of the band axes of a single precursor, all being length scales, will remain approximately proportional. SOC causes all properties of the system to be related through power law relations, including their probabilities of having any given value. In the specific case of a length, we know that the probability of an acoustic emission having an amplitude, χ is proportional to χ^{-2}. As the amplitude of the acoustic wave is a length, we therefore infer from the fractal geometry of the system that the probability distribution of a precursor axis, also a length, is the same.

The power law behaviour only occurs up to some maximum value however, it is truncated by a cut off function at some maximum value. The exact origin of the cut off size is yet unknown, however it is likely some geometrical or dislocation structure related spatial limit as it has been related to the rate of work hardening [77]. At the very beginning of deformation, this limit serves as some constant limiting length scale, that is shown in figure 9.2 as a dashed red line, all precursor sizes too big for it do not activate at any rate, and correspond to the red shaded region below the probability curve.

As the strain rate increases, the time available for dislocations to organise into avalanche precursors decreases. Whilst the exact process is not yet known, we can generally say that as the rate increases, the maximum precursor (and therefore avalanche) size that can form will decrease. If the system is driven very slowly, then rate will have no significant effect, as the size limit due to formation time will be well in excess of the experimentally observed spatial limit. However, as the rate increases and the time limited precursor size decreases, at some rate, identified by Brown [64] to be 10^4 s^{-1}, the maximum avalanche size as limited

by formation time will pass through the spatial limit. The originally constant maximum avalanche size will now decrease as some function of increasing rate; the largest avalanches will be progressively frozen out.

As we discussed earlier, the avalanches occur across many orders of size, it is therefore possible for the largest avalanches to cease being able to form, while the smaller avalanches remain unaffected. We will therefore assume that avalanches that are still below the now rate depending size limit still form unhindered and obey SOC, the system instead organises around the new size threshold. The effect of rate above the transition is then simply to lower the size at which the avalanche distribution truncates. This new truncation can be seen in the post-transition scenario as the dashed blue line in figure 9.2, and the blue shaded region under the curve corresponds to avalanches that would be allowed by the spatial limit but are now forbidden because they form too slowly.

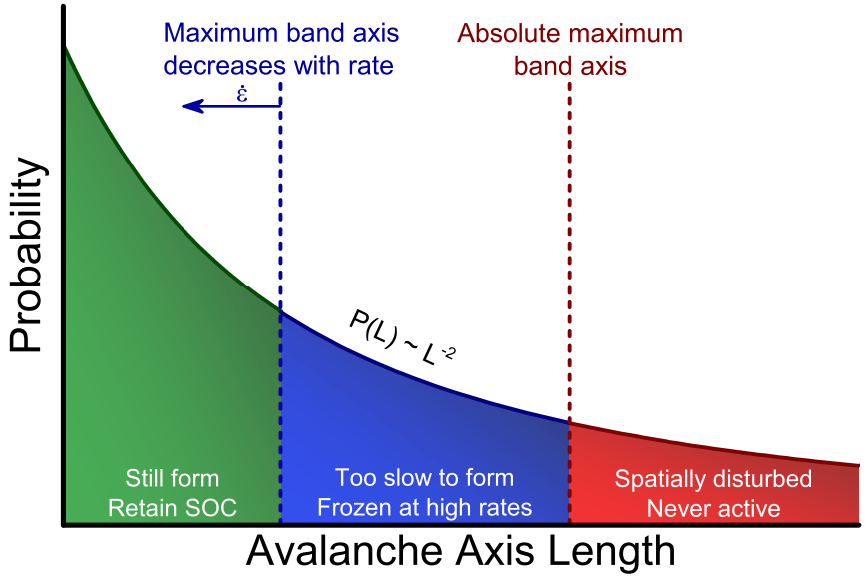

Fig. 9.2 The probability distribution, $P(L)$, of an avalanche having some axis length, L, which follows the power law $P(L) \propto L^{-2}$. Initially the maximum avalanche axis is limited by some yet understood spatial effect, observed in low rate testing, shown by the dashed red line. Above some transition rate the distribution becomes further truncated as the time available for avalanche formation is too short to form avalanches of axes equal the spatial limit, instead the maximum avalanche length now falls as a function of strain rate, indicated by the blue dashed line.

9.3 Consequences of Decreasing Avalanche Size

If the avalanche distribution is truncated at ever decreasing maximum lengths as the rate increases, the consequences are likely to affect all types of material behaviour. Some behaviours may be kept constant by self-organisation, however, others such as the initial rate of work hardening, Θ_0, may be expected to change.

An immediate requirement of truncating the probability distribution of avalanche sizes is that the distribution must renormalize: as the avalanches become smaller, more must occur in order to achieve the same amount of strain. To consider potential consequences for slip activation (ie, ϕ), we remember that the probability of an avalanche occurring typically scales with the imparted slip increment by said avalanche, $\Delta\gamma$, as $\Delta\gamma^{-1.5}$. The strain imparted by avalanches of size $\Delta\gamma$ will be proportional to $P(\gamma)\Delta\gamma$ and therefore scales as $\Delta\gamma^{-0.5}$. The probability distribution of the slip increments shows that they are proportional to some area in in the system. Remembering our scale free relations, whatever this area is, we can calculate its range using what we know of the length scales in the system. As previously discussed, the amplitude of acoustic waves emitted in slip, a length scale, varies by over 3.5 orders of magnitude. We therefore expect areas in the system to scale by 7 orders of magnitude, and as the strain is proportional to some area in the system, the strain imparted by any single avalanche will also span 7 orders of magnitude. This gives rise to a rather counter-intuitive result, although the largest avalanches impart the most strain in a single event, their probability decays faster than their imparted strain increases, so they are only responsible for a very small fraction of the imparted strain. Furthermore if we were to consider some thermal activation term, like the instantaneous rate scalar ϕ, the term will be dominated by the smaller avalanches, that are as much as 10^7 times more frequent.

Structurally however, the largest avalanches are both the easiest to activate and impart the largest strain in a single event. Therefore the largest avalanches may be expected to be limit both strength and work hardening. Simulation studies have found [77] that the rate of

work hardening appears to be inversely proportional to the maximum avalanche size,

$$\Theta \propto \frac{1}{\Delta\gamma_{max}}. \tag{9.1}$$

Whilst the mechanism is not immediately clear, the largest avalanche size will determine the largest obstacle free region, as an avalanche sweeps away many obstacles in its path. The softest region of the crystal will likely directly inherit its strength from the properties of the largest avalanche to occur, furthermore the macroscopic strength of the crystal will be limited by its softest region.

Decreasing avalanche size is consistent with, and can provide very intuitive understanding of, the observations of Armstrong. If we consider the 'activation volume' parameter discussed by Armstrong to be a real physical volume, a good candidate is the volume of the avalanche precursor. Above the transition, we expect the volume of the precursor to continuously decrease with rate from the original spatially limited volume to that of a lone dislocation when no avalanches are capable of forming. Armstrong proposes that after the transition, the activation volume will asymptotically approach a value $\frac{1}{1000}$th of that above the transition. We can rationalise this using microstructural observations and arguments already partially developed by Brown [4]. The remnant dislocation cells from avalanches anchored by secondary slip have an average diameter, u_B, of 1.5 μm, and make an angle, θ_e up to 3° to the slip plane. Brown [4] argues that the misalignment to the slip plane is due to the avalanche being across many planes, and tilting as it slips (in shear). The misorientation can therefore be used to find original avalanche length as it represents the difference in size between the two axes of the precursor that grew as the avalanche underwent radial expansion and the axis normal to the slip planes that was not changed in the avalanche;

$$\sin(\theta_m) = 2\frac{L_c}{u_B}. \tag{9.2}$$

Where L_c is the length of the axis approximately normal to the slip planes. Using the values obtained by microstructural observations, the largest avalanche precursors acted on approximately 20 slip planes, therefore having an axis of approximately 10 inter-planar spacings. If we then recall the fractal nature of the system, we expect each of the band axes to decrease by approximately a factor of 10 between the largest possible avalanche and the single dislocation scenario, and therefore the decrease in the activation volume would be expected to be a factor of 1,000, as observed by Armstrong.

Finally, we will consider truncation of the avalanche size distribution within the context of the observations of dislocation structure, as reviewed by Gray. The first topic raised is an increasingly uniform distribution of cell sizes, which is explicitly predicted by our model. As the distribution becomes truncated and the more extreme sizes cease forming, the distribution will become more uniform. The second point raised is that discrete dislocation cell formation is hindered, this would appear to be equivalent to precursors failing to form avalanches during the required time scale. The third point, that the dislocation cell sizes decrease, is also simply predicted by the nature that the largest avalanches are being frozen out. As an aside we also note that the dislocation density will be expected to increase, as dislocations form the surface of the avalanche and therefore occupy a volume scaling as bL^2, while the volume of the inclusion will vary as L^3. Increased strength almost always correlates with dislocation density in some way [197] and is partially why Taylor models are adopted so widely.

Overall, we see that a brief study of the fundamental proposal that slip bands freeze out progressively, largest first, can already qualitatively explain many observations in the literature. The consistency with experimental observations inspires some confidence in the proposal. However, in order to obtain a clear picture to examine further, we will now attempt to model the communication mechanism for avalanche formation.

9.4 Avalanche Precursor Synchronisation

In order to picture what the avalanche formation mechanism is likely to be, we will begin by imagining a failure event. We will assume currently, that some precursors already exist with the correct arrangement of dislocations already in place, no physical dislocation motion is required. This arrangement can be a number of loops on parallel planes, a dislocation dipole of some size or combinations of both. We show the initial arrangement (of only the edge dislocations) in Figure 9.3, where the dislocations have already moved to form what is approximately a closed ellipsoidal volume, which is being tilted under an applied local shear stress. A likely way for an avalanche to fail is if any one of the dislocations in the precursor were either to slip alone, or in the wrong direction, illustrated in the figure by the orange arrows showing a single loop stepping forward without any of the others on the surface. Doing so would break down the ellipsoidal interface and prevent collective slip. Such a failure event is consistent with observation 4 in Gray's review; more failure events, driven by insufficient organisation time, lead to more dislocations appearing inside the elastic

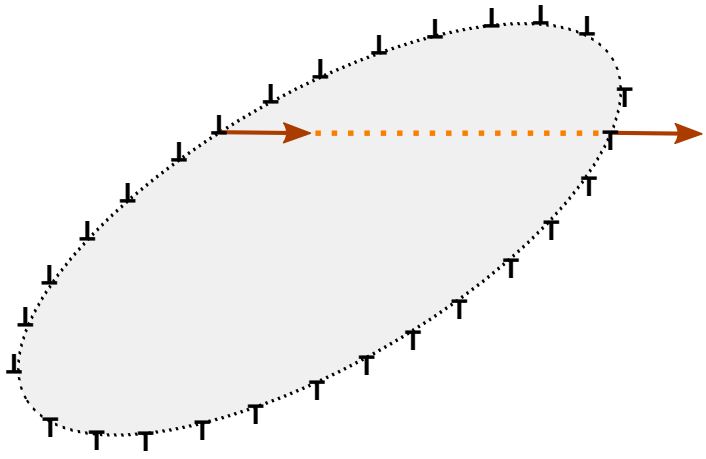

Fig. 9.3 An example of a precursor breakdown event. The dislocations are not yet synchronised and the force is not perfectly focused. Brown's relations are not yet obeyed. Any one of the dislocations (in this image a loop) may slip alone breaking down the surface before it can synchronise completely.

inclusion, that we can see occurring as the prematurely moving dislocation on the left will become trapped inside the inclusion.

In order for these failure events not to occur, all dislocations in the avalanche must slip at approximately the same time and in the same direction, thus they must undergo some kind of synchronisation. The important timescale is thus the time required to synchronise the dislocations in the interface. There are (to the author's knowledge) no experimental, analytical or computational studies providing insight into such a mechanism, except the already established formation time of several μs [4].

We will propose a rudimentary picture; the interface between the inclusion and the outside lattice is formed by some N_p dislocations, where N_p is the number of planes the band axis L_c crosses. Each dislocation (length $L(N)$, where N is the current plane number) is formed of $\frac{L(N)}{b}$ nearest neighbour sites, each of which are discrete and must synchronise. The exact nature of synchronisation is unknown, one could consider the problem as the following, if a multi component system is already oscillating, and another component is added to the system, how long does it take for the new component to be integrated into the normal modes of said system. The scenario is likely very complex, however the result of a successful formation is that the dislocations will slip together, triggering the avalanche, rather than alone, destroying the precursor. We will use a very rudimentary picture that the process occurs in a 'zip up' mechanism, where each atom along the length of a dislocation synchronises to the bulk system one by one, when dislocation N is completely synchronised, synchronisation begins on dislocation $N+1$. The synchronisation of any one site along the length of a dislocation requires motion from the entirety of the dislocation and we will therefore assume it takes a time equal to vibrational period of said dislocation. This is of course the inverse of the dislocations vibrational frequency, $f_D(L)$. We therefore arrive at an

expression for the formation time t_f of

$$t_f(N_p, L_a) \approx \int_0^{N_p} \frac{L(N)}{b} \frac{1}{f_D(L)} dN. \tag{9.3}$$

The oscillatory period of a dislocation of length L, either pinned at both ends or in a complete loop, is generally accepted to be inversely proportional to its length. Suzuki, Takeuchi and Hideo determine an expression for the fundamental vibrational frequency of a dislocation [198] by considering a standing wave along its length, and determining the shear wave speed from the line tension $\frac{1}{2}Gb^2$ and an effective cross sectional mass density of $\pi b^2 \rho_m$;

$$f_D(L) \approx \frac{1}{2L}\sqrt{\frac{\frac{1}{2}Gb^2}{\pi b^2 \rho_m}} = \frac{C_s}{2L}\sqrt{\frac{1}{2\pi}}\,. \tag{9.4}$$

Substituting for the frequency we find the expression

$$t_f(N_p, L_a) \approx 2\frac{\sqrt{2\pi}}{b\,C_s} \int_0^{N_p} L^2(N)\, dN\,. \tag{9.5}$$

Then all that remains is to determine the line length of dislocation N. We know that the surface is that of an ellipsoid, and we know that the plane normal axis can be defined as being N_p units in length. As there is no source of directional bias in the plane of slip (remembering that the stress inside the inclusion is uniform), we will assume, like Brown [4], that the in plane axes of the precursor, L_a and L_b are equal. At this point, the dislocation in plane N is approximately a circle of diameter L_a and thus has a length of

$$L(N_p, L_a) \approx \pi L_a \sqrt{1 - \left(\frac{2N}{N_p}\right)^2} \qquad 0 \le N' \le N/2\,. \tag{9.6}$$

We note that the equation is only valid on one half of the ellipsoid, expected due to the non-unique mapping of co-ordinates on any closed 2D surface. In the case of an ellipsoid the

problem is symmetric about $\frac{1}{2}N$, so we can simply calculate the integrand on that half of the surface and double the final result;

$$\begin{aligned} t_f(N_p, L_a) &\approx 2 \times 2\pi^2 \frac{\sqrt{2\pi}}{b\, C_s} \int_0^{\frac{N}{2}} L_a^2 \left(1 - \frac{4N'^2}{N^2}\right) dN' \,, \\ &= \sqrt{2\pi}\, \frac{4\pi^2}{3} \frac{L_a^2\, N_p}{b\, C_s} \,. \end{aligned} \tag{9.7}$$

We thus arrive at an expression for the formation time. We cannot however test this expression as L_a has only been measured for stabilised bands (as discussed earlier, $u_B \approx 1.5\mu$m). However, based on the observation that the largest avalanches take several μs to form [64], and the already established $N_p \approx 20$, we can estimate L_a. Depending on the time used, L_a is predicted to line in the range $10^{-7} - 3 \times 10^{-7}$ m, a realistic value given that the plane-normal band axis measured from microscopy is approximately 7.9×10^{-8} m. The band precursor would appear to be much closer to a sphere than the blade like post-avalanche state of the ellipsoid, slightly elongated by the applied shear.

9.5 Avalanche Breakdown & Work Hardening

Recalling the fractal nature any system exhibiting SOC, we note that as L_c is proportional to N_p, all axes must be. We can therefore infer for any length scale in the precursor, L, if rate limited, varies as

$$L \propto N_p \propto t^{\frac{1}{3}} \propto \dot{\gamma}^{-\frac{1}{3}} \propto \dot{\varepsilon}^{-\frac{1}{3}}. \tag{9.8}$$

We can then use the expected variation in length scale with rate in combination with Brown's relation [4] for the slip imparted by a single avalanche;

$$\Delta\gamma = \Psi_B \frac{u_B}{L_c}, \tag{9.9}$$

where Ψ_B is the volume fraction of the band (i.e. its volume over the specimen volume) and we recall that u_B is the distance travelled by the band before stabilisation (observed to be constant in Stage II [4]). As u_B is constant, $\Delta\gamma$ is proportional to a band volume over a band length, and is thus proportional to L^2.

The model therefore predicts that slip will scale as area properties of the system. An area in the system has a probability distribution of $P(\Delta\gamma) \propto \Delta\gamma^{3/2}$ (shown in Chapter 2), a power law and exponent that is consistent with experimental observation [199]. The two scaling laws combined give

$$\Delta\gamma_{max} \propto \dot{\varepsilon}^{-2/3}. \tag{9.10}$$

Relating the strain increment or any other property of the band to work hardening from first principles is an extensive theoretical task, and studying it analytically will currently be left as further work. We will instead use the result of Zaiser *et al.* [77];

$$\Theta \propto \frac{1}{\Delta\gamma_{max}}. \tag{9.11}$$

The relation is the result of computational simulation and is rationalised through the idea that the system only remains in an SOC state if it remains below the critical stress for spontaneous motion (a similar concept to the mechanical threshold). Therefore SOC organises such that the product $\Theta\Delta\gamma_{max}$ is always restrained below an increment that would cause the system to become super-critical.

We can therefore describe Θ_0 as part of a two region model;

$$\Theta_0(\dot{\varepsilon}) = \max\left[\Theta_{00}, \Theta_{01}\dot{\varepsilon}^{2/3}\right], \tag{9.12}$$

where Θ_{00} is the pre-transition value of Θ_{00} and Θ_{01} is the coefficient relating the post transition rate of work hardening to the strain rate. Currently Θ_{01} is a fitting parameter, however its value could be extracted from analytical and computational study.

9.6 Modelling at Fixed Strain and Loading Path

In Chapters 5-8 we collected a range of different types of SHPB data. We can use one of these data sets to parametrise Θ_{01} and use the remainder as verification data. We will begin by modelling experiments at fixed strain.

We will use the relations parametrised earlier for the instantaneous variables ϕ and η;

$$\phi(\dot{\varepsilon},T) = \frac{G(T)}{G(0\text{K})}\left\{1-\left[\frac{k_BT}{U_\phi Gb^3}\ln\left(\frac{\dot{\varepsilon}_\phi}{\dot{\varepsilon}}\right)\right]^{2/3}\right\}^2, \tag{9.13}$$

and

$$\eta(\dot{\varepsilon},T) = \eta_0\left(\frac{\dot{\varepsilon}}{\dot{\varepsilon}_\eta}\right)^{\frac{k_BT}{U_\eta G(T)b^3}} \tag{9.14}$$

For which we have established the values $U_\phi = 0.8$, $\dot{\varepsilon}_\phi = 10^7$ s^{-1}, $\eta_0 = 900$ MPa, $U_\eta = 0.206$ and $\dot{\varepsilon}_\eta = 10^{11}$ s^{-1}. Work hardening will be in principle be determined by Brown's physically derived Voce law [4];

$$\frac{\partial\sigma_p}{\partial\varepsilon_p} = \Theta_0\left(1-\frac{\sigma_p}{\eta}\right)^2. \tag{9.15}$$

However, every experiment in this chapter will undergo all work hardening at a single condition, and thus the relation can be integrated along that single path [9];

$$\sigma_p = \eta\left\{1-\left[\varepsilon_p\frac{\Theta}{\eta}+\left(1-\frac{\Sigma}{\eta}\right)^{-1}\right]^{-1}\right\}. \tag{9.16}$$

Σ is the initial mechanical threshold stress in the specimens, and was measured to be 37.3 MPa. All of which combine to give the flow stress,

$$\sigma_f = \sigma_0 + \phi\sigma_p. \tag{9.17}$$

We will also model for friction using,

$$\sigma_{fric} = \sigma_f \left(1 + \mu \frac{3r}{2l}\right) \tag{9.18}$$

where r is the specimen radius which varies throughout the experiment, l is the specimen thickness that also varies, μ is the friction coefficient, varying with technique and calibrated in Chapter 4. We should emphasise that the simple friction model used here only applies in the case of small strains, and will not remain accurate at strains close to unity. Finally we model inertia,

$$\sigma_{pred} = \sigma_{fric} + \rho_M \left[\frac{r^2}{16} + \frac{l^2}{6}\right] \dot{\varepsilon}^2. \tag{9.19}$$

Where σ_{pred} is the final prediction of the new model. In this section we will be dealing with modelling reload data, and at the standard condition inertia is negligible.

Using the forms outlined above, values of Θ_{00} and Θ_{01} were found by fitting to the reload data obtained in Chapter 7. The resulting curves are shown in Figure 9.4, which also shows the step by step build up of the model (excluding illustrations of friction and inertia correction). The extracted values were $\Theta_{00} = 2.2$ GPa and $\Theta_{01} = 6.3$ MPa $\text{s}^{2/3}$.

The model begins at the green dotted line, that illustrates the specimen strength at the standard condition before any deformation, effectively $\sigma_0 + \phi_{SC}\Sigma$. The blue and red dotted curves then correspond to the effects that work hardening would have on the reload stress in the absence of saturation effects; $\sigma_0 + \phi_{SC}(\Sigma + \Theta_0\varepsilon)$. The blue curve specifically shows the predicted stress if there is no spatial limit in our avalanche model, we note that as the avalanches can be arbitrarily large the level of work hardening becomes negligibly small at low rates. The red curve introduces this spatial limit, providing a relatively constant level of work hardening until the transition rate, which is where the blue and red curves meet. Finally, the model must account for saturation effects, the purple curve depicts the strength the material would be expected to have if reloaded at its saturation stress, $\sigma_0 + \phi_{SC}\eta$. In

reality, the work hardening reduces as this value is approached, and the solid orange line corresponds to the prediction through the Voce work hardening law used to account for saturative effects.

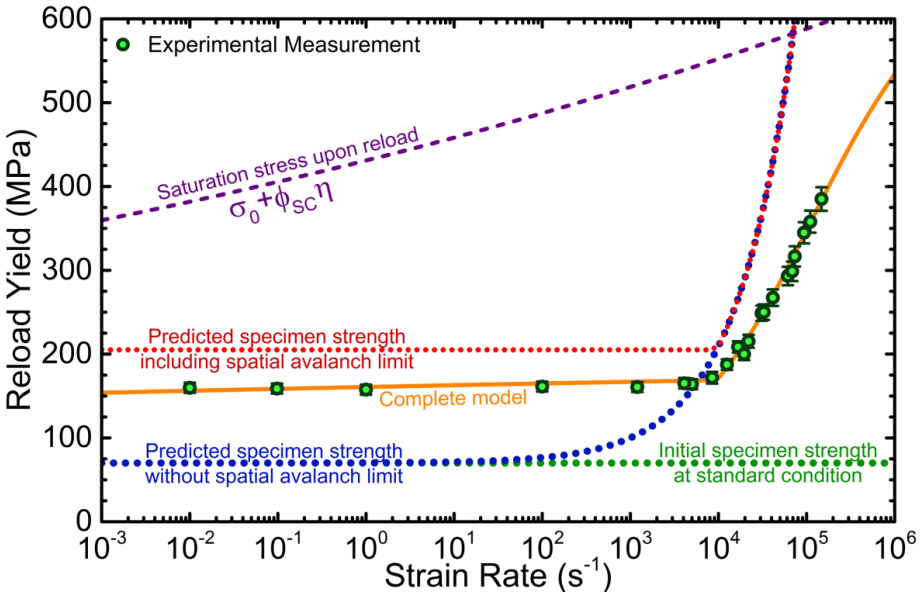

Fig. 9.4 The data from Chapter 7 and a progressive build up of the proposed model, outlined in the body text.

Based on these values and the complete parametrisation of η, we can again use the single path curve to predict the mechanical threshold, σ_p and thus the reload stress, $\sigma_0 + \phi_{SC}\sigma_p$ for the variety of temperatures tested in Chapter 8. In the current model, the only apparent temperature dependence is the value of η in particular condition (pre-strain) loading. The specimens are predicted to be softened due to the increase in saturation effects as η decreases with temperature. The predictions of the model are compared to the experimental data in Figure 9.5, whilst the room temperature data is used in parametrising Θ, the raised temperature points were not used in the parametrisation of Θ or η, which was parametrised using high strain data. The data appears to be well fit at fixed strain but a variety of rates and temperatures, especially considering many of the data points at 570 K are too high to allow proper interrupt at high strains, and thus no direct measurement of the plateau stress can be observed for those rates.

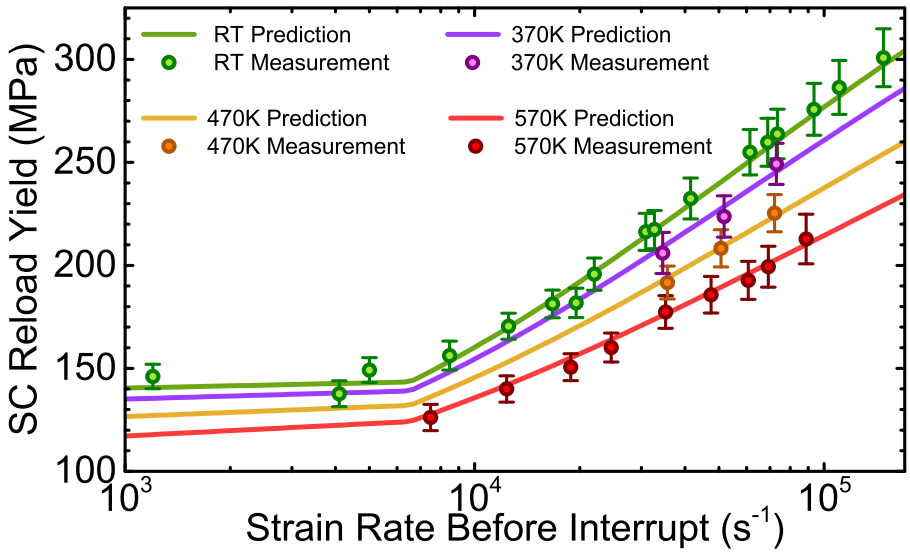

Fig. 9.5 The predictions of the parameterised model against the fixed strain reload yield of specimens deformed under a variety of strain rates and temperatures, the room temperature values were used in parameterisation of the model, however all of the raised temperature measurements are pure verification data.

The model appears to portray the measurements well, implying that both the proposed form for the increase in work hardening with rate ($\sim \dot{\varepsilon}^{2/3}$) and the assumption that Θ_0 remains weakly temperature dependence are accurate.

9.7 Modelling Along a Varying Loading Path

A more strenuous test of the model is presented by the measurements in Chapter 5, that go to larger strains, and due to significant adiabatic work will vary in temperature throughout the experiment, providing a continuously changing loading path. As this is at-rate data rather than reload data, both the forms of ϕ and inertia will also be included in the model. We can no longer use the single path integral of Gould, and instead will use an incremental step based method. The initial mechanical threshold stress, Σ, was set using measurements of the value from the previous chapters. The initial temperature from the thermocouple measurements at the start of each experiment. The strain rate was assumed to be fixed at the average rate throughout the experiment, no rise time effects were accounted for. The strain increment was chosen to be 10^{-4}. The incremental loop performed was:

1. Calculate the instantaneous properties $G(T)$, $\phi(\dot{\varepsilon},T)$ and $\eta(\dot{\varepsilon},T)$.
2. Determine the flow stress, $\sigma_0+\phi(\dot{\varepsilon},T)\sigma_p$.
3. Use the current value of the specimen dimensions to apply friction and inertia corrections.
4. Increment the strain, mechanical threshold stress using the voce law, and the temperature change by approximating that 90% of the mechanical work is converted into heat.
5. Return to 1.

The comparison of the model to the experimental data is shown in Figure 9.6. Even across the more complex loading paths the model generally lies within the uncertainty region of the experimental measurements. There are two ways in which the model appears not to fit very well and we will attempt to address why. Firstly, the model often diverges from the measured value at high strains. This is most likely the limit of our model for friction; the corrected form, earlier in this chapter, is specifically for use in 'upsetting' i.e. small strain scenarios. Above small levels of strain and friction is greatly complicated by mechanisms such as the specimen rolling around itself during radial expansion.

Secondly, at low strain the model appears to under predict the stress relatively consistently. Under prediction of the flow stress is a complicated issue to separate from experimental error as this region is typically undergoing (and part of the effect is undeniably caused by) ring up. We should also remember experimentally that Pochammer-Chree oscillations tend to cause a relatively high leading edge to the arriving waves, for example, the first oscillation in a typically dispersed top hat pulse is an upwards one. There is however a chance that some of the effect is due to dislocation drag effects in the very early stages of strain, when too few dislocations exist for slip bands to begin forming and dislocation densities are very low. Unfortunately, the split Hopkinson bar apparatus used were not designed to optimise observation of this region of the stress strain curve, experiments that have been optimised to do so [33], do appear to show drag like behaviour at the very early stages of deformation.

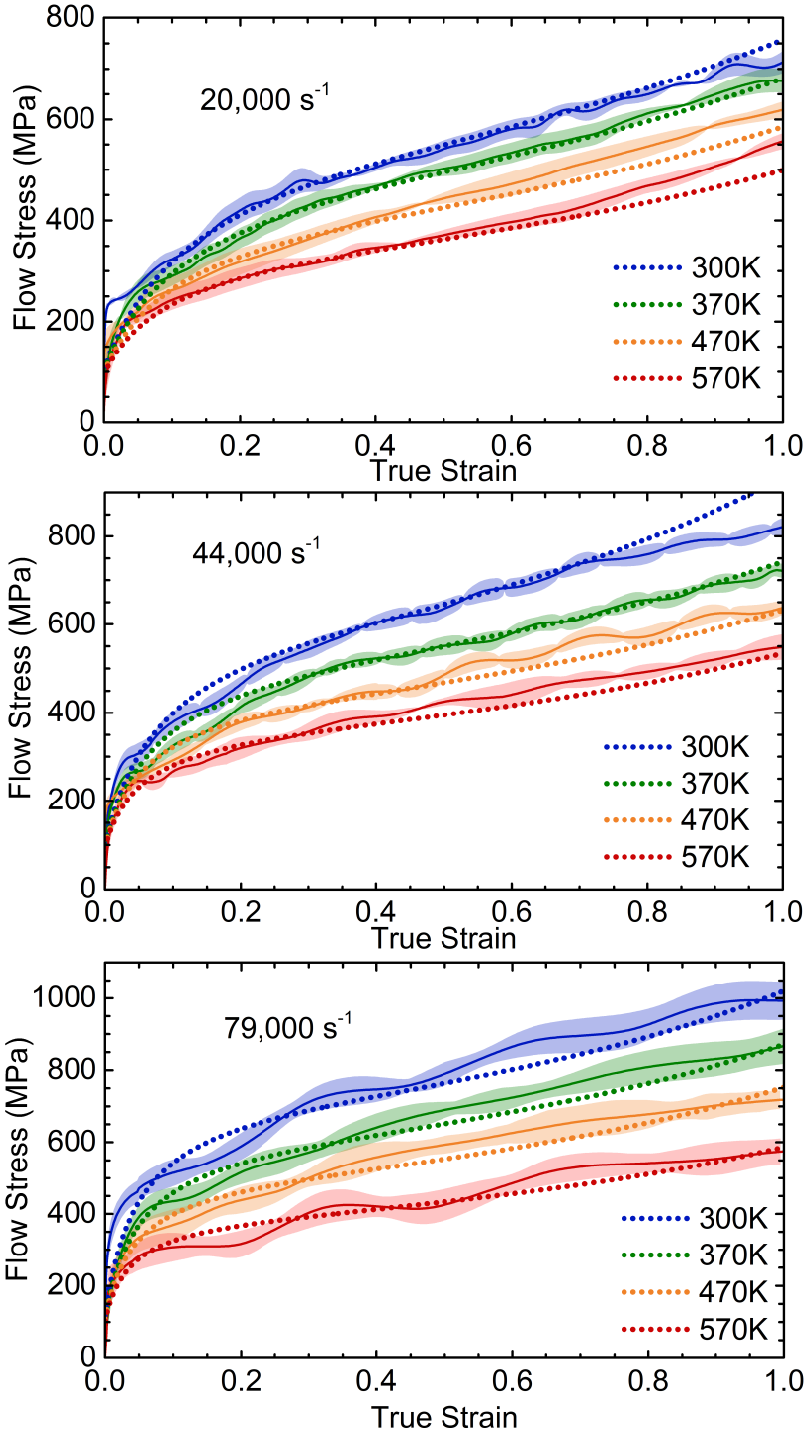

Fig. 9.6 A comparison between the experimental results of high rate, high temperature adiabatic deformation tests from Chapter 5. The model predictions correspond to dotted lines, experimental measurements are solid lines with the standard error regions being shown by shading around the measurement line.

9.8 Summary

In this chapter, we collated our own understanding based on the Hopkinson pressure bar work in this thesis, and combined it with external micrographical, computational and analytical studies. We then attempted to address these observations using avalanche plasticity considerations that are largely absent in high rate metal theory, despite their acknowledged importance in structural evolution. A model was proposed in which the increasing rate reduces time scale available for the largest avalanches to form, forcing the system to adopt progressively finer, unfavourable, modes of slip.

Based on this picture, an expression was derived determining the relation between various length scales in the band. Typically these are all proportional due to the scale free behaviour of systems exhibiting SOC. It was found that a length in the band should be approximately proportional to the cube root of the formation time. The transition is believed to correspond to the rate at which avalanche sizes cease being limited by some fixed spatial constraint and instead become limited by the time required to form the largest avalanches. The decrease in maximum band size with rate was expected to affect work hardening due to the smallest bands being strength limiting, but have limited effect on thermal activation as smaller bands correspond to most of the activation events and consequently impart most the overall strain, despite their smaller size.

The model was used to generate a two region expression for the work hardening coefficient, which included a constant value below the transition and a value proportional to $\dot{\varepsilon}^{2/3}$ above the transition. The coefficient for the post-transition rate of work hardening was parametrised using the room temperature data obtained in Chapter 7. It was then compared to independent verification data at increased temperatures initially at fixed small strains constituting a single loading path (Chapter 8), and subsequently to the varying temperature adiabatic tests performed in Chapter 5.

The model closely predicted the deformation curves. There were small discrepancies at the very lowest and very highest rates, but both cases were considered as being likely driven by issues outside of the material model, notably the use of split Hopkinson bar in which experiments are unreliable before ring-up has completed, and that at extremely large strains frictional effects are far more complex than the simple form used to model them.

Overall, the model approach used serves both to unify high rate plasticity with the more modern views of low rate plasticity as self organising avalanche behaviour, and provides a physical mechanism with which to explain the measurements of increased stage II work hardening form earlier chapters. Obvious continuation of the model as a constitutive form would be to apply it to experiments such as symmetric Taylor impact, that provide more complex but relatively friction free deformation. The next step towards properly understanding the underlying dislocation mechanisms however would be to attempt to identify and study either precursors during loading or the properties of dislocation cells (anchored avalanches) and failed precursors after loading. We will briefly discuss both possibilities in the next chapter.

Chapter 10

Conclusions & Further Work

10.1 Conclusions

In this thesis, a progressive series of dynamic and quasi-static experiments were presented, providing empirical evidence to improve the understanding of the deformation of FCC metals above strain rates of 10^4 s^{-1}. Particular emphasis was given to the interplay between strain rate and temperature, and separating instantaneous and structural contributions to strength. The studies performed will help to both improve the physical understanding of material behaviour and thus the accuracy of future material models.

Chapters 2 and 3 introduced structural and instantaneous strength mechanisms. Structural barriers were shown to give rise to thermal softening, whilst phonon drag mechanisms acted to increase material strength with temperature. Different theories of phonon drag were shown to have varying predictions of the interplay between phonon scattering effects and structural evolution. The key predictions of the theories were used to determine the early stages of the experimental work; checking for signs of reduced thermal softening with predicted by phonon theories, and increased work hardening as a sign of changes in the evolution of dislocation structure.

Chapter 4 introduced two of the experimental methods used to measure strength, Instron compression and split Hopkinson pressure bars (SHPBs). Both methods were critically analysed for flaws arising from effects such as friction, inertia, dispersion and the finite modulus and strengths of the testing systems. In each case a methodology was detailed for experimental minimisation of the effect, or, if unavoidable, to subsequently account for the effect in post-processing. To enable SHPB systems to reliably obtain high fidelity measurements at high temperatures and impact speeds, the Cavendish SHPB system was outfitted with a multi-channel photon Doppler velocimetry (PDV) system. Both the practical implementation and subsequent data analysis of the SHPB system were described. Finally, the C103 copper specimen material was introduced, with emphasis on its simultaneous ability to produce very small specimens, increasing the achievable strain rate whilst minimising inertial effects, and to provide repeatable measurements, acting as a true bulk polycrystal.

Chapter 5 presented the first full experimental study of the thesis. Specimens were deformed at a range of temperatures at rates in the order of magnitude immediately above the transition. Despite having strengths over twice that at the transition rate, no decrease in thermal softening was observed. Phonon based strength mechanisms were inferred to not yet have become significant. The observed levels of thermal softening were in fact seen to increase with rate, an observation more in line with models proposing an increase in the mechanical threshold of the material. Rudimentary analysis attempting to account for variations in the mechanical threshold did not manage to completely account for the increase in thermal softening observed.

Before performing further studies, the SHPB was deemed insufficient to provide the required experimental conditions. The requirement to perform high strain rate deformation and subsequently arrest at a low strain, to minimise saturative effects complicating the data set, led to experimental durations becoming extremely short. The rise time of the input pulse in miniaturised SHPB experiments was deemed too gradual to consider the tests would

be truly performed at a single strain rate. To improve the rise time of the loading in the experiments a direct impact Hopkinson bar arrangement (DIHB) was adopted, in which the input bar is removed and the striker impacts the specimen directly. At the start of this work, DIHB experiments were hindered by the loss of any information about the impacted specimen face due to the absence of the input bar. A method was developed in which PDV was applied directly to the striker bar itself, allowing measurements of the rise time of the applied stress, creating evidence that the technique can provide experiments that approximate to deformation at a single strain rate. Separation of the wave and bulk components of the striker velocity also allowed conversion of the striker bar into a second output bar, providing a measurement of the normal reaction force at the input face of the specimen, allowing DIHB systems to explicitly verify mechanical equilibrium during experiments. Mechanical equilibrium is a core requirement for Hopkinson bar experiments to be valid, and before this study no measurements were available to provide such confirmation. Finally, the stress measurement at the input face was noted to potentially provide novel measurements in specimens that undergo progressive collapse, an example which was demonstrated in measurements of metallic foams.

In Chapter 7, a series of specimens were deformed to 10% true strain at a range of true strain rates between 10^{-2} and 10^{5} s^{-1}. After being recovered the specimens were reloaded to yield at ambient temperature and at a strain rate of 10^{-2}. The increase in strength above the transition was observed to remain even after variations in the instantaneous conditions of deformation were removed. Instantaneous effects were quantified using the ratio of the rate dependent parts of the final flow stress in initial deformation and in the yield stress upon reloading at 10^{-2} s^{-1}. No obvious change in the instantaneous contributions to strength was observed across the transition. Based on these observations, it was concluded that the increase in strength is due to an undetermined change in the evolution of the metals dislocation structure, leading to an increase in the rate of work hardening in the material. The

data set acquired is the first of its kind: simultaneously providing a comprehensive sweep across many orders of magnitude and separating instantaneous and structural effects well above the strength transition.

Chapter 8 expanded on the conclusions of the previous chapter; given that the transition appeared to be caused by a change in the early stages of structural evolution, a study was performed seeking for any change in the high strain saturative behaviour of the materials. Strain arresting and reload techniques were expanded to general rates and elevated temperatures. The saturation of the mechanical threshold was observed to behave consistently (within error) above and below the transition, however the measurements of the saturative plateau were sparse due to the limited supply of material.

Finally, in Chapter 9, we discussed the disparity between the current Orowan-Taylor basis of high rate plasticity models and recent realisations that a large fraction of plasticity occurs in collective avalanches. Based on our own observations and a combination of high rate and avalanche plasticity observations, we propose a mechanism in which avalanche processes in the metal begin to progressively break down. A mechanism is discussed in which the maximum size an avalanche is forced to decrease with strain rate above the transition, due to decreasing time being available to organise dislocations to slip collectively. The model is then related to literature results relating work hardening to the largest avalanche size in the material to develop a simple constitutive relation for work hardening. Combined with an exhaustion based Voce law and literature models for instantaneous strengthening, the proposed work hardening model closely reproduces all the experimental results of the thesis.

10.2 Further Work

Two major avenues exist for immediate further work; performing experiments to better understand the underlying physics of the change in structural evolution, or exploiting the

newly available measurements to improve the fidelity of constitutive models across the transition.

10.2.1 Improving physical understanding

Based on the results of Chapter 9, we now have an explicit picture of a process in which the structural changes can rationalised. It is also one in which progressive changes in the nature of FCC plasticity can be understood, from very low rates up to shock. However, the equations derived are rudimentary and partially rely on relations taken from simulation data to bridge avalanche scales to macroscopic behaviour. More work is required to understand the link between the largest avalanche dimension and work hardening. Furthermore, the powerful but simple relations from self organisation may make many other useful results obtainable, a variety have been found at quasi-static rates [64]. It is therefore immediately favourable to perform a broader theoretical study on what high rate properties and behaviours can be linked through self organised criticality.

To complement theoretical work, and to fill a major gap in the current results of this study, micro-structural studies are necessary. However, micro-structural observations are not necessarily simple given the proposed behaviours of avalanche plasticity. Firstly, sample preparation is extremely difficult, as avalanches sweep away the remnants of previous avalanches when they slip. All forms of micro-structural preparation, from grit to ion beam polishing, all impart macroscopic shear into the specimen, that may trigger avalanches, eradicating some of the more subtle features of the mesostructure. A potential polishing method that may not apply macroscopic shear is electrolytic polishing. However, even given an ideal preparation process, the desired features may in fact be removed during deformation, as the strain arresting methods have a finite fall time, due to the interrupting rings finite acoustic impedance. A small but non zero plastic strain is imparted into every specimen during interrupt, which will be at rates well below the target rate; below the transition. A final complication is that it is not apparent what structural feature one should be looking

for, or where it would be found. An initial guess at a potential micro-structure feature could be the remnants of failed precursor events, that may correlate to the number of individual dislocations which have become trapped inside dislocation cells.

Finally, computational studies could be performed to attempt to simulate dislocation avalanches with varying driving rates. However, given current limits on computational studies, the proposed phenomena cannot be studied. Currently molecular dynamics studies are required to remain at strain rates above 10^5 s^{-1} and dimensions of the order of 1 μm. The proposed mechanism in our material is occurring across distances of tens of microns (due to self organisation), and would require studying at rates both above and below 10^4 s^{-1}. Whilst another possible avenue could be 3D discrete dislocation dynamics, the quantised nature of the synchronisation process (lattice point by lattice point) may render discrete dislocation models too simple.

10.2.2 Constitutive Model Development

All models prior to this study have relied on largely speculative functions to describe the relative effects of work hardening and instantaneous conditions. We have provided a good data set with which to properly inform and, importantly, calibrate a constitutive model. Throughout this thesis a collection of forms were proposed and calibrated, leading to a constitutive model that has closely predicted every experimental measurement in the thesis (only a subset of which were used for calibration).

The next step in model development, is, typically to compare the parametrised model to more complex loading scenarios. In Chapter 1, we introduced the Taylor impact experiment. Taylor impact provides a simple specimen geometry, yet a complex loading path, stress geometry, and unlike our equilibrated experiments, interaction between adjacent regions under different conditions. Comparing finite element or hydrocode simulations provides a strong test of the material model, only weakened by the new dependency of the model predictions on the specifics of how the simulations are performed.

References

[1] M.A. Meyers. *Dynamic Behaviour of materials*. 1994.

[2] S. Ward, C. Braithwaite, and A. Jardine. The effects of nanostructure upon the dynamic ductile fracture of high purity copper. *Procedia Engineering*, 197:23 – 32, 2017. DYMAT 23rd Technical Meeting - International Conference on Dynamic Fracture of Ductile Materials.

[3] P.M. Anderson, J.P. Hirth, and J. Lothe. *Theory of Dislocations, Third Edition*. Cambridge University Press, 2017.

[4] L.M. Brown. Constant intermittent flow of dislocations: central problems in plasticity. *Materials Science and Technology*, 28(11):1209–1232, nov 2012.

[5] A.H. Cottrell. *Theory of Crystal Dislocations*. Blackie and Son, London, 1964.

[6] Fionn Dunne and Nik Petrinic. *Introduction to computational plasticity*. Oxford University Press on Demand, 2005.

[7] U Fred Kocks, Carlos Norberto Tomé, and H-R Wenk. *Texture and anisotropy: preferred orientations in polycrystals and their effect on materials properties*. Cambridge university press, 2000.

[8] J. Klepaczko. Thermally activated flow and strain rate history effects for some polycrystalline FCC metals. *Materials Science and Engineering*, 18(1):121–135, 1975.

[9] P.J. Gould and B.D. Goldthorpe. A path-dependent constitutive model for gilding copper. *J. Phys. IV*, 10, 2000.

[10] E. O. Hall. The Deformation and Ageing of Mild Steel: III Discussion of Results. *Proceedings of the Physical Society. Section B*, 64(9):747–753, 1951.

[11] N. J. Petch. *J. Iron Steel inst.*, 174:25–28, 1953.

[12] R. Townsley S.M. Walley, P.D..Church and J.E. Field. Validation of a path-dependent constitutive model for fcc and bcc metals using "symmetric" taylor impact. *J. Phys. IV France*, 2000.

[13] F.J. Zerilli and R.W. Armstrong. Dislocation-mechanics-based constitutive relations for material dynamics calculations. *Journal of Applied Physics*, 61(5):1816–1825, 1987.

[14] G. Regazzoni, U.F. Kocks, and P.S. Follansbee. Dislocation kinetics at high strain rates. *Acta Metallurgica*, 35(12):2865 – 2875, 1987.

[15] P.S. Follansbee and U.F. Kocks. A constitutive description of the deformation of copper based on the use of the mechanical threshold stress as an internal state variable. *Acta Metallurgica*, 36(1):81–93, 1988.

[16] P. Follansbee, G. Regazzoni, and U. Kocks. The transition to drag-controlled deformation in copper at high strain rates. *Mechanical Properties at High Rates of Strain*, 70:71–80, 1984.

[17] J.L. Jordan, C.R. Siviour, G. Sunny, C. Bramlette, and J.E. Spowart. Strain rate-dependant mechanical properties of ofhc copper. *Journal of Materials Science*, 48(20):7134–7141, 2013.

[18] R.W. Armstrong and S.M. Walley. High strain rate properties of metals and alloys. *International Materials Reviews*, 53(3):105–128, may 2008.

[19] A. Hunter and D. L. Preston. Analytic model of the remobilization of pinned glide dislocations from quasi-static to high strain rates. *International Journal of Plasticity*, 70:1–29, 2015.

[20] E. Orowan. Problems of plastic gliding. *Proceedings of the Physical Society*, 52(1):8, 1940.

[21] G.I. Taylor. Plastic strain in metals. *J. Inst. Metals*, 62:307–324, 1938.

[22] H Kolsky. An investigation of the mechanical properties of materials at very high rates of loading. *Proceedings of the Physical Society. Section B*, 676, 1949.

[23] D. Gorham, P. Pope, and J. Field. An Improved Method for Compressive Stress-Strain Measurements at Very High Strain Rates. *Proceedings of the Royal Society A: Mathematical, Physical and Engineering Sciences*, 438(1902):153–170, jul 1992.

[24] S.B. Brown, K.H. Kim, and L. Anand. An internal variable constitutive model for hot working of metals. *International Journal of Plasticity*, 5(2):95–130, 1989.

[25] N.F. Mott and F.R.N. Nabarro. An attempt to estimate the degree of precipitation hardening, with a simple model. *Proceedings of the Physical Society*, 52(1):86–89, 1940.

[26] E. Voce. The relationship between stress and strain for homogeneous deformation. *J Inst Metals*, 1948.

[27] G.R. Johnson and W.H. Cook. *A constitutive model and data for metals subjected to large strains, high strain rates and high temperatures*, volume 547, pages 541–547. 1983.

[28] V. Volterra. Sur l'équilibre des corps élastiques multiplement connexes. *Annales scientifiques de l'École Normale Supérieure*, 24:401–517, 1907.

[29] G. Taylor and H. Quinney. *Proc. R. Soc. Lond. A*, (143):307–326, 1934.

[30] Juan et al. Dislocations and torsion in graphene and related systems. *Nucl.Phys. B828*, 2010.

[31] F.R.N. Nabarro. The Peierls stress for a wide dislocation. *Mater. Sci. Engng A*, 113:315–326, 1989.

[32] J.M. Burgers and W.G. Burgers. Dislocations in crystal lattices. In F R Eirich, editor, *Rheology*, pages 141–199. Academic Press, New York, 1956.

[33] R.W. Armstrong and Q. Li. Dislocation Mechanics of High-Rate Deformations. *Metallurgical and Materials Transactions A*, (1), 2015.

[34] E. Schmid and W. Boas. *Kristallplastizität*. Springer, 1935.

[35] U.F. Kocks and H. Mecking. Physics and phenomenology of strain hardening: The FCC case. *Progress in Materials Science*, 48(3):171–273, jan 2003.

[36] G.K. Williamson and R.E. Smallman. X-ray extinction and the effect of cold work on integrated intensities. *Proceedings of the Physical Society. Section B*, 68(9):577, 1955.

[37] J.S. Koehler. On the dislocation theory of plastic deformation. *Phys. Rev.*, 60:397–410, 1941.

[38] W. Blum and F. Roters. Spontaneous dislocation annihilation explains the breakdown of the power law of steady state deformation. *Phys. Stat. Sol. A*, 184:257–261, 2001.

[39] E. Nes. Modelling of Work Hardening and Stress Saturation in Fcc Metals. 41(97), 1997.

[40] F.R.N. Nabarro. Fifty-year study of the Peierls-Nabarro Stress. *Materials Science and Engineering A*, XI(November 1956):810–814, 1980.

[41] H.B. Huntington. Modification of the Peierls-Nabarro model for edge dislocation core. *Proc. Phys. Soc. Lond. B*, 68:1043–1048, 1955.

[42] Y. Kamimura, K. Edagawa, and S. Takeuchi. Experimental evaluation of the Peierls stresses in a variety of crystals and their relation to the crystal structure. *Acta mater.*, 61:294–309, 2012.

[43] L.K. Wickham, K.W. Schwarz, and J.S. Stölken. Rules for forest interactions between dislocations. *Phys. Rev. Lett.*, 83:4574–4577, Nov 1999.

[44] M. Peach and J.S. Koehler. The forces exerted on dislocations and the stress fields produced by them. *Phys. Rev.*, 80:436–439, 1950.

[45] F.R.N. Nabarro. The law of constant resolved shear stress in crystal plasticity. *Philos. Mag. (Ser. 7)*, 42:213–214, 1951.

[46] A.H. Cottrell. *Theory of Crystal Dislocations*. Blackie and Son, London, 1964.

[47] M. Huang, P.E.J. Riverz-Díaz-del Castillo, and O Bouaziz. A constitutive model for high strain rate deformation in fcc metals based on irreversible thermodynamics. *Mech. Mater.*, 41:982–988, 2009.

[48] C.Y. Gao and L.C. Zhang. Constitutive modelling of plasticity of fcc metals under extremely high strain rates. *International Journal of Plasticity*, 32–33:121 – 133, 2012.

[49] F.C. Salvado, F. Teixeira-Dias, S.M. Walley, L.J. Lea, and J.B. Cardoso. A review on the strain rate dependency of the dynamic viscoplastic response of fcc metals. *Progress in Materials Science*, 88:186 – 231, 2017.

[50] L.P. Kubin, R. Madec, and B. Devincre. Dislocation intersections and reactions in fcc and bcc crystals. *MRS Proceedings*, 779, 2003.

[51] T. Narutami and J. Takamura. *Acta Metall*, 1981.

[52] B. Gurrutxaga-Lerma, D.S. Balint, D. Dini, and A.P. Sutton. The mechanisms governing the activation of dislocation sources in aluminum at different strain rates. *Journal of the Mechanics and Physics of Solids*, 84:273–292, 2015.

[53] K. Lücke and H. Mecking. Dynamic recovery. *The inhomogeneity of plastic deformation*, page 223, 1973.

[54] F.J. Zerilli and R.W. Armstrong. Dislocation mechanics based constitutive equation incorporating dynamic recovery and applied to thermomechanical shear instability. *Shock compression of condensed matter*, page 215–218, 1997.

[55] F. Kocks and H. Mecking. A mechanism for static and dynamic recovery. *Proc. Int. Conf. Strength of Metals and Alloys*, page 345, 1979.

[56] U. F. Kocks. A statistical theory of flow stress and work-hardening. *Philosophical Magazine*, 13(123):541–566, 1966.

[57] W.D. Nix, J.C. Gibeling, and D.A. Hughes. Time-dependent deformation of metals. *Metall. Trans. A*, 16:2215–2226, 1985.

[58] J. J. Gilman. Influence of dislocation dipoles on physical properties. *Discuss. Faraday Soc.*, 38:123–137, 1964.

[59] J. Washburn and Th. Cass. DISLOCATION DIPOLES IN MgO. *Journal de Physique Colloques*, 27(C3):C3–168–C3–177, 1966.

[60] J. Washburn, G.W. Groves, A. Kelly, and G.K. Williamson. Electron microscope observations of deformed magnesium oxide. *Philosophical Magazine*, 5(58):991–999, 1960.

[61] H. Alexander and S. Mader. Elektronenmikroskopische beobachtungen von versetzungen in germanium. *Acta Metallurgica*, 10(9):887 – 890, 1962.

[62] J. T. Fourie. Dislocation dipoles in deformed copper single crystals. *Philosophical Magazine*, 10(108):1027–1041, 1964.

[63] Papanikolaou S, Y. Cui, and N. Ghoniem. Avalanches and plastic flow in crystal plasticity: An overview. 2017.

[64] L. M. Brown. A brief reply to comments on: 'Constant intermittent flow of dislocations: central problems in plasticity'. *Materials Science and Technology*, 30(1):127–128, 2014.

[65] L. M. Brown. A dipole model for the cross-slip of screw dislocations in fcc metals. *Philosophical Magazine A*, 82(9):1691–1711, 2002.

[66] J. Weiss, T. Richeton, F. Louchet, F. Chmelik, P. Dobron, D. Entemeyer, M. Lebyodkin, T. Lebedkina, C. Fressengeas, and R. McDonald. Evidence for universal intermittent crystal plasticity from acoustic emission and high-resolution extensometry experiments. *Physical Review B*, 76(22):224110, 2007.

[67] W. Schaarwächter and H. Ebener. *Acta Metall. Mater.*, page 193–205, 1990.

[68] P. Bak, C. Tang, and K. Wiesenfeld. Self-organized criticality: An explanation of the 1/f noise. *Phys. Rev. Lett.*, 59:381–384, Jul 1987.

[69] R.F Tinder and J.P Trzil. Millimicroplastic burst phenomena in zinc monocrystals. *Acta Metallurgica*, 21(7):975 – 989, 1973.

[70] J. Weiss, F. Lahaie, and J.R. Grasso. Statistical analysis of dislocation dynamics during viscoplastic deformation from acoustic emission. *Journal of Geophysical Research: Solid Earth*, 105(B1):433–442, 2000.

[71] J. Weiss and J.R. Grasso. Acoustic emission in single crystals of ice. *The Journal of Physical Chemistry B*, 101(32):6113–6117, 1997.

[72] Miguel et al. Intermittent dislocation flow in viscoplastic deformation. *Nature*, pages 667–671, 2001.

[73] B Sprušil and F Hnilica. Fractal character of slip lines of cd single crystals. *Czechoslovak Journal of Physics B*, 35(8):897–900, 1985.

[74] D.M. Dimiduk, M.D. Uchic, and T.A. Parthasarathy. Size-affected single-slip behavior of pure nickel microcrystals. *Acta Materialia*, 53(15):4065 – 4077, 2005.

[75] M.D. Uchic, D.M. Dimiduk, R.W., P.A. Shade, and H.L. Fraser. Application of micro-sample testing to study fundamental aspects of plastic flow. *Scripta Materialia*, 54(5):759 – 764, 2006. Viewpoint set no. 39: Statistical mechanics and coarse graining of dislocation behavior for continuum plasticity.

[76] D.S. Fisher. Collective transport in random media: from superconductors to earthquakes. *Physics Reports*, 301(1):113 – 150, 1998.

[77] F Csikor, C Motz, D Weygand, M Zaiser, and S Zapperi. Dislocation avalanches and the intermittency of crystal plasticity, 2008.

[78] P.D. Ispánovity, L. Laurson, M. Zaiser, I. Groma, S. Zapperi, and M.J. Alava. Avalanches in 2D Dislocation Systems: Plastic Yielding Is Not Depinning. *Physical Review Letters*, 112(23):235501, jun 2014.

[79] Brown LM. *Philos. Mag.*, 84:2501, 2004.

[80] J.D. Eshelby, F.C. Frank, and F.R.N. Nabarro. Xli. the equilibrium of linear arrays of dislocations. *The London, Edinburgh, and Dublin Philosophical Magazine and Journal of Science*, 42(327):351–364, 1951.

[81] J. D. Eshelby. The determination of the elastic field of an ellipsoidal inclusion, and related problems. *Proceedings of the Royal Society of London A: Mathematical, Physical and Engineering Sciences*, 241(1226):376–396, 1957.

[82] JD Eshelby. In progress in solid mechanics; sneddon, in; hill, r., eds, 1961.

[83] X. Markenscoff. On the shape of the eshelby inclusions. *Journal of Elasticity*, 49(2):163–166, 1997.

[84] X. Markenscoff. Inclusions with constant eigenstress. *Journal of the Mechanics and Physics of Solids*, 46(12):2297 – 2301, 1998.

[85] X. Markenscoff. Inclusions of uniform eigenstrains and constant or other stress dependence. *Journal of applied mechanics*, 65(4):863–866, 1998.

[86] V.A. Lubarda and X. Markenscoff. On the absence of eshelby property for non-ellipsoidal inclusions. *International Journal of Solids and Structures*, 35(25):3405 – 3411, 1998.

[87] J.P. Hirth and J. Lothe. *Theory of Dislocations, second ed.* Krieger Publishing Co., 1992.

[88] L.M. Brown. Slip bands, ellipsoids, pile-ups and cracks. *Transactions of the Royal Society of South Africa*, 58(2):103–110, 2003.

[89] B. Tippelt, J. Breitschneider, and P. Hähner. *Phys. Stat. Sol. A*, 163A:11, 1997.

[90] J.G Antonopoulos, L.M. Brown, and A.T. Winter. Vacancy dipoles in fatigued copper. *Philos. Mag.*, 34:549, 1976.

[91] J.G. Antonopoulos and A.T. Winter. *Philos. Mag.*, 33:87, 1976.

[92] A.S. Argon. *Strengthening Mechanisms in Crystal Plasticity*. Oxford University press.

[93] A. Donev, I. Cisse, D. Sachs, E.A. Variano, F.H. Stillinger, R. Connelly, S. Torquato, and P. M. Chaikin. Improving the density of jammed disordered packings using ellipsoids. *Science*, 303(5660):990–993, 2004.

[94] A. S. Malin and M. Hatherly. Microstructure of cold-rolled copper. *Metal Science*, 13(8):463–472, 1979.

[95] P. B. Hirsch and J. S. Lally. The deformation of magnesium single crystals. *Philosophical Magazine*, 12(117):595–648, 1965.

[96] J. A. Gorman, D. S. Wood, and T. Vreeland Jr. Mobility of dislocations in aluminum. *Journal of Applied Physics*, 40(2):833–841, 1969.

[97] U.F. Kocks, A.S. Argon, and M.F. Ashby. Thermodynamics and kinetics of slip. *Prog. Mater. Sci.*, 19:1–288, 1975.

[98] D. M. Goto, R. K. Garrett, J. F. Bingert, S. R. Chen, and G. T. Gray. The mechanical threshold stress constitutive-strength model description of hy-100 steel. *Metallurgical and Materials Transactions A*, 31(8):1985–1996, 2000.

[99] P.S. Follansbee and C. Frantz. Wave propagation in the SHPB. *Trans. ASME: J. Engng Mater. Technol.*, 105:61–66, 1983.

[100] D.A. Gorham. An effect of specimen size in the high strain rate compression test. *Le Journal de Physique IV*, 1991.

[101] W.G. Johnston and J.J. Gilman. Dislocation velocities, dislocation densities, and plastic flow in lithium fluoride crystals. *Journal of Applied Physics*, 30(2):129–144, 1959.

[102] V. R. Parameswaran, N. Urabe, and J. Weertman. Dislocation mobility in aluminum. *Journal of Applied Physics*, 43(7):2982–2986, 1972.

[103] A. Kumar. Viscous Drag on Dislocations at High Strain Rates in Copper. *Journal of Applied Physics*, 40(9):3475, 1969.

[104] A. Kumar. Viscous Drag on Dislocations at High Strain Rates in Copper. *Journal of Applied Physics*, 40(9):3475, 1969.

[105] A. Roos, J. De Hosson, H. Cleveringa, and E. Van der Giessen. *Fast-moving dislocations in high strain rate deformation*. University Library Groningen, 1999.

[106] G. Leibfried. Über den einfluß thermisch angeregter schallwellen auf die plastische deformation. *Zeitschrift für Physik*, 127(4):344–356, 1950.

[107] J. Hirth and J. Lothe. *Theory of Dislocations, 1st Edition*. 1968.

[108] J. Lothe. Theory of dislocation mobility in pure slip. *Journal of Applied Physics*, 33(6):2116–2125, 1962.

[109] A.V. Granato, F.A. McClintock, T. Vreeland, and K.M. Jassby. *Microscopic Mechanisms of Dislocation Drag*, pages 255–275. Springer US, Boston, MA, 1973.

[110] K. Yoshiaki and H. Yoshio. Lattice thermal conductivity of crystals containing dislocations. *Journal of the Physical Society of Japan*, 38(2):471–479, 1975.

[111] V. Al'shitz and V. Indenbom. Dynamic dragging of dislocations. *Soviet Physics Uspekhi*, 18(1):1, 1975.

[112] A.D. Brailsford. Anharmonicity contributions to dislocation drag. *Journal of Applied Physics*, 43(4):1380–1393, 1972.

[113] F.R.N. Nabarro. *Theory of crystal dislocations*. Clarendon Pr., 1967.

[114] J. Eshelby. *Phys. Rev.*, 90:248, 1953.

[115] J. Weertman. *Response of Metals to High Velocity Deformation*. 1961.

[116] J. Weertman and J. Weertman. *Dislocations in Solids*. 1980.

[117] J. Taylor. *Hypervelocity Impact Phenomena*. 1968.

[118] J.J. Gilman. The plastic resistance of crystals. *Aust. J. Phys.*, 13, 1960.

[119] J.J. Gilman. The limiting speeds of dislocations. *Metallurgical and Materials Transactions A*, 31(3):811–814, 2000.

[120] J. Gilman. Toward physically-based rate laws for dislocations. *Materials Science and Engineering A*, 322:126–131, 2002.

[121] A. Granato. Miscroscopic mechanissms of dislocation drag. *Metallurgical Effects at High Strain Rates*, page 319, 1973.

[122] G. I. Kanel, S. V. Razorenov, K. Baumung, and J. Singer. Dynamic yield and tensile strength of aluminum single crystals at temperatures up to the melting point. *Journal of Applied Physics*, 90(1):136–143, 2001.

[123] G.I. Kanel, V.E. Fortov, and S.V. Razorenov. Shock waves in condensed-state physics. *Physics-Uspekhi*, 50(8):771, 2007.

[124] G I Kanel. Unusual behaviour of usual materials in shock waves. *Journal of Physics: Conference Series*, 500(1):012001, 2014.

[125] B. Gurrutxaga-Lerma, M.A. Shehadeh, D.S. Balint, D. Dini, L. Chen, and D.E. Eakins. The effect of temperature on the elastic precursor decay in shock loaded fcc aluminium and bcc iron. *International Journal of Plasticity*, 96:135 – 155, 2017.

[126] R.A. Austin and D.L. McDowell. A dislocation-based constitutive model for viscoplastic deformation of fcc metals at very high strain rates. *International Journal of Plasticity*, 27(1):1 – 24, 2011.

[127] D.L. Olmsted, L.G. Hector, W.A. Curtin, and R.J. Clifton. Atomistic simulations of dislocation mobility in al, ni and al/mg alloys. *Modelling and Simulation in Materials Science and Engineering*, 13(3):371, 2005.

[128] K. J. Frutschy, R. J. Clifton, and M. Mello. High-temperature pressure-shear plate impact studies on ofhc copper and pure wc. *AIP Conference Proceedings*, 429(1):463–466, 1998.

[129] S.E. Grunschel and R.J. Clifton. Dynamic plastic response of aluminum at temperatures approaching melt. *Metallurgical and Materials Transactions A*, 38(12):2885–2890, Dec 2007.

[130] S. Grunschel, R.J. Clifton, and T. Jiao. Shearing resistance of aluminum at high strain rates and at temperatures approaching melt. *AIP Conference Proceedings*, 1426(1):1335–1338, 2012.

[131] L. Chen, D.C. Swift, R.A. Austin, J.N. Florando, J. Hawreliak, A. Lazicki, M. D. Saculla, D. Eakins, J. V. Bernier, and M. Kumar. Temperature dependence of dynamic deformation in fcc metals, aluminum and invar. *AIP Conference Proceedings*, 1793(1):110008, 2017.

[132] P.S. Follansbee and G.T. Gray. Dynamic deformation of shock prestrained copper. *Materials Science and Engineering: A*, 138(1):23 – 31, 1991.

[133] M.A. Meyers. A mechanism for dislocation generation in shock-wave deformation. *Scripta Metallurgica*, 12(1):21 – 26, 1978.

[134] H. Donth. Zur theorie des tieftemperaturmaximums der inneren reibung von metallen. *Z. Phys.*, 149:111–130, 1957.

[135] D. Preston, D. Tonks, and D. Wallace. Model of plastic deformation for extreme loading conditions. *Journal of Applied Physics*, pages 211–220, 2003.

[136] A.S. Khan and H. Liu. Strain rate and temperature dependent fracture criteria for isotropic and anisotropic metals. *International Journal of Plasticity*, 37:1 – 15, 2012.

[137] B.G. Sterling. Controlling in materials testing, 1968. US Patent 3,391,572.

[138] J. Mescall, R. Papirno, and J. McLaughlin. *Stress and deformation states associated with upset tests in metals", in "Compression Testing of Homogeneous Materials and Composites*. American Society for Testing and Materials, 1983).

[139] S.M. Walley. *Friction In Compression Testing*. DYMAT conference booklet, 2001.

[140] T. Male and V. Depierre. The validity of mathematical solutions for determining friction from the ring compression test. *Trans. ASME: J. Lub. Tech.*, 92:389–397, 1970.

[141] S.M. Walley, J.E. Field, P.H. Pope, and N.A. Safford. The rapid deformation behaviour of various polymers. 1:1889–1925, 1991.

[142] M.L. Lovato and M.G. Stout. Compression testing techniques to determine the stress/strain behavior of metals subject to finite deformation. *Metallurgical Transactions A*, 23(3):935–951, 1992.

[143] B. Hopkinson. A method of measuring the pressure produced in the detonation of high explosives or by the impact of bullets. *Philosophical Transactions of the Royal Society of London. Series A, Containing Papers of a Mathematical or Physical Character*, 213:437–456, 1914.

[144] H. Kolsky. The propagation of longitudinal waves along circular bars. *Philos. Mag. 7th Ser.*, 45:712–726, 1954.

[145] E.D.H. Davies and S.C. Hunter. The dynamic compression testing of solids by the method of the split Hopkinson pressure bar (SHPB). *J. Mech. Phys. Solids*, 11:155–179, 1963.

[146] A. Love. *A Treatise on the Mathematical Theory of Elasticity*. Cambridge University Press, 1927.

[147] B.A. Boley and C.C. Chao. Some solutions of the Timoshenko beam equations. *Trans. ASME: J. Appl. Mech.*, 22:579–586, 1955.

[148] P. D. Flynn and M. M. Frocht. On saint venant's principle under dynamic conditions. *Experimental Mechanics*, 1(1):16–20, 1961.

[149] C. Siviour. *High Strain Rate Properties of Materials using Hopkinson Bar Techniques*. PhD thesis, University of Cambridge, 2005.

[150] P. Pope D. Gorham and J. Field. An improved method for compressive stress-strain measurements at very high strain rates. *Proceedings: Mathematical and Physical Sciences*, 438(1902):153–170, 1992.

[151] G. Gary. Study of some aspects of dynamic testing with bars. In W K Nowacki and J R Klepaczko, editors, *New Experimental Methods in Material Dynamics and Impact*, pages 179–221. Institute of Fundamental Technological Research, Warsaw, Poland, 2001.

[152] DYMAT. Test recommendation: Dynamic compression testing using the split hopkinson pressure bar. 1999.

[153] N. Safford. *High strain rate studies with the direct impact Hopkinson bar*. Phd, 1988.

[154] N. Taylor. *Hot spots in Ammonium Nitrate, PhD Thesis*. PhD thesis, 2011.

[155] U.S. Lindholm. Some experiments with the split hopkinson pressure bar. *Journal of the Mechanics and Physics of Solids*, 12:317–335, 1964.

[156] H. Couque. The use of the direct impact hopkinson pressure bar technique to describe thermally activated and viscous regimes of metallic materials. *Philosophical Transactions of the Royal Society of London A: Mathematical, Physical and Engineering Sciences*, 372(2023), 2014.

[157] C. Avinadav, Y. Ashuach, and R. Kreif. Interferometry-based kolsky bar apparatus. *Review of Scientific Instruments*, 82(7):073908, 2011.

[158] L.J. Lea and A.P. Jardine. Application of photon doppler velocimetry to direct impact hopkinson pressure bars. *Review of Scientific Instruments*, 87(2):023101, 2016.

[159] L.J. Lea and A.P. Jardine. Two-wave photon Doppler velocimetry measurements in direct impact Hopkinson pressure bar experiments. *EPJ Web of Conferences*, 94:01063, sep 2015.

[160] O. T. Strand, D. R. Goosman, C. Martinez, T. L. Whitworth, and W. W. Kuhlow. Compact system for high-speed velocimetry using heterodyne techniques. *Review of Scientific Instruments*, 77(8):083108, 2006.

[161] N. Taylor. Camhetv, initial release. https://doi.org/10.5281/zenodo.884506, September 2017.

[162] Kulite Semiconductor Products INC. Kulite strain gage manual, 2011.

[163] D. Gabor. Theory of communication. part 1: The analysis of information. *Electrical Engineers - Part III: Radio and Communication Engineering, Journal of the Institution of*, 93(26):429–441, November 1946.

[164] H. Kuhn and D. Medlin, editors. *ASM Handbook Vol 8: Mechanical Testing and Evaluation*, chapter 6. 2000.

[165] H. Couque. The use of the direct impact Hopkinson pressure bar technique to describe thermally activated and viscous regimes of metallic materials The use of the direct impact Hopkinson pressure bar technique to describe thermally activated and viscous regimes of me. 2014.

[166] L. Pochhammer. Über Fortpflanzungsgeschwindigkeiten kleiner Schwingungen in einem unbegrenzten isotropen Kreiszylinder. *J. reine angew. Math.*, 81:324–336, 1876.

[167] C. Chree. The equations of an isotropic elastic solid in polar and cylindrical coordinates: Their solution and application. *Trans. Camb. Philos. Soc.*, 14:250–369, 1889.

[168] S.K. Samanta. *J Mech.Phys.Solids*, 19:117–135, 1971.

[169] D. A. Gorham. *J. Phys. D: Appl. Phys*, 22:1888–1893, 1989.

[170] S. Walley, J. Field, P. Pope, and N. Safford. Comparison of two methods of measuring the rapid temperature rises in split hopkinson bar specimens. *Rev. Sci. Instrum.*, (71):1766–1771, 2000.

[171] A. Eleiche and J. Duffy. Effects of temperature on static and dynamic stress-strain characteristics in torsion of 1100-0 aluminum. *Int. J. Mech. Sci.*, (17):85–95.

[172] C. Bacon. Measure de la tenacité dynamique de matériaux fragiles en flexion-trois-points á haute température - utilisation des barres de hopkinson, phd thesis, 1993.

[173] J. Lankford. Compressive strength and microplasticity in polycrysatalline alumina. *J. Mater. Sci.*, (12):791–796, 1977.

[174] H. Sizek and G. Gray. Deformation of polycrystalline ni3al at high strain rates and elevated temperatures. *Acta Metall. Mater.*, (41):1855–1860., 1993.

[175] J. Chiddister and L. Malvern. Compression-impact testing of aluminium at elevated temperatures. *Exper. Mech.*, (3):81–90, 1963.

[176] R. Kandasamy and N. Brar. Flow stress and material model study at high strain rate and low temperature. *High Pressure Science and Technology*, pages 1031–1034, 1994.

[177] S. Walley. Hopkinson bar testing at non-ambient temperatures. *DYMAT 2000 Booklet*, 2000.

[178] W. Ferguson, A. Kumar, and J. Dorn. Dislocation damping in aluminum at high strain rates. *Journal of Applied Physics*, 38(4):1863–1869, 1967.

[179] R.W. Armstrong. The yield and flow stress dependence on polycrystal grain size. *Yield, flow and fracture of polycrystals*, pages 1–31, 1982.

[180] H. H. Liu, S. Schmidt, H. F. Poulsen, A. Godfrey, Z. Q. Liu, J. A. Sharon, and X. Huang. Three-dimensional orientation mapping in the transmission electron microscope. *Science*, 332(6031):833–834, 2011.

[181] H. Couque. On the importance of recrystallization to reproduce the taylor impact specimen shape of a pure nickel. *EPJ Web of Conferences*, 94:02024", 2015.

[182] G. Benchabane, Z. Boumerzoug, I. Thibon, and T. Gloriant. Recrystallization of pure copper investigated by calorimetry and microhardness. *Materials Characterization*, 59(10):1425 – 1428, 2008.

[183] J. Davis. *Copper and Copper Alloys*. ASM International.

[184] B.L. Hansen, I.J. Beyerlein, C.A. Bronkhorst, E.K. Cerreta, and D. Dennis-Koller. A dislocation-based multi-rate single crystal plasticity model. *International Journal of Plasticity*, 44(Complete):129–146, 2013.

[185] D. Gorham. *Inst. Phys. Conf. Ser.*, (47):16–24, 1980.

[186] R. A. Govender and R. J. Curry. The "open" hopkinson pressure bar: Towards addressing force equilibrium in specimens with non-uniform deformation. *Journal of Dynamic Behavior of Materials*, 2(1):43–49, 2016.

[187] William N. Sharpe. *Springer Handbook of Experimental Solid Mechanics, Section 33.1.3*. 2008.

[188] V. Deshpande and N. Fleck. High strain rate compressive behaviour of aluminium alloy foams. *International Journal of Impact Engineering*, 24(3):277 – 298, 2000.

[189] B. Jiang, C. He, N. Zhao, P. Nash, C. Shi, and Z. Wang. Ultralight metal foams. *Scientific reports*, 5, 2015.

[190] L.C Forde, W.G Proud, and S.M Walley. Symmetrical taylor impact studies of copper. *Proceedings of the Royal Society of London A: Mathematical, Physical and Engineering Sciences*, 465(2103):769–790, 2009.

[191] R. Boddy. Damage in energetic materials, phd thesis, 2014.

[192] H. Kangarlou and A. Abdollahi. Thermodynamic properties of copper in a wide range of pressure and temperature within the quasi-harmonic approximation. *International Journal of Thermophysics*, 35(8):1501–1511, Aug 2014.

[193] M.H. Nadal and P. Le Poac. Continuous model for the shear modulus as a function of pressure and temperature up to the melting point: Analysis and ultrasonic validation. *Journal of Applied Physics*, 93(5):2472–2480, 2003.

[194] R.W. Armstrong, W. Arnold, and F.J. Zerilli. Dislocation mechanics of copper and iron in high rate deformation tests. *Journal of Applied Physics*, 105(2):023511, 2009.

[195] G.T Gray III. High-strain-rate deformation: mechanical behavior and deformation substructures induced. *Annual Review of Materials Research*, 42:285–303, 2012.

[196] M. Kiritani, T. Sota, T. Tawara, H. Arimura, K. Yasunaga, Y. Matsukawa, and M. Komatsu. Defect structures introduced in fcc metals by high-speed deformation. *Radiation Effects and Defects in Solids*, 157(1-2):53–74, 2002.

[197] A.A. Brown and D.J. Bammann. Validation of a model for static and dynamic recrystallization in metals. *International Journal of Plasticity*, 32–33:17 – 35, 2012.

[198] T. Suzuki, S. Takeuchi, and H. Yoshinaga. *Dislocation Dynamics and Plasticity*. Springer-Verlag Berlin Heidelberg, 1991.

[199] D.M. Dimiduk, C. Woodward, R. LeSar, and M.D. Uchic. Scale-free intermittent flow in crystal plasticity. *Science*, 312(5777):1188–1190, 2006.

[200] S.R. Bodner and Y.Y. Partom. Constitutive equations for elastic-viscoplastic strain-hardening materials. *ASME. J. Appl. Mech.*, 1975.

[201] U. Kocks. Laws for work-hardening and low temperature creep. *J Eng Mater Technol*, 1976.

[202] D.J. Steinberg, Cochran S. G., and Guinan M. W. A constitutive model for metals for applicable at high-strain rate. *J. Appl. Phys.*, 51:1498, 1980.

[203] D.J. Steinberg and C. M. Lund. A constitutive model for strain rates from 10 -4 to 10 6 s -1. *Journal of Applied Physics*, 65(4):1528–1533, 1989.

[204] S. Nemat-Nasser and Y. Li. Flow stress of f.c.c. polycrystals with application to ofhc cu. *Acta Materialia*, 46(2):565 – 577, 1998.

[205] S. Nemat-Nasser, W.G. Guo, and D.P. Kihl. Thermomechanical response of al-6xn stainless steel over a wide range of strain rates and temperatures. *Journal of the Mechanics and Physics of Solids*, 49(8):1823 – 1846, 2001.

[206] A. Rusinek and J.R Klepaczko. Shear testing of a sheet steel at wide range of strain rates and a constitutive relation with strain-rate and temperature dependence of the flow stress. *International Journal of Plasticity*, 17(1):87 – 115, 2001.

[207] A. Molinari and G. Ravichandran. Constitutive modeling of high-strain-rate deformation in metals based on the evolution of an effective microstructural length. *Mechanics of Materials*, pages 737 – 752, 2005.

[208] B. Farrokh and A.S. Khan. Grain size, strain rate, and temperature dependence of flow stress in ultra-fine grained and nanocrystalline cu and al: Synthesis, experiment, and constitutive modeling. *International Journal of Plasticity*, 25(5):715 – 732, 2009.

[209] R. Austin and D. McDowell. Parameterization of a rate-dependent model of shock-induced plasticity for copper, nickel and aluminium. *International Journal of Plasticity*, pages 134–154, 2012.

Appendix A

List of constitutive models

The models presented in this table are all covered in more detail in the author's review [49], with the exepction of the models of Hunter [19] and Hansen [184].

Year	Model	Citation	Modelled Rates	Main Features
1975	Bodner & Parton	[200]	10^{-3} - 1 s^{-1}	Work Hardening No temperature effects
1976	Voce & Kocks	[26, 201]	10 s^{-1}	Path dependent hardening
1980	Steinberg & Guinan	[202]	10^{5} s^{-1}	Temperature effects Shock waves
1983	Johnson & Cook	[27]	Up to 10^{4} s^{-1}	Instantaneous $\dot{\varepsilon}$ and T No path dependence
1987	Zerilli-Armstrong	[13]	4×10^{3} s^{-1}	Thermal activation Dislocation mechanics Grain size effects
1988	Mechanical Threshold Stress	[15]	10^{-4} - 10^{4} s^{-1}	Thermal activation Dislocation mechanics State variables
1989	Anand & Brown	[24]	10^{-2} s^{-1}	Activation energy Dynamic recovery

Year	Model	Citation	Modelled Rates	Main Features
1989	Steinberg and Lund	[203]	10^{-4} - 10^{6} s^{-1}	Extends Steinberg & Guinan to below shock
1998	Nemat-Nasser and Li	[204]	10^{-3} - 10^{4} s^{-1}	Dislocation based Thermal activation
2000	Gould &, Goldthorpe	[9]	Up to 10^{4} s^{-1}	Plastic stress state variable
2001	Nemat-Nasser, Guo & Kihl	[205]	10^{-3} - 10^{4} s^{-1}	Viscous drag
2001	Rusinek & Klepaczo	[206]	10^{-3} - 10^{9} s^{-1}	Thermal activation Multiple stress variables
2003	Preston, Tonks & Wallace	[135]	10^{-3} - 10^{9} s^{-1}	Thermal activation Shock waves
2005	Molinari Ravichandran	[207]	10^{-3} - 10^{5} s^{-1}	Characteristic mircostructural length
2009	Huang *et al.*	[47]	10^{-5} - 10^{6} s^{-1}	Phonons generating dislocation density
2009	Khan, Liang Farrokh	[208]	10^{-4} - 10^{3} s^{-1}	Thermal activation Grain size effects
2011	Austin & McDowell	[126, 209]	10^{-4} - 10^{8} s^{-1}	Includes weak shocks
2012	Gao & Zhang	[48]	10^{-3} - 10^{4} s^{-1}	Based on MTS model Uses drag at high rates
2015	Hunter & Preston	[19]	10^{-3} - 10^{8} s^{-1}	Adresses breakdowns in Arrhenius approximations
2013	Hansen *et al.*	[184]	10^{-3} - 10^{8} s^{-1}	Separates slip systems Separates barrier types